MAX-PLANCK-INSTITUT FÜR POLYMERFORSCHUNG IN MAINZ

Organic Radicals for Magnetic Materials through Controlling of Magnetic Exchange Interactions

Dissertation
zur Erlangung des Grades
“Doktor der Naturwissenschaften”
am Fachbereich Chemie, Pharmazie und Geowissenschaften der
Johannes Gutenberg-Universität in Mainz

Vorgelegt von

KUBANDIRAN KOLANJI

Ko. Pavazhangudi at Tamilnadu in India

Mainz, 2018

Dekan: Prof. Dr.

1. Berichterstatter: Prof. Dr.

2. Berichterstatter: Prof. Dr.

Tag der mündlichen Prüfung:

Die vorliegende Arbeit wurde in der Zeit von January 2015 bis November 2018 im Max-Planck-Institut für Polymerforschung in Mainz unter der Betreuung von Prof. Dr. Martin Baumgarten durchgeführt.

Ich danke Prof. Dr. Martin Baumgarten für seine wissenschaftliche und persönliche Unterstützung sowie für seine ständige Diskussionsbereitschaft.

Dedicated to My Parents

Table of Contents

Symbols and Abbreviations

Symbols

a_{ij}	Hyperfine coupling constant
a_{iso}	Isotropic hyperfine coupling (Fermi contact)
a_N	Nitrogen hyperfine coupling
a_H	Proton hyperfine coupling
B_o	Applied external magnetic field tensor
$\Delta B_{1/2}$	Peak width (Full width at half maximum)
C	Curie constant
D	Zero–field splitting parameter (axial)
d_{rr}	Distance between two spins
E	Zero–field splitting parameter (rhombic)
ΔE_{ST}	Singlet–triplet energy difference
g_e	Electron g–factor, $g_e = 2.0023$
g	Observed g–value
h	Planck's constant $\hbar = h/(2\pi) = 1.0545\times10^{-34}$ J·s
H	Spin Hamiltonian
H_{Ze}	Electron–Zeeman interaction
H_{HF}	Hyperfine interaction
I	Nuclear spin angular momentum
J_{intra}	Intra–molecular spin-spin exchange coupling constant
J_{inter}	Inter–molecular spin-spin exchange coupling constant
k_B	Boltzmann constant
L	Orbital angular momentum
M	Magnetization
M_S	Magnetic quantum number
N_A	Avogadro number
S	Spin quantum number
$\hat{S}_a\hat{S}_b$	Electron–pin operators
T	Temperature
T_C	Curie temperature
T_N	Néel temperature
y	Degree of biradical character
Ε	Extinction coefficient (cm^{-1}mol^{-1})
θ	Weiss constant
μ_B	Bohr magneton ($\beta = e\hbar/(2m_ec) = 9.2740 \times 10^{-24}$ J·T^{-1})
μ_{eff}	Effective magnetic moment
v	Frequency
χ_{mol}	Molar magnetic susceptibility

Abbreviations

AF	Antiferromagnetic
UB3LYP	Unrestricted Becke 3-Parameter (Exchange), Lee, Yang and Parr
BEC	Bose-Einstein condensation
BHA	2,3-Dimethyl-2,3-bis(hydroxylamino)-butane
BS	Broken-symmetry
CV	Cyclic voltammetry
DCM	Dichloromethane
DEP	Dynamic electron polarization
DMF	N,N-dimethylformamide
DMSO	Dimethylsulfoxide
DPPH	N,N’-diphenyl-N’-picrylhydrazyl
DFT	Density functional theory
EPR	Electron paramagnetic resonance
ESR	Electron spin resonance
eV	Electron volt
FD-MS	Field desorption mass spectrometry
HC	Hydrocarbon
HDVV	Heisenberg-Dirac-van Vleck
HF	Hartree-Fock
hfc	Hyperfine coupling constant
HOMO	Highest occupied molecular orbital
HRMS	High resolution mass spectrometry
HCl	Hydrochloric acid
IN	Imino nitroxide
LUMO	Lowest unoccupied molecular orbital
MeOH	Methanol
M.P.	Melting point
NBMOs	Non-bonding molecular orbitals
NBS	N-bromosuccinimide
nm	Nanometer
NN	Nitronyl nitroxide
NMR	Nuclear magnetic resonance
OFETs	Organic field effect transistors
QC	Quantum computing
QIP	Quantum information processing
RT	Room temperature
SOMO	Singly occupied molecular orbital
SQUID	Superconducting quantum interference device
TDAE	Tetrakis(dimethylamino) ethylene
Bu_4NF_4	Tetra-n-butylammonium fluoride
TEMPO	2,2,6,6-Tetramethyl-4-piperidine-1-oxyl
TLC	Thin layer chromatography
THF	Tetrahydrofuran
UNOs	Unrestricted non-bonding orbitals
UV-Vis	Ultraviolet-visible
ZFS	Zero field splitting

CHAPTER 1

INTRODUCTION

1.1 Magnetism

Magnetic materials play a significant role in the day–today's electronic technology. These materials are used in large number of devices and those are already employed in many electromagnetic instruments.[1] The two most common types of magnetism are accounted for the most of the periodic table of elements at room temperature. These main magnetic properties are known as diamagnetism and paramagnetism. All the electrons are paired and the overall net spin is zero in diamagnetic materials. On the other hand, paramagnetic materials have free/unpaired electrons and the net spin is non–zero.

The magnetic strength of the materials is determined by the magnetic susceptibility (χ) using the superconducting quantum interference device (SQUID) susceptometer by applying variable temperature in the presence of an applied magnetic field.

The susceptibility is represented by the ratio of magnetization *M* (magnetic moment per unit volume) to the applied magnetizing field intensity *H*.

$$\chi = M / H \tag{1—1}$$

The molar susceptibility [χ_M] of a paramagnetic substance is proportional to the thermodynamic temperature [T], which is given by,

$$\chi_M = C/T \tag{1—2}$$

Where C is the Curie constant:

$$C = N_A\beta^2g^2 S(S+1)/ 3k_B \text{ or } C = 0.125\, g^2 S(S+1) \text{ cm}^3 \text{ K /mol}^{-1} \tag{1—3}$$

and N_A is Avogadro's number, k_B is the Boltzmann constant, β is a constant called the Bohr magneton (BM). The Curie constant provides the convenient check of the spin concentration of the sample (C = 0.375 *emu K/mol* for S = ½).

After modification of the Curie law, based on the interactions among the individual magnetic moments, Curie–Weiss law is obtained, stating that,

$$\chi_M = C/(T - \theta) \tag{1—4}$$

where θ is the Weiss constant in temperature units, a characteristic of the material. It relates the total dipole–dipole exchange interactions [*J*] of magnetically active centers with all its magnetic neighbors' *z* (nearest, next nearest, etc.).

$$\theta = [2S(S+1) / 3k_B] \Sigma z_i J_i \quad (1—5)$$

When the spins are coupled in a parallel manner χ is enhanced i.e. $\theta > 0$ [ferromagnetic], and when the spins are coupled in an antiparallel manner χ is suppressed i.e. $\theta < 0$ [antiferromagnetic].

$$\chi_M = N_A\beta^2g^2 S(S+1)/ 3k_B (T-\theta) \quad (1—6)$$

In case substances with interacting magnetic moments, and where the orbital contribution to the magnetic moment is significant, the molar susceptibility is represented as

$$\chi_M = N_A\beta^2g^2 J(J+1)/ 3k_B (T-\theta) \quad (1—7)$$

Here the resultant total angular momentum [*J*] becomes,

$$J(J+1) = L(L+1) + S(S+1) \quad (1—8)$$

The quantum number L is the resultant orbital angular momentum of the unpaired electron present in the atom (i.e. L is zero for a completely filled orbital). Such that *J = S* the equation is simplified. It can be done by defining effective magnetic moment (η_{eff}) as $g\sqrt{S(S+1)}$ or $\eta^2_{eff} = g^2 S(S+1)$ and combining all of the constants to give

$$\chi_M = N_A\beta^2/3k_B]\eta^2_{eff}/ (T-\theta) \approx 0.125\, \eta^2_{eff}/(T-\theta) \quad (1—9)$$

This eq. 1—9 allows us to calculate the η_{eff} of an ion or radical which can be rewritten as

$$\eta_{eff} = 2.828\, [\chi_M (T-\theta)]^{1/2} \quad (1—10)$$

1.1.1 Type of magnetic materials

Based on their bulk magnetic behavior, the magnetic materials are classified in six categories in presence of applied external magnetic field (H). The electrons in a magnetic material are aligned/opposed to the direction of the field and those give rise to the bulk magnetic properties. These magnetic properties are diamagnetism, paramagnetism, ferromagnetism, antiferromagnetism, ferrimagnetism and metamagnetism (canted ferrimagnetism) depending on their bulk magnetic behavior (figure 1.1.1). Any materials are falling into one of these categories.

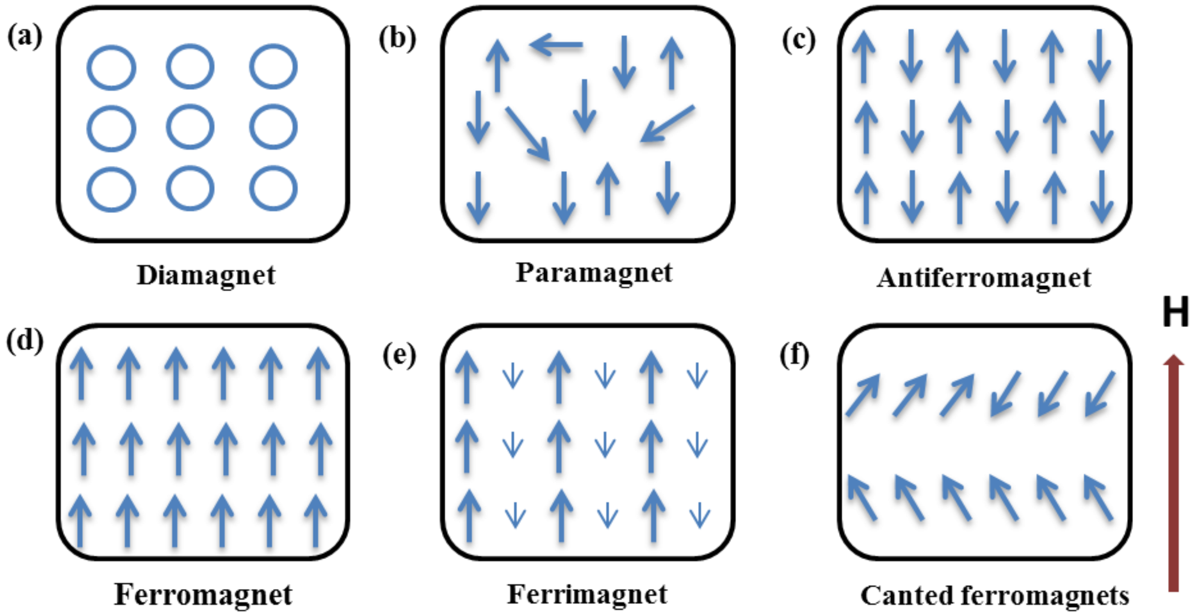

Figure 1.1.1: The arrangement of spins for (a) diamagnet, (b) paramagnet, (c) antiferromagnet, (d) ferromagnet, (e) ferrimagnet and (f) canted ferromagnets.

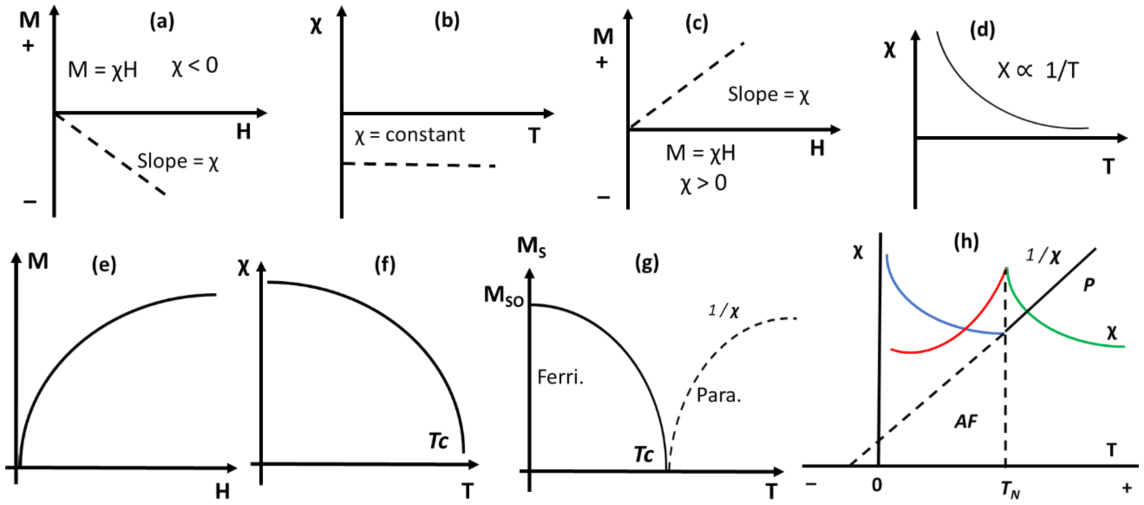

Figure 1.1.2: Schematic representation for variation of magnetization in presence of the magnetic field (H) and variation of susceptibility *(χ)* with respect to temperature (T) for (a), (b) diamagnetic, (c), (d) paramagnetic, (e), (f) ferromagnetic and (g) ferrimagnetic materials respectively. (h) Variation of susceptibility and inverse susceptibility with respect to temperature for antiferromagnetic materials.

(a) Diamagnetism

The diamagnetic substance contains only spin–paired electrons. However, when this substance is exposed to an applied magnetic field, all the electrons are opposed to the field (figure 1.1.1.a) and a magnetization is produced. The magnetic response inside the material opposes in the applied field, thus susceptibility *(χ)* is small and negative figure 1.1.2.a. There are no magnetic interactions occur with neighboring units, it tends to exclude a magnetic field from its interior. Note that when the field is zero the magnetization is also zero. The other characteristic behavior of diamagnetic material is that the susceptibility is temperature independent (figure 1.1.2.b), thus, there is no change in susceptibility with variable temperature.

(b) Paramagnetism

In circumstance where the adjacent unpaired electrons have not any effect on each other and the spins are in random directions, then the corresponding magnetism is known as paramagnetism (figure 1.1.2.b). In a paramagnetic substance, the individual magnetic moments do not interact magnetically i.e. $J = 0$, like diamagnetism. The magnetization is zero in absence of external magnetic field. Hence, there is no change in the magnification curve due to an unpaired electron and randomized spin moments not aligned. However, in the presence of a field, there is a partial alignment of the magnetic moments in the direction of the field, resulting in a net positive magnetization and positive susceptibility. According to figure 1.1.2.c, for a paramagnetic substance, χ is zero and the magnetic interaction also zero ($J = 0$) at room temperature, upon further cooling to low temperature, there are changes in χ and the magnetization of the substance is higher than that of empty space. Further, paramagnetic substances have a temperature dependent susceptibility (figure 1.1.2.d) which obeys the Curie Law. The paramagnetic susceptibility is small at ordinary temperatures (>>100 K) and in moderate fields, (but larger than the diamagnetic contribution). On the other hand, when the temperature is very low (<<100 K) or the field is very high paramagnetic susceptibility is independent of the applied field.

(c) Ferromagnetism

The spins can be easily switched to a uniform direction with adjacent spins and they are aligned parallel then they are classified as ferromagnetic. For a ferromagnetic substance, the spins are spontaneously parallel to one another in microscopic domains leading to a permanent magnetization. The application of a magnetic field causes the domains to point along the field even when the field is removed (figure 1.1.1.d). The χ is large and positive, dependent on the magnetic field, temperature, and the nature of the sample. For a substance, that shows bulk ferromagnetism, a transition occurs at a temperature known as Curie temperature (T_c). The saturation of the magnetization goes to zero at the Curie temperature. A typical plot of magnetization *vs* temperature for magnetite is shown figure 1.1.2.f.

(d) Antiferromagnetism

For the antiferromagnetic materials, neighboring spins of equal moments are coupled in an antiparallel fashion, in other words, neighboring spins are pointing in opposite directions (figure 1.1.1.c). This type of magnetic ordering is called antiferromagnetism, resulting in a lowering of the magnetization. The susceptibility of these materials are nearly non–zero at room temperature, while cooling, the susceptibility is increased. The magnetic interaction J is smaller than zero ($J < 0$) i.e. negative or positive, in which is depending on definition of Hamiltonian $H = J.S_i.S_j$ or $H = -J.S_i.S_j$. The indication to antiferromagnetic material (AFM) is the characteristic behavior of susceptibility above a critical temperature, called the Néel temperature (T_N). The magnetic susceptibility is a maximum at T_N. Thus, above T_N, the susceptibility decreases and obeys the Curie-Weiss law for paramagnets as shown in the figure 1.1.2.h, a negative intercept indicating negative exchange interactions.

(e) Ferrimagnetism

The ferrimagnetism occurs when unequal spin moments couple with opposite signs in a way to leave a net magnetization of the materials. The spins are aligned in an antiparallel arrangement, but the spins in each direction have different magnitudes (figure 1.1.1.e) and thus the substances have an overall magnetic moment, in which case the substance is known as ferrimagnet. These materials follow a temperature dependence of magnetization and susceptibility at Curie transition (Néel transition) in a similar behavior as the ferromagnetic materials shown in figure 1.1.2.g. These materials show significantly large magnetization below the magnetic transition temperature, like ferromagnetic materials. Hence, the temperature dependent behavior is clubbed with that of ferromagnetic materials.

(f) Metamagnetism or canted ferrimagnetism

The transformation from the antiferromagnetic state to high spin state, i.e., the spin alignment showed in figure 1.1.1.c is transformed to that shown in figure 1.1.1.d by the applied magnetic field. This is called metamagnetism (figure 1.1.1.f).

1.2 General aspects of molecular design of organic magnetic materials

During the past few decades, organic chemistry has been playing a major role in the design and synthesis of potentially useful magnetic materials.[2-6] To achieve, novel properties of these materials one requires a combination of multidisciplinary expertise in the areas of chemistry, physics, and engineering. Different approaches are used to obtain relevant magnetic properties of these materials. For examples, inter– and intra–molecular magnetic exchange interactions are essentially considered to analyze ground state spin multiplicities of the organic molecules.

At the beginning of the 1930's, mostly the neutral conjugated open–shell molecules, known as non–Kekulé molecules were a focused for the organic magnetic materials.[7] Hund's rule was applied for open–shell organic molecules to analyze atomic ground state of the spin multiplicities.[8, 9] Based on the number of unpaired electrons, the triplet ground state is expected for all the diradical system. In accord with to Hund's rule, the spin multiplicities were expected to be spin equivalent to afford the highest spin state, but this model was applied to only few stable diradical systems. Further, Hückel proposed[10] in 1936, that the ground state multiplicities of the non–Kekulé molecules are not necessarily governed by Hund's rule. He explained by an equivalent of modern fragment molecular orbital (FMO) approach. The triphenylmethyl radical is taken into account for the Schlenk–Brauns hydrocarbon, where it is possible to isolate the two unpaired spins in non–interacting portions of the molecule leading to a singlet ground state or near degeneracy of triplet and singlet states of the molecule (figure 1.2.1).[11]

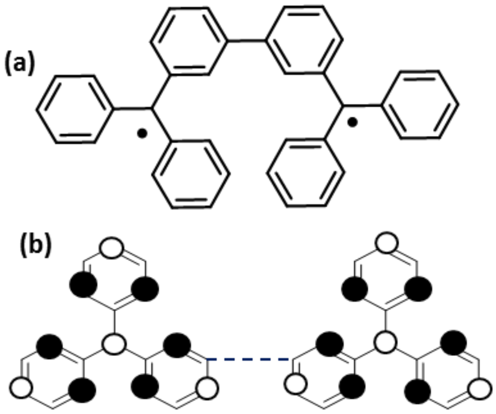

Figure 1.2.1: Schlenk–Brauns hydrocarbon (a) molecular structures and (b) molecular orbital modeled by weak interaction of triphenylmethyl radical of singly–occupied molecular orbitals.

In the 1950's Longuet–Higgins reported[12] parity (electron pairing into *pi*–bonds) models which described a connectivity–based approach for predicting the ground state multiplicity of alternant conjugated organic molecules given in equation 1.2—1, 1.2—2 and figure 1.2.2.

$$\text{NBMOs} = \text{N}-2\text{T} \qquad (1.2—1)$$

$$S = 0.5\,(n^{*} - n^{\circ}) = 1 \qquad (1.2—2)$$

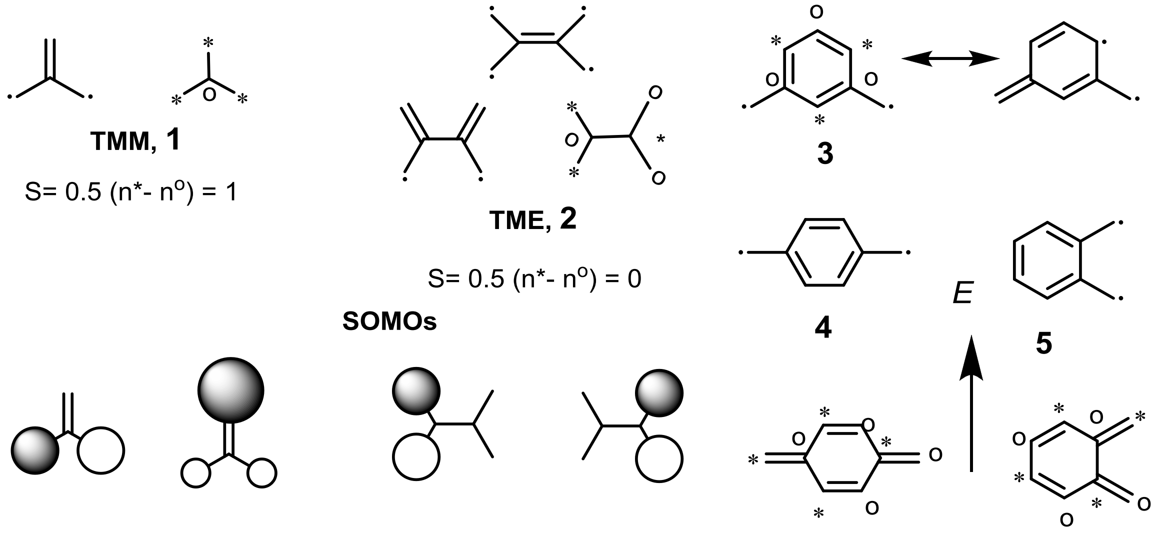

Figure 1.2.2: Structure and spin state of **TMM, (1)**, **TME, (2)**, The SOMO distribution in **1** and **2** are given as illustration of disjoint and non-disjoint scaffolds, diradical of **4** and **5** vs. quinoid for *p*- and *o*–xylylene.

For example, the trimethylenemethane (**TMM, 1**), tetramethyleneethane (**TME, 2**) and *m*–xylylene, **3** are expected to have triplet high–spin ground states, (figure 1.2.2) while *p*– and *o*–xylyene **4**, **5** should prefer the quinoid spin paired structure, being much lower in energy than the open shell geometry.

Mataga reported in 1968 that the *m*–phenylene linkage of unpaired spin acts as a universal ferromagnetic (FM) exchange unit. In 1977–1978 Ovchinnikov,[13] described a model for alternant conjugated *non*– Kekulé molecules that is based on a reorganization of the Pariser–Parr–Pople Hamiltonian describing electron exchange. He went beyond simple non–Kekulé molecules as putative targets of his model. Using this approach, both **TMM** and ***m*–xylylene** are expected to have triplet high–spin ground states, but **TME** is expected to have a singlet ground state. In 1982 Klein illustrated a model for alternant conjugated non– Kekulé molecules that is similar in principle to that of Ovchinnikov.[13] In 1983 Tyutyulkov and coworkers[14, 15] extended the parity approach to non–alternant systems, which they termed as non–classical polymers. In 1977 Borden and Davidson first described[16] the joint *vs.* non–disjoint classification of non–Kekulé molecules. They pointed out that linkage across inactive sites results in very small exchange interactions, a near–degeneracy of spin states, and the possibility of a low spin ground state. The **TME** is similarly treated by fragment analysis but it is predicted by equation 1.2—2 to have a low spin ground state, while pentamethylenepropane **(PMP)** is predicted to have a high spin ground state.

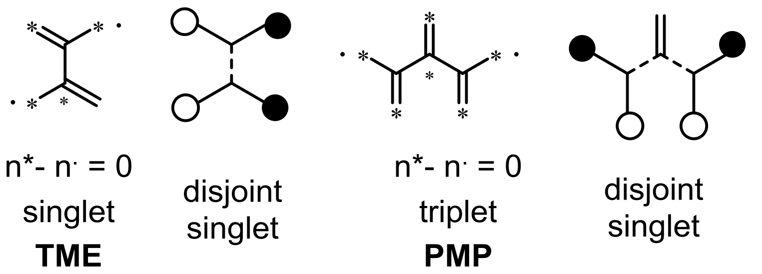

Figure 1.2.3: Structure and spin state of TME, and PMP

The spin polarization (SP) model proposed by McConnell and Ovchinnikov[13, 17], these arguments are used for *non*–Kekulé molecules. The predictions of the SP models are related in most cases to those of equation 1.2—2. However, the SP model allows generalization beyond radicals and alternant systems. One may incorporate atoms with two electrons in a single π–orbital center (2e/lc) such as oxygen and nitrogen, to give super exchange coupling between the connected sites. One may treat non-alternant systems; if one considers that any two connected sites with the same sign of electron spin will have near-zero spin density. One may also treat systems with more than one type of exchange, such as carbenes and nitrenes, in which a large localized sigma spin density site polarizes the π–spin density on the same atom to have the same sign. Itoh[18, 19] has shown that a valence bond SP approach is quantitatively successful in describing ground state spin multiplicities and spin density distributions for polycarbenes.[18] Initially Lahti, [20-23] and lwamura [24, 25] have proved the qualitative success of the SP model for a variety of dinitrenes. Hence, the SP model is simple and intuitive to apply, and successfully describes the qualitative ground state of the large majority of conjugated non– Kekulé molecules examined up to date.

1.3 Molecular design for stable organic radical for magnetic materials

Stable organic molecules which have one or more "*unpaired*" electrons are known as organic free radicals. These molecules can be used to obtain magnetic materials with different approaches. The unpaired electron spins can be delocalized onto multiple atoms, particularly for organic π–conjugated aromatic molecules and poly–radical systems. In some cases, the electrons are localized on only N–O units, for example TEMPO based materials. Several examples of the radical spin units are shown in the figure **1.3.1**.[26]

In order to achieve desired magnetic properties of the organic radical molecules, the cooperative interactions between their unpaired electrons is very important. The control of such long–range spin–spin interactions turned out to be extremely hard to achieve in the magnetic materials. It is therefore not surprising that three decades passed by since high–spin molecules with parallel spin alignment in the bulk materials were developed. In the year 1963, McConnell suggested the theoretical possibility of organic based magnetic materials. According to this, the spin carrier interaction occurs by through–space models to build up the bulk magnetization of ferromagnetic materials. The assembling of the long-range interactions among spin carriers consist of the following sequence of steps: (1) the design of the isolated molecular unit with one or two interacting entities; (2) a large molecule with several interacting entities; (3) mesoscopic–size molecules with added complexities; and (4) assembly of molecules to supramolecular clusters, monomolecular layers, or bulk solids.

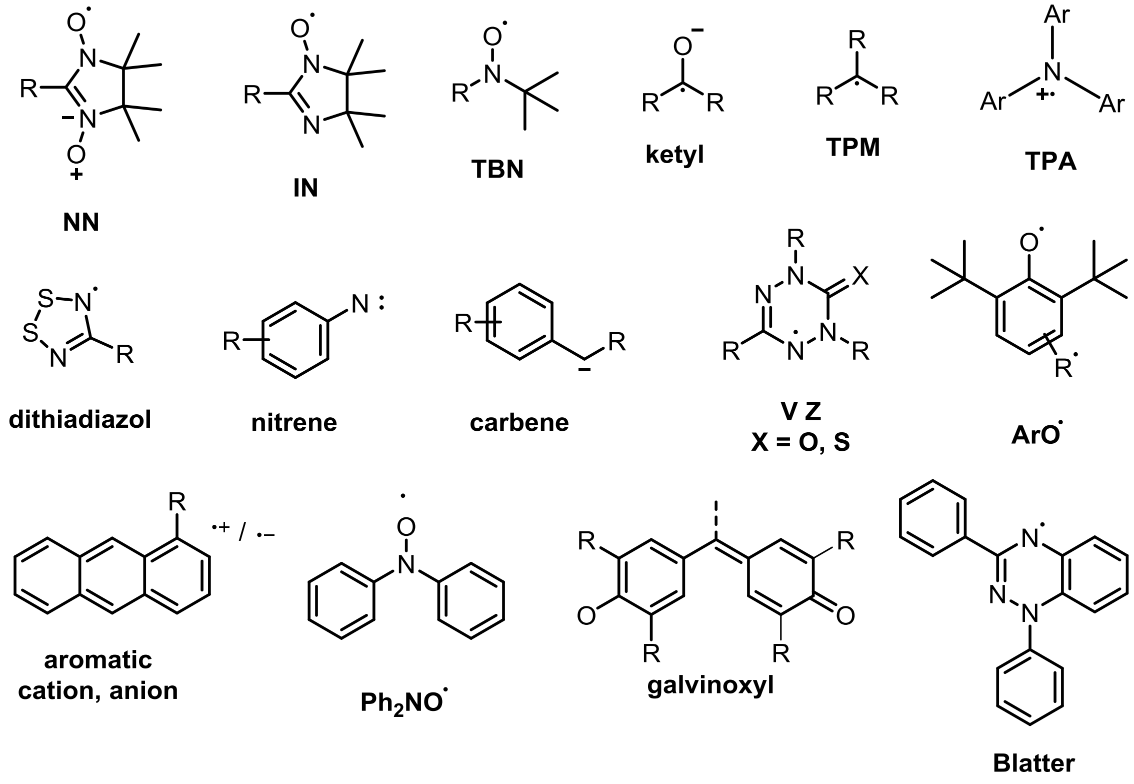

Figure 1.3.1: Some examples of organic stable radicals (NN = nitronyl nitroxides, IN = Imino nitroxides, TBN = *tert*–butyl–nitroxides, TPM = triphenylmethyl, TPA = triphenylamine, VZ = Verdazyl, ArO$^{\cdot}$ = Phenoxyl radical, and Blatter = benzotriazinyl radicals.

The purposes of such a methodology over rational design and synthesis of molecules and molecular assemblies are to prepare either materials with superior properties compared to their existing "natural" or artificial counterparts, or to gain better insight to more complex systems. From the synthetic organic chemist's viewpoint, the first point is crucial. This suggests the research of novel spin–containing building blocks (i.e. free radicals and radical ions) and the definition of their intra– and Inter–molecular magnetic exchange coupling. Henceforth, among the several radical spin carriers, we focus on the work to nitroxides based radicals due to their stability, liability of the spin and easiness to handle.[27]

1.4 Nitroxides radicals

A nitrogen atom attached to an oxygen atom with one free electron (>N—O•) is called nitroxide radical. These molecules are stabilized by two resonance structures shown in figure 1.4.1, where the R_1 and R_2 are attributed to the stability of the molecular systems.[28]

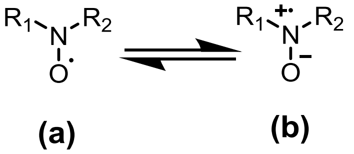

Figure 1.4.1: Resonance structures of nitroxide radicals

Most of the nitroxide derivatives are stable under ambient conditions. The steric factor and the conjugation are responsible for the stability of the molecules. Steric effect helps to avoid the dimerization, polymerization, or some other side reaction of the molecules. Furthermore, the free electron is stabilized by conjugation in the molecules. Hence, both are crucial to stabilize the nitroxides radical molecules. Most of the nitroxides derivatives of the radical are easily purified by column chromatography and crystallization methods. The nitroxide radical material chemistry is described in several books and reviews.[26]

1.4.1 Type of nitroxides radicals

Nitroxides radical are classified into various types based on substituents present in the molecule and these are explained below.

(a) *tert*–butyl–nitroxides (NO)

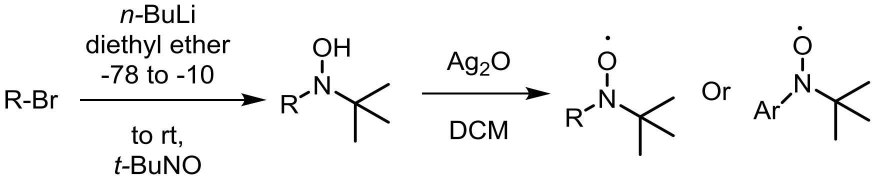

Figure 1.4.2: Synthetic route and structure of the **NO** radicals

The **NO** structure is carrying a radical (>N—O•) moiety with *tert*–butyl group and different substituents of R groups. The R groups may vary with different aliphatic and aromatic units. They have been extensively studied in spin probes and spin traps. The synthetic path way and structure is given in the figure 1.4.2. The synthesis involved mainly two steps reaction, such as alkyl or aryl bromides treated with *n*-butyllithium followed by *t*–BuNO. The molecules have enough stability, easiness to synthesis and ability to delocalize over π–spacer on the aryl groups.

(b) Nitronyl nitroxides radicals (NN)

Ullmann first synthesized nitronyl–nitroxides (NN) in 1972.[29] Generally NN is synthesized from saturated aldehydes. The synthesis route and structure of the NN is given the figure 1.4.3. Synthesis involves condensation of aldehyde with bishydroxylamine followed by oxidation. The R group varies with different substituents.[30-33]

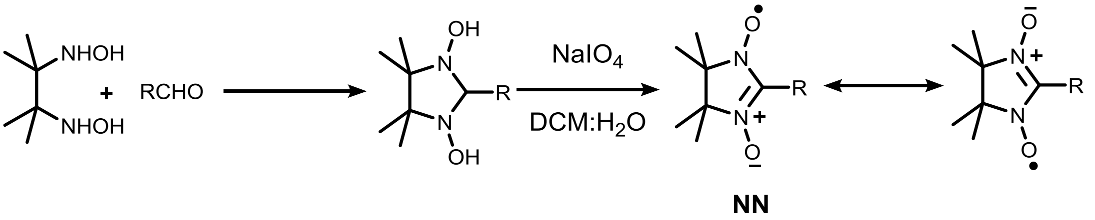

Figure 1.4.3: Synthesis of organic stable nitronyl nitroxides **(NN)** radicals

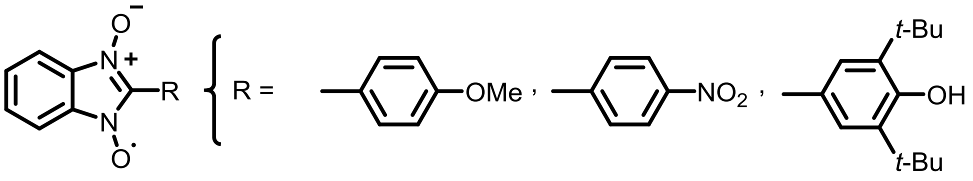

Figure 1.4.4: Structure of the benzannelated derivatives nitronyl nitroxides **(NN)** radicals

The two >N—O units connected by carbon atom in the five membered ring occupied by one free electron with Zwitterion structure is known to be NN radicals. The electronic structure of NN is well described previously. Most of the NN derivatives are more stable at room temperature. Similarly other structural NN radicals are also known, for example, Rey has synthesized pyrimidinyl based NN molecules and benzannelated derivatives. The electronic structures are nearly similar to those of NN radical structure. These building blocks are used for the organic magnetic materials and several other applications.[34, 35]

(c) Imino nitroxides (IN)

The synthesis and structure of the imino nitroxides (IN) is given in figure 1.4.5. In this, >N—O group is conjugated to a C=N moiety, in the five membered ring. The IN is generally more stable compared to the corresponding nitronyl nitroxides.[36] determined by EPR spectroscopy, neutron diffraction, and computational studies indicate that spin on the nitroxide nitrogen is substantially larger than on the imino nitrogen, though the latter nitrogen does possess substantial spin density. In contrast to the NN in the imino nitroxides the carbon atom of the NCNO moiety is not necessarily a node of the SOMO, but experimentally negative spin population is observed on this carbon atom.[37]

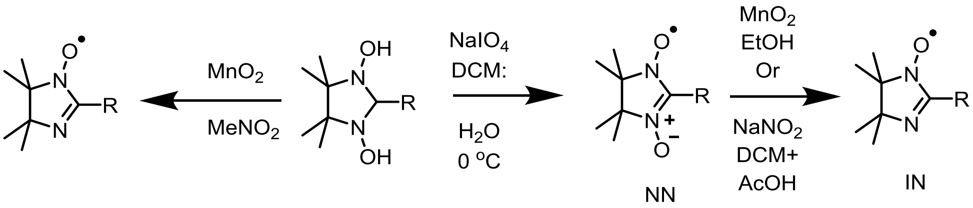

Figure 1.4.5: Organic synthesis and structure of the stable imino nitroxide radicals

1.5 Application of organic radicals

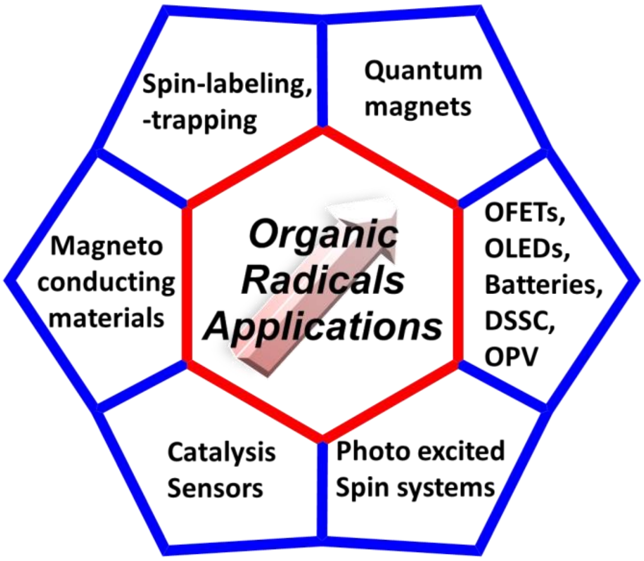

Figure 1.5.1. Some of the applications of organic radicals.

Organic materials are suitable for numerous applications, because of a number of advantages such as, the versatile molecular designs, adaptable synthetic procedures, soluble in organic solvents, ease of processing, optical transparent, possessing controllable electronic properties, lightweight, and low-cost manufacturing. Besides having the above merits for organic radical materials and possess an additional advantage, which is that they are powerful spin probe of the unpaired electrons in the system. They are used for variety of specific application, some of them represented in figure 1.5.1 and explained below.[38-40]

1.5.1 Quantum computers

The potentially most fascinating applications of organic radicals are employed in the development of quantum computers.[41, 42] This is one of the very recent advanced topics in information technology which gives all the advantages of quantum computing and quantum information processing (QC/QIP) in quantum science–related fields. The main important core of the quantum computer is the quantum *bit*, or *qubit*, as a two–level system that not only can access the two states $|0\rangle$ and $|1\rangle$, but also can be arranged in any *superposition* of these two states $\Phi = \alpha|0\rangle + \beta|1\rangle$. Qubits can be atoms, ions, photons and electrons. They can be used as both computer memory and processor. Because a quantum computer can access multiple qubit states simultaneously, it has the potential to be millions of times more powerful than today's most powerful supercomputers.

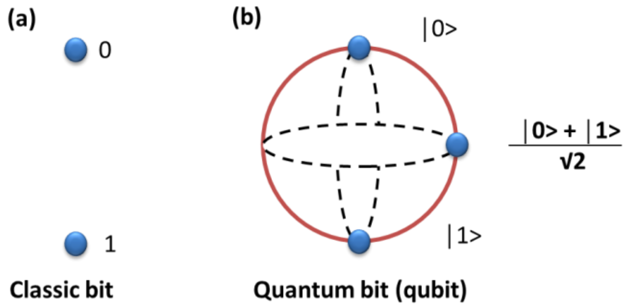

Figure 1.5.2. Diagrammatic representation of classic bit and quantum bit

The quantum algorithms reduce the CPU time by many orders of magnitude. Preparation and propagation of the quantum state occur within the quantum hardware framework (or QPU).[43]

The optimization of the parameters of the quantum state is achieved on the CPU by minimizing an objective function (Guerreschi and Smelyanskiy, 2017). The same scheme is applied to other algorithms such as quantum autoencoders.[44, 45]

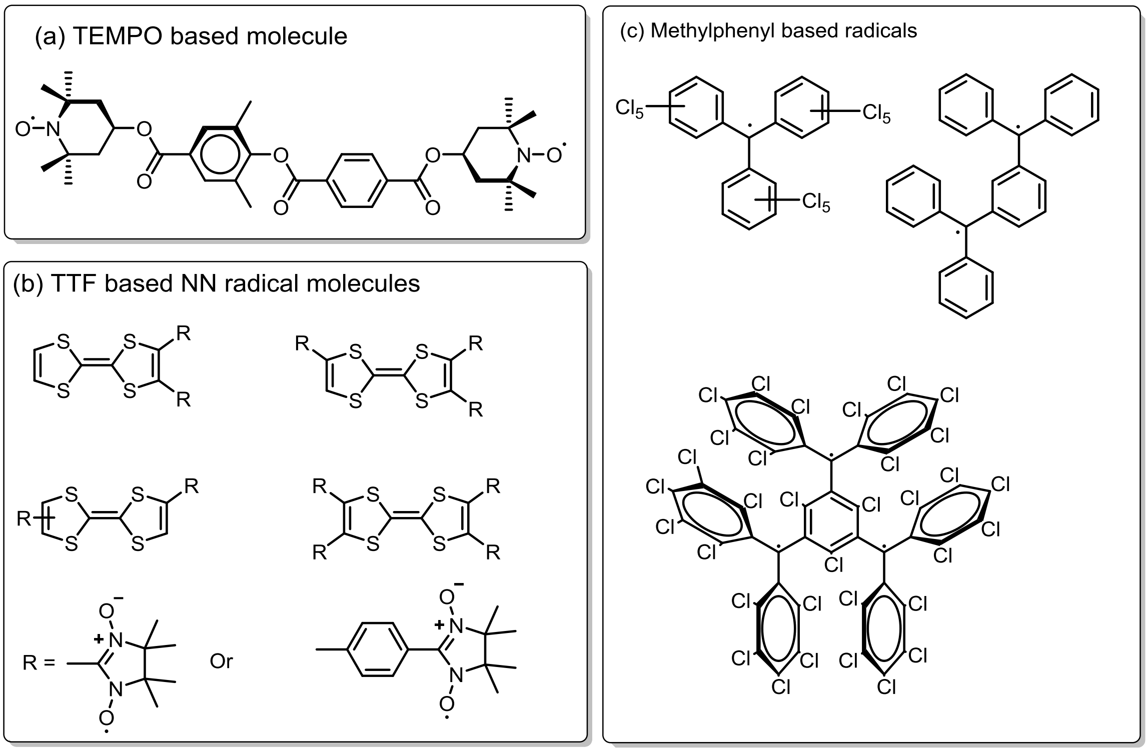

Figure 1.5.3: (a) TEMPO based molecule, (b) TTF based NN radicals and (c) Methylphenyl based molecules for spin qubit systems.

The currently available qubits face the drawback of stability and scalability. The electron spin qubits are a beneficial over nuclear spin qubits in the preparation of initialized states. This is due to the gyromagnetic ratio for the nuclear spin which is 103 times smaller than that of electron spin. This contributes to the low polarization of spin on the system.[46, 47] Takui and co-workers reported in 2012 that a weakly coupled biradical might act as a qubit. Such qubit forms a constructing QC providing the possibility of building controlled–NOT (CNOT) gate operations.[48] The CNOT gate operations are essentially important gates to constitute a universal set of quantum gates together with well–defined single qubit operation. Other examples of the spin qubits are organic electron donors or acceptors such as tetrathiafulvalene (TTF) which can fulfil the same role, given in the figure 1.7.3.b.[49]

1.5.2 Organic field effect transistors (OFETs)

Organic field-effect transistors (OFETs) are extensively studied due to their potential application in integrated circuits. Most of the research works are primarily focused on improving the fundamental electrical properties of the organic semiconductors and on developing the device fabrication techniques. Further radical substituted organic molecules are also used for the semiconducting materials (figure 1.7.5).[50-54]

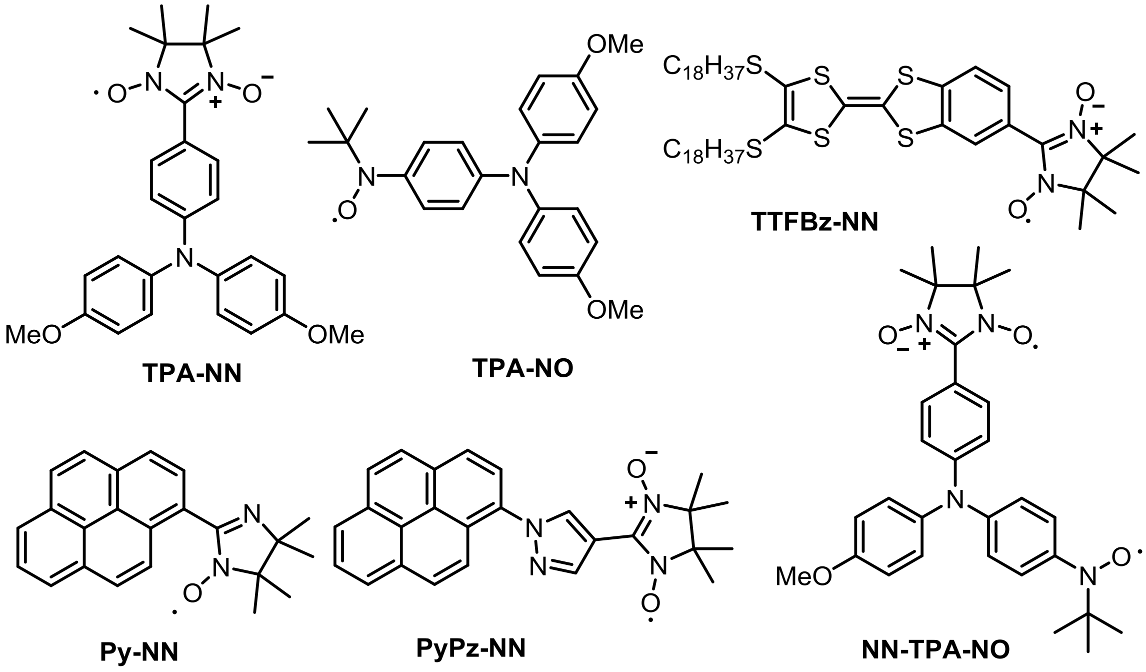

Figure 1.5.4: Organic radical molecules for organic field-effect transistor (OFETs) applications

1.5.3 Organic light-emitting diodes

Organic light-emitting diodes (OLEDs) are one of the very active research areas in organic electronics.[55-57] This is being expected for the next generation flat panel displays and light sources. Most of the research work focuses on the fluorescent and phosphorescent materials using closed–shell molecules. Recently, the open–shell organic molecules are used as an emitter of OLEDs device.[58-60]

Moreover, radical substituted organic molecules are used for the novel method to suppress polaron pair recombination at the donor–acceptor domain interfaces. Due to that, the efficiency was improved in the organic bulk heterojunction photovoltaic solar cells (BHJ–OPV) by doping the device active layer with galvinoxyl spin 1/2 radical.[61, 62] In addition, the radical containing molecules are used in dye sensitized solar cells DSSC,[63-65] a cathode and/or anode materials in batteries.[66, 67] Further, organic radical are used in catalysis,[68, 69] sensors,[70-72] magneto conducting materials,[73-75] photo excited spin systems,[76, 77] spintronics.[3, 78, 79] And they were finding in quantum molecular magnets,[80, 81] spin–labeling,[82] spin–trapping,[83] magnetoconducting materials,[73, 74] magnetic resonance imaging,[84] biomedicine,[85] organic photo excited spin systems,[76] potential use in bio-applications.[86] They also have been used as a ligand to form metal-organic complexes with transition metals and observed ferromagnetism, ferrimagnetism or anti–ferromagnetism.[87]

1.6 Magnetic exchange interaction

The exchange between two or more unpaired electrons is known as the magnetic exchange interactions.[88] Mostly, these interactions are occurred among the neighboring spins, which might be ferromagnetic or antiferromagnetic interactions. The exchange interactions are mediated by different kind of mechanisms, which are depending on the nature of the materials. For the magnetic materials, magnetic exchange interactions are typically determined in the Heisenberg spin Hamiltonian.[89] According to this, the exchange energy of the two magnetically interacting atoms/molecules i and j are bearing electron spins S_i and S_j (eq. 1.6.1) is given by

$$H = -2J\,\mathbf{S}_i.\mathbf{S}_j \tag{1.6.1}$$

where J is the magnitude of the magnetic exchange interaction. The spin distribution of a system depends on whether the two spins are parallel or antiparallel. The Pauli principle excludes two electrons of the same spin are being at the same place at the same time. It does not exclude two electrons of opposite spin. Thus, the electrostatic energy of a system is depending on the relative orientation of spins. If there are direct coupling between the direction of the two electrons, and the exchange energy of the two electrons is $2J\,\mathbf{S}_i.\mathbf{S}_j$. This approximation is suitable for ferromagnetism to treat as classical angular momentum vectors.

Most of the organic molecules have closed shell electronic structure. Hence, they possess singlet ground state with an equal number of electrons having α and β spin. They are the therefore diamagnetic nature. Some of the organic molecules have open–shell structures where the electrons are not paired. These molecules have one odd electron and therefore doublet ground state. These free radicals are paramagnetic compounds. The arrangement of spins in organic molecular systems becomes an issue when there is an interaction between two doublet centers as in diradicals/biradicals and radical pairs. Then Coulombic repulsion between electrons lifts the zeroth–order degeneracy and gives rise to singlet and triplet states of different total energy for these chemical pieces. The doublet radical center pair's state have the lower in energy. The conditions for having the ground triplet states and the importance of the singlet—triplet radical pairs in free radical reactions are sufficiently discussed in the literature.[88]

Most of the research groups are working for the high spin molecules, which is known as ferromagnetic material prospered on the basis of McConnell's theory on the basis of on two approaches. First, for the advantage of a weak hyper conjugative interaction of a short chain is considered facilitating high–spin molecules. The other approach focuses on a design of molecular stacking of spin–distributed aromatic rings leading to intermolecular spin alignment. Hence, the molecular self–assembly is significantly important in designing AFM coupled spin dimer systems. Through the self–assembly and molecular interactions of the materials are converted to ferrimagnets in the macroscopic scale. The design of molecular stacking of spin–distributed aromatic rings could lead to intermolecular spin alignment. Very recently, a summary of the basic understanding of the molecular design and the importance of the high spin organic molecules was published.[26]

1.6.1 Intramolecular antiferromagnetic (AFM) exchange interactions in the nitroxides biradicals

Intramolecular AFM exchange interaction arises between two or more spins within the same molecule. Hence, let us consider the two spins *α* and *β* which are connected through a π–bridge (figure 1.6.1.1) and are interacting in the AFM manner.

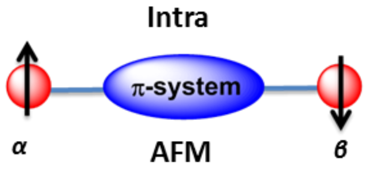

Figure 1.6.1.1: Intramolecular AFM exchange interaction

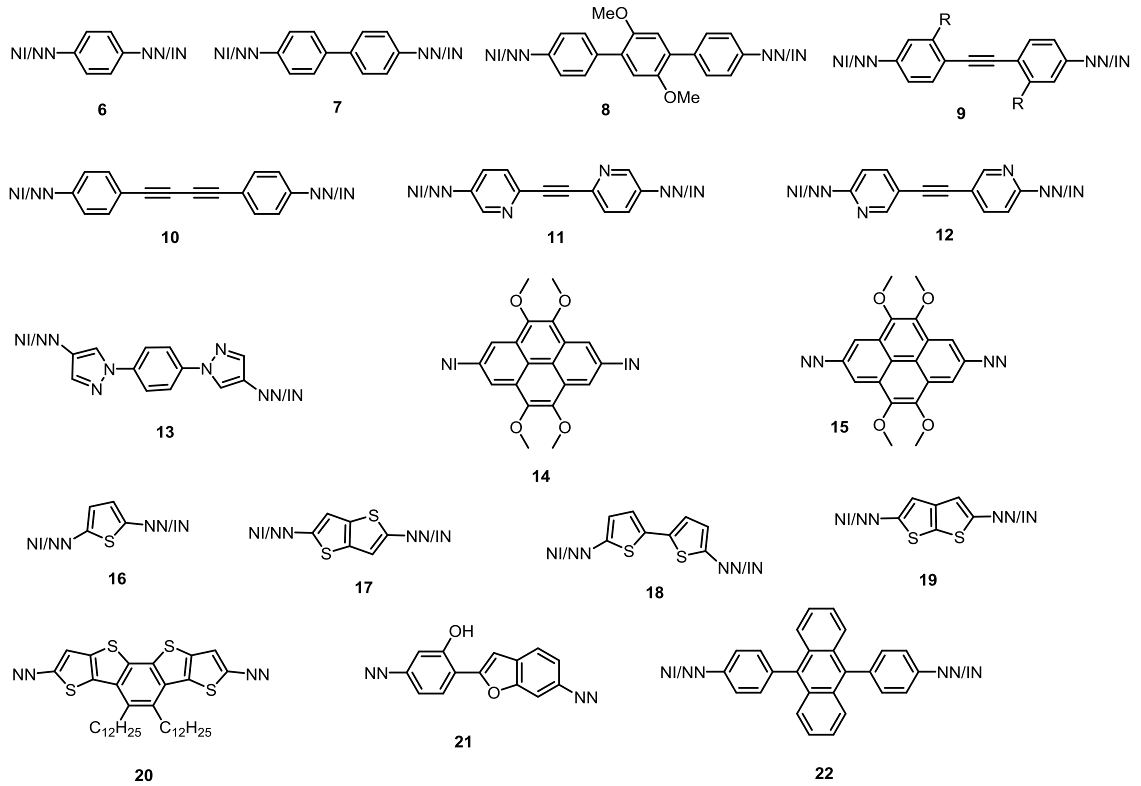

Figure 1.6.1.2: Some examples of intramolecular AFM coupled spin dimer molecules.

Normally, these π–bridges are associated with an aromatic conjugated core in organic molecules. The AFM interactions occur when the two spins are polarized through a conjugated π–electron between the two magnetic centers. In the AFM materials, the neighboring spins oppose to each other, and they are aligned anti–parallel (↑↓) with one another. These coupling forces are responsible for the alignment of the magnetic spins. Spontaneous alignment of the magnetic dipoles in antiferromagnetic states needs some positive energy of interaction between the neighboring spins. Several examples of these types' of molecules are reported, and some of the molecules are given in the figure 1.6.1.2 (these references are cited in chapter 2 and 3).

1.6.2 Intermolecular interactions

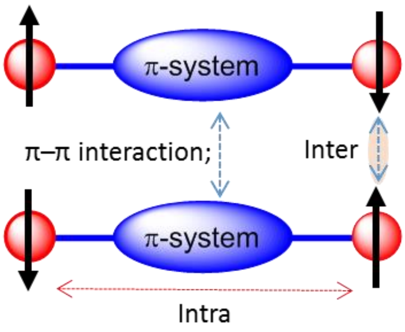

Figure 1.6.2.1: Intermolecular exchange interaction

Intermolecular exchange interaction occurs between two or more magnetic centers within different molecules in a crystal lattice. Conjugated π–bridge linked to nitroxides biradicals are known to mediate intermolecular interactions (figure 1.6.2.1). This interaction arises through π–π interaction of the aromatic core. These interactions may be ferromagnetic or AFM based on the nature of the molecular arrangement in the crystal lattice. A weak intermolecular antiferromagnetic coupling happens in many nitroxides biradicals. However, the intermolecular interaction is formed by aggregation under certain conditions with antiferromagnetic manner. It seems to be the rule rather than exception that the intermolecular interaction between open—shell organic molecules should be antiferromagnetic. Therefore, it is necessary for obtaining the spin alignment in macroscopic scale throughout the molecular assembly to design systems in which molecular interaction could become 3D ordering.

1.6.3. Self–assembly of the radicals systems

Self–assembly is a process in which organization of molecular components of the materials in a crystal lattice takes place. As already described, the intermolecular interactions are responsible for the formation of structures or patterns between the molecules. The interaction may be hydrogen bonding, Vander Waals forces, or π–π interactions. Further, self–assembly plays an important role in deciding the state of the magnetic materials in the crystal lattice.

1.7 Objective and motivation

The unpaired electron acts as a spin carrying units. Some of the organic spin units were already presented in figure 1.3.1. These organic radicals are used in magnetic materials. In this thesis, we focused on the **NN** and **IN** as spin caring units because these radical spins are capable being handled at the laboratory bench, allows their isolation and purification as stable materials. The aromatic conjugated π–bridged connected organic spins have more opportunities to form π–stacking, H–bonding, and mixed organic–inorganic hybrid structures. In addition, the chelating properties of both NN and IN moieties are readily providing coordination sites to metal acetylacetonates.

1.7.1 Weakly antiferromagnetic (AFM) coupled spin–dimers for Bose–Einstein condensation (BEC) in the solid state organic magnetic materials

The Bose–Einstein condensation (BEC) in the solid state property is current interest for future application. Varies approaches were applied to achieve BEC phenomena. For the organic material, it is essential to control intra– and –inter–molecular magnetic exchange interactions.

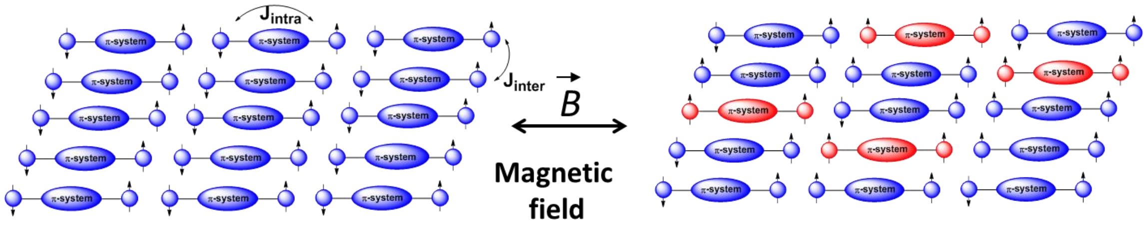

Figure 1.7.1.1: Graphic picture of magnetic field induced quantum phase transition (Reprinted with permission from Prince Ravat, *thesis* **2014**).

The π–bridges provide to tune the intra–molecular magnetic interactions over appropriate design of a spacer between the radicals and type of the radical units. The inter–molecular magnetic exchange interactions, highly depends on the crystal packing of the molecules which is operated by hydrogen bond or other short inter–molecular contacts and they are quite difficult to predict or control.

We are interested in a weakly coupled organic spin–dimer system with singlet ground state molecules. It is believed that in such spin networks the few triplet state molecules can be formed which can move in the crystal lattice upon influence of an external magnetic field (figure 1.7.1.1). To afford through space spin–spin interactions within the network the intramolecular exchange interactions should be roughly double the size of the intermolecular interactions and in the range of 5–15 K to be suitable for the laboratory magnet application.

The π–bridge coupled spin–dimers were considered as a source of interacting bosons. Mainly, preliminary small triplet state population in weakly AF coupled biradicals can be switched into larger in the presence of applied magnetic field. Such biradical systems are favorable molecular models for studying BEC properties.

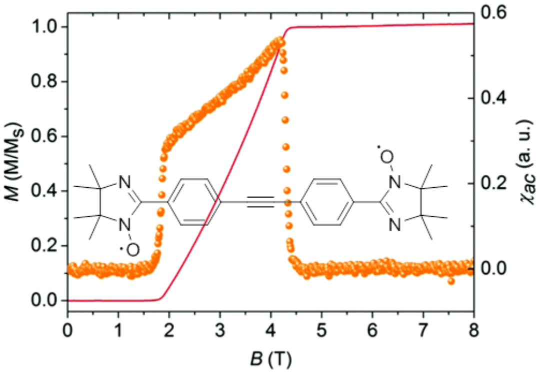

Figure 1.7.1.2: Magnetization $M(B)$ of (solid red line, left scale) at 28 *mK* normalized to the saturation magnetization together with the magnetic AC–susceptibility $\chi_{ac}(B)$ (orange full circles, right scale). Inset: Molecular structure of biradical. (Reprinted with permission from *J. Mater. Chem. C,* **2017**, *5*, 9053–9065).

The main motivation is very recently our group demonstrated magnetic field induced Bose Einstein condensate (BEC) of triplons in tolane bridged bis(imino nitroxide) molecules (figure 1.7.1.2). This field induced ordered state are observed between 1.8 to 4.3 T in AC–susceptibility measurements. This result is highlight a more pronounced double–peak feature in χ_{ac}, an evidence of a field–induced ordered state between B_{c1} = 1.8 T and B_{c2} = 4.3 T at 0.028 K. Such field–induced phases are anticipated for a coupled–dimer system where the lower edge of a band of magnetic excitations crosses the ground state at B_{c1}. Here, B_{c2} corresponds to the saturation field B_s where the full magnetization of the system is obtained. The differences at the critical fields B_{c1} and B_{c2} are much sharper than the one found in a quasi–2D system.[11] Therefore, the inter–dimer coupling in tolane bridged bis(imino nitroxide) molecules has a 3D character, and therefore, this field-induced ordered phase can be defined in terms of a BEC of triplons.

Therefore, we would like to extend our work to synthesis and investigation of the similar kind of the molecule. Such as where the weakly antiferromagnetic interacting two spins are linked by conjugated aromatic π–bridges. The intra–molecular interaction can be tuned by with different π–bridges and radical units. Heterocyclic compounds are known to be best intermolecular interaction behavior by hydrogen bonding and other intermolecular forces.

Thus, this above aspect were consider in chapter 2 and 3. In chapter–2, we were focused on mixed phenyl and thiophene oligomer as π–bridge linked with NN biradicals systems. In chapter-3, planar π–bridges were introduced for best self–assembly and better intermolecular interaction.

1.7.2. Organic high spin molecules

Organic high spin molecules were focused in chapter 4. These high spin molecules have been more interesting because of the future application in the molecular spintronic application, MRI contrast agents and molecular magnets. Different kind of the approaches were used to getting high spin molecules. Among them cations mixed with stable radical molecules are more familiar. Especially easily oxidizable amines combined with stable radical entities were more focused due to the strong exchange interaction was found between oxidized ammonium cation radical and stable radical unit.

Hence, we were interested in high spin molecules, where planar conjugated aromatic amine have been linked with stable radical molecules. The dithieno[*3,2–b:2',3'–d*]pyrrole (DTP) is one of the easily oxidized planar amine, thus three novel molecules of NN substituted with DTP derivatives were designed and synthesized. Further, these molecules were oxidized and have been demonstrated formation of the high spin molecules by CV, UV–Vis, EPR spectroscopy. In addition, the magnetic interactions were calculated by DFT (chapter 4).

1.7.3. Metal–organic radical approach for magnetic materials

The metal–radical approach was used in the chapter 5. Nitroxide radicals can interact with paramagnetic metal {Cu(II), Mn(II), Ni(II), and Co(II)} ions, and form a variety of molecular structures, depending on the nature of the metal ions, ligands and reaction conditions. These molecular structures might be monomeric, 1–D liner chain, 2–D sheet and 3-D structures. Additionally, the magnetic behaviors are also depending on the molecular arrangement in the solid state. It is believed that the investigation of the exchange interaction in such metal–radical complexes are open up new opportunities to design and develop new low dimensional molecular compounds through appropriate choice of ligands, and metals. Thus, the investigations of the crystal structures, both theoretical and experimental magnetic exchange interactions are a more importance in the field of molecular magnetism.

Therefore, we were motivated to complete study of the metal–radical interactions. Particularly formation of the metal– radical complexes and interaction between organic radical and transition metal ions of the Co(II), and Mn(II). Thus, NN substituted benzene (***R*1)** and thiophene (***R*2)** molecules were synthesized. Further, four metal complexes **(*R*1Co, *R*2Co, *R*1Mn** and ***R*2Mn**), using *M*(hfac)$_2$, (where *M* = Co(II) or Mn(II), hfac: hexafluroacetylacetonate) were prepared. The single crystal structures analysis, and magnetic properties, particularly exchange interactions have been investigated both experimentally and theoretically.

The description of the detailed work were documented in chapters 2 to 5, followed by appendixes, list of the publication, curriculum vitae and acknowledgements.

The appendix-I (A-I) is given for the experimental section, analytical techniques, conversion chart for EPR units and energy conversion chart.

1.8. REFERENCES

1. Oliver, G.; A., W. M.; Ekkes, B.; H., C. C.; G., S. S.; Ping, L. J., Magnetic Materials and Devices for the 21st Century: Stronger, Lighter, and More Energy Efficient. *Adv. Mater.* **2011,** *23*, 821-842.

2. Gatteschi, D., Magnetic Molecular Materials. *Curr. Opin. Solid State Mater. Sci.* **1996,** *1*, 192-198.

3. Ratera, I.; Veciana, J., Playing with Organic Radicals as Building Blocks for Functional Molecular Materials. *Chem. Soc. Rev.* **2012,** *41*, 303-349.

4. Tuček, J.; Holá, K.; Bourlinos, A. B.; Błoński, P.; Bakandritsos, A.; Ugolotti, J.; Dubecký, M.; Karlický, F.; Ranc, V.; Čépe, K.; Otyepka, M.; Zbořil, R., Room Temperature Organic Magnets Derived from Sp_3 Functionalized Graphene. *Nat. Commun.* **2017,** *8*, 14525.

5. Miller, J. S.; Drillon, M., *Magnetism: Molecules to Materials I, Models and Experiments*. **2001**.

6. Miller, J. S.; Drillon, M., *Magnetism: Molecules to Materials*. **2003**; Vol. I–IV.

7. Berson, J. A., Structural Determinants of the Chemical and Magnetic Properties of Non-Kekule Molecules. In *Magnetic Properties of Organic Materials*, Lahti, P. M., Ed. Marcel Dekker: New York **1999**; pp 7-26.

8. Hund, F., Linienspektren Periodisches System der Elements. *Springer-Verlag: Berlin* **1927**, 124.

9. Hund, F., To the Interpretation of the Molecular Spectra. IV. *Z. Phys.* **1928,**51, 759-795.

10. Hückel, E., Theory of the Magnetism of so-Called Biradicals. *Zeitschrift Physik. Chem.* **1936,** *B34*, 339-347.

11. Schlenk, W.; Brauns, M., Questioning Metachinoide. *Berichte Der Deutschen Chemischen Gesellschaft* **1915,** *48*, 661-669.

12. Longuet-Higgins, H. C.; Rector, C. W.; Platt, J. R., Molecular Orbital Calculations on Porphine and Tetrahydroporphine. *J. Chem. Phys.* **1950,** *18*, 1174-1181.

13. Ovchinnikov, A. A., Multiplicity of the Ground State of Large Alternant Organic Molecules with Conjugated Bonds. *Theoretica chimica acta* **1978,** *47*, 297-304.

14. Tyutyulkov, N., Band Structure of Nonclassical Polymers. *Theor. Chim. Acta.* **1983,** *63*, 291.

15. Tyutyulkov, N. K., S.; and Ivanov, C.; , *Mol. Cryst. Liq. Cryst. Inc. Nonlinear Opt.* **1989,** *176,* , 139.

16. Borden, W. T.; Davidson, E. R., Effects of Electron Repulsion in Conjugated Hydrocarbon Diradicals. *J. Am. Chem. Soc.* **1977,** *99*, 4587-4594.

17. McConnell, H. M., Theory of Singlet-Triplet Splittings in Large Biradicals. *J. Chem. Phys.* **1960,** *33*, 115-121.

18. Itoh, K., Electronic Structures of Aromatic Hydrocarbons with High Spin Multiplicities in the Electronic Ground State. *Pure Appl. Chem.* **1978,** *50*, 1251.

19. Teki, Y. T., T.; Kitano, M.; Itoh, K, Spin Alignment in Organic High-Spin Molecules. A Heisenberg Hamiltonian Approach. *Chem. Phys. Lett.* **1987,** *142*, 181-186.

20. Ling, C.; Minato, M.; Lahti, P. M.; Van, W. H., Models for Intramolecular Exchange in Organic π-Conjugated Open-Shell Systems. A Comparison of 1,1-Ethenediyl and Carbonyl Linked Bis(Arylnitrenes). *J. Am. Chem. Soc.* **1992,** *114*, 9959-9969.

21. Ling, C.; Lahti, P. M., Models for Intramolecular Exchange in Organic π -Conjugated Open-Shell Systems: 3-Nitrenophenyl and 4-Nitrenophenyl Units Connected by 2,5-Furandiyl, 2,5-Thiophenediyl, and 2,5-Pyrrolediyl Nonalternant Exchange Linkers. *J. Am. Chem. Soc.* **1994,** *116*, 8784-8792.

22. Minato, M.; Lahti, P. M., Intramolecular Exchange Coupling of Arylnitrenes by Oxygen. **1994,** *7*, 495-502.

23. Lahti, P. M.; Minato, M.; Ling, C., Experimental Investigation of Exchange in Organic Open-Shell Molecular Building Blocks for Magnetic Materials. *Molecular Crystals and Liquid Crystals Science and Technology. Section A. Molecular Crystals and Liquid Crystals* **1995,** *271*, 147-154.

24. Matsumoto, T.; Ishida, T.; Koga, N.; Iwamura, H., Intramolecular Magnetic Coupling Between Two Nitrene Or Two Nitroxide Units Through 1,1-Diphenylethylene Chromophores. Isomeric Dinitrenes and Dinitroxides Related In Connectivity to Trimethylenemethane, Tetramethyleneethane, and Pentamethylenepropane. *J. Am. Chem. Soc.* **1992,** *114*, 9952-9959.

25. Iwamura, H.; Murata, S., Magnetic Coupling of Two Triplet Phenylnitrene Units Joined Through an Acetylenic or a Di-Acetylenic Linkage. *Mol. Cryst. Liq. Cryst. Inc. Nonlinear Opt.* **1989,** *176*, 33-47.

26. Baumgarten, M., High Spin Organic Molecules. In *World Scientific Reference on Spin in Organics*, **2017**; pp 1-93.

27. Keana, J. F. W., Newer Aspects of the Synthesis and Chemistry of Nitroxide Spin Labels. *Chem. Rev.* **1978,** *78*, 37-64.

28. Rozantsev, E. G.; Sholle, V. D., *Synthesis* **1971**, 190.

29. Ullman, E. F.; Osiecki, J. H.; Boocock, D. G. B.; Darcy, R., Stable Free Radicals. X. Nitronyl Nitroxide Monoradicals and Biradicals as Possible Small Molecule Spin Labels. *J. Am. Chem. Soc.* **1972,** *94*, 7049-7059.

30. Ullman, E. F.; Boocock, D. G. B., Conjugated Nitronyl-Nitroxide and Imino-Nitroxide Biradicals. *J. Chem. Soc. D* **1969**, 1161-1162.

31. Boocock, D. G. B.; Darcy, R.; Ullman, E. F., Studies of Free Radicals. II. Chemical Properties of Nitronylnitroxides. A Unique Radical Anion. *J. Am. Chem. Soc.* **1968,** *90*, 5945-5946.

32. Boocock, D. G. B.; Ullman, E. F., Stable Free Radicals. III. 1,3-Dioxy-2-midazolidone Zwitterion and its Stable Nitronyl Nitroxide Radical Anion. *J. Am. Chem. Soc.* **1968,** *90*, 6873-6874.

33. Kreilick, R. W.; Becher, J.; Ullman, E. F., Stable Free Radicals. V. Electron Spin Resonance Studies of Nitronylnitroxide Radicals with Asymmetric Centers. *J. Am. Chem. Soc.* **1969,** *91*, 5121-5124.

34. Kusaba, Y.; Tamura, M.; Hosokoshi, Y.; Kinoshita, M.; Sawa, H.; Kato, R.; Kobayashi, H., Isolation of Crystals of a Planar Nitronyl Nitroxide Radical: 2-Phenylbenzimidazol-1-ylN,N′-dioxide (PBIDO). *J. Mat. Chem.* **1997,** *7*, 1377-1382.

35. Zakrassov, A.; Shteiman, V.; Sheynin, Y.; Tumanskii, B.; Botoshansky, M.; Kapon, M.; Keren, A.; Kaftory, M.; Vos, T. E.; Miller, J. S., Synthesis, Structural, and Magnetic Characterization of Substituted Benzoimidazole-l-yl N,N′-Dioxides. *J. Mat. Chem.* **2004,** *14*, 1827-1837.

36. Ullman, E. F.; Call, L.; Osiecki, J. H., Stable Free Radicals. VIII. New Imino, Amidino, and Carbamoyl Nitroxides. *J. Org. Chem.* **1970,** *35*, 3623-3631.

37. Zheludev, A.; Bonnet, M.; Delley, B.; Grand, A.; Luneau, D.; Örström, L.; Ressouche, E.; Rey, P.; Schweizer, J., An Imino Nitroxide Free Rical: Experimental and Teoretical Sin Dnsity and Etronic Sructure. *J. Magn. Magn. Mater.* **1995,** *145*, 293-305.

38. Turro, N. J.; Chen, J. Y.-C.; Likhtenshtein, G. L.; Yamauchi, J.; Nakatsuji, S.; Smirnov, I. A.; Tamura, R., Nitroxides. Applications in Chemistry, Biomedicine, and Materials Science. **2008,** *47*, 9596-9597.

39. Makarova, T. L. P., F.; , Carbon Based Magnetism. *Elsevier Science* **2006**.

40. Hicks, R. G., *Stable Radicals: Fundamentals and Applied Aspects of Odd-Electron Compounds*. **2010**.

41. Aspuru-Guzik, A.; Dutoi, A. D.; Love, P. J.; Head-Gordon, M., Simulated Quantum Computation of Molecular Energies. **2005,** *309*, 1704-1707.

42. Lloyd, S., A Potentially Realizable Quantum Computer. **1993,** *261*, 1569-1571.

43. Simon Bone., M., Castro, A Brief History of Quantum Computing. *http://www.doc.ic.ac.uk/~nd/surprise_97/journal/vol4/spb3/*.

44. Aromí, G.; Aguilà, D.; Gamez, P.; Luis, F.; Roubeau, O., Design of Magnetic Coordination Complexes for Quantum Computing. *Chem. Soc. Rev.* **2012,** *4*, 537-546.

45. Troiani, F.; Affronte, M., Molecular Spins for Quantum Information Technologies. *Chem. Soc. Rev.* **2011,** *4*, 3119-3129.

46. Sato, K.; Nakazawa, S.; Nishida, S.; Rahimi, R. D.; Yoshino, T.; Morita, Y.; Toyota, K.; Shiomi, D.; Kitagawa, M.; Takui, T., Novel Applications of ESR/EPR: Quantum Computing/Quantum Information Processing. In *EPR of Free Radicals in Solids II: Trends in Methods and Applications*, Lund, A.; Shiotani, M., Eds. Springer Netherlands: Dordrecht, **2012**; pp 163-204.

47. Sato, K.; Nakazawa, S.; Rahimi, R.; Ise, T.; Nishida, S.; Yoshino, T.; Mori, N.; Toyota, K.; Shiomi, D.; Yakiyama, Y.; Morita, Y.; Kitagawa, M.; Nakasuji, K.; Nakahara, M.; Hara, H.; Carl, P.; Höfer, P.; Takui, T., Molecular Electron-Spin Quantum Computers and Quantum Information Processing: Pulse-Based Electron Magnetic Resonance Spin Technology Applied to Matter Spin-Qubits. *J. Mat. Chem.* **2009,** *19*, 3739-3754.

48. Nakazawa, S.; Nishida, S.; Ise, T.; Yoshino, T.; Mori, N.; Rahimi, R. D.; Sato, K.; Morita, Y.; Toyota, K.; Shiomi, D.; Kitagawa, M.; Hara, H.; Carl, P.; Höfer, P.; Takui, T., A Synthetic Two-Spin Quantum Bit: g-Engineered Exchange-Coupled Biradical Designed for Controlled-NOT Gate Operations. **2012,** *124*, 9998-10002.

49. Lehmann, J.; Gaita-Ariño, A.; Coronado, E.; Loss, D., Quantum Computing with Molecular Spin Systems. *J. Mat. Chem.* **2009,** *19*, 1672-1677.

50. Aoki, K.; Akutsu, H.; Yamada, J.-i.; Nakatsuji, S.; rsquo; ichi; Kojima, T.; Yamashita, Y., The First Organic Radical Compounds Exhibiting n-Type FET Properties. *Chem. Lett.,* **2009,** *38*, 112-113.

51. Figueira-Duarte, T. M.; Müllen, K., Pyrene-Based Materials for Organic Electronics. *Chem. Rev.* **2011,** *111*, 7260-7314.

52. Wang, Y.; Wang, H.; Liu, Y.; Di, C.-a.; Sun, Y.; Wu, W.; Yu, G.; Zhang, D.; Zhu, D., 1-Imino Nitroxide Pyrene for High Performance Organic Field-Effect Transistors with Low Operating Voltage. *J. Am. Chem. Soc.* **2006,** *128*, 13058-13059.

53. Kurata, T.; Koshika, K.; Kato, F.; Kido, J.; Nishide, H., Triarylamine-combined Nitronyl Nitroxide and its Hole-Transporting Property. *Polyhedron* **2007,** *26*, 1776-1780.

54. Kurata, T.; Koshika, K.; Kato, F.; Kido, J.; Nishide, H., An Unpaired Electron-Based Hole-Transporting Molecule: Triarylamine-Combined Nitroxide Radicals. *Chem. Commun.* **2007**, 2986-2988.

55. Burroughes, J. H.; Bradley, D. D. C.; Brown, A. R.; Marks, R. N.; Mackay, K.; Friend, R. H.; Burns, P. L.; Holmes, A. B., Light-emitting Diodes Based on Conjugated Polymers. *Nature* **1990,** *347*, 539-541.

56. Uoyama, H.; Goushi, K.; Shizu, K.; Nomura, H.; Adachi, C., Highly Efficient Organic Light-Emitting Diodes From Delayed Fluorescence. *Nature* **2012,** *492*, 234-238.

57. Li, W.; Pan, Y.; Xiao, R.; Peng, Q.; Zhang, S.; Ma, D.; Li, F.; Shen, F.; Wang, Y.; Yang, B.; Ma, Y., Employing ∼100% Excitons in OLEDs by Utilizing a Fluorescent Molecule with Hybridized Local and Charge-Transfer Excited State. *Adv. Funct. Mater.* **2014,** *24*, 1609-1614.

58. Peng, Q.; Obolda, A.; Zhang, M.; Li, F., Organic Light-Emitting Diodes Using a Neutral π Radical as Emitter: The Emission from a Doublet. *Angew. Chem. Int. Ed* **2015,** *54*, 7091-7095.

59. Bin, Z.; Liu, Z.; Duan, L., Organic Radicals Outperform LiF as Efficient Electron-Injection Materials for Organic Light-Emitting Diodes. *J. Phys. Chem. Lett.,* **2017,** *8*, 4769-4773.

60. Castellanos, S.; Velasco, D.; López-Calahorra, F.; Brillas, E.; Julia, L., Taking Advantage of the Radical Character of Tris(2,4,6-trichlorophenyl)methyl To Synthesize New Paramagnetic Glassy Molecular Materials. *J. Org. Chem.,* **2008,** *73*, 3759-3767.

61. Zhang, Y.; Basel, T. P.; Gautam, B. R.; Yang, X.; Mascaro, D. J.; Liu, F.; Vardeny, Z. V., Spin-Enhanced Organic Bulk Heterojunction Photovoltaic Solar Cells. *Nat. Commun.* **2012,** *3*, 1043.

62. Zhang, Y.; Gautam, B. R.; Basel, T. P.; Mascaro, D. J.; Vardeny, Z. V., Organic Bulk Heterojunction Solar Cells Enhanced by Spin Interaction. *Synth. Met.* **2013,** *173*, 2-9.

63. Kato, F.; Kikuchi, A.; Okuyama, T.; Oyaizu, K.; Nishide, H., Nitroxide Radicals as Highly Reactive Redox Mediators in Dye-Sensitized Solar Cells. *Angew. Chem. Int. Ed.* **2012,** *51*, 10177-10180.

64. Yang, W.; Soderberg, M.; Eriksson, A. I. K.; Boschloo, G., Efficient Aqueous Dye-Sensitized Solar Cell Electrolytes Based on a TEMPO/TEMPO+ Redox Couple. *RSC Advances* **2015,** *5*, 26706-26709.

65. Yang, W.; Vlachopoulos, N.; Hao, Y.; Hagfeldt, A.; Boschloo, G., Efficient Dye Regeneration at Low Driving Force Achieved in Triphenylamine Dye LEG4 and TEMPO Redox Mediator Based Dye-Sensitized Solar Cells. *PCCP* **2015,** *17*, 15868-15875.

66. Janoschka, T.; Hager, M. D.; Schubert, U. S., Powering up the Future: Radical Polymers for Battery Applications. *Adv. Mater.* **2012,** *24*, 6397-6409.

67. Tomlinson, E. P.; Hay, M. E.; Boudouris, B. W., Radical Polymers and Their Application to Organic Electronic Devices. *Macromolecules* **2014,** *47*, 6145-6158.

68. N., D. S. M. V., *Mini-Rev. Org. Chem* **2006,** *3*, 155-165.

69. Adam, W.; Saha-Möller, C. R.; Ganeshpure, P. A., Synthetic Applications of Nonmetal Catalysts for Homogeneous Oxidations. *Chem. Rev.* **2001,** *101*, 3499-3548.

70. Nam, H.; Kwon, J. E.; Choi, M.-W.; Seo, J.; Shin, S.; Kim, S.; Park, S. Y., Highly Sensitive and Selective Fluorescent Probe for Ascorbic Acid with a Broad Detection Range through Dual-Quenching and Bimodal Action of Nitronyl-Nitroxide. *ACS Sensors* **2016,** *1*, 392-398.

71. Borozdina, Y. B.; Kamm, V.; Laquai, F.; Baumgarten, M., Tuning the Sensitivity of Fluorophore–Nitroxide Radicals. *J. Mater. Chem.* **2012,** *22*, 13260-13267.

72. Beldjoudi, Y.; Nascimento, M. A.; Cho, Y. J.; Yu, H.; Aziz, H.; Tonouchi, D.; Eguchi, K.; Matsushita, M. M.; Awaga, K.; Osorio-Roman, I.; Constantinides, C. P.; Rawson, J. M., Multifunctional Dithiadiazolyl Radicals: Fluorescence, Electroluminescence, and Photoconducting Behavior in Pyren-1′-yl-dithiadiazolyl. *J. Am. Chem. Soc.* **2018,** *140*, 6260-6270.

73. Itkis, M. E.; Chi, X.; Cordes, A. W.; Haddon, R. C., Magneto-Opto-Electronic Bistability in a Phenalenyl-Based Neutral Radical. *Science* **2002,** *296*, 1443-1445.

74. Jasiński, M.; Szczytko, J.; Pociecha, D.; Monobe, H.; Kaszyński, P., Substituent-Dependent Magnetic Behavior of Discotic Benzo[e][1,2,4]triazinyls. *J. Am. Chem. Soc.* **2016,** *138*, 9421-9424.

75. Ravat, P.; Marszalek, T.; Pisula, W.; Müllen, K.; Baumgarten, M., Positive Magneto-LC Effect in Conjugated Spin-Bearing Hexabenzocoronene. *J. Am. Chem. Soc.* **2014,** *136*, 12860-12863.

76. Hayes, R. T.; Walsh, C. J.; Wasielewski, M. R., Competitive Electron Transfer from the S2 and S1 Excited States of Zinc meso-Tetraphenylporphyrin to a Covalently Bound Pyromellitimide: Dependence on Donor−Acceptor Structure and Solvent. *J. Phys. Chem. A* **2004,** *108*, 2375-2381.

77. Teki, Y.; Miyamoto, S.; Iimura, K.; Nakatsuji, M.; Miura, Y., Intramolecular Spin Alignment Utilizing the Excited Molecular Field between the Triplet (S = 1) Excited State and the Dangling Stable Radicals (S = 1/2) as Studied by Time-Resolved Electron Spin Resonance: Observation of the Excited Quartet (S = 3/2) and Quintet (S = 2) States on the Purely Organic π-Conjugated Spin Systems. *J. Am. Chem. Soc.* **2000,** *122*, 984-985.

78. Sugawara, T.; Komatsu, H.; Suzuki, K., Interplay between magnetism and conductivity derived from spin-polarized donor radicals. *Chemical Society Reviews* **2011,** *40* (6), 3105-3118.

79. Coronado, E.; Day, P., Magnetic Molecular Conductors. *Chem. Rev.* **2004,** *104*, 5419-5448.

80. Dunbar, K. R., Editorial for the Virtual Issue on Quantum Molecular Magnets. *Inorg. Chem.* **2012,** *51*, 12055-12058.

81. Blundell, S. J.; Pratt, F. L., Organic and Molecular Magnets. *J. Phys. Condens. Matter* **2004,** *16*, R771-R828.

82. Das, K.; Pink, M.; Rajca, S.; Rajca, A., Synthesis and Structure of a Nucleoside with π-Conjugated Nitroxide Spin Label Forming a One-Dimensional Ferromagnetic Chain. *J. Am. Chem. Soc.* **2006,** *128*, 5334-5335.

83. Wang, J.; He, C.; Wu, P.; Wang, J.; Duan, C., An Amide-Containing Metal–Organic Tetrahedron Responding to a Spin-Trapping Reaction in a Fluorescent Enhancement Manner for Biological Imaging of NO in Living Cells. *J. Am. Chem. Soc.* **2011,** *133*, 12402-12405.

84. Rajca, A.; Wang, Y.; Boska, M.; Paletta, J. T.; Olankitwanit, A.; Swanson, M. A.; Mitchell, D. G.; Eaton, S. S.; Eaton, G. R.; Rajca, S., Organic Radical Contrast Agents for Magnetic Resonance Imaging. *J. Am. Chem. Soc.* **2012,** *134*, 15724-15727.

85. Liu, Y.; Zhao, J.; Li, Z.; Mu, C.; Ma, W.; Hu, H.; Jiang, K.; Lin, H.; Ade, H.; Yan, H., Aggregation and Morphology Control Enables Multiple Cases of High-Efficiency Polymer Solar Cells. *Nat. Commun.* **2014,** *5*, 5293.

86. Sowers, M. A.; McCombs, J. R.; Wang, Y.; Paletta, J. T.; Morton, S. W.; Dreaden, E. C.; Boska, M. D.; Ottaviani, M. F.; Hammond, P. T.; Rajca, A.; Johnson, J. A., Redox-Responsive Branched-Bottlebrush Polymers for in Vivo MRI and Fluorescence Imaging. *Nat. Commun.* **2014,** *5*, 5460.

87. Demir, S.; Jeon, I.-R.; Long, J. R.; Harris, T. D., Radical Ligand-Containing Single-Molecule Magnets. *Coord. Chem. Rev.* **2015,** *289–290*, 149-176.

88. *Magnetic Properties of Organic Materials*. 1999.

89. Heisenberg, W. J. Z. f. P., Zur Theorie des Ferromagnetismus. **1928,** *49*, 619-636.

CHAPTER 2

Mixed Phenyl and Thiophene Oligomers for Bridging Nitronyl Nitroxides

Abstract: The four π–bridges conjugatively linked with nitronyl nitroxide (NN) biradicals (**PPP–NN**, **TTT–NN**, **TPT–NN**, and **PTP–NN**) are described and synthesized. To synthesize these (NN) molecules, we first utilized Suzuki and Stille coupling reactions through protection and deprotection protocols. The intra–molecular magnetic exchange interactions are adjusted through using different π–bridges such as p–ter–phenyl (PPP), ter–thiophene (TTT) and alternating phenylene (P) and thiophene (T) units as PTP and TPT. Thereby much smaller torsions between the NN and thiophene units (~10°) in **TTT–NN** and **TPT–NN** than for NN and phenyl units (~29°) in **PPP–NN** were observed due to smaller hindrance for a five vs. a six membered ring. All four biradicals were examined by EPR and optical spectroscopy. The magnetic susceptibility was studied by SQUID measurements for **TTT–NN** and **TPT–NN**. Single crystals were efficiently grown for radical precursors of **3, 5, 6, PPP–NNSi, PTP–NNSi** and final biradicals of **TTT–NN, TPT–NN,** and **PPP–NN**, of which structures and their molecular packing were examined by X–ray diffraction studies. The intra–molecular exchange interactions were calculated by broken symmetry DFT calculations for all biradicals using x–ray crystal structures and optimized structures. Among all the calculation, using x–ray crystal structure with UBLYP functional and 6–31G(d) basis gives best results.

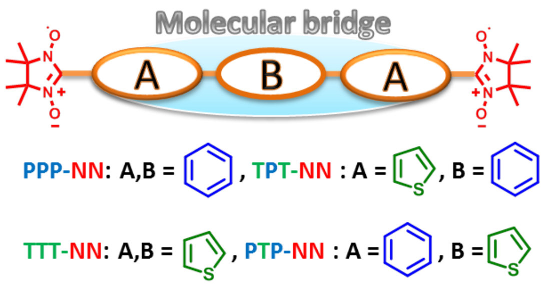

Note: This chapter was published in *J. Org. Chem.,* **2017**, *82*, 7764 –7773.

2.1 Introduction

The Bose–Einstein Condensation (BEC) of magnetic excitations has gained recent interest in the field of magnetic materials. It was first obtained in supercooled dilute atomic vapor so called ultracold gases.[1-3] Some of the molecular examples of copper dimer based materials were found to reveal intriguing phenomena related to interacting Bosons in reduced dimensions where a Berezinski–Kosterlitz–Thouless scenario was observed.[4] Weakly antiferromagnetically (AFM) coupled spin–dimers with singlet ground state molecules can be switched into a triplet state by the application of a magnetic field and a gas of triplet excitations (triplons) is formed which shows critical properties similar to those of a BEC as described by Tchernyshyov.[5, 6]

Our fundamental interest focused on the development of novel organic magnetic materials. Recently the focus was transformed on the aromatic conjugated molecules linked with spin ($S = ½$) dimer system.[7-10] The BEC properties of spin dimer systems mainly depend on the spin–spin interactions where usually it is differentiated between *intra*– and *inter*–molecular exchange interactions.[7-11] Hence, i*ntra*–molecular interaction can be controlled by varying distance, topology and torsion between the radical centers connected to the π–bridges.[7-16] The magnetic interaction between the stable free radicals such as nitronylnitroxides (NN), *tert*–butylnitroxides, iminonitroxides (IN), and verdazyl (VZ) can be fine–tuned by their combination with conjugated oligomers.[17-28] Previously reported NN biradicals where built upon biphenyl[12], terpyridine[29], pyrene[13], and tolane[8] as a π–bridge and their optical, electrochemical, EPR, and magnetic properties were studied.

The spin–dimer molecules are used for the development of solid–state BEC materials[4, 5, 30], where two guiding principles should hold: (1) The intra molecular exchange coupling should dominate and exceed the intermolecular coupling. (2) The intramolecular coupling should be small enough for laboratory–scaled magnets to switch the spin state (ground state singlet into the triplet state). Recently we found that tolane bridged NN biradicals undergo quasi two dimensional magnetic field induced quantum phase transition at very low temperatures in the routine laboratory magnetic field up to 11 T.[7, 9] While thiophene extension with NN biradical entities were explored[31, 32], mixed thiophene and phenylene oligomers with NN radicals are not reported to the best of our knowledge to tune the magnetic and electronic properties of biradical systems. From our previous observations, the aromatic π–bridges are important tool to control both inter and intra–magnetic interaction. Therefore, it is a necessary to better–understand the effect of the aromatic bridge on the spin–spin interaction between the radical units.

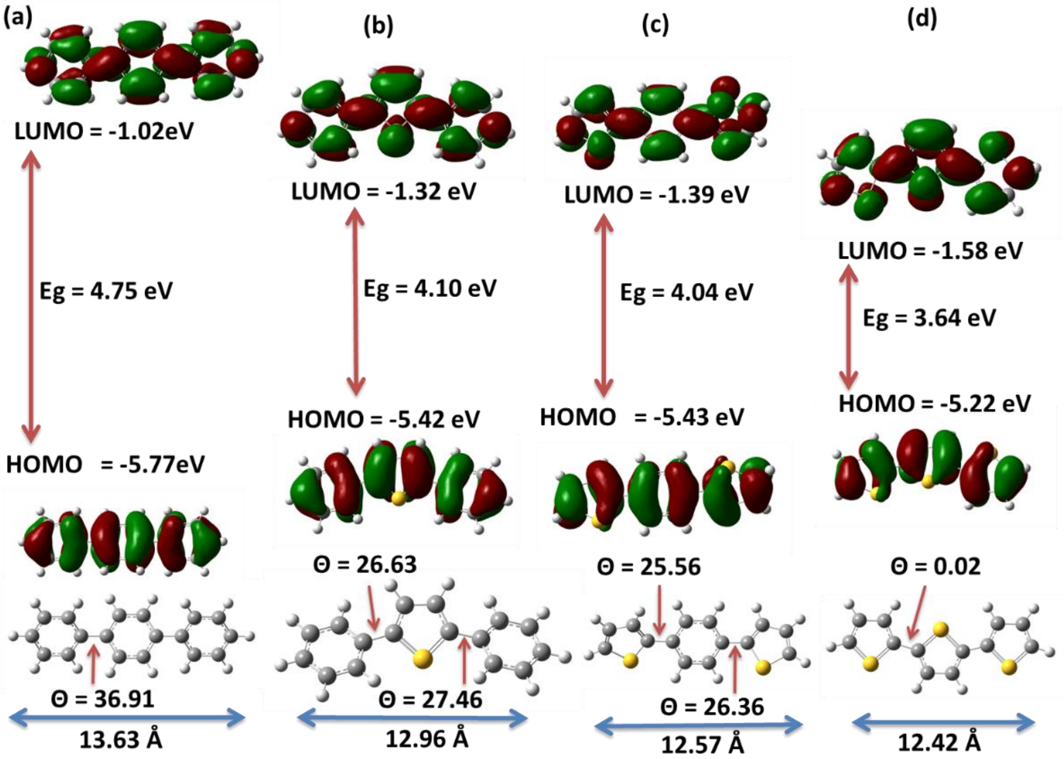

Figure 2.1: Optimized structure of (a) **PPP**, (b) **PTP**, (c) **TPT** and (d) **TTT** by using the B3LYP functional and 6–31G(d) basis set and HOMO, LUMO and energy gap (Eg) of the bridging oligomers.

Hence we designed four molecular bridges, *p–ter*-phenyl, (PPP), *ter*–thiophene, (TTT) and two mixed thiophene and phenylene oligomers (TPT and PTP) (figure 2.1) and investigated the molecular length and torsion angles as well as their HOMO, LUMO, electron density distribution and the energy gap (E_g) by density functional theory (DFT). The E_g of TTT is 3.64 eV which is much lower than for PPP

(4.75 eV), TPT (4.10 eV) and PTP (4.04 eV). Based on these π–units (PPP, TTT, TPT and PTP), four (NN) biradicals (**TPT–NN, PPP–NN, TTT–NN,** and **PTP–NN**) were designed (figure 2.2). The NN radical units are attached to para–position of the phenyl unit for **PPP–NN**, and **PTP–NN**. And the NN are attached to the 5th–position of the thiophene ring for **TTT–NN**, and for **TPT–NN**. In the molecular design, we predicted by spin polarization rule that the spins on the NN groups are AFM coupled to each other.

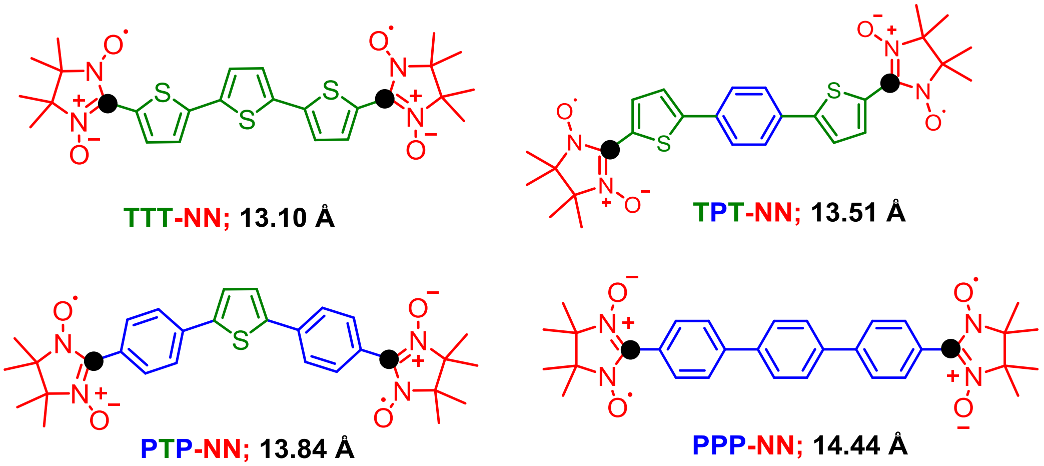
TTT-NN; 13.10 Å

TPT-NN; 13.51 Å

PTP-NN; 13.84 Å

PPP-NN; 14.44 Å

Figure 2.2: Structures of **TTT–NN, TPT–NN, PTP–NN** and **PPP–NN**; distance between C2–C2′ of NN (labeled as black dot).

In this chapter reported that, four biradicals (**TTT–NN, TPT–NN, PTP–NN** and **PPP–NN**) were designed, synthesized and characterized by EPR, UV–vis spectrometry, single crystal X–ray structural analysis and their magnetic properties were investigated by SQUID magnetometry for (**TTT–NN, TPT–NN**). The intra–molecular magnetic interaction were calculated for the all the biradicals by the quantum chemical density functional theory (DFT) calculations.

Results and discussion

2.2 Synthesis of biradicals

The dialdehydes are important precursors for the synthesis of nitronyl nitroxide biradicals.[27] The dialdehyde of 5,5'–(1,4–phenylene)bis(thiophene–2–carbaldehyde), (**Di–CHO**), was prepared by reaction between 1,4-bis(4,4,5,5-tetramethyl-1,3,2-dioxaborolan-2-yl)benzene and 5-bromothiophene-2-carbaldehyde.

Scheme 2.1: Synthesis of **Di-NNOH**.

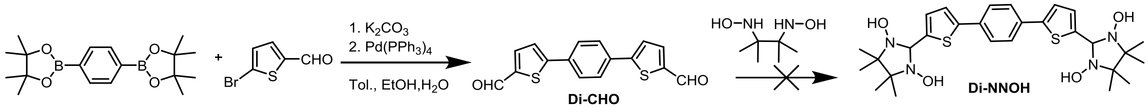

Scheme 2.2: Synthetic route for biradical precursors.

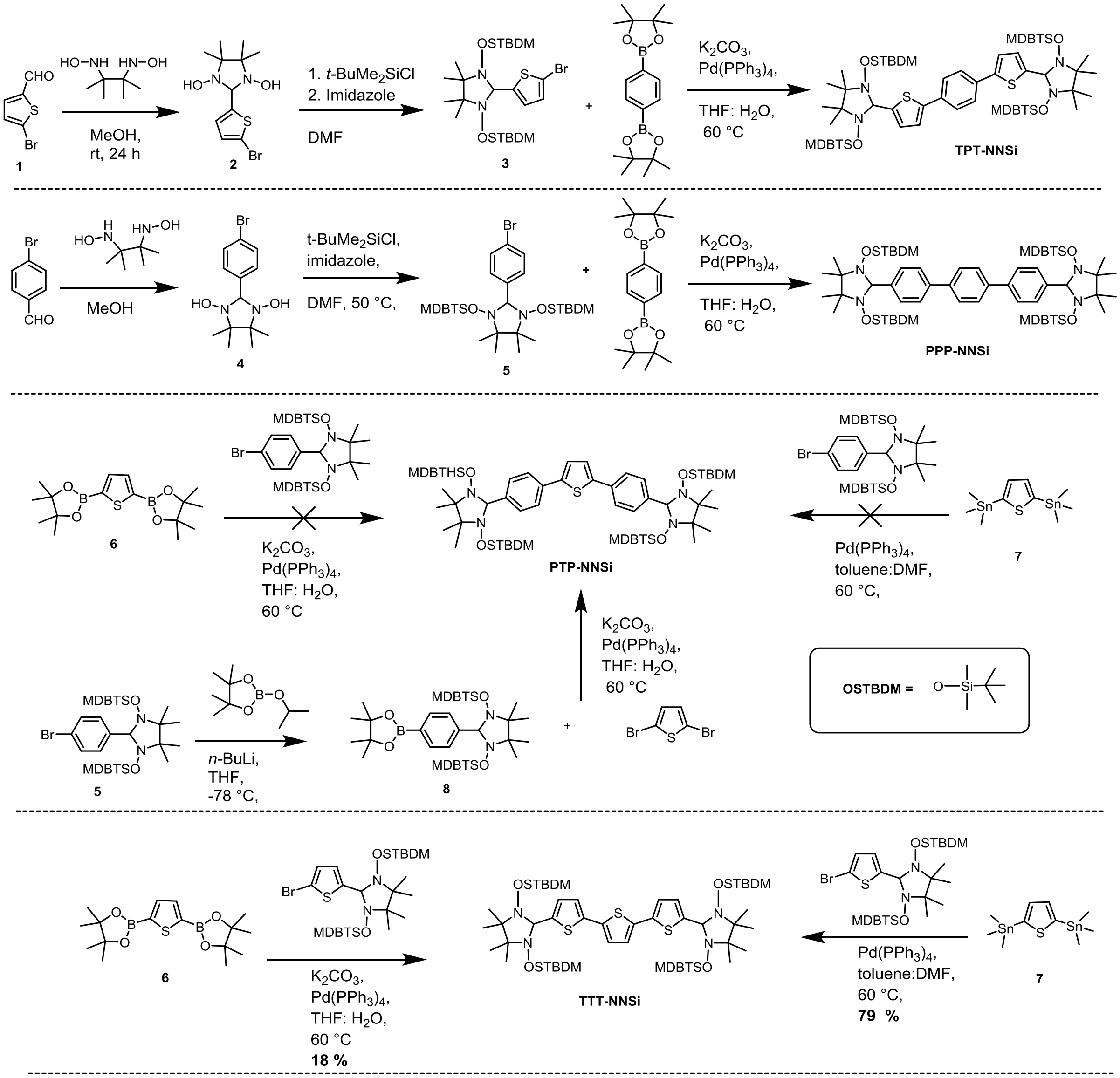

Then the (**Di–CHO)** was reacted with 2,3-bis(hydroxyamino)-2,3-dimethylbutane **(BHA**). The reaction failed (scheme 2.1) although often announced in the literature as suitable step.[27] In addition, the **PPP–NN** was also synthesised from di–aldehydes with low (5.2%) yield.[33] This was mainly because of the poor solubility of the corresponding di–aldehyde precursor in common organic solvents.

Moreover, the *tert*–butyldimethylsilyl (TBDMS) protected bromothiophene mono radical moiety **3** was introduced by Suzuki coupling reaction with 1,4–benzenediboronic acid bis(pinacol) ester and deprotection to obtain **TPT–NN** (scheme 2.2). Later a similar synthetic protocol was applied to synthesize the other three biradicals. Reaction of the 5-bromo-2-thiophenecarboxaldehyde or 4-bromobenzaldehyde with **BHA** at room temperature in methanol yielded compounds **2** and **4** with good yields (>80 %). Then the N–OH groups were protected with TBDMS by *tert*-butyldimethylsilyl chloride (*t*-BuMe$_2$SiCl) in the presence of imidazole in DMF as solvent to afford **3** and **5** with excellent yields (>90 %). The highly stable biradical precursors **TPT–NNSi** and **PPP–NNSi** were obtained by Suzuki coupling reactions between **3** or **5** with 1,4-benzenediboronic acid bis(pinacol) ester in moderate to good (>60 %) yield. The preparation of **PTP–NNSi** from **5** either by Suzuki coupling between **5** and thiophene-2,5-diboronic- bis(pinacol) ester,(**6**) or Stille coupling of **5** and 2,5-bis(trimethylstannyl)thiophene,(**7**) were unsuccessful. Therefore boronic-bis(pinacol)ester,(**8)** was prepared from **5** by its treatment with *n*-BuLi, followed by 2-isopropylboronic acid, pinacol ester. The Suzuki coupling of 2,5-dibromothiophene and **8** successfully yielded **PTP–NNSi** in 66 % yield. An attempt to synthesize **TTT–NNSi** by Suzuki coupling with **3** and thiophene-2,5-diboronic-bis(pinacol)ester provided only 18 % along with 51 % mono substituted side product obtained. The yield of **TTT–NNSi** could be highly improved by Stille coupling reaction between **3** and 2,5-bis(trimethylstannyl)thiophene, (74%). All the precursors were characterized by NMR and mass spectra, and the precursors **3**, **5**, **8, PPP–NNSi** and **PTP–NNSi** were also verified by single crystal X–ray structure analysis in appendix–(A–II).

Scheme 2.3: Synthetic of biradical by deprotection.

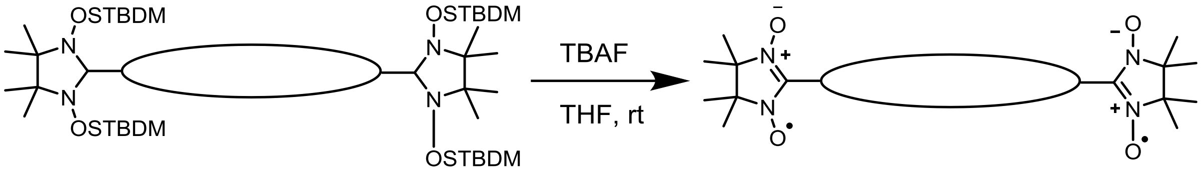

TPT-NNSi, PPP-NNSi, PTP-NNSi and TTT-NNSi **PPP-NN, PTP-NN and TTT-NN**

All biradicals (**TPT–NN TTT–NN, PTP–NN**, and **PPP–NN**) were obtained by subsequent cleavages of the (TBDMS) protecting groups in one step with tetrabutylammonium fluoride (TBAF) in THF (scheme 2.3). The reaction was carefully monitored by TLC to get best yield of NN biradicals, which were purified by column chromatography. These biradicals were characterized ESI–HRMS mass spectrometry.

2.3 Optical properties

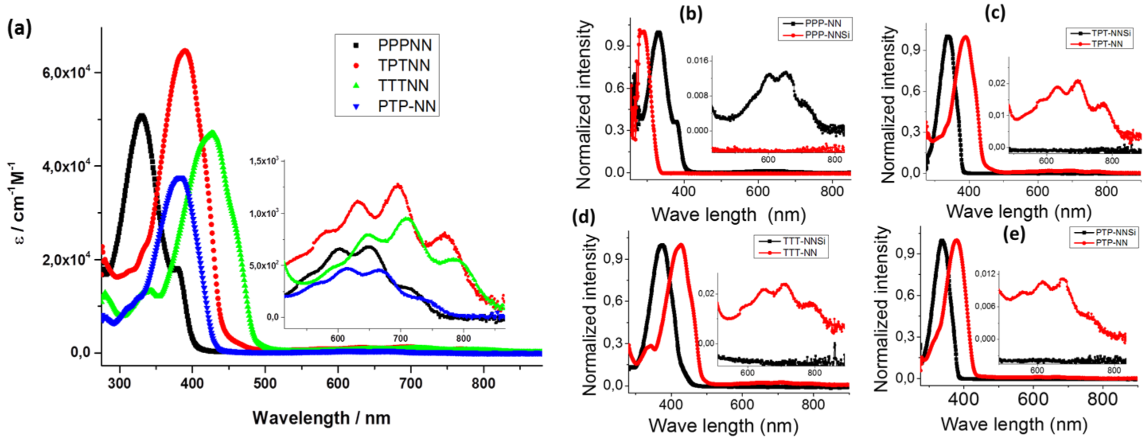

Figure 2.3: (a) UV–vis absorption spectra of **PPP–NN PTP–NN, TPT–NN,** and **TTT–NN** (~10^{-5} M in toluene), and (b-e) compared absorption spectra of the biradicals with their precursors.

The UV–vis absorption spectra of the biradicals (**TTT–NN, TPT–NN, PTP–NN**, and **PPP–NN**) were measured in toluene (c⍰10^{-5} M) at room temperature and are depicted in figure 2.3(a). The absorption data of biradicals (λ_{max}, ε and optical gap E_g) are given in table 2.1. The absorption spectra of the biradicals are compared with their precursors (figure 2.3(b-e)) together with their data summarized in table 2.1. Only one absorption band was observed for all precursors (**TPT–NNSi**, **PPP–**

NNSi, PTP–NNSi and **TTT–NNSi**) due to the π–π* transition of the π-bridge. All the four biradicals exhibited two absorption bands, around 280–500 nm due to the π–π* transition of the conjugated backbone, and the characteristic n–π* transition of the NN radical moieties around 510-840 nm. The UV–vis spectra clearly indicate the presence of pure NN biradicals, without contamination by imino–nitroxide. The effect of the π–bridge on the absorption spectra for NN biradicals were investigated previously[34]. The π–π* transitions of the radicals are red shifted compared to their protected precursors by 40–50 nm demonstrating the conjugation enhancement upon radical formation (figure 2.3(b-e)).

Table 2.1: Optical properties of protected precursors, optical and EPR, properties of biradicals (**TTT–NN, TPT–NN, PPP–NN, and PTP–NN**).

Precursors	λ_{max} (nm), ^{a}Eg (eV)^{OP}	Radicals	λ_{max}(nm), (ε $cm^{-1}M^{-1}$)	^{a}Eg(eV)^{OP}	$^b a_{N/2}$/mT (±0.03)	^{b}g
TTT–NNSi	375 (2.84)	**TTT–NN**	427 (47315), 709 (956)	1.46	0.375	2.0067
TPT–NNSi	338 (3.22)	**TPT–NN**	390 (64795), 695 (1267)	1.45	0.370	2.0065
PTP–NNSi	337 (3.22)	**PTP–NN**	384 (37885), 669 (468)	1.63	0.381	2.0065
PPP–NNSi	291 (3.73)	**PPP–NN**	331 (50757), 651 (680)	1.64	0.371	2.0066

^{a,}Optical energy gap calculated according to the absorption edge; ^{b}calculated from EPR spectra.

Differences between the n–π* transitions can be traced back to better conjugation between a thiophene unit with NN than a phenylene with NN unit (larger torsion). The optical gaps E_g derived from the onset of the absorption edge of the n–π* transition for **TPT–NN** and **TTT–NN** are 1.45 and 1.46 eV which are smaller than for **PPP–NN** (1.64 eV) and **PTP–NN** (1.63 eV), respectively. The optical properties are thus tuned by enhancing the number and position of thiophenes in the molecular bridge.

2.4 EPR studies

EPR spectra of the all four biradicals were recorded in argon saturated toluene solutions. The room temperature along with simulated EPR spectra's are displayed in figure 2.4.

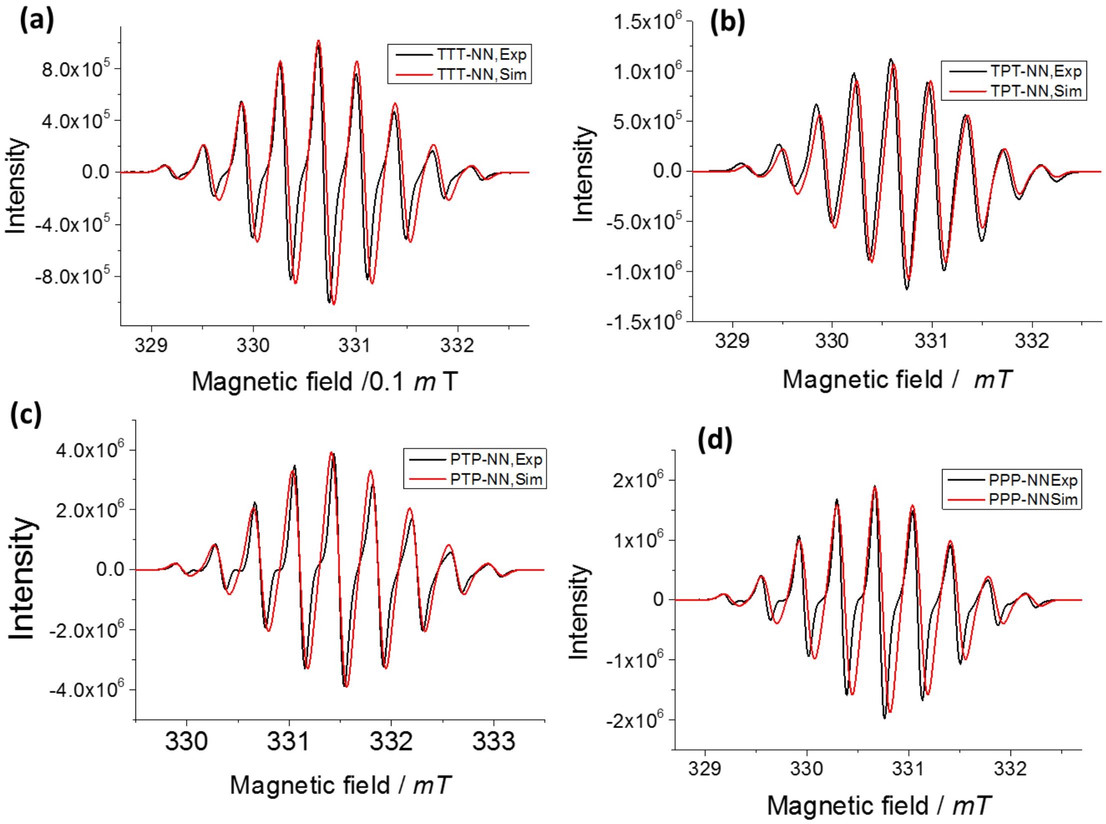

Figure 2.4: EPR spectra's of the biradicals (a) **TTT–NN,** (b) **TPT–NN,** (c) **PTP–NN** and (d) **PPP–NN** in toluene (~10^{-4} M in toluene) at room temperature, experimental (black), and simulated (red).

All the π–bridged nitronyl nitroxides (NN) biradicals exhibited nine line spectra at room temperature due to effective through–bond coupling via spin–polarization effects of the nitronyl nitroxides, indicating that exchange interactions *J* are much larger than the hyperfine coupling constants (*J* >> a_N). The calculated *g* factors and hyperfine coupling constants ($a_{N/2}$) for all biradicals are summarized in table 2.1. These values are in agreement with those typically observed in the NN biradicals found in the literature.

The frozen solution spectra of biradicals (**TTT–NN, TPT–NN** and **PPP-NN**) were recorded at 130 K (figure 2.5). The different kind of the shoulders (left more up and right more down) were observed for **TTT–NN** and **TPT–NN** in the outermost region while **PPP–NN** shows symmetric nature. We verified the anisotropic nature by comparison with thiophene mono radical (**Th–NN**) frozen solution spectra at 130 K demonstrated in (figure 2.5d). The half field $\Delta M_S = 2$ transition although weak due to small zero field splitting, however, is clear evidence for the biradical nature of **TPT–NN**.

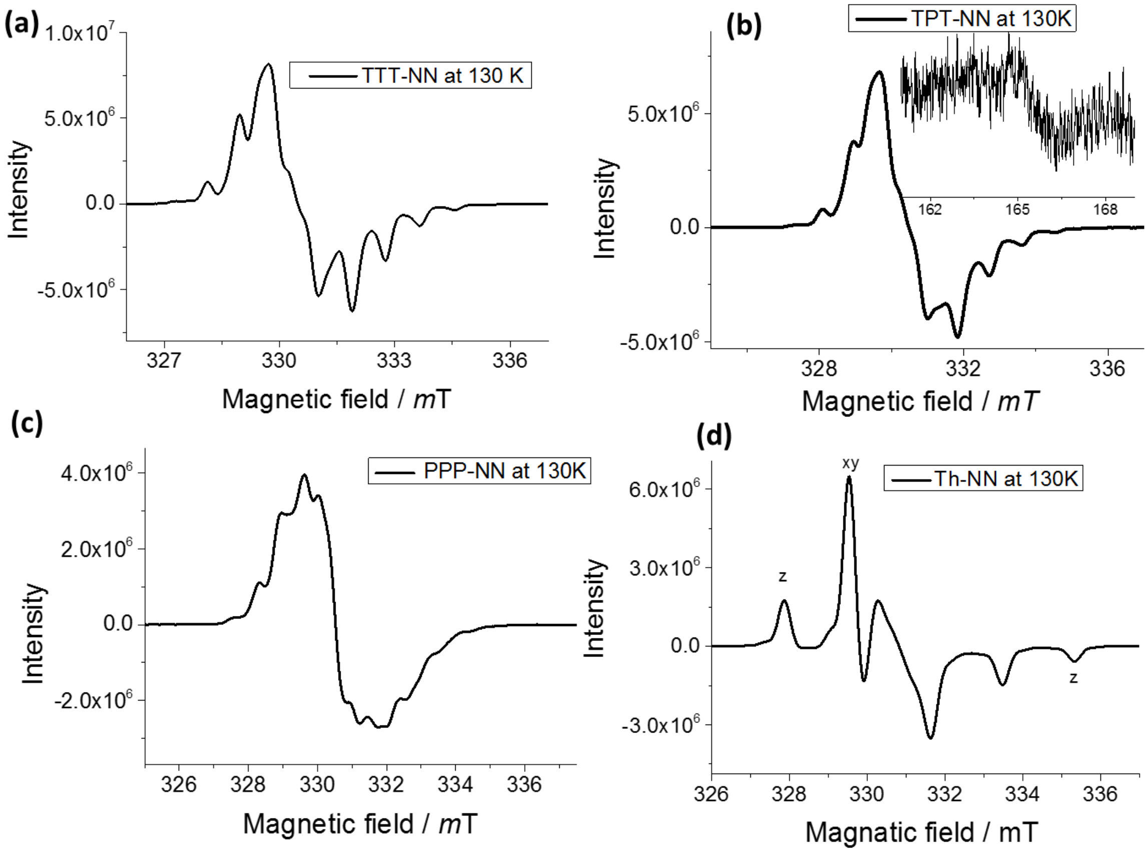

Figure 2.5: The $\Delta M_S = 1$, EPR transition of spectra of the biradicals (a) **TTT–NN,** (b) **TPT–NN,** inset: half field $\Delta M_S = 2$ transition, (c) **PPP–NN**, (d) **Th–NN** in (~10^{-4} M in toluene).

2.5 Crystal structure analysis

The magnetic interactions highly depend on the geometry and packing of the molecules in the crystal lattice. Therefore crystal structure analysis is a vital requirement to understand magnetic interactions operating in synthesized biradical systems. While the crystals suitable for single crystal

X–ray analysis were obtained by slow evaporation of DCM solution of biradicals for the **TPT–NN** and **TTT–NN**, the crystals of **PPP–NN** were grown by slow diffusion of hexane to its solution in DCM.

Table 2.2: Crystal data and structure refinement details of **TPT–NN, TTT–NN**, and **PPP–NN.**

	TPT–NN	**TTT–NN**	**PPP–NN**
Formula	$C_{28}H_{32}N_4O_4S_2$	$C_{26}H_{30}N_4O_4S_3$	$C_{32}H_{36}N_4O_4$
Formula weight[g/mol]	552.20	558.74	540.65
Crystal system	monoclinic	monoclinic	monoclinic
Space group	P 21/c	P 21/n	P 21/n
a /Å	10.9341(19)	12.5445(12)	11.5064(9)
b/Å	11.8693(18)	11.1792(7)	9.9143(10)
c/Å	11.054(2)	20.4146(21)	12.9226(12)
β°	104.497(7)	107.466(8)	112.061(7)
Z	2	4	2
wR2	0.1100	0.2159	0.2959
R1	0.0776	0.0709	0.0963
Density	1.322	1.359	1.314
μ/mm^{-1}	0.23	0.31	0.70
no. independent reflections	3331	6703	2446
no. of refined parameter	176	342	186
Goodness of fit	1.140	1.013	0.961
CCDC	1501331	1501330	1501332

The green needle of **TPT–NN** crystallized in monoclinic, $P2_1/c$ space group, which has an inversion center of C2 symmetry and thus is symmetric to the central phenyl ring (figure 2.6a). There is an intramolecular contact between thiophene sulfur (S) and the radical oxygen atom 2.85 Å (S9…O15) and the torsions between the radical moiety and thiophene unit are very small, such as 9.5° for (S9–C7–C10–N11) and 11.1° (C6–C7–C10–N14), thus the average (10°) is given in the figure 2.5.a. The torsions between the central phenyl ring and the thiophene unit is 25° obtained from the average of 25.7° for (C1–C2–C4–C5) and 24.2° for (C3–C2–C4–S9). The molecular packing of the **TPT–NN** is displayed in figure 2.6b and the molecules are arranged in two different directions. The **TPT–NN** molecules are networking over radical (N–O) unit through adjacent molecules of thiophene carbon as

3.2 Å for (O15–C5) and at the same time the nearest molecule of N–O units also interact with first molecule of thiophene 3.2 Å (C5–O15). The π–π distance between two **TPT-NN** as edge–to–edge (between thiophene and thiophene) approach of the molecules is 3.5 Å. The slipped π–stacked structures are shown in figure 2.6c.

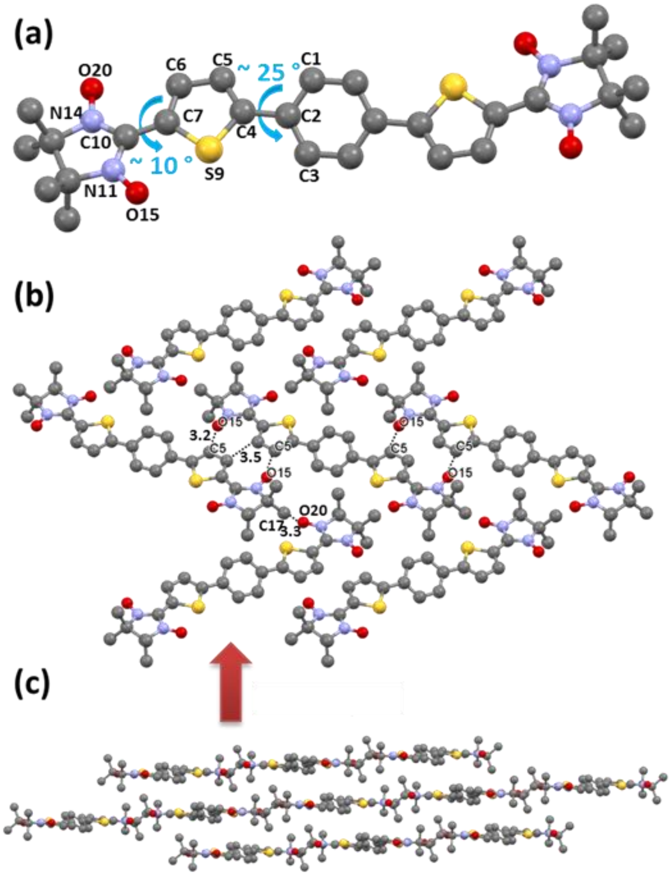

Figure 2.6: X–ray crystal structure of **TPT–NN** (a) molecule, (b) edge–to–edge packing model, (c) face–to–face model of crystal packing, hydrogen atoms are omitted for clarity.

The green plate of **TTT–NN** crystallized in monoclinic, P21/n space group and the X–ray single crystal structure is displayed in figure 2.7a. The crystal data and refinement details are listed in the table 2.2. From the single crystal X–ray structure analysis, the slightly different bond lengths are observed among thiophene and radical (NN) units, which are 1.434 Å for (C1–C12) and 1.426 Å for (C24–C27). Further investigation of crystal structure of the **TTT–NN** shows that both terminal thiophene and radical moiety (NN) are linked with different torsions which are 9.7° (N2–C1–C12–C16), 12.0° (N5–C1–C12–S13) and 3.3° (S23–C24–C27–N28) and 3.2° (C25–C24–C27–N31). Also all the three thiophenes are connected with different torsions 10.6° (S13–C14–C17–C21), 11.1° (C15–C14–C17-S18), 7.3° (C20–C19–C22–S23), 9.1° (S18–C19–C22–C26). The molecular packing of the **TTT–NN** is given in the figure 2.7.b.

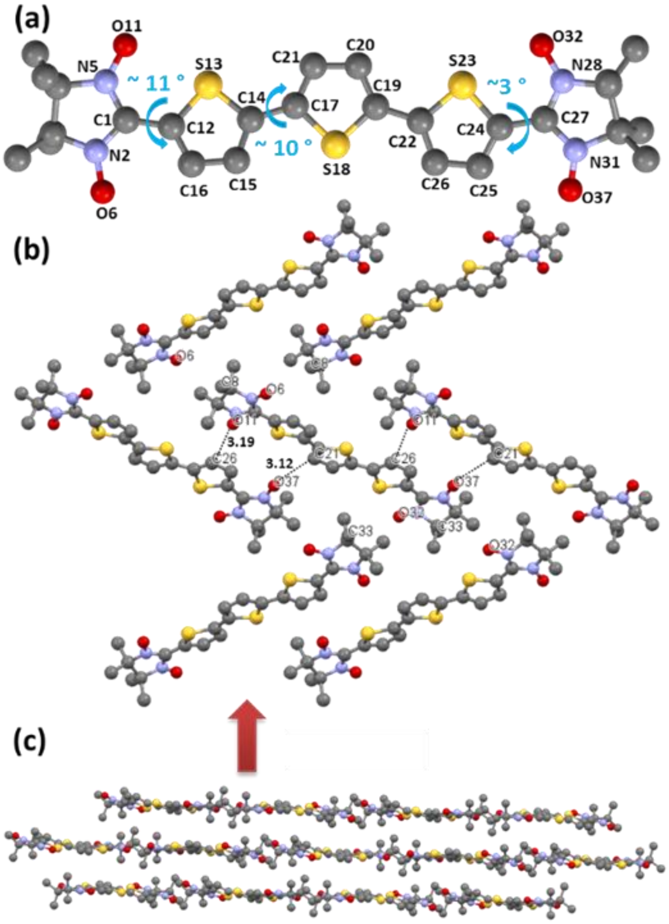

Figure 2.7: X–ray crystal structure of **TTT–NN** (a) molecule, (b) crystal packing 2D mode (c) crystal packing 3D mode, hydrogen atoms are omitted for clarity.

Further analysis of molecular packing revealed that the molecules interact through N–O unit with neighboring molecules of thiophene as 3.19 Å (O11–C26) at the same time second molecule N–O interact with first molecule 3.12 Å (C21–O37).

The single crystal structure of **PPP–NN** is provided in figure 2.8.a and crystallographic parameters are listed in table 2.2. The dark blue plate of **PPP–NN** crystallized in monoclinic, $P2_1/n$

space group and C_i symmetry. The radical NN unit was connected with phenyl ring with torsion of 29° and the phenyl rings are linked with the torsion of 27°. The molecular packing of the **PPP–NN** is shown in figure 2.8.b. The molecules are extended through hydrogen bonding with adjacent molecules. There is no direct intermolecular π electron contact between molecules but the intermolecular distance between molecules (edge to edge) is 3.42 Å for (N–O15…C1) and (face to face) molecular distance is 4.66 Å for (C10–C10).

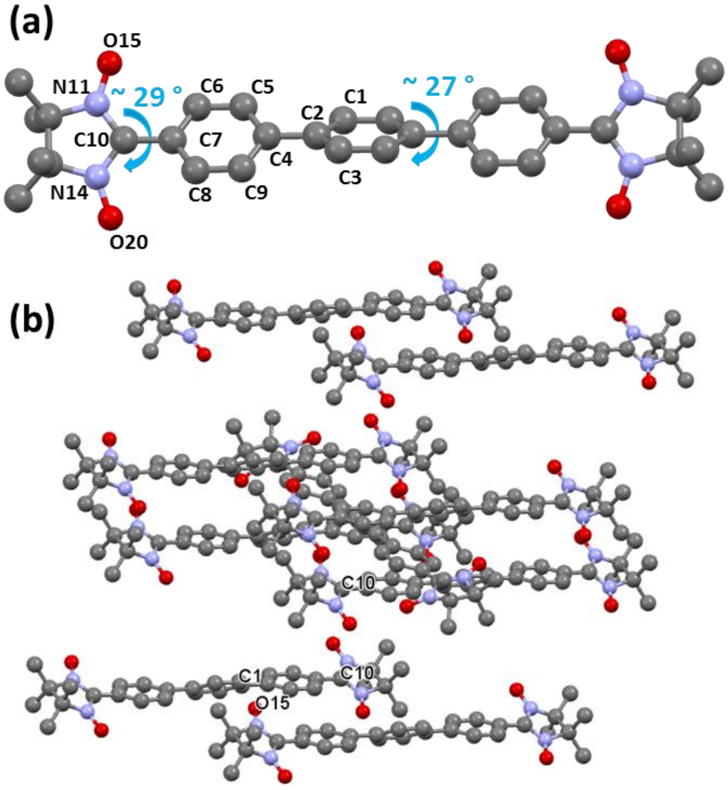

Figure 2.8: X–ray crystal structure of **PPP–NN** (a) molecule, (b) crystal packing.

2.6 DFT calculations

The DFT calculations (Gaussian 09 program package)[35] were carried out to find the influence of the π–bridge on the electronic properties and especially the intra–molecular exchange interactions of the biradicals. The geometries were optimized by UB3LYP/6–31G(d) level. The optimized structures of

TPT–NN, TTT–NN, PTP–NN, and **PPP–NN** are shown in figure 2.9. The simplest Hamiltonian for the molecule with two exchange coupled unpaired electrons is given by $H = -2J_{12}S_1S_2$. The calculations were carried out by the broken-symmetry (BS) approach where the exchange interaction J becomes, $J/k_B = (E(BS) - E(T)) / (S^2(T) - S^2(BS))$, with E(BS) energy of broken symmetry and E(T) the triplet energy. S^2 are the eigenvalues of the spin operator and for $S^2(BS)$ close to 1 and $S^2(T)$ close to 2 the direct exchange becomes $J/k_B = E(BS) - E(T)$. Thus we applied Heisenberg-Dirac-Van Vleck (HDVV) Hamiltonian.[36-40]

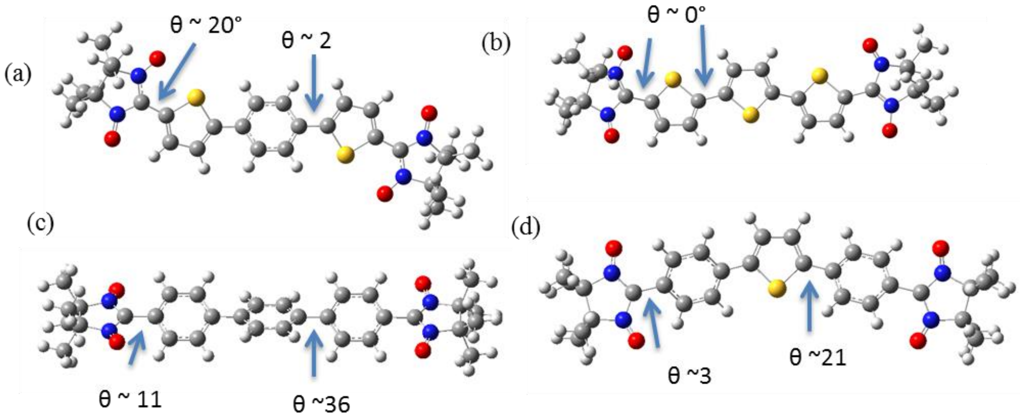

Figure 2.9: The structure of (a) **PPP-NN**, (b) **TTT-NN**, (c) **TPT-NN** and (d) **PTP-NN** obtained by optimized by DFT UB3LYP/6–31G(d) level.

The UBLYP functional and 6–31G(d) basis set was used to elucidate J_{calc} from optimised structure and compared with those from X–ray structure of **TPT–NN, TTT–NN** and **PPP–NN** (first two columns table 2.3). The large deviation here is mainly due to different geometries from optimization versus X–ray structures differing mainly in the torsional angles between the radical unit NN and the π-bridge. The J_{calc} from X-ray structure provided very close values to the ones obtained from magnetization measurements J_{exp} (table 2.3) as found also in other cases before.[41,45] The UBLYP functional and 6–31G(d) basis set is necessary since when calculating J values with UB3LYP functional and 6–31G(d) basis set, it is well known, that over estimation of $J_{intra}(calc)$ occurs, due to the spin contamination from Hartree–Fock contributions.[41] This was also found here (table 2.3). The theoretical exchange interaction of the **TTT–NN** was studied previously with UB3LYP functional,[42] leading to stronger exchange than with BLYP functional.

Table 2.3: The intra–dimer magnetic exchange coupling calculated $J_{calc,}$ and experimental J_{exp} values. The T_{max} denotes the position of the maximum in χ_{mol}(T), (cm^3/mol) as a function of temperature and Φ/K represents the Weiss temperature.

Radicals	J_{calc}/K^a	J_{calc}/K^b	J_{calc}/K^c	J_{calc}/K^d	Φ/K^e	T_{max}/K^f	J_{exp}/K^g
TTT–NN	–99.8	–54.4	–23.9	–14.7	–25.7	10.0	–11.9
TPT–NN	–44.1	–20.1	–11.1	–5.3	–32.4	3.8	–6.2
PTP–NN	–29.1	—	–2.7	—	—	—	—
PPP–NN	–10.9	–9.1	–2.1	–2.5	—	—	—

The magnetic exchange coupling calculated J_{calc} by ^{a}optimized structure using U3BLYP/6-31G(d), ^{b}X–ray structure using U3BLYP/6-31G(d), ^{c}Calculated from optimized structure using UBLYP/6–31G(d), ^{d}Calculated from X–ray structure using UBLYP/6–31G(d), ^{e}Estimated from Curie–Weiss model, ^{f,g}Calculated from molar magnetic susceptibility, χ_{mol} (cm^{-1}mol^{-1}) as function of temperature, ^{h}not determined.

From the triplet state the spin density distributions were derived for **TPT–NN, TTT–NN, PPP–NN** and **PTP–NN.** The spin density is delocalized most on the O-N-C-N-O fragment of NN with small spin density distribution into the connected thiophenes and very minor spin found at the central phenyl ring in **TPT–NN** and the central thiophene unit in **TTT–NN** and **PTP–NN** (figure 2.10).

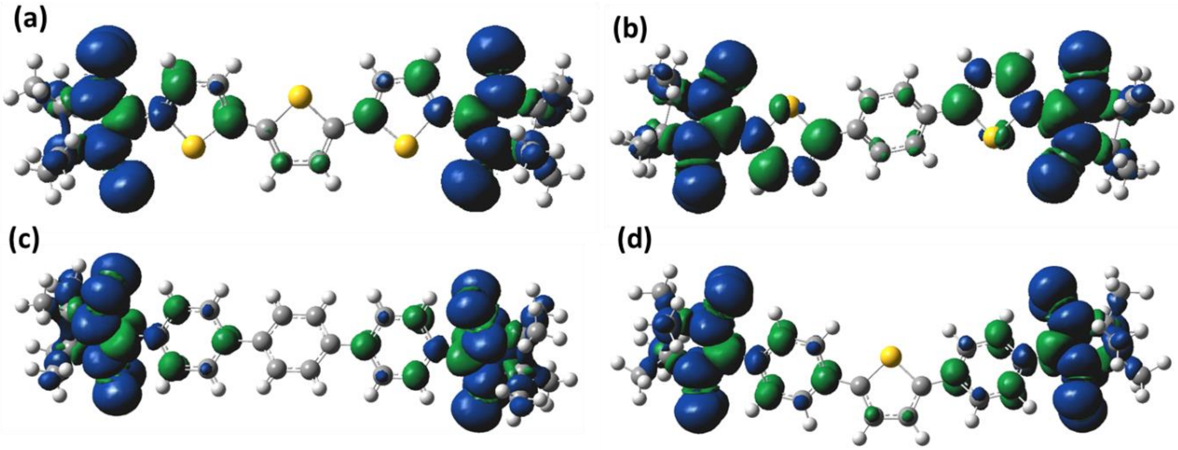

Figure 2.10: Calculated spin density distribution of the triplet state of (a) **TTT–NN**, (b) **TPT–NN**, and (c) **PPP–N**N from X–ray structure, and (d) for **PTP–NN** used for optimized structure using UBLYP/6–31G(d).

2.7 Magnetic properties

The molar magnetic susceptibility, (χ_{mol}) of polycrystalline sample for **TTT–NN** and **TPT–NN** were recorded by Artem S. Bogomyakov in the group of Victor I. Ovcharenko at International Tomography Center, Siberian Branch, Russian Academy of Sciences, Institutskaya Str. Novosibirsk, Russian Federation using a SQUID magnetometer in the temperature range 2 K ≤ T ≤ 300 K to elucidate magnetizations and magnetic exchange interaction as shown in figure 2.11.

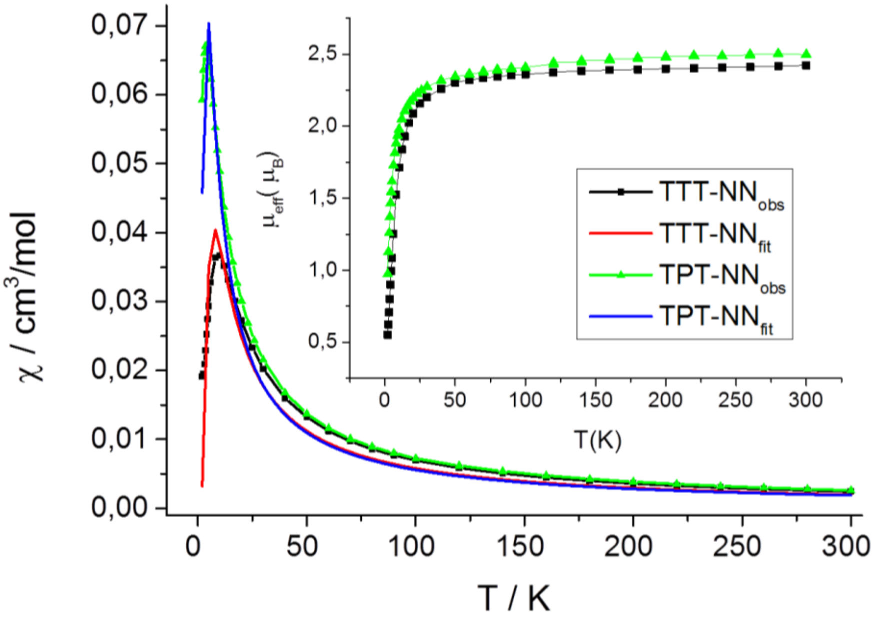

Figure 2.11: Molar magnetic susceptibility χ_{mol} (cm^{3}mol^{-1}) of **TPT–NN** and **TTT–NN** and Inset: Effective magnetic moment, μ_{eff}, as function of temperature.

The data reveal that both the samples behave almost temperature independent in the range from about 100 K to 300 K. The molar magnetic susceptibility (χ_{mol}) initially increased by decreasing the temperature with the Curie–Weiss behaviour at higher temperature region (~150-10 K for **TTT–NN** and 150–3.8 K for **TPT–NN**). Moreover, decreased by decreasing the temperature at lower temperature (< 10 ± 0.5 K for **TTT–NN** and < 3.8 ± 0.5 K for **TPT–NN)** mainly caused by intramolecular antiferromagnetic (AF) interactions, which means that the biradicals switch from a thermally populated magnetic spin triplet state to a non–magnetic spin singlet ground state.

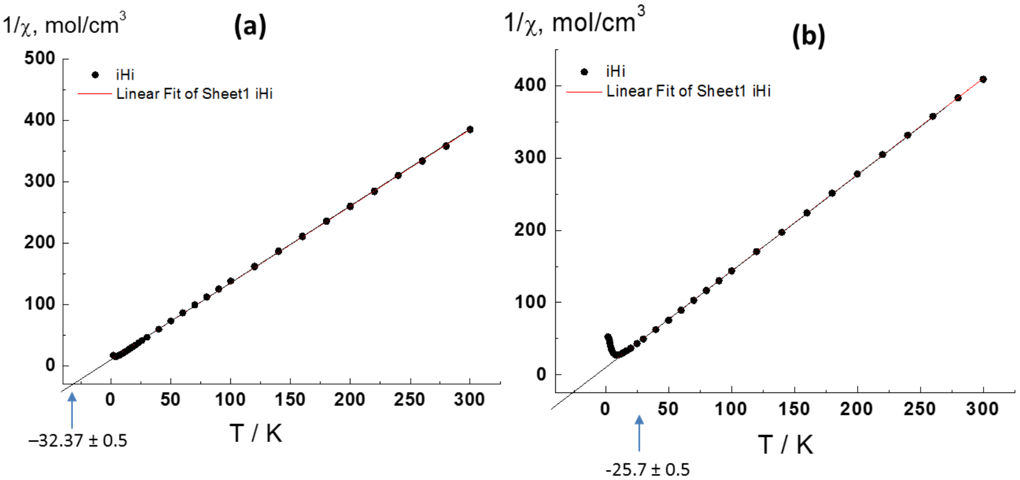

Figure 2.12: Curie–Weiss model straight line of (a) **TPT–NN** and (b) **TTT–N**N.

The mean value for the magnetic exchange coupling at high–temperature regime can be obtained by fitting the curve with inverse magnetic susceptibility $1/\chi_{mol}$ by a Curie–Weiss model straight line (figure 2.12). The fitting gave negative Weiss temperatures are ΦW = –32.4 ± 0.5 K and –25.7 ± 0.5 K for **TTT–NN** and **TPT–NN** respectively. These negative Weiss constants are indicating that there are intramolecular antiferromagnetic coupling interaction between NN radical units through the π-bridge. For a more precise determination of the intradimer coupling constant J_{intra} of **TTT–NN** and **TPT–NN** was estimated by the temperature dependence of the molar magnetic susceptibility over the temperature range 2 K ≥ T ≤ 300 K using the Bleaney–Bowers equation for isolated dimer model.[43] The intra-dimer magnetic exchange coupling constant J_{intra} between two S = 1/2 spins used in this expression refers to a Hamiltonian of the form $H = -2J_{12}S_1S_2$, which was taken also for the DFT calculations. These coupling constants are $J/k_B = -6.2$ K for **TPT-NN** and $J/k_B = -11.9$ K for **TTT–NN**, respectively. The observed effective magnetic moment (μ_{eff}) values for **TTT–NN** and **TPT–NN** are calculated from temperature dependence of magnetic susceptibility as a function of temperature (inset of figure 2.11).

At room temperature the magnetic moments are close to the theoretical value 2.45 μB for magnetically uncorrelated spins of biradicals. The theoretical exchange coupling constants, as J/k_B

calculated from optimized structure using UBLYP/6–31G(d) which are listed in the table 2.3. We did not further inspect the susceptibility experiment for **PPP–NN** and **PTP–NN** because the calculated coupling constant from DFT are very low as $J/k_B = -2.1$ K for **PPP–NN** and $J/k_B = -2.7$ K for **PTP–NN** which are less interesting for the molecular quantum magnets.

2.8 Conclusions

In summary, we have designed and synthesized four nitronyl nitroxide biradicals with different numbers of phenyl and thiophene units as molecular bridge. The intramolecular magnetic interaction were predicted by spin polarization rule, the NN groups are AFM coupled to each other. All the precursors were characterised by NMR spectroscopy, mass spectrometry and **3**, **5, 6, PPP–NNSi** and **PTP–NNSi** were confirmed by single crystal X-ray studies. The structure of biradicals (**TPT–NN**, **TTT–NN**, and **PPP–NN)** were confirmed by single crystal X-ray studies and their intra and inter molecular packing were investigated. All the biradicals were characterised by EPR spectroscopy and compared with computer simulation. A variable temperature and low temperature EPR studies as $\Delta M_S = 1$ and $\Delta M_S = 2$ were carried out. The biradicals were examined by UV–Vis spectroscopy. The thiophene containing biradicals demonstrated more red shifted absorption than the *p-ter*-phenyl based biradicals.

The strength of intra molecular magnetic interactions depends on the distance of the π-bridges and torsion between the aromatic rings in the π–bridge and among π–bridge and NN unit. The distance between the radical centers follows the trend **PPP–NN > PTP–NN > TPT–NN > TTT–NN** and the order of the planarity of the π–bridges were PPP < PTP < TPT < TTT. The torsion of the thiophene and NN are smaller than for the neighboring phenyl and NN units due to smaller steric hindrance of five *vs* six membered rings. The calculated magnetic interactions for the optimized structures deviated more than those estimated from single crystal X–ray structure with experimental values. This deviation may be due to optimized structures are more planar than single crystal X–ray structures. The calculated magnetic interactions from single crystal X–ray structure are quite similar with experimental values for **TTT–NN** and **TPT–NN**. The biradicals (**TPT–NN** and **TTT–NN)** are promising molecules for further assessment because the magnetic coupling constants are –6.2 K for **TPT–NN** and –11.9 K for **TPT–NN** respectively.

2.9 Experimental section

2-(5-Bromothiophen-2-yl)-4,4,5,5-tetramethylimidazolidine-1,3-diol (**2**).

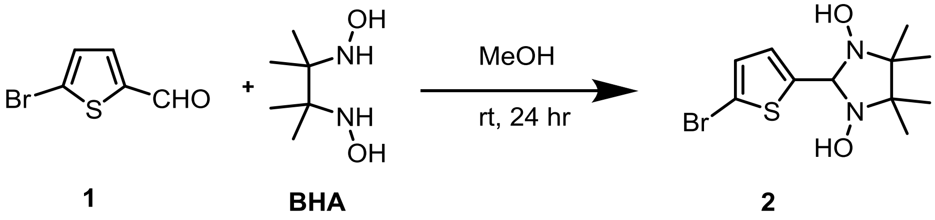

A mixture of 2,3-bis(hydroxylamino)-2,3-dimethylbutane, (1.02 g, 6.75 mmol) and of 5-bromo-2-thiophenecarboxaldehyde (1.31 g, 6.75 mmol) in 10 mL of methanol was taken in the 50 mL round bottom flask and the reaction mixture was stirred for 24 h at room temperature under argon atmosphere. The solution was filtered to obtain **2** as white powder (1.73 g, 80%). ^{1}H NMR (300 MHz, DMSO-d_6) δ: 1.02 (s, 6H), 1.04 (s, 6 H) 4.69 (s, 1 H), 6.9 (d, *J* = 3.9 Hz, 1H), 7.04 (d, *J* = 3.91 Hz, 1 H), 8.02 (s, 2 H). ^{13}C NMR (75 MHz, CDCl$_3$), δ: 17.2, 24.1, 66.4, 86.6, 110.6, 126.4, 129.5, 149.4. ESI HRMS calculated for $C_{11}H_{17}BrN_2O_2SNa$: 343.0092; found 343.0090, [M+Na]$^+$.

2-(5-Bromothiophen-2-yl)-1,3-bis((tert-butyldimethylsilyl)oxy)-4,4,5,5-tetramethylimidazolidine (**3**).

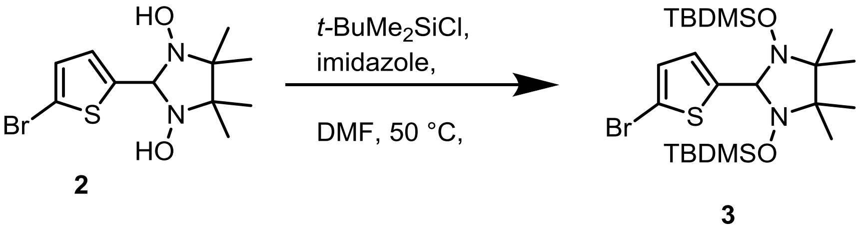

A DMF solution (10 ml) of **2** (1.01 g, 3.11 mmol), *t*-butyldimethylsilyl chloride (2.34 g, 5.56 mmol), and imidazole (2.14 g, 31.44 mmol) in 50 mL Schlenk flask and the reaction mixture was stirred for 24 h at 50 °C under argon atmosphere. Solvent was removed under reduced pressure then the crude product was extracted with ether, and washed with water. The ether layer was dried over magnesium sulfate, and concentrated under reduced pressure. The residue was chromatographed on silica gel with hexane as the eluant to give **3** (1.60 g, 93%). mp 69−70 °C, ^{1}H (300 MHz, CD_2Cl_2) δ: -0.52 (s, 6 H, $SiCH_3$), -0.04 (s, 6 H, $SiCH_3$), 0.83 (s, 18 H, Si-*t*-Bu), 1.13 (s, 12 H, CCH_3), 4.87 (s, 1 H, CH), 6.75 (d, 2 H, *J* = 4.0 Hz, Ar), 6.84 (d, 2 H, *J* = 4 Hz). ^{13}C NMR (75 MHz, $CDCl_3$) δ: -4.6, -3.7, 17.5, 18.5, 24.6, 26.6, 68.7, 90.6, 113.9, 128.7, 129.9, 149.2. ESI HRMS calculated for $C_{23}H_{46}BrN_2O_2SSi_2$: 549.2002; found: 549.2000, $[M+H]^+$.

Synthesis of the TPT–NNSi.

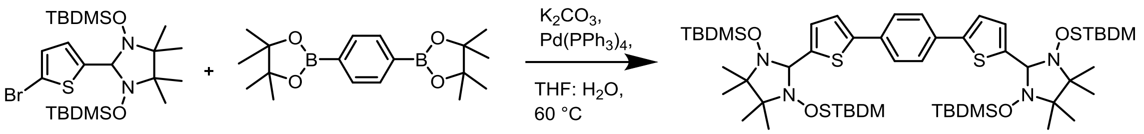

3

TPT-NNSi

1,4-Benzenediboronic acid bis(pinacol) ester, (0.15 g, 0.45 mmol), **3** (0.59 g, 1.08 mmol), K_2CO_3 (0.38 g, 2.71 mmol) and $Pd(PPh_3)_4$ (0.105 g, 0.09 mmol) were taken in 50 mL Schlenk tube and argon purged THF (15 mL) and water (3 mL) were added then the mixture was stirred for 24 h at 60 °C under argon atmosphere. The mixture was poured into water and extracted with ether. The ether layer was dried over magnesium sulfate, and the solution was concentrated under reduced pressure. The residue was chromatographed on silica gel with hexane as eluant to obtain **TPT–NNSi** (0.37 g, 81%). mp 236−237 °C, ^{1}H NMR (300 MHz, CD_2Cl_2) δ: -0.51 (s, 12 H, $SiCH_3$), -0.05 (s, 12 H, $SiCH_3$), 0.83 (s, 36 H, Si-*t*-Bu), 1.16 (s, 24 H, CCH_3), 4.92 (s, 2 H, CH), 6.96 (d, 2 H, *J* = 4 Hz, Ar), 7.15 (d, 2 H, *J* = 4 Hz), 7.62 (s, 4 H). ^{13}C NMR (175 MHz; $CDCl_3$) δ: –4.8, -3.7, 17.6, 18.5, 25.2, 26.6, 30.3, 68.7, 91.0, 121.9, 126.3, 130.6, 134.4, 145.4, 147.4. ESI HRMS calculated for $C_{52}H_{95}N_4O_4S2Si_4$: 1015.5872; found: 1015.5897, $[M+H]^+$.

Synthesis of the TPT–NN.

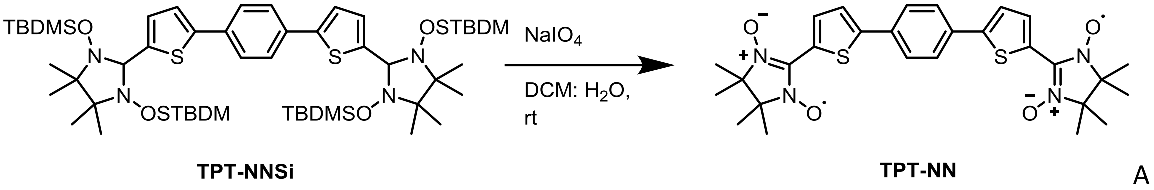

precursor **TPT–NNSi** (0.20 g, 0.21 mmol) was dissolved in dry THF (15 mL) in the round bottom flask and (4.7 mL) Bu_4NF, 1 M solution in THF was added then the mixture was stirred for 16 h at room temperature and while the reaction was monitored by TLC. The product was concentrated under reduced pressure and the mixture was purified by column chromatography, DCM and MeOH (0-2 %) as eluant to provide **TPT–NN** as green solid (90 mg, 83%). mp, decompd. 245−246 °C, ESI HRMS calculated for $C_{28}H_{32}N_4O_4NaS_2$: 575.1763; found: 575.1759 $[M+Na]^+$.

2-(4-Bromophenyl)-4,4,5,5-tetramethylimidazolidine-1,3-diol, (4).

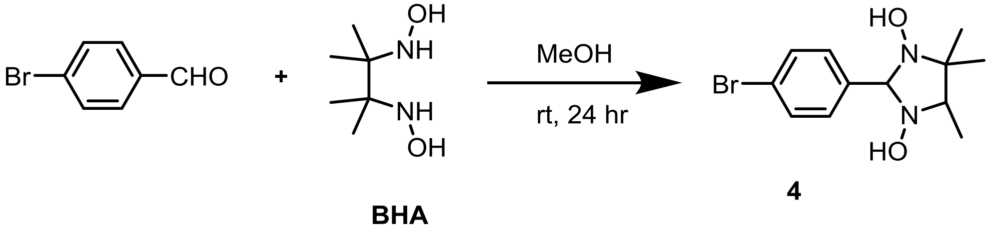

A mixture of 2,3-bis(hydroxylamino)-2,3-dimethylbutane (2.9 g, 19.6 mmol) and of 4-bromobenzaldehyde (3.6 g, 19.6 mmol) in 30 mL of methanol in 50 mL round bottom flask was stirred for 24 h at room temperature under argon atmosphere. The solution was filtered to obtain **4** as a white powder (5.3 g, 86%). ^1H NMR (300 MHz, DMSO-d_6) δ: 1.03 (s, 6 H, CH_3), 1.06 (s, 6 H, CH_3), 4.47 (s, 1 H, CH), 7.41 (d, 2 H, *J* = 9.0 Hz, Ar), 7.50 (d, 2 H, *J* = 8.0 Hz, Ar), 7.81 (s, 2 H, OH). ^{13}C NMR (75 MHz, DMSO-d^6) δ: 17.2, 24.4, 66.2, 89.6, 120.4, 130.5, 130.6,141.4. ESI HRMS calculated for $C_{13}H_{20}BrN_2O_2$ 315.0703 found 315.10694 $[M+H]^+$.

2-(4-Bromophenyl)-1,3-bis((tert-butyldimethylsilyl)oxy)-4,4,5,5-tetramethylimidazolidine, (**5**).

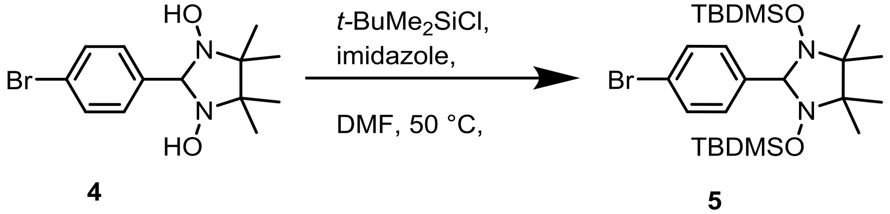

4

5

The 2-(4-Bromophenyl)-4,4,5,5-tetramethylimidazolidine-1,3-diol, **4** (3.0 g, 9.5 mmol), *t*-butyldimethylsilyl chloride (7.2 g, 47.6 mmol), and imidazole (6.5 g, 95.2 mmol) were dissolved in dry DMF (45 mL) in 100 mL Schlenk flask and the mixture was stirred for 24 h at 50 °C under argon atmosphere. DMF was removed under reduced pressure and extracted with diethyl ether and washed with water. The organic layer was dried over magnesium sulfate, and concentrated under reduced pressure. The residue was purified by column chromatography on silica gel with hexane as the eluant to give **5** as white powder (4.8 g, 92%). ^{1}H NMR (300 MHz, CD_2Cl_2) δ: -0.84 (s, 6 H, $SiCH_3$), -0.04 (s, 6 H, $SiCH_3$), 0.79 (s, 18 H, Si-*t*-Bu), 1.16 (s, 12 H, CCH_3), 4.59 (s, 1 H, CH), 7.26 (d, 2 H, *J* = 10 Hz, Ar), 7.40 (d, 2 H, *J* = 10 Hz). δ: ^{13}C NMR (125 MHz, CD_2Cl_2) δ: -19.1, -17.6, –3.2, -3.9, 10.52, 12.1, 54.2, 79.5, 107.8, 116.7, 118.8. ESI HRMS calculated for $C_{25}H_{48}BrN_2O_2Si_2$: 543.2438; found 543.2419, $[M+H]^+$.

Synthesis of the PPP–NNSi.

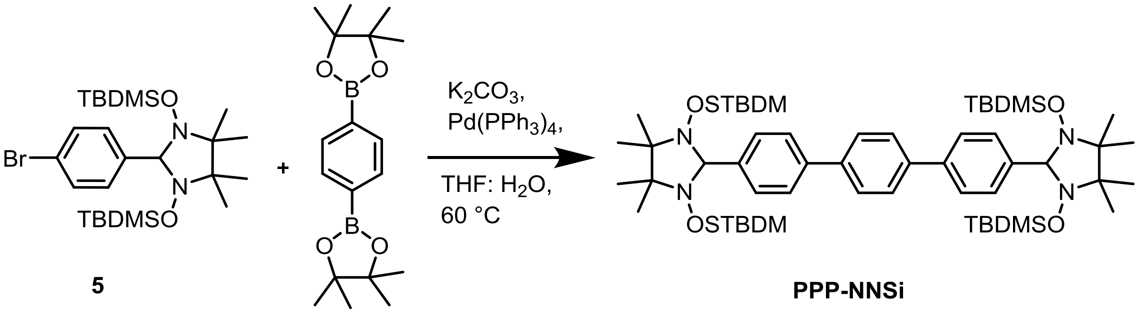

5

PPP-NNSi

A mixture of 1,4-benzenediboronic acid bis(pinacol) ester, (0.15 g, 0.45 mmol), 2-(4-Bromophenyl)-1,3-bis((tert-butyldimethylsilyl)oxy)-4,4,5,5-tetramethylimidazolidine, **5**, (0.50 g, 0.91 mmol), K_2CO_3 (0.19 g, 1.38 mmol), and $Pd(PPh_3)_4$ (0.05 g, 0.09 mmol), was taken in a 50 mL Schlenk tube and argon purged THF (20 mL) and water (5 mL) were added. Then the mixture was stirred for 24 h at 60 °C under argon atmosphere. The mixture was poured into water and filtered to give **PPP–NNSi** as white solid (0.34 g, 74%). mp 248−249 °C, ^{1}H NMR (300 MHz, CD_2Cl_2) δ: -0.77 (s, 12 H, $SiCH_3$), -0.02 (s, 12 H, $SiCH_3$), 0.82 (s, 36 H, Si-*t*-Bu), 1.22 (s, 24 H, CCH_3), 4.71 (s, 1 H, CH), 7.49 (d, 2 H, *J* = 10 Hz, Ar), 7.65 (d, 2 H, *J* = 10 Hz), 7.71 (s, 4 H). ^{13}C NMR (125 MHz, CD_2Cl_3) δ: -4.5, -3.3, 17.8, 18.8, 25.9, 26.9, 30.7, 69.3, 95.0, 126.9, 128.0, 132.2, 140.7, 141.6. ESI HRMS calculated for $C_{56}H_{99}N_4O_4Si_4$: 1003.6743; found 1003.6768, $[M+H]^+$.

Synthesis of the PPP–NN.

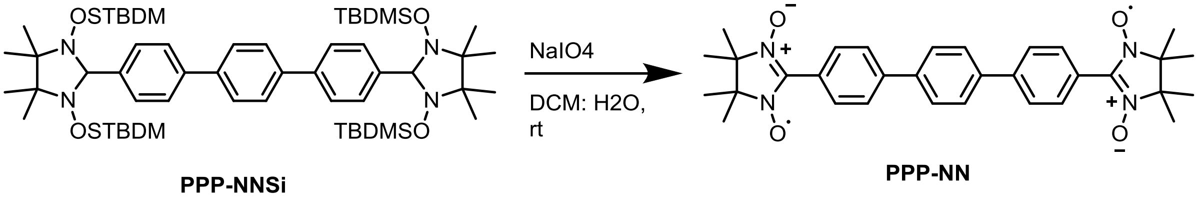

PPP–NNSi (0.10 g, 0.10 mmol) was dissolved in dry THF (10 mL) and (2.4 mL,) and 1 M solution of Bu_4NF in THF was added then the mixture was stirred for 3 h at room temperature, while the reaction was monitored by TLC. The reaction mixture was concentrated under reduced pressure, and then the crude product was purified by column chromatography, DCM and MeOH (0-2 %) as eluant to obtain **PPP–NN** as a blue solid (0.037 g, 68%). mp, decompd. 260−261 °C, ESI HRMS calculated for $C_{32}H_{36}N_4O_4Na$: 563.2634; found 563.2650, $[M+Na]^+$.

1,3-Bis((tert-butyldimethylsilyl)oxy)-4,4,5,5-tetramethyl-2-(4-(4,4,5,5-tetramethyl-1,3,2-dioxaborolan-2-yl)phenyl)imidazolidine, (8).

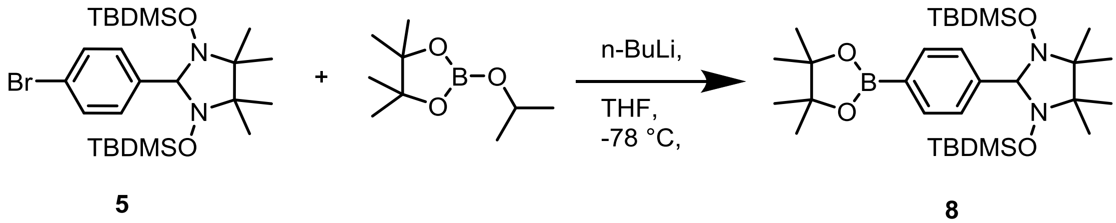

The compound **5** (4.80 g, 8.83 mmol), was dissolved in dry THF (50 mL) in the 100 mL Schlenk tube and cooled to -78 °C then *n*- butyllithium (1.6 M solution) in hexane (6.7 mL, 10.56 mmol) was added and the mixture was stirred at same temperature for 1 h, then 2-isopropylboronic acid, pinacol ester (1.97 g, 2.16 mL, 10.59 mmol), was added and the reaction mixture was stirred at same temperature for further 1 h then quenched with water (10 mL), and extracted with ether. The ether layer was dried over magnesium sulfate, and concentrated under reduced pressure. The residue was chromatographed on silica gel with hexane as eluant to obtain **8** (4.9 g, 94%). mp 132-133 °C, ^{1}H NMR (300 MHz, CD_2Cl_2) δ: -0.90 (s, 6 H, $SiCH_3$), -0.04 (s, 6 H, $SiCH_3$), 0.79 (s, 18 H, *t*-Bu), 1.17 (s, 12 H, CCH_3), 4.62 (s, 1 H, CH), 7.39 (d, 2 H, *J* = 6 Hz), 7.65 (d, 2 H, *J* = 9 Hz). ^{13}C NMR (125 MHz; CD_2Cl_2) δ; -4.7, -3.5, 17.7, 18.4, 25.1, 25.4, 26.6, 68.7, 84.3, 94.9, 129.2, 130.9, 134.5, 145.2. ESI HRMS calculated for $C_{31}H_{60}BN_2O_4Si_2$: 590.4215; found: 590.4205 $[M+H]^+$.

Synthesis of the PTP–NNSi.

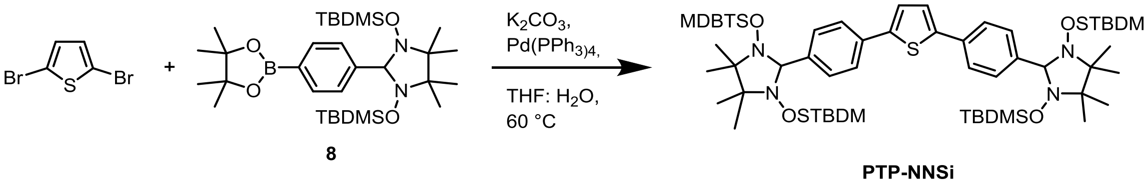

2,5-Dibromothiophene, (0.10 g, 0.42 mmol), **8**(0.50 g, 0.85 mmol), K_2CO_3 (0.35 g, 2.53 mmol), and $Pd(PPh_3)_4$ (0.11 g, 0.09 mmol) were taken in 50 mL Schlenk tube. And then argon purged THF (15 mL), and water (5 mL) was added then the mixture was stirred for 24 h at 60 °C under argon atmosphere. Then the mixture was poured into water and extracted with ether. The ether layer was dried over magnesium sulfate, and concentrated under reduced pressure. The residue was chromatographed on silica gel with hexane to obtain **PTP-NNSi** (0.28 g, 66%). mp 210–211 °C, ^{1}H NMR (250 MHz, CD_2Cl_2) δ: -0.78 (s, 12 H, $SiCH_3$), -0.01 (s, 12 H, $SiCH_3$), 0.81 (s, 36 H, Si-*t*-Bu), 1.19 (s, 24 H, CCH_3), 4.65 (s, 1 H, CH), 7.35 (s, 2 H), 7.42 (d, 2 H, *J* = 7.5 Hz), 7.60 (d, 4 H, *J* = 7.5 Hz). ^{13}C NMR (125 MHz; CD_2Cl_3) δ: -4.6, -3.5, 17.6, 18.4, 25.1, 26.6, 68.6, 94.1, 124.3, 125.1, 132.1, 134.3, 141.7, 143.9. ESI HRMS calculated for $C_{54}H_{97}N_4O_4Si_4S$: 1009.6308; found 1009.6298 $[M+H]^+$.

Synthesis of the PTP–NN.

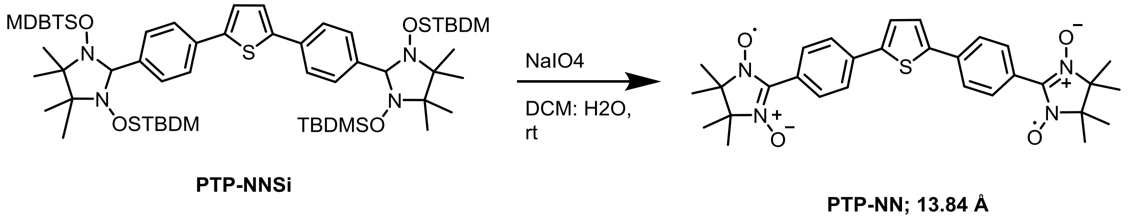

PTP–NNSi (0.05 g, 0.05 mmol) was dissolved in dry THF and (1.19 mL) and Bu_4NF, 1 M solution in THF was added then the mixture was stirred for 16 h at room temperature, while the reaction was monitored by TLC. The reaction mixture was concentrated under reduced pressure and the mixture was purified by column chromatography, DCM and MeOH (0-2 %) as eluant to obtain **PTP–NN** (18 mg, 70%). mp, decompd. mp 206−207 °C, MALDI-TOF calculated for $C_{30}H_{34}N_4O_4S$; 546.6900; found: 546.2100 $[M]^+$.

Synthesis of the TTT–NNSi.

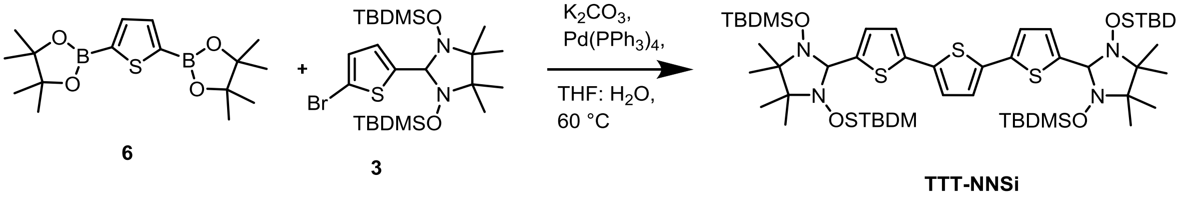

Thiophene-2,5-diboronic acid bis(pinacol) ester (0.20 g, 0.59 mmol), **3** (0.72 g, 1.31 mmol), K_2CO_3 (0.49 g, 3.57 mmol) and $Pd(PPh_3)_4$ (0.07 g, 0.06 mmol) were taken in a Schlenk tube and argon purged THF (30 mL) and water (10 mL) were added then the mixture was stirred for 24 h at 60 °C under argon atmosphere. Then the mixture was poured into water and extracted with diethyl ether. The ether layer was dried over magnesium sulfate, concentrated under reduced pressure. The residues were chromatographed on silica gel with hexane as an eluent, and to TTT-NNSi obtain (0.11 g, 18 %). ^1H NMR (300 MHz, CD_2Cl_2) δ: -0.51 (s, 12 H, $SiCH_3$), -0.05 (s, 12 H, $SiCH_3$), 0.83 (s, 36 H, Si-*t*-Bu), 1.16 (s, 24 H, CCH_3), 4.92 (s, 1 H, CH), 6.96 (d, 2 H, *J* = 4 Hz, Ar), 7.15 (d, 2 H, *J* = 4 Hz), 7.62 (s, 4 H). ^{13}C NMR (125 MHz, $CDCl_3$) δ: -4.7, -3.7, 17.5, 18.5, 25.1, 26.5, 30.3, 68.7, 122.4, 124.3, 130.1, 137.1, 138.7, 146.9. ESI HRMS calculated for $C_{50}H_{93}N_4O_4S_3Si_4$: 1021.5436; found 1021.5461, [M+H].$^+$ **Mono coupled product**. 0.171 g, 51 %; ^{1}H NMR (300 MHz, CD_2Cl_2) δ: -0.51 (s, 12 H, $SiCH_3$), -0.05 (s, 12 H, $SiCH_3$), 0.83 (s, 36 H, Si-*t*-Bu), 1.16 (s, 24 H, CCH_3), 4.92 (s, 1 H, CH), 6.96 (d, 2 H, *J* = 4 Hz, Ar), 7.15 (d, 2 H, *J* = 4 Hz), 7.62 (s, 4 H).

Synthesis of the TTT–NNSi.

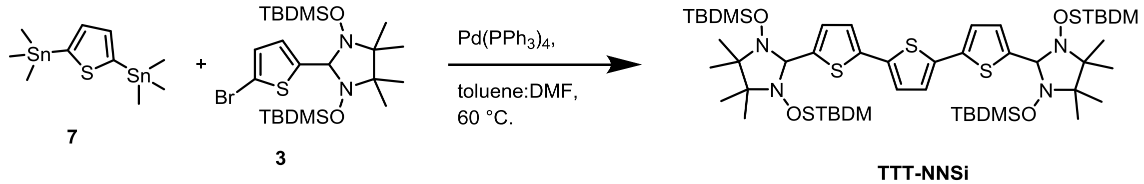

By Stile coupling. 2,5-bis(trimethylstannyl)thiophene (0.10 g, 0.23 mmol), **3** (0.33 g, 0.61 mmol), and $Pd(PPh_3)_4$ (0.06 g, 0.05 mmol), were taken in 50 mL Schleck tube and argon purged dry DMF (10 mL), was added then the mixture was stirred for 30 h at 60 °C. Then DMF was removed under reduced pressure. The residue was extracted with diethyl ether (2 X 50 mL). The ether layer was dried over magnesium sulfate, and concentrated under reduced pressure. The residue was chromatographed on silica gel with hexane to obtain **TTT–NNSi** (0.18 g, 79 %).

Synthesis of the TTT–NN.

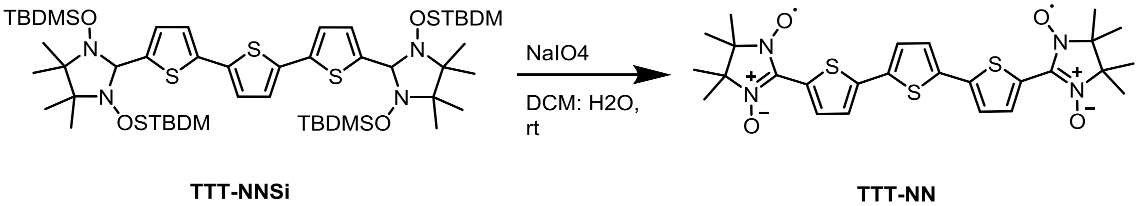

TTT–NNSi (0.10 mg, 0.10 mmol) was dissolved in dry THF (7 mL) and (2.4 mL) Bu_4NF, 1 M solution in THF was added then the mixture was stirred for 16 h at room temperature, while the reaction was monitored by TLC. The solution was concentrated under reduced pressure and the mixture was purified by column chromatography, DCM and MeOH (0-2 %) as eluant to obtain **TTT–NN** as green solid (36 mg, 66%). mp, decompd. 219−220 °C, ESI calculated for $C_{26}H_{30}N_4O_4S_3$: 558.14, found: 558.16 [M]$^+$.

The appendix-II (**A-II**) is given for chapter–2.

Structures, refinement details of **3, 5, 6, PPP-NNSi**, **PTP-NNSi**, structures of the **TPT-NN, TTT-NN**, and **PPP-NN**, variable temperature (290-210 K) EPR spectra of the biradicals for **PPP-NN** and **TTT-NN** in toluene (≈10−4 M in toluene), NMR spectra of new compounds for **PPP-NNSi**, **TPT-NNSi TTT-NNSi** and **PTP-NNSi**, and details of the DFT calculations using Gaussian 09.

2.10. REFERENCES

1. Anderson, M. H.; Ensher, J. R.; Matthews, M. R.; Wieman, C. E.; Cornell, E. A., Observation of Bose-Einstein Condensation in a Dilute Atomic Vapor. *Science* **1995,** *269*, 198-201.
2. Pethick, C. J.; Smith, H., *Bose-Einstein Condensation in Dilute Gases*. Cambridge University Press: **2002**.
3. Griffin, A.; Nikuni, T.; Zaremba, E., *Bose-Condensed Gases at Finite Temperatures*. Cambridge University Press: **2009**.
4. Tutsch, U.; Wolf, B.; Wessel, S.; Postulka, L.; Tsui, Y.; Jeschke, H. O.; Opahle, I.; Saha-Dasgupta, T.; Valentí, R.; Brühl, A.; Remović-Langer, K.; Kretz, T.; Lerner, H. W.; Wagner, M.; Lang, M., Evidence of a Field-Induced Berezinskii–Kosterlitz–Thouless Scenario in a Two-Dimensional Spin–Dimer System. *Nature Commun.* **2014,** *5*, 5169.
5. Giamarchi, T.; Ruegg, C.; Tchernyshyov, O., Bose-Einstein condensation in magnetic insulators. *Nat Phys* **2008,** *4*, 198-204.
6. Sachdev, S., Quantum Magnetism and Criticality. *Nat. Phys.* **2008,** *4*, 173-185.
7. Borozdina, Y. B.; Mostovich, E.; Enkelmann, V.; Wolf, B.; Cong, P. T.; Tutsch, U.; Lang, M.; Baumgarten, M., Interacting Networks of Purely Organic Spin–1/2 Dimers. *J. Mater. Chem. C* **2014,** *2*, 6618-6629.
8. Ravat, P.; Borozdina, Y.; Ito, Y.; Enkelmann, V.; Baumgarten, M., Crystal Engineering of Tolane Bridged Nitronyl Nitroxide Biradicals: Candidates for Quantum Magnets. *Crystal Growth & Design* **2014,** *14*, 5840-5846.
9. Borozdina, Y. B.; Mostovich, E. A.; Cong, P. T.; Postulka, L.; Wolf, B.; Lang, M.; Baumgarten, M., Spin-Dimer Networks: Engineering Tools to Adjust the Magnetic Interactions in Biradicals. *J. Mater. Chem. C* **2017,** *5*, 9053-9065.
10. Barone, V.; Cacelli, I.; Ferretti, A., Magnetic Coupling in Bis-Nitronylnitroxide Radicals: The Role of Aromatic Bridges. *J. Chem. Phys.* **2009,** *130*, 094306.

11. Wautelet, P.; Le Moigne, J.; Videva, V.; Turek, P., Spin Exchange Interaction through Phenylene-Ethynylene Bridge in Diradicals Based on Iminonitroxide and Nitronylnitroxide Radical Derivatives. 1. Experimental Investigation of the Through-Bond Spin Exchange Coupling. *J. Org. Chem.* **2003,** *68*, 8025-8036.

12. Mostovich, E. A.; Borozdina, Y.; Enkelmann, V.; Remović-Langer, K.; Wolf, B.; Lang, M.; Baumgarten, M., Planar Biphenyl-Bridged Biradicals as Building Blocks for the Design of Quantum Magnets. *Crystal Growth & Design* **2012,** *12*, 54-59.

13. Ravat, P.; Ito, Y.; Gorelik, E.; Enkelmann, V.; Baumgarten, M., Tetramethoxypyrene-Based Biradical Donors with Tunable Physical and Magnetic Properties. *Org. Lett.* **2013,** *15*, 4280-4283.

14. Kolanji, K.; Ravat, P.; Bogomyakov, A. S.; Ovcharenko, V. I.; Schollmeyer, D.; Baumgarten, M., Mixed Phenyl and Thiophene Oligomers for Bridging Nitronyl Nitroxides. *J. Org. Chem* **2017,** *82*, 7764-7773.

15. Ravat, P.; Baumgarten, M., "Tschitschibabin Type Biradicals": Benzenoid or Quinoid? *Phys. Chem. Chem. Phys.* **2015,** *17*, 983-991.

16. Sarbadhikary, P.; Shil, S.; Panda, A.; Misra, A., A Perspective on Designing Chiral Organic Magnetic Molecules with Unusual Behavior in Magnetic Exchange Coupling. *J. Org. Chem.* **2016,** *81*, 5623-5630.

17. Koivisto, B. D.; Hicks, R. G., The Magnetochemistry of Verdazyl Radical-Based Materials. *Coord. Chem. Rev.* **2005,** *249*, 2612-2630.

18. Matuschek, D.; Eusterwiemann, S.; Stegemann, L.; Doerenkamp, C.; Wibbeling, B.; Daniliuc, C. G.; Doltsinis, N. L.; Strassert, C. A.; Eckert, H.; Studer, A., Profluorescent Verdazyl Radicals - Synthesis and Characterization. *Chem. Sci.* **2015,** *6*, 4712-4716.

19. Train, C.; Norel, L.; Baumgarten, M., Organic Radicals, a Promising Route Towards Original Molecule-Based Magnetic Materials. *Coord. Chem. Rev.* **2009,** *253*, 2342-2351.

20. Onal, E.; Yerli, Y.; Cosut, B.; Pilet, G.; Ahsen, V.; Luneau, D.; Hirel, C., Nitronyl and Imino Nitroxide Free Radicals as Precursors of Magnetic Phthalocyanine and Porphyrin Building Blocks. *New J. Chem.* **2014,** *38*, 4440-4447.

21. Reis, S. G.; Briganti, M.; Martins, D. O. T. A.; Akpinar, H.; Calancea, S.; Guedes, G. P.; Soriano, S.; Andruh, M.; Cassaro, R. A. A.; Lahti, P. M.; Totti, F.; Vaz, M. G. F., First Coordination Compounds Based on a Bis(Imino Nitroxide) Biradical and 4f Metal Ions: Synthesis, Crystal Structures and Magnetic Properties. *Dalton Trans.* **2016,** *45*, 2936-2944.

22. Akita, T.; Mazaki, Y.; Kobayashi, K.; Koga, N.; Iwamura, H., Crystal Structures and Magnetic Properties of Nitronyl Nitroxide and Imino Nitroxide Radicals Attached to Thieno[3,2-b]- and Thieno[2,3-b]thiophene Rings. *J. Org. Chem.* **1995,** *60*, 2092-2098.

23. Zheludev, A.; Bonnet, M.; Delley, B.; Grand, A.; Luneau, D.; Örström, L.; Ressouche, E.; Rey, P.; Schweizer, J., An Imino Nitroxide Free Radical: Experimental and Theoretical Spin Density and Electronic Structure. *J. Magn. Magn. Mater.* **1995,** *145*, 293-305.

24. Ravat, P.; Teki, Y.; Ito, Y.; Gorelik, E.; Baumgarten, M., Breaking the Semi-Quinoid Structure: Spin-Switching From Strongly Coupled Singlet to Polarized Triplet State. *Chem. Eur. J.* **2014,** *20*, 12041-5.

25. Ravat, P.; Baumgarten, M., Positional Isomers of Tetramethoxypyrene-based Mono- and Biradicals. *J. Phys. Chem. B* **2015,** *119*, 13649-55.

26. Borozdina, Y. B.; Mostovich, E.; Enkelmann, V.; Wolf, B.; Cong, P. T.; Tutsch, U.; Lang, M.; Baumgarten, M., *J. Mater. Chem. C* **2014,** *2*, 6618-6629.

27. Osiecki, J. H.; Ullman, E. F., Studies of Free Radicals. I. .Alpha.-Nitronyl Nitroxides, A New Class of Stable Radicals. *J. Am. Chem. Soc.* **1968,** *90*, 1078–1079.

28. Caneschi, A.; Gatteschi, D.; Sessoli, R.; Rey, P., Toward Molecular Magnets: The Metal-Radical Approach. *Acc. Chem. Res.* **1989,** *22*, 392-398.

29. Zoppellaro, G.; Ivanova, A.; Enkelmann, V.; Geies, A.; Baumgarten, M., Synthesis, Magnetic Properties and Theoretical Calculations of Novel Nitronyl Nitroxide and Imino Nitroxide Diradicals Grafted on Terpyridine Moiety. *Polyhedron* **2003,** *22*, 2099-2110.

30. Rüegg, C.; Kiefer, K.; Thielemann, B.; McMorrow, D. F.; Zapf, V.; Normand, B.; Zvonarev, M. B.; Bouillot, P.; Kollath, C.; Giamarchi, T.; Capponi, S.; Poilblanc, D.; Biner, D.; Krämer, K. W., Thermodynamics of the Spin Luttinger Liquid in a Model Ladder Material. *Phys. Rev. Lett.* **2008,** *101*, 247202.

31. Tretyakov, E.; Okada, K.; Suzuki, S.; Baumgarten, M.; Romanenko, G.; Bogomyakov, A.; Ovcharenko, V., Synthesis, Structure and Properties of Nitronyl Nitroxide Diradicals with Fused-Thiophene Couplers. *J. Phys. Org. Chem.* **2016,** *29*, 725–734.

32. Mitsumori, T.; Inoue, K.; Koga, N.; Iwamura, H., Exchange Interactions between Two Nitronyl Nitroxide or Iminyl Nitroxide Radicals Attached to Thiophene and 2,2'-Bithienyl Rings. *J. Am. Chem. Soc.* **1995,** *117*, 2467-2478.

33. Higashiguchi, K.; Yumoto, K.; Matsuda, K., Evaluation of the β Value of the Phenylene Unit by Probing Exchange Interaction between Two Nitroxides. *Org. Lett.* **2010,** *12*, 5284-5286.

34. Yokojima, S.; Kobayashi, T.; Shinoda, K.; Matsuda, K.; Higashiguchi, K.; Nakamura, S., π-Conjugation of Two Nitronyl Nitroxides-Attached Diarylethenes. *J. Phys. Chem. B* **2011,** *115*, 5685-5692.

35. Frisch, M. J.; Trucks, G. W.; Schlegel, H. B.; Scuseria, G. E.; Robb, M. A.; Cheeseman, J. R.; Scalmani, G.; Barone, V.; Mennucci, B.; Petersson, G. A.; Nakatsuji, H.; Caricato, M.; Li, X.; Hratchian, H. P.; Izmaylov, A. F.; Bloino, J.; Zheng, G.; Sonnenberg, J. L.; Hada, M.; Ehara, M.; Toyota, K.; Fukuda, R.; Hasegawa, J.; Ishida, M.; Nakajima, T.; Honda, Y.; Kitao, O.; Nakai, H.; Vreven, T.; Montgomery, J., J. A.; Peralta, J. E.; Ogliaro, F.; Bearpark, M.; Heyd, J. J.; Brothers, E.; Kudin, K. N.; Staroverov, V. N.; Kobayashi, R.; Normand, J.; Raghavachari, K.; Rendell, A.; Burant, J. C.; Iyengar, S. S.; Tomasi, J.; Cossi, M.; Rega, N.; Millam, N. J.; Klene, M.; Knox, J. E.; Cross, J. B.; Bakken, V.; Adamo, C.; Jaramillo, J.; Gomperts, R.; Stratmann, R. E.; Yazyev, O.; Austin, A. J.; Cammi, R.; Pomelli, C.; Ochterski, J. W.; Martin, R. L.; Morokuma, K.; Zakrzewski, V. G.; Voth, G. A.; Salvador, P.; Dannenberg, J. J.; Dapprich, S.; Daniels, A. D.; Farkas, Ö.; Foresman, J. B.; Ortiz, J. V.; Cioslowski, J.; Fox, D. J., *Gaussian 09, Revision D.01*, **2009**.

36. Noodleman, L., Valence Bond Description of Antiferromagnetic Coupling in Transition Metal Dimers. *J. Chem. Phys.* **1981,** *74*, 5737-5743.

37. Noodleman, L.; Davidson, E. R., Ligand Spin Polarization and Antiferromagnetic Coupling in Transition Metal Dimers. *Chem. Phys.* **1986,** *109*, 131-143.

38. Yamaguchi, K.; Jensen, F.; Dorigo, A.; Houk, K. N., A Spin Correction Procedure for Unrestricted Hartree-Fock and Møller-Plesset Wavefunctions for Singlet Diradicals and Polyradicals. *Chem. Phys. Lett.* **1988,** *149*, 537-542.

39. Soda, T.; Kitagawa, Y.; Onishi, T.; Takano, Y.; Shigeta, Y.; Nagao, H.; Yoshioka, Y.; Yamaguchi, K., Ab Initio Computations of Effective Exchange Integrals For H–H, H–He–H And Mn_2O_2 Complex: Comparison of Broken-Symmetry Approaches. *Chem. Phys. Lett.* **2000,** *319*, 223-230.

40. Shoji, M.; Koizumi, K.; Kitagawa, Y.; Kawakami, T.; Yamanaka, S.; Okumura, M.; Yamaguchi, K., A General Algorithm For Calculation Of Heisenberg Exchange Integrals J In Multi Spin Systems. *Chem. Phys. Lett.* **2006,** *432*, 343-347.

41. Plakhutin, B. N.; Gorelik, E. V.; Breslavskaya, N. N.; Milov, M. A.; Fokeyev, A. A.; Novikov, A. V.; Prokhorov, T. E.; Polygalova, N. E.; Dolin, S. P.; Trakhtenberg, L. I., Anomalous Values of $\hat{S}2$ Before and After Annihilation of the First Spin Contaminant in UHF Wave Function. *J. Struct. Chem.* **2005,** *46*, 195-203.

42. Nishizawa, S.; Hasegawa, J.-y.; Matsuda, K., Theoretical Investigation on the Decaying Behavior of Exchange Interaction in Quinoid and Aromatic Molecular Wires. *J. Chem. Phys. C* **2015,** *119*, 5117-5121.

43. Bleaney, B.; Bowers, K. D., Anomalous Paramagnetism of Copper Acetate. *Proc. R. Soc. London, Ser. A* **1952,** *214*, 451-465.

CHAPTER 3

Planar Benzo[1,2–*b*:4,5–*b'*]dithiophene Derivatives Decorated with Nitronyl– and Imino–Nitroxides

Abstract: Four weakly antiferromagnetic interacting biradicals of benzo[1,2–*b*:4,5–*b*']dithiophene (BDT), and BDT extended with two thiophene (BDTTh$_2$) linked with nitronyl– and imino–nitroxides (NN and IN) as (**BDT–NN, BDT–IN, BDTTh$_2$–NN** and **BDTTh$_2$–IN**) were designed and synthesized. They were characterized by mass, UV–Vis, EPR, single crystal X–ray diffraction, DFT calculations, and SQUID studies. In all molecules, the radical units were linked to a thiophene of the planar π–bridges resulting in small torsions. The **BDT–NN** and **BDT–IN** crystallized in dimeric forms, while **BDTTh$_2$–NN** was found as monomeric structure. The short inter–molecular π–π distance found (3.42 Å) for **BDT–NN** whereas the larger π–π distance for **BDT–IN** (3.83 Å) and **BDTTh$_2$–NN** (3.67 Å), respectively. The *intra*–molecular magnetic interaction ($J_{intra,exp}/k_B$) of the **BDT–NN** (–26 K) is much larger than for **BDT–IN** (–5.3 K), while it is reduced for the dithiophene extended molecule **BDTTh$_2$–NN** (–2.3 K). The inter–molecular interactions ($J_{inter,exp}/k_B$) of **BDT–NN** (–6.5 K) and **BDT–IN** (–6.0 K) are stronger than for **BDTTh$_2$–NN (**–4.6 K). Such large intermolecular couplings resulting from good π-stacking and marks **BDT-IN** a highlight for well promising crystalline materials with similar sized J_{intra} and J_{inter}. In addition, we also extracted a coupling within the chain of J_{chain}/k_B = –2.2 K and a coupling between the chains of $zJ_{int\text{-}chain}$ = –1.5 K for **BDTTh$_2$–NN** by Heisenberg chain model. Further, the *intra*– and *inter*–molecular interactions and spin densities were examined by density functional theory (DFT) studies to understand the magnetic properties.

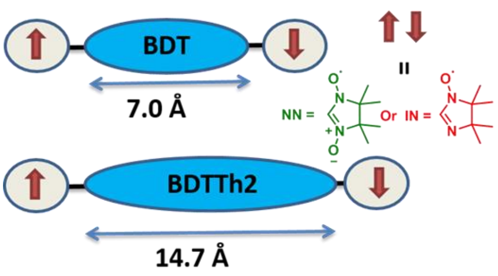

Note: This chapter was published in *J. Org. Chem.*, **2018**, DOI: 10.1021/acs.joc.8b02499

3.1 Introduction

As mentioned in the chapter two before, our fundamental interest is focused on to develop novel organic magnetic materials. Recently reported molecules were promising molecules, which are aromatic conjugated π–bridge linked with spin (S = ½) dimer systems.[1-4] The *intra*– and *inter*–molecular exchange interactions are fundamental tool in the spin dimer systems for BEC properties.[1-3, 5] Hence, i*ntra*–molecular interactions are tuned by varying π–bridge distance, topology and torsion between the radical centers.[1-3, 5-10] The *inter*–molecular interaction is controlled by supra–molecular approaches as the π–stacking of the molecules and or hydrogen bonding.[6] Planar π–bridges are thus better candidates than twisted ones for good self–assembly properties.[1, 3, 8, 11] Therefore, the structure of π–bridges plays a major role in determining both the *intra and inter* spin–spin exchange interactions.

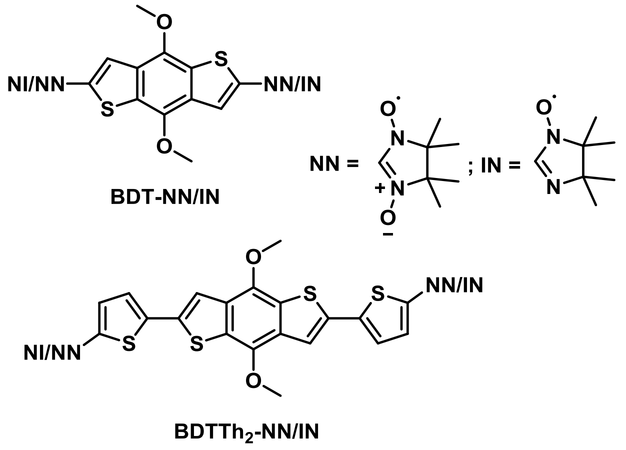

Chart 3.1: Structures of **BDT–NN, BDTTh$_2$-NN, BDT–IN**, and **BDTTh$_2$–IN.**

The current work is concerned with stable conjugated organic radicals as spin units (NN and IN) linked to π–conjugated bridges. Here, two planar benzodithiophene containing π–bridges such as 4,8–dimethoxybenzo[1,2–*b*:4,5–*b*']dithiophene (**BDT**) and 4,8–dimethoxy–2,6–di(thiophen–2–yl)benzo[1,2–*b*:4,5–*b*']dithiophene (**BDTTh$_2$**) were connected with nitronyl nitroxide (NN) and imino nitroxide (IN) radical units (Chart1). The **BD**T is a symmetric and planar conjugated π–bridge structure which can easily realize ordered π–π stacking and thereby facilitate also *inter*–molecular interactions. Furthermore, the **BDT** core provides two positions on the central benzene core for attaching different substituents where methoxy groups were introduced to ensure good solubility and tune the energy levels of π–bridge in a kind of donor acceptor manner.[12-14] In the other derivative (**BDTTh$_2$**), the π–bridge is extended with thiophenes on each side of **BDT** towards more extended biradicals which clearly should change the electronic properties and the exchange interactions.

Result and discussion

3.2 Synthesis

Scheme 3.1: Synthesis of **BDT–NN, BDT–IN, BDTTh$_2$–NN,** and **BDTTh$_2$–IN**.

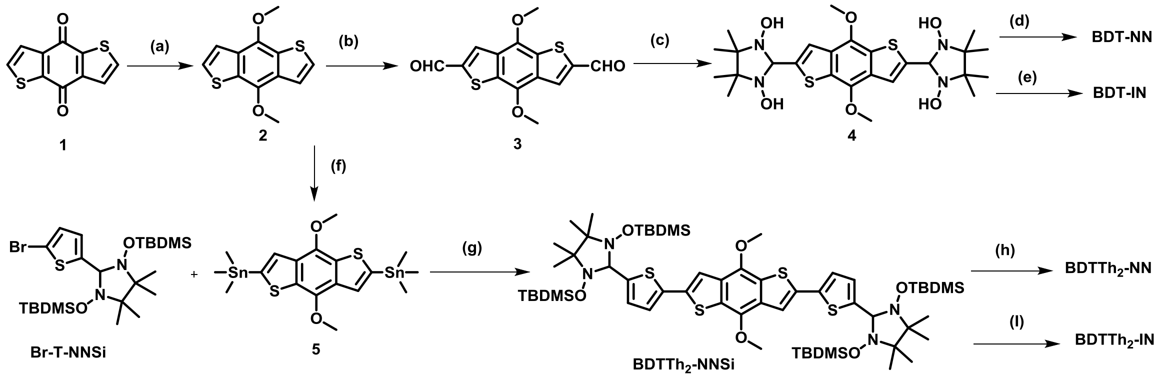

Reaction conditions: (a) Zn dust, NaOH, H$_2$O, MeI and Bu$_4$NBr,100 °C, 18h, (b) *n*–BuLi, THF, –78 °C, 1 h, –10°C, 30 min, and –78 °C, DMF, 30 min, and rt, 30 min, H$_2$O, (c) BHA, DMF, 65 °C,16 h, (d) NaIO$_4$, DCM/H$_2$O, (e) MeNO$_2$, MnO$_2$, (f) *n*–BuLi, THF, 0 °C, Me$_3$SnCl, (g) Pd(PPh$_3$)$_4$, toluene:DMF, (h) TBAF, THF and (i) TBAF, THF followed by excess MnO$_2$ in MeNO$_2$.

The syntheses of the biradicals are described in scheme 1. The key precursor **BDT** (**2**) was prepared by reduction of benzo[1,2–*b*:4,5–*b'*]dithiophene–4,8–dione with Zn dust in presence of NaOH followed by treatment with MeI and Bu$_4$NBr in 81 % yield. The dialdehyde **3** was synthesized by treating **2** with *n*–butyllithium followed by addition of DMF (70%). Ullman condensation of **3** with 2,3–bis(hydroxyamino)–2,3–dimethylbutane (BHA) yielded **4** (65%). The oxidation of **4,** by NaIO$_4$ led to **BDT–NN** (62%) and **BDT-IN** was obtained with excess of MnO$_2$ in MeNO$_2$ (67%). Compound **2** reacted with *n*–BuLi, followed by Me$_3$SnCl to achieve **5** (91%). Then stable biradical precursor **BDTTh$_2$–NNSi** was prepared by Stille coupling between **5** and **BrTh–NNSi**[8] in 82% yield. The **BDTTh$_2$–NN** was gained by subsequent cleavages of TBDMS protecting groups in one step by tetrabutylammonium fluoride, (TBAF) in THF (71%).[8] The **$BDTTh_2$–IN** was obtained by cleavages of TBDMS protecting groups followed by oxidation with MnO_2 in $MeNO_2$ (68%). All the precursors were characterized by NMR spectroscopy and mass spectrometry. All biradicals were characterized by EPR and UV–vis spectroscopy and mass spectrometry. The structures of compounds (**BDT**, **$BDTTh_2$–NNSi**, **BDT-NN, BDT-IN,** and **$BDTTh_2$-NN**) and molecular packing were investigated by single crystal X–ray structure analysis and thermal ellipsoid plot are placed in appendix (A-III).

3.3 Optical absorption studies

The UV–vis absorption spectra of biradicals **BDT–NN, –IN**, and **$BDTTh_2$–NN, –IN** were measured in toluene (c ~ 10^{-5} M) solution at room temperature (figure 3.1). Two principal absorption bands were obtained for NN biradicals (**BDT–NN** and **$BDTTh_2$–NN**).

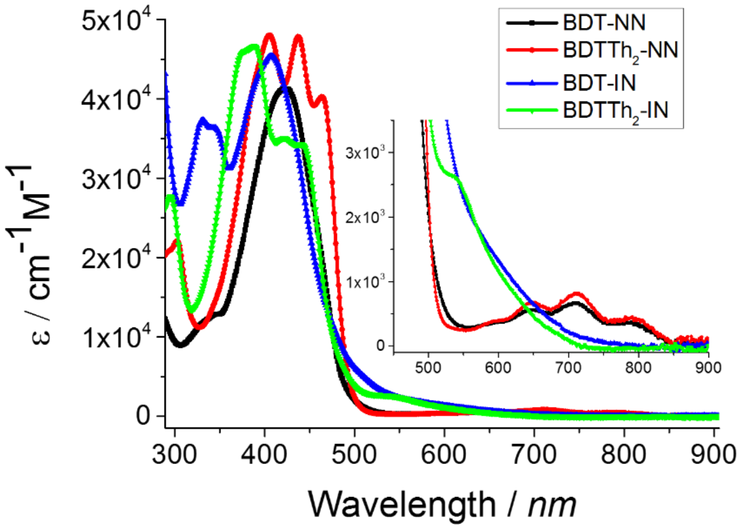

Figure 3.1: UV–vis absorption spectra for **BDT–NN** (black), **$BDTTh_2$–NN** (red)**, BDT–IN** (blue), and **$BDTTh_2$–IN** (green) in toluene (~10^{-5} M) solution at room temperature.

The high energy band covers from ~ 320 to 500 nm due to π–π* transition of π–bridge and the low energy band between 550 to 800 nm for n–π* transitions of radical moieties very similar with those earlier reported nitronyl nitroxides.[8] The π–π* transition for **$BDTTh_2$–NN** was slightly broadened in comparison with **BDT–NN** due to the extended bridge conjugation**.** The **BDT–IN** and **$BDTTh_2$–IN** showed broad absorption bands around ~ 350 to 500 nm for π–π* and weak band around 550 nm for the n–π* transitions. The absorption data of biradicals (λ_{max}, and extinction ε) are summarized in table 1.

Table 3.1: UV–vis, EPR and calculated exchange interactions of **BDT–NN, BDT–IN, BDTTh₂–NN** and **BDTTh₂–IN.**

	λ_{max}(nm)[a]	ε($cm^{-1}M^{-1}$)[b]	$a_{N/2}$(mT)[b]	g[b]	$J_{intra,calc}$/K[c]	$J_{inter,calc}$/K[c]
BDT-NN	422, 712	41295, 674	0.37	2.0068	–61.5	–9.4
BDT-IN	407, 550	45435	0.44, 0.24	2.0062	–3.7	–5.7
BDTTh₂-NN	437, 711	47855, 815	0.37	2.0067	–5.5	–4.2
BDTTh₂-IN	390, 550	46882	0.45, 2.3	2.0064	–1.3	—

[a]Calculated from UV–vis absorption spectra, [b]calculated from EPR spectra. [c]calculated from X–ray structure using UBLYP/6–31G(d) by DFT.

3.4 EPR studies

The EPR spectra of all four biradicals were recorded in argon saturated toluene (~10^{-4} M) solution. The room temperature EPR spectra of biradicals (**BDT–NN, BDT–IN, BDTTh₂–NN** and **BDTTh₂–IN)** associated with computer simulated spectra are displayed in figures 3.2(a-d). The **BDT–NN** and **BDTTh₂–NN** biradicals exhibited nine line and **BDT–IN** and **BDTTh₂–IN** showed 13 line spectra due to effective through–bond coupling of radicals via spin–polarization effects over the molecular bridges. These spectra indicated that the exchange interactions *J* are much larger than the hyperfine coupling constants ($J >> a_N$) in the limit of EPR spectroscopy.[1-3, 7, 8]

The EPR spectra of the biradicals in frozen (toluene) solution for **BDT–NN** (figure 3.2(e), **BDT–IN** and **BDTTh₂–NN** are given in figure 3.2(f). A zero–field–splitting $|D|$ (*zfs)* is detected for **BDT–NN** (38.0 ±0.5G) and **BDT–IN** (37.5, ±0.5 G) whereas a fine coupling was not resolved for **BDTTh₂–NN**. This is due to large intramolecular radical distances leading to a strong decrease in the magnitude of the *zfs* component. Further, the forbidden half–field transition, $\Delta Ms = 2$, is found for the **BDT–NN** and not detectable for other molecules. Therefore, the $|D|$ value in axial systems is associated with the averaged radical distances according to the point–dipole approximation.[15, 16] For **BDT–NN**, the carbon–carbon (C2–C2′) distance is equal to 9.87 Å, which is related to the D $\sim c/r^3 = 77924\ (g/g_e)/r^3 = 78095.2/961.5 = 81$ MHz ~ 29 G. Similarly $|D|$ calculated for **BDTTh₂–NN** (C2–C2′) = 17.22 Å) is D = 5.5 G. The calculated D value for **BDT-NN** is slightly smaller (29 G) than the experimentally deduced one (38 G), which is assumed to be due to spin delocalization into the bridge. Vide infra a decent match was found.

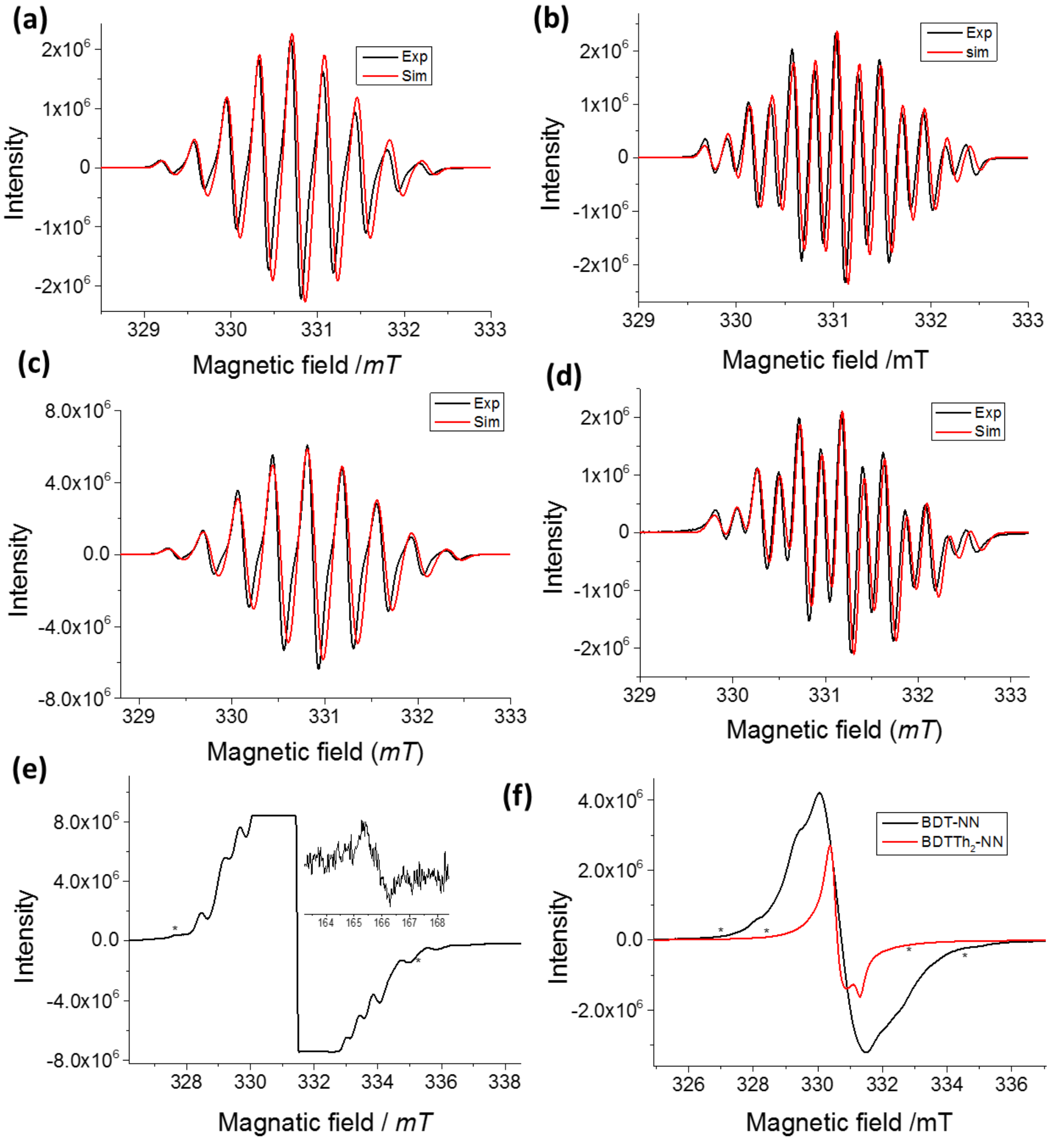

Figure 3.2: The EPR spectra for in toluene (10^{-4}) solution (a) **BDT–NN**, (b) **BDT–IN**, (c) **BDTTh$_2$–NN** and (d) **BDTTh$_2$–IN**, room temperature (black) and simulated (red). (e) $\Delta M_S = 1$ and (inset) half field $\Delta M_S = 2$ transition at 130 K for **BDT–NN** and (f) $\Delta M_S = 1$ transition for **BDT–IN** and **BDTTh$_2$–NN** at 130 K.

3.5 Single crystal x-ray structure studies

The single crystals of **BDT–NN, BDT–IN,** and **BDTTh$_2$–NN** were grown by slow evaporation in DCM solution whereas **BDT** and **BDTTh$_2$–NNSi** crystallized from CD_2Cl_2 solution. The crystallographic parameters are listed in table 2. The single crystal X–ray diffraction analysis revealed that colorless **BDT** crystallizes in monoclinic system with P $2_{1/n}$ space group and molecule has center of symmetry (C_i) (figure 3.3(a–b)). The molecular packing is given in the figure 3.3(c). The conjugated aromatic π–unit was nearly planar and two methyl groups of methoxy were bent out of the π–plane (113^{o}). The two sulfur atoms at thiophenes showed anti conformation to each other.

Table 3.2. Crystal data and structure refinement details of **BDT**, **BDTTh$_2$–NNSi BDT–NN, BDT–IN,** and **BDTTh$_2$–NN**

	BDT	**BDTTh$_2$–NNSi**	**BDT–NN**	**BDT–IN**	**BDTTh$_2$–NN**
formula	$C_{12}H_{10}O_2S_2$	$C_{58}H_{98}N_4O_6S_4Si_4$	$C_{26}H_{32}N_4O_6S_2$	$C_{26}H_{32}N_4O_4S_2$	$C_{34}H_{36}N_4O_6S_4$
formula weight [g/mol]	250.32	1188.00	560.67	528.67	724.91
Crystal system	monoclinic	monoclinic	monoclinic	triclinic	monoclinic
Space group	P 2_1/n	C 2/c	P 2_1/c	P –1	P 2_1/c
a (Å)	7.9063(9)	48.0321(15)	7.368(2)	10.3012(7)	16.173(8)
b (Å)	8.9584(7)	10.6191(2)	19.751(6)	11.4840(9)	6.265(3)
c (Å)	7.9434(10)	14.3112(5)	19.406(6)	12.6110(9)	16.682(8)
α	—	—	—	81.906(6)	—
β°	99.907(9)	98.054(3)	98.020(9)	107.466(8)	102.457(9)
γ	—	—	—	68.197(6)	—
Z	2	4	4	4	2
temperature °C	–80°	–80	–100	–80	–100
*w*R2	0.0788	0.1077	0.3472	0.1643	0.1724
R1	0.0286	0.0401	0.1178	0.0528	0.0768
density gcm^{-3}	1.500	1.092	1.332	1.335	1.459
absorption μ (mm^{-1})	0.46	0.242	0.237	0.242	0.34
no. of independent reflections	1337	9067	6148	6481	3864
no. of refined parameter	91	383	390	363	230
goodness of fit, S	1.049	0.969	1.027	1.017	0.998
CCDC	1862382	1862542	1862543	1862544	1862545

The yellow needle of the **BDTTh$_2$–NNSi** crystallized in monoclinic $C_{2/c}$ space group with Ci symmetry and solvent molecules were included (probably what else could be CD_2Cl_2) which are not being refined. The X–ray structure is displayed in the figure 3.3(d–e). The aromatic core possesses planar structure and the methyl groups in the imidazolidine were disordered in nature. Due to the bulky protection groups, the π–bridge and imidazolidine parts are strongly twisted relative to each other figure 3.3(d).

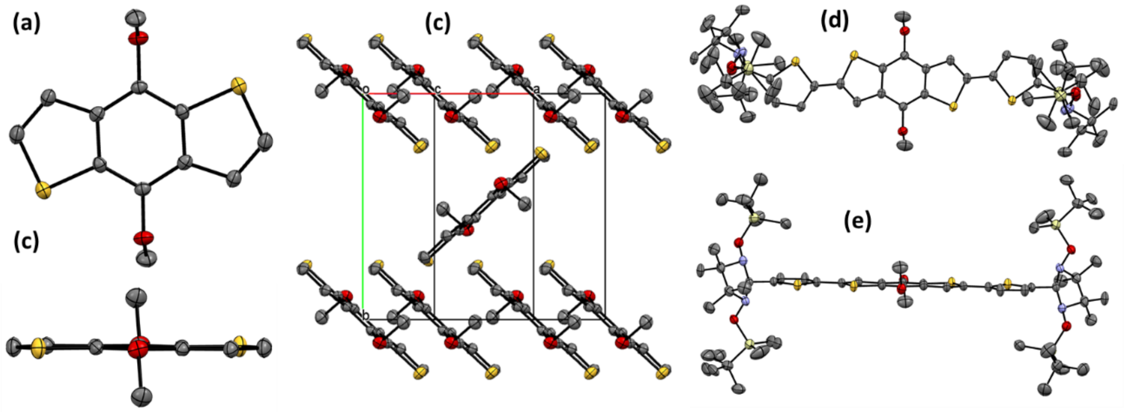

Figure 3.3: Single crystal X–ray structure of (a) and (b) for **BDT**, (c) molecular packing, (d), and (e) structure of **BDTTh$_2$-NNSi**; Hydrogen atoms are omitted for clarity.

The black needle of **BDT–NN** single crystal structure is provided in figure 3.4. The dimeric structures of the molecules (**BDT–NN–A** and **BDT–NN–B**) were crystallized together with inversion symmetry (C_i), monoclinic and $P2_1/c$ space group. The shortest π–π distance (3.423 Å) found between two molecules of **BDT–NN–A** and **BDT–NN–B** (C2A–C2B). This short distance between dimer molecules are extremely important for intermolecular interactions to increase the dimensionality of triplet excitations in the solid. The **BDT–NN–B** structure has disorder at methyl groups. The molecular structure of **BDT–NN–A** is provided in figure 3.4(c) and the molecular packing of **BDT–NN** is given in figure 3.4(d). In **BDT, (2)** molecule (figure 3.3), the two OMe groups bent out of plane of the aromatic π–unit but in **BDT–NN** methyl groups are nearly parallel to the π–bridge. The investigation of torsions angles are mandatory because those have a strong influence on the magnetic exchange interactions in biradicals.[1-3, 6, 8] The planar BDT π–unit connected with NN units with torsions of **BDT–NN–A** 4.2° for N8A–C7A–C5A–C4A, 10.0° for N11A–C7A–C5A–S6A (figure 3.4c), and **BDT–NN–B,** 10.9°, for N8B–C7B–C5B–C4B, and 9.4° for N11B–C7B–C5B–S6B (appendix A-III). There are several intermolecular short contacts and hydrogen bonds found between the molecules in molecular packing.

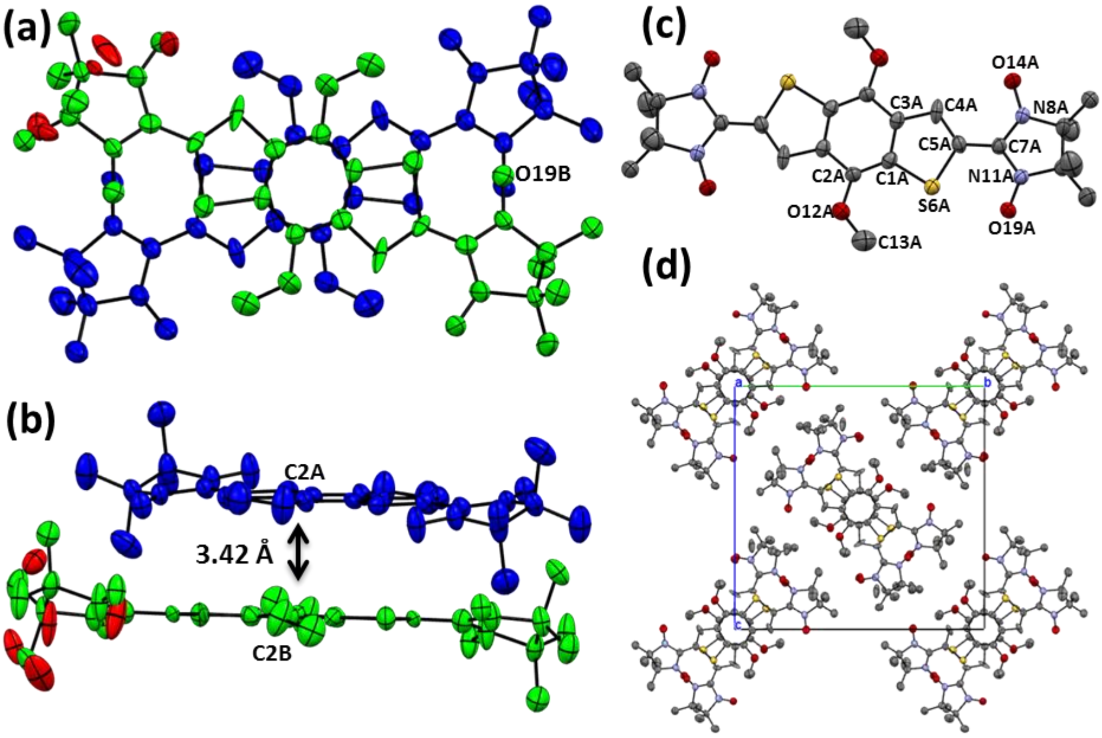

Figure 3.4: Single crystal X–ray structure of (a) dimeric structures of (**BDT–NN–A** (blue), (b) **BDT–NN–B** (green), disordered atoms (red), (c) single molecule (**BDT–NN–A)** structure and (d) molecular packing along the crystallographic a axes; Hydrogen atoms are omitted for clarity.

The brown plate dimeric molecules of **BDT–IN–A** and **BDT–IN–B** were crystallized together in triclinic with P–1 space group. The X–ray single crystal structure and packing of **BDT–IN** are depicted in figure 3.5. The molecule has almost a planar structure. The π–π stacking distance between the two molecules is (C5A and C7B) 3.832 Å and those are stacked nearly perpendicular to each other along the crystallographic c axes. The torsions of the NN and aromatic core are 6.59° for S1A–C6A–C7A–N11A, 4.37° for C5A–C6A–C7A–N8A, 2.40° for S1B–C6B–C7B–N11B, and 1.49° for C5B–C6B–C7B–N8B (appendix A-III) respectively. The crystal packing of the **BDT–IN** is given in figure 3.5(c) demonstrating that three molecules are placed nearly orthogonal to each other forming a star like structure with crystallographic c axes. The molecules are further extended forming a helical structure (figure 3.5e).

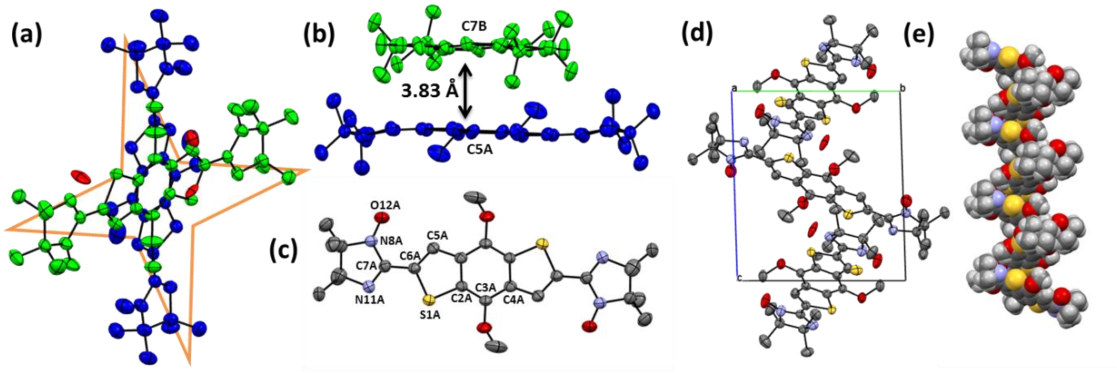

Figure 3.5: Single crystal X–ray structure of (a) dimeric structures of (**BDT–IN–A** (blue), (b) **BDT–IN–B (**green**)**, disordered atoms (red), (c) single molecule (**BDT–NN–A)** structure and (d) and (e) molecular packing along the crystallographic a axes; Hydrogen atoms are omitted for clarity.

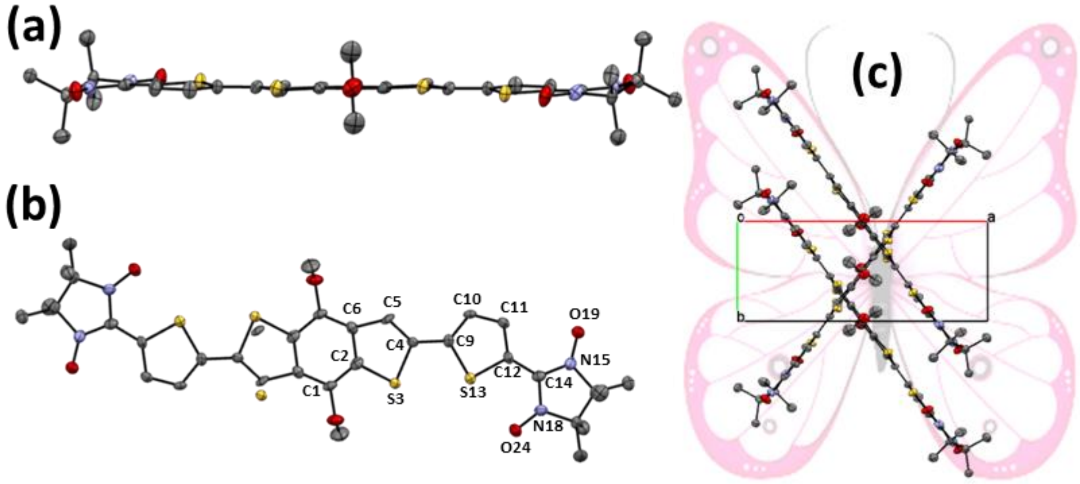

Figure 3.6: (a) and (b) are single crystal X–ray structure of **BDTTh$_2$–NN**, (c) Molecular packing along the crystallographic c axes; Hydrogen atom are omitted for clarity.

The brown/green plate of **BDTTh$_2$–NN** was crystalized in monoclinic crystal system with P 2_1/c space group. The molecule has Ci symmetry and the central ring system is rotated around 180° with respect to site occupancy factor (SOF) due to that **BDTTh$_2$–NN** has the disorder structure in center. The X–ray structure of **BDTTh$_2$–NN** is displayed in figure 3.6. The molecule is nearly planar. The radical units and π–bridge were placed in nearly same plane with extremely low torsions (< 1°) for (C11–C12–C–14–N15) and (S13–C12–C14–N18). The molecular packing is given in the figure 3.6c. The shortest π–π distance is (3.67 Å) is found between the two neighboring molecules for C3–S5 in the molecular packing.

3.6 Computational investigations of π–bridges

The role of delocalized *p*–electrons in aromatic π–bridges have contributed significantly to singlet–triplet energy gap in diradicals systems.[4, 17] Misra and coworkers theoretically predicted that magnetic interactions of diradicals are influenced through the HOMO, LUMO and energy gap (Eg) of the π–bridges.[10, 18]

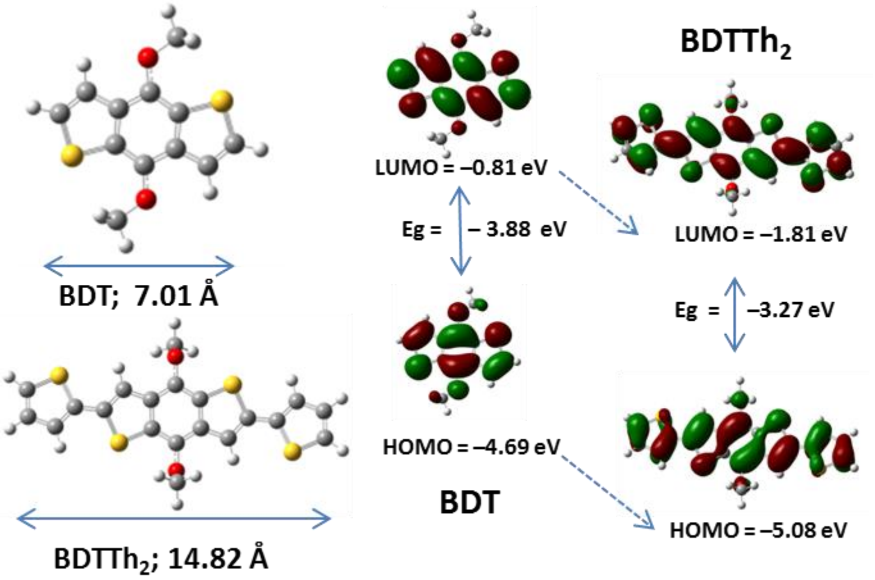

Figure 3.7: The energy levels (HOMO and LUMO) with electron density, and energy gap (Eg) of the **BDT** and **BDTTh₂** were calculated by DFT using B3LYP as hybrid functional and 6-31g(d) basis set.

Therefor we calculated the energy levels and Eg of the π–bridge. The structure optimisation was carried out by density functional theory (DFT) calculations using B3LYP/6–31G(d) level with the Gaussian 09 program set.[19] The chosen π–bridges differ mainly by C–C distances of terminal thiophenes (7.01 Å for **BDT** and 14.82 Å for **BDTTh₂**), HOMO, LUMO and Eg which are shown in figure 3.7. The calculated energy levels of the **BD**T are HOMO (–4.69 eV), LUMO (–0.81 eV) and Eg (–3.88 eV). For **BDTTh₂** lower HOMO (–5.08 eV), LUMO (–1.81 eV) and Eg (–3.27 eV) were found. For **BDT** and **BDTTh₂**, the electron densities are delocalized through the π–bridges (both HOMO and LUMO).

3.7 Calculation of exchange interaction by DFT studies

The X–ray structures were taken to compute the exchange interactions by DFT calculation. They were required for best estimation due to large error obtained by optimized structures.[1-3, 8] The geometry for **BDT–NN, BDT–IN,** and **BDTTh$_2$–NN** were directly applied for the calculations while for **BDTTh$_2$–IN**, the two oxygen atoms were deleted from **BDTTh$_2$–NN** on NN radical part to get IN, further the computation was executed. All calculations were performed by Gaussian09 package.[19]

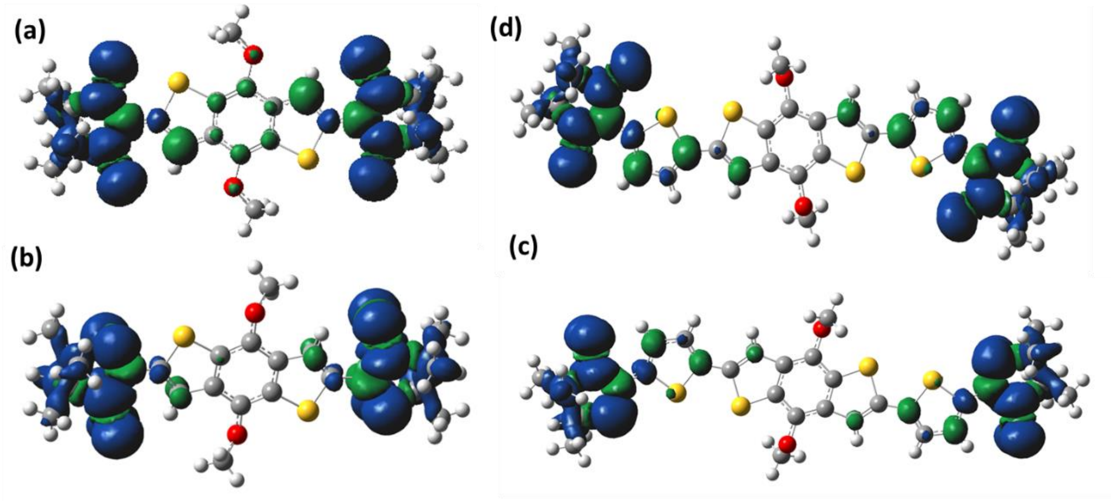

Figure 3.8: Spin density distributions of the triplet state for (a) **BDT–NN**, (b) **BDT–IN**, (c) **BDTTh$_2$–NN** and (d) **BDTTh$_2$–IN**.

The simplest Hamiltonian for the molecule with two exchange coupled unpaired electrons is given by $H = -2J_{12}S_1S_2$. The calculations were carried out by the broken-symmetry (BS) approach where the exchange interaction *J* becomes, $J/k_B = (E(BS) - E(T)) / (S^2(T) - S^2(BS))$, with E(BS) energy of broken symmetry and E(T) the triplet energy. S^2 are the eigenvalues of the spin operator and for $S^2(BS)$ close to 1 and $S^2(T)$ close to 2 the direct exchange becomes $J/k_B = E(BS) - E(T)$. Thus we applied Heisenberg–Dirac-Van Vleck (HDVV) Hamiltonian.[20-24] The singlet and triplet energy were calculated by BLYP hybrid function and 6–31G basic set (to avoid Hartree–Fock contamination) whereas B3LYP hybrid function with 6–31G basic set is over estimating. The calculated exchange interactions for all the biradicals ($J_{intra,cal}/k_B$) are given in table 3.1. The $J_{intra,cal}/k_B$ for **BDT–NN**, (–

61.5 K) is much higher than for **BDTTh$_2$–NN** (–5.5K), **BDT–IN** (–3.7 K), and **BDTTh$_2$–IN.** Spin density distributions for biradicals of triplet states were calculated by using single crystal geometries with DFT by UBLYP hybrid function and 6–31G/d basis set (figure 3.8).

The intermolecular magnetic interactions ($J_{inter,cal}/k_B$) were calculated to explain the effect of the molecular packing for **BDT–NN, BDT–IN** and **BDTTh$_2$–NN** of dimer structures. For calculation, the X–ray dimer structures geometry was selected and the one more distant NNs on each diradical was deleted (figure 3.9). Furthermore, the singlet and triplet energy levels calculations were carried out by UBLYP hybrid function with 6–31G basic set.

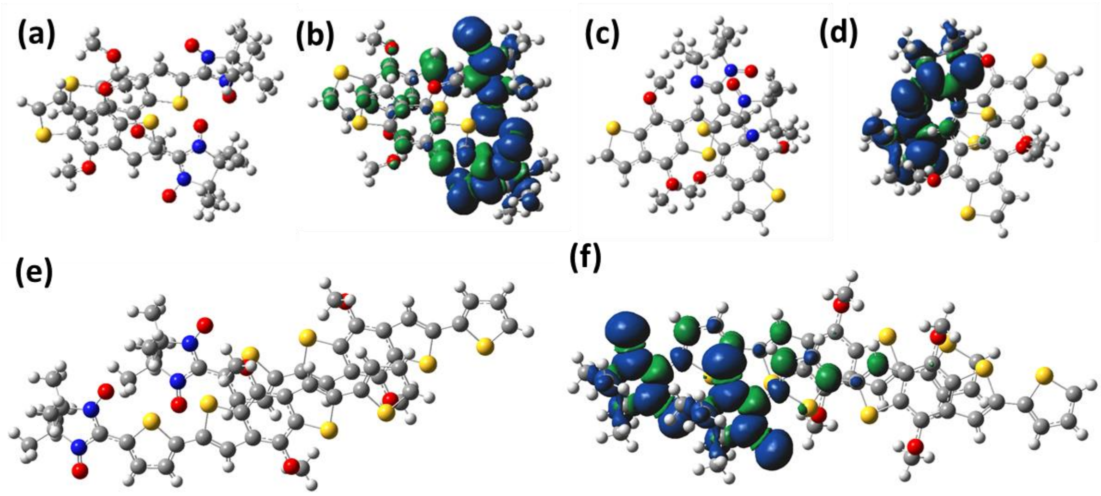

Figure 3.9: Spin density distributions of the triplet state for (a) **BDT–NN**, (b) **BDT–IN**, (c) **BDTTh$_2$–NN** and (d) **BDTTh$_2$–IN**.

The calculated $J_{inter,cal}/k_B$ of **BDT–NN, BDT–IN** and **BDTTh$_2$–NN** were –9.4 K, –5.7 K and –4.2 K respectively. These results suggest that shorter π–π distances correspond to higher $J_{inter, cal}/k_B$ values. The spin density distributions of the triplet state for mono radical of dimer structures are given in figure 3.9. The spins were mainly located on the NN radical part with some delocalization on the π–bridge for **BDT–NN, BDT–IN,** and **BDTTh$_2$–NN**. Especially for **BDT-IN** this intermolecular exchange interaction was even a little larger than the intramolecular exchange.

3.8 Magnetic susceptibility measurements

To gain further inside to the magnetic exchange interactions the molar magnetic susceptibility, (χ_{mol}) of the polycrystalline samples **BDT–NN, BDT–IN** and **BDTTNh$_2$–NN** were measured in a temperature range of 2 K ≤ T ≤ 270 K at a field of B = 1 T using a SQUID magnetometer. These measurements and their analysis were done by Lars Postulka, Dr. Wolf Bernd in the group of Lang, Michael in Physikalisches Institut, J.W. Goethe–Universität Frankfurt, and Frankfurt, Germany.

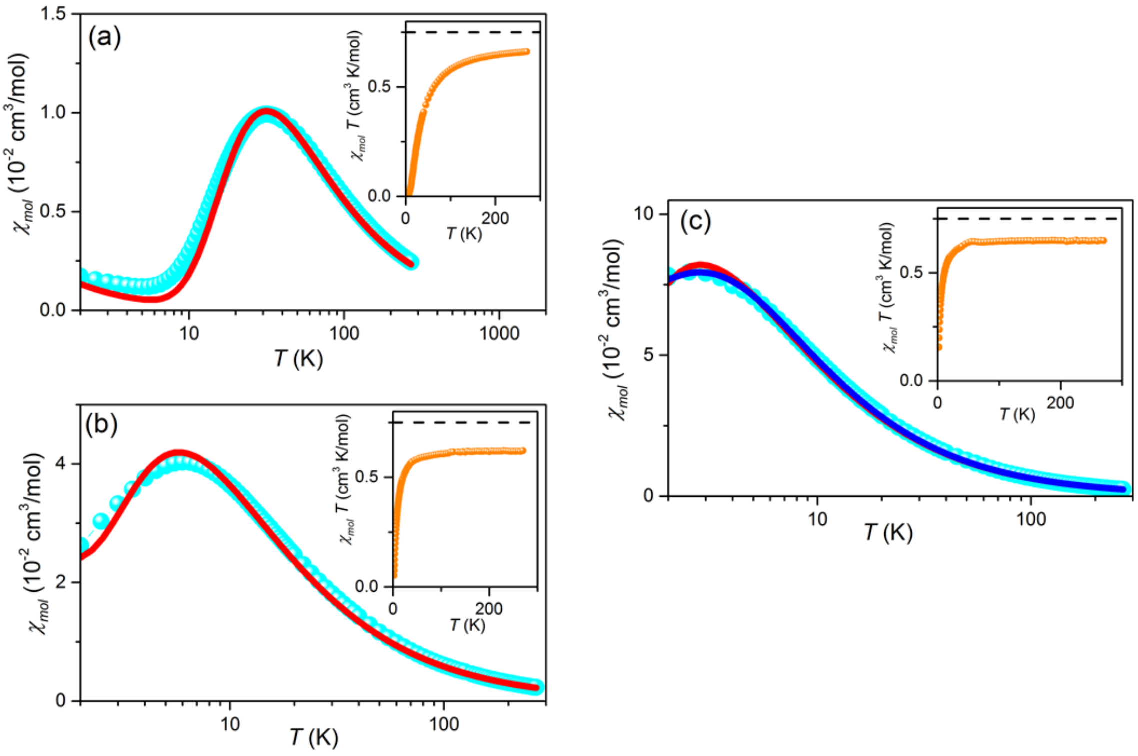

Figure 3.10: The main panels shows the measured molar susceptibility χ_{mol} (cm^3/mol) vs. temperature in a semi logarithmic representation together with a theoretical fit for weakly coupled spin–dimers, were inter–dimer coupling has been taken under account within a mean–field approximation (red solid line) for (a) **BDT–NN**, (b) **BDT–IN** and (c) **BDTTh$_2$–NN** (cyan green circles). The straight blue line in 6c represents a description of the data as a AFM coupled Heisenberg chain. (See text for more details). **Inset:** The temperature dependence of $\chi mol\ T$ (cm^3 K/mol) vs T (K) together with theoretically expected value of 0.75 (cm^3 K/mol) for two uncoupled spin S = ½ per molecule.

The obtained data were corrected for the temperature independent diamagnetic core contribution as well as magnetic contribution of the sample holder, which had been determined by an independent measurement of the empty sample holder. The results are shown in the form of as χ_{mol} vs. T in the main panel, and $\chi_{mol}T$ vs. T in the insets of figures 3.10. All investigated biradicals show similar magnetic behavior. As displayed in the insets of figures 3.10(a–c), $\chi_{mol}T$ levels of at a value above 0.6 (cm^3 K/mol) for high temperatures (~ 150 K – 270 K) while for lower temperature a rapid drop of this value can be observed. The expected value at high temperature for two uncoupled S = ½ units would be 0.75 (cm^3 K/mol). We address this reduced magnetic moment additional nonmagnetic material in the sample, probably rest of solvents. For this nonmagnetic contribution a weight percentage of x = 0.12 for **BDT–NN,** x **= 0.**17 for **BDT–IN** and x **= 0.**14 for **BDTTNh$_2$–NN** was obtained. The drop for low temperatures can be attributed to the dominant antiferromagnetic intra–dimer coupling $J_{intra.}$

This dominant coupling within a molecule leads to a formation of dimers and as it is typical for weakly coupled spin dimers, all measured radicals reveal a characteristic maximum in the susceptibility as clearly visible in the main panels of figure 3.10. In order to derive the dominant intra-dimer J_{intra} coupling constant, these curves are fitted (red solid line) to the Bleany–Bowers equation[25] which models the susceptibility for isolated dimer χ_{iso}. As shown in eq. (3—1), the weight percentage x of nonmagnetic material was taken and a small contribution x' of S = ½ paramagnetic impurities considered. Weak inter–dimer couplings J_{inter} are taken under account by applying a mean-field correction. From this fitting, the value of dominant coupling inside the dimer J_{intra} and between the dimers J_{inter} multiplied by the number of nearest neighbors z can be derived.

$$\chi_{mol} = (1-x')\left[(1-x)\chi_{iso} / [1 - (z\,J_{inter}\cdot k_B/(N_A g^2 \mu_B^2)\,(1-x)\chi_{iso}]\right] + x'\,C/T \quad (3—1)$$

Here x is the weight percentage of nonmagnetic material, calculated form the high temperature $\chi_{mol}T$ values, x' the concentration of S = ½ paramagnetic impurities and C the Curie constant. Further constants are k_B, the Boltzmann, N_A, the Avogardro constant, g, the g–factor, and μ_B, the Bohr magneton.

The results for **BDT-NN** are presented in figure 3.10(a). For this compound the magnetic susceptibility χ_{mol} increases with decreasing temperature till it reaches a maximum at T = 32 K ±1 K. On further decreasing the temperature a minimum at T = 5 K ±0.5 K can be observed. We address the upturn at temperatures T < 5K to paramagnetic impurities. From the best fitting it could be concluded that the concentration x' of these impurities are below 0.01. Further on we obtain a dominant coupling constant of $J_{intra}/k_B = -26 \pm 1$ K and an antiferromagnetic inter dimer coupling of $zJ_{inter}/k_B = -6.5 \pm 2$ K.

For **BDT–IN** the position of the maximum in χ_{mol} vs. T has shifted to lower temperatures (T_{max} = 6 K) compared to **BDT-NN** as it can be seen in figure 3.10(b). From the fit we obtain a dominant coupling constant $J_{intra}/k_B = -5.3 \pm 0.5$ K and $zJ_{inter}/k_B = -6 \pm 2$ K. Here the paramagnetic impurities are about $x' = 0.04 \pm 0.02$. Assuming a small amount of nearest neighbors z the inter dimer coupling is only slightly weaker than the dominant coupling. Therefor the description of the data as isolated dimer with mean field corrections due to nearest neighbor interaction can only be a first approach and consequently a deviation between the calculated curve and the measured data occurred.

Table 3.3: Position of the maximum in the susceptibility T_{max} as well as the intra dimer coupling J_{intra} and the inter dimer coupling J_{inter} which is multiplied by the amount of nearest neighbours z. For **BDTTh₂-NN** a model assuming an AFM Heisenberg chain has been additionally used, obtaining a coupling within the chain J_{chain} and coupling $zJ_{int\text{-}chain}$ between the chains. z denotes the number of nearest neighbour chains.

	T_{max} (K)	J_{intra}/k_B (K)	$zJ_{inter,\mathrm{exp}}/k_B$ (K)	J_{chain}/k_B (K)	$zJ_{int\text{-}chain}/k_B$ (K)
BDT-NN	32 (±1)	−26.0 (±1)	−6.5 (±2)		
BDT-IN	6 (±0.5)	−5.3 (±0.5)	−6 (±2)		
BDTTh$_2$-NN	2.6 (±0.5)	−2.3 (±0.5)	−4.6 (±1)	−2.2 (±0.3)	−1.5 (±0.5)

For **BDTTh$_2$–NN** this effect is even more pronounced as can be seen in figure 3.10(c). The susceptibility measured for **BDTTh$_2$–NN** shows a maximum T = 2.6 K ± 0.5 K. Fitting the previously described dimer model, an inter-dimer coupling of $J_{intra}/k_B = -2.3$ K ± 0.5 K and an inter-dimer coupling of $zJ_{inter}/k_B = -4.6 \pm 1$ K was derived. The concentration of paramagnetic S = ½ impurities

x' is less than $x' = 0.01$. Assuming an amount of nearest neighbor $z = 2$, would mean that the coupling between the dimer is of the same size than within the dimer. Consequently another magnetic model e. g the description as AFM coupled Heisenberg chain is also be possible. Therefore, we performed a second fit which combines a parametrization of the Bonner–Fischer curve done by Johnson *et al.*[26] with the mean–field approach (blue straight line). For this model we extracted a coupling within the chain of J_{chain}/k_B = –2.2 K ± 0.3K and a coupling between the chains of $zJ_{int\text{-}chain}$ = –1.5 ± 0.5 K. As it can be observed in Fig.6c such a model describes the experimental data below 6 K (~ 3 J_{intra}) more accurate compared to the dimer model. Nevertheless, even at the lowest measured at temperature of T = 2K, the extracted coupling constants for both scenarios are of the same order compared to the thermal energy. Consequently a proper discrimination of these scenarios is not possible. Therefore, measurements to temperatures at T << 2K are necessary. In table 3 we summarize all results obtained by the measurement of the magnetic susceptibility. It should be emphasized here that the significant magnetic inter–dimer interaction zJinter,exp / kB of a few Kelvin is due to the π–π stacking of the planar benzo[1,2–b:4,5–b']dithiophene bridging units. Note that an antiferromagnetic coupling of strength of a few tens of Kelvin resulting from a π–π stacking has been reported for 1,3,7-triphenyl-1,4-dihydrothiazolo[5‘,4‘:4,5]benzo[1,2-e][1,2,4]triazin-4-yl molecule.[27]

3.9 Summary

Four weakly AFM coupled spin dimer molecules were designed, synthesized and characterized. The inter– and intra–molecular interactions were tuned by altering the π–bridge and varying the radical units. The molecular structures and packing behavior were explained through X–ray structure analysis. The magnetic properties were studied by SQUID and the experimentally obtained magnetic coupling constants of the biradicals were –26 ± 1 K, –5.3 ± 0.5 K and –2.3 ± 0.5 K, for **BDT–NN**, **BDT–IN** and **BDTTh$_2$–NN**. From the X–ray structure geometries, inter– and intra–molecular interactions, electronic resonances and spin distribution were analyzed by DFT calculation. The calculated intramolecular interactions were –61.5 K, –5.5 K, –3.7 K, and –1.3 K for **BDT–NN**, **BDTTh₂-NN**, **BDT–IN** and **BDTTh₂–IN,** respectively. The calculated intramolecular interactions are very close to experimental values for **BDT–IN** and **BDTTh₂–NN** while there was some deviation for **BDT–NN** due to shorter intermolecular interaction found between the molecules. The calculated intermolecular interaction of the dimeric mono radical of **BDT–NN,** **BDT–IN**, and **BDTTh₂–NN** were –9.4 K, –5.7 K and –4.2 K. Especially for **BDT–IN** a very similar sized J_{intra} and J_{inter} were determined both experimentally and theoretically, making this molecule a fantastique probe for determining the dimensionality of triplet excitations at ultracold temperatures. Therefore, AC magnetic susceptibility properties investigations are in progress.

3.10 Experimental section

The **Br–T–NNSi** was synthesized by reported procedure.[8]

X-ray crystallography.

The X–ray crystallographic data were collected on a STOE IPDS 2T diffractometer using a graphite monochromator Mo–Kα as a radiation source for **BDT, BDT–IN** and **BDTTh₂–NNSi** at –80 °C. And Smart CCD diffractometer using a graphite monochromator, Mo–Kα as a radiation source was used for **BDT–NN** and **BDTTh₂–NN** at –100 °C. The structures were solved by direct methods (SIR–2004) and refined by SHELXL–2014 (full matrix), 91 refined parameters for **BDT**, 390 for **BDT–NN,** 366 for **BDT–IN** 383 for **BDTTh₂–NNSi** and 230 for **BDTTh₂-NN** were used.

Synthesis of 4,8-bis(methoxy)benzo[1,2-b:4,5-b']dithiophene, (2 or BDT).[28, 29]

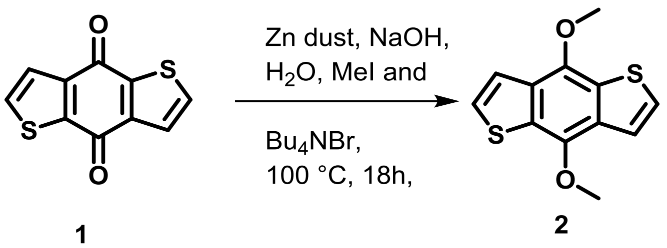

1 **2**

In the two neck round bottom flask charged with benzo[1,2-b:4,5-b′]dithiophene-4,8-dione, (**1**), (1.00 g, 4.54 mmol), zinc dust (0.65 g, 9.94 mmol), NaOH (2.72 g, 68.00 mmol) and then deoxygenated water (30 mL) was added and the mixture was refluxed for 2 h. Then the reaction mixture was cool down to room temperature and tetrabutylammoniumbromide (0.15 g, 0.47 mmol), and MeI (1.93 g, 1.2 mL, 3.62 mmol) were added to the reaction mixture. The mixture was refluxed further 16 h under nitrogen atmosphere, then cool down to room temperature and further extracted with DCM. The organic layers was dried over anhydrous Na_2SO_4, then solution was concentrated under reduced pressure and purified by column chromatography (SiO_2) by using dichloromethane (0–20%) and hexane as the eluent to afford the required compound as a white solid, yield, 0.93 g, 3.71 mmol, 82 %. ^{1}H NMR (CD_2Cl_2, 300 MHz): δ, 7.52 (d, *J* = 6 Hz, 2H), 7.42 (d, *J* = 6 Hz, 2H), 4.13 (s, 6H); ^{13}C NMR (CD_2Cl_2, 75 MHz): δ, 145.9, 131.7, 130.3, 126.9, 120.6, 61.5; HRMS (ESI–TOF) *m/z*: $[M+H]^+$ calculated for $C_{12}H_{11}O_2S_2$: 251.0200, found: 251.0196.

Synthesis of 4,8-dimethoxybenzo[1,2-b:4,5-b']dithiophene-2,6-dicarbaldehyde, (3).[28]

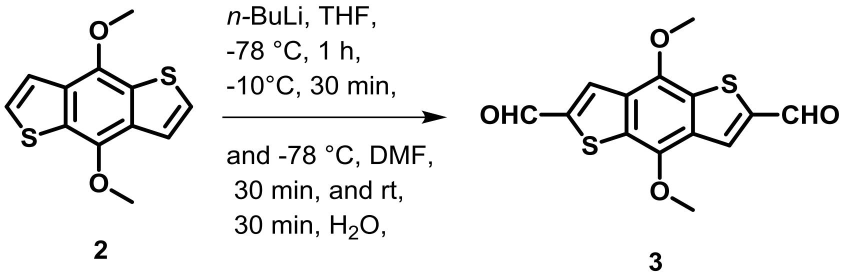

n-Butyl lithium (5.5 mL, 8.9 mmol, 1.6 M solution in hexane,) was added drop wise to a stirred solution of **2** (1. 00 g, 3.99 mmol) in anhydrous THF (30 mL) maintained at 0 °C for 15 min and the mixture was stirred for 1 h, at the same temperature. Then anhydrous DMF (10 mL) was added at 0°C, the reaction mixture was brought to room temperature and stirred for overnight at room temperature. The reaction mixture was poured into ice cooled water and extracted with diethyl ether (3×100 mL).The combined organic phases was washed with water (2×100 mL), dried over anhydrous Na_2SO_4 and evaporated to dryness in vacuum. Recrystallization of the residue from dichloromethane afforded the compound **3** as orange yellow powder (0.94 g, 3.06 mmol, 77%).

^{1}H NMR (CD_2Cl_2, 250 MHz): δ, 10.13 (s, 2H), 8.26 (s, 2H), 4.22 (s, 6H); HRMS (ESI–TOF) *m/z*: $[M+H]^+$ calculated for $C_{14}H_{11}O_4S_2$:307.0093, found: 307.0093.

Synthesis of 2,2'-(4,8-dimethoxybenzo[1,2-b:4,5-b']dithiophene-2,6-diyl)bis(4,4,5,5-tetramethylimidazolidine-1,3-diol), (4).

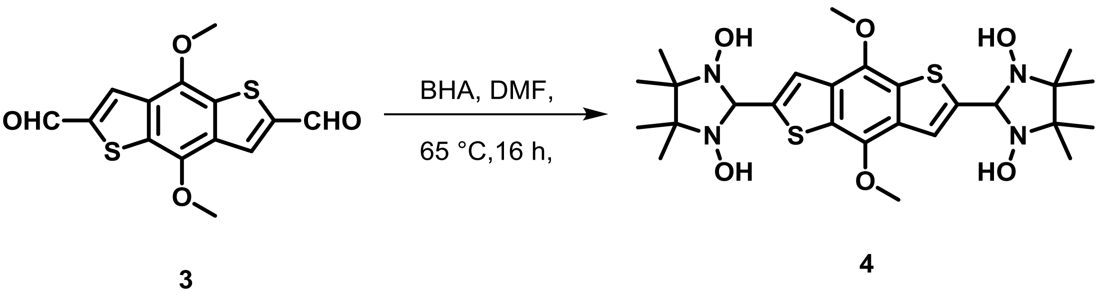

A mixture of **3** (0.290 g, 0.947 mmol) and 2,3-bis(hydroxylamino)-2,3-dimethylbutane (0.420 g, 2.839 mmol) in 30 mL of DMF were stirred at 65 C, for 16 h. The solution was concentrated and obtained red residue was washed with ethyl acetate to yield **4**, as yellow solid (0.302 g, 56%).^{1}H NMR (DMSO-d_6, 300 MHz): δ, 8.12 (s, 4 H, N-OH), 7.49 (s, 2 H), 4.85 (s, 2 H), 4.03 (s, 6 H), 1.10 (s, 24 H).^{13}C NMR (75 MHz, DMSO-d_6) δ, 148.3, 144.2, 130.2, 128.9, 118.2, 87.0 66.6, 60.8, 24.3, 17.2; HRMS (ESI–TOF) *m/z*: calculated for $C_{26}H_{38}N_4O_6S_2$, 566,7320 found:$[M]^+$, 566.7323.

Synthesis of BDT-NN.

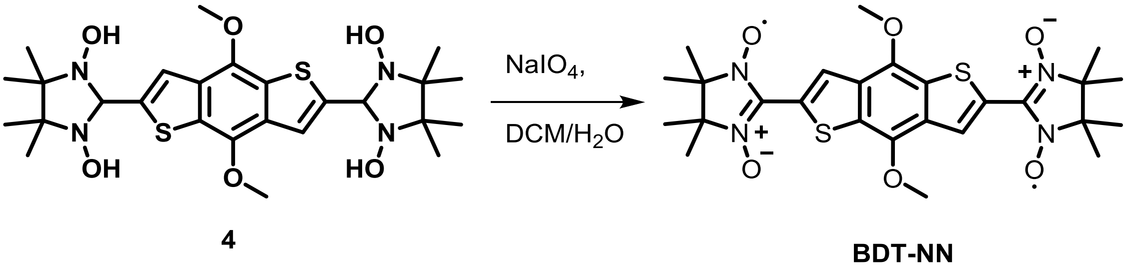

A mixture of 2,2'-(4,8-dimethoxybenzo[1,2-b:4,5-b']dithiophene-2,6-diyl)bis(4,4,5,5-tetramethylimidazolidine-1,3-diol), **4** (0.150 g, 0.264 mmol) and 0.5 M, $NaIO_4$ solution in water was added and mixture was stirred for 6 h, at 0 °C, mean time reaction was monitored by TLC. After the reaction was completed, the dark green organic phase extracted by dichloromethane and washed with water, brine and dried over $MgSO_4$ and the residue was chromatographed over silica gel using hexane: and ethylacetate as eluent to obtain green crystalline product yielded (0.095 g) 64 %; EPR (298 K, ~10^{-4} M in toluene): nine lines, g_{iso} = 2.0066, $a_{N1/2}$ = 0.373 *mT;* HRMS (ESI–TOF) *m/z*: $[M+H]^+$ calculated for $C_{26}H_{33}N_4O_6S_2$: 561.1842, found: 561.1828.

Synthesis of BDT-IN.

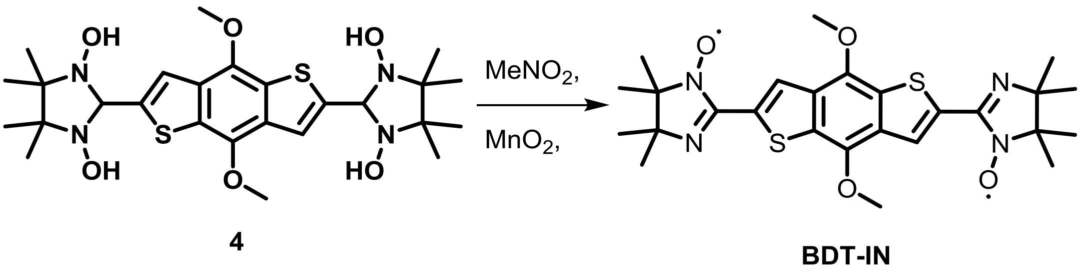

4

BDT-IN

A mixture of 2,2'-(4,8-dimethoxybenzo[1,2-b:4,5-b']dithiophene-2,6-diyl)bis(4,4,5,5-tetramethylimidazolidine-1,3-diol), **4** (0.150 g, 0.264 mmol) and MnO_2 (0.32 mmol) were suspended in $MeNO_2$ (20 mL) the reaction mixture was stirred for 6 h, mean time reaction was monitored by TLC. The $MeNO_2$ was removed under reduced pressure. The organic phase was extracted with dichloromethane, washed with water, brine and dried over $MgSO_4$. The residue was chromatographed over silica gel using hexane: ethylacetate as eluent to obtain brown crystalline product (0.091 g) in 65 %; EPR (298 K, ~10^{-4} M in toluene): 13 lines, g_{iso} = 2.0062, $a_{N/2}$ = 0.44, 0.24 *mT;* HRMS (ESI–TOF) *m/z*: $[M+H]^+$ calculated for$C_{26}H_{33}N_4O_4S_2$: 529.1938, found: 529.1936.

Synthesis of 5, 2,6-bis(trimethyltin)-4,8-bis(methoxy)benzo[1,2-b:4,5-b']dithiophene, (5).[30]

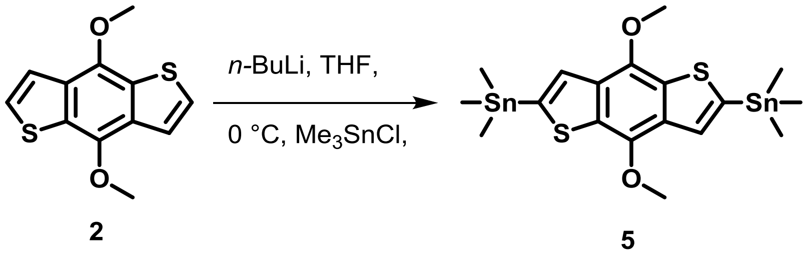

2

5

n-butyl lithium (5.5 mL, 8.9 mmol, 1.6 M solution in hexane,) was added drop wise to a stirred solution of **2** (1.00 g, 3.99 mmol) in anhydrous THF (30 mL) maintained at 0 °C. The mixture was stirred for 1 h, at same temperature. Then trimethyltinchloride (2.39 g, 11.98 mmol) in anhydrous THF (10 mL) solution was added at 0 °C. The reaction mixture was brought to room temperature and stirred for overnight. The reaction mixture was poured into ice cooled water and extracted with diethyl ether (3×50 mL). The combined organic phases was washed with water (2×100 mL), dried over anhydrous $MgSO_4$ and evaporated to dryness in vacuum. Recrystallization of the residue from DCM and isopropanol afforded the compound **5** as colorless needles (1.85 g, 3.21 mmol, 80 %). ^{1}H NMR (CD_2Cl_2, 300 MHz): δ, 7.57 (s, 2H), 4.13 (s, 6H), 0.47 (s, 18H); ^{13}C NMR, ($CDCl_3$, 75 MHz): δ, 144.5, 141.9, 134.2, 133.2, 128.3, 61.3, -8.1. HRMS (ESI–TOF) *m/z*: $[M+H]^+$ calculated for $C_{18}H_{27}O_2S_2[^{118}Sn]_2$: 574.9479, found: 574.9469. Also found HRMS (ESI–TOF) *m/z*: $[M+H]^+$ calculated for $C_{18}H_{27}O_2S_2[^{120}Sn]\,[^{118}Sn]$: 576.9485, found: 576.9467.

Synthesis of BDTTh₂–NNSi.

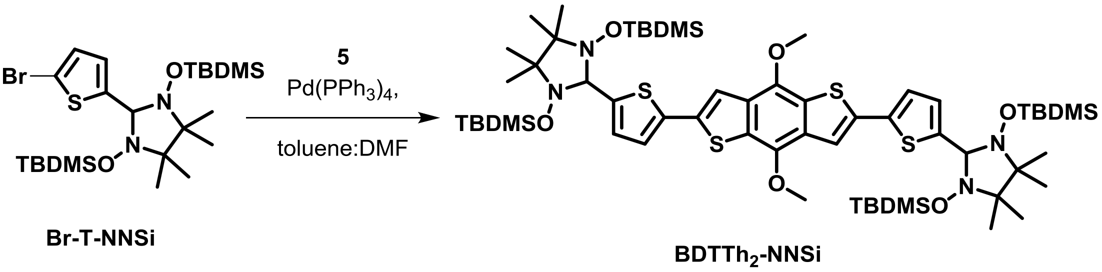

A mixture of **5** (0.10 g, 0.23 mmol), Br–T–NNSi (0.33 g, 0.61 mmol), and $Pd(PPh_3)_4$ (0.06 g, 0.05 mmol), were taken in Schleck tube and argon purged dry DMF (10 mL), was added then the mixture was stirred for 24 h at 60 °C, then the DMF was removed under reduced pressure. The residue was extracted with diethyl ether (2 X 50 mL) and washed with water. The ether layer was dried over magnesium sulfate, and concentrated under reduced pressure. The residue was chromatographed on silica gel with hexane to obtain light brown solid as **BDTTh₂–NNSi** (0.18 g, 79 %). ^{1}H NMR (CD_2Cl_2, 300 MHz): δ, 7.57 (s, 2H), 7.17 (d, 2H), 6.98 (d, 2H), 4.97 (s, 2H), 1.20 (s, 24H), 0.87 (s, 36H), 0.10 (s, 12H), 0.44 (s, 12H). ^{13}C NMR, ($CDCl_3$, 75 MHz): δ, 144.7, 138.3, 137.4, 132.2, 129.9, 128.8, 123.7, 115.3, 90.3, 68.2, 60.9, 29.6, 26.1, 25.9, 17.9, –4.1, –5.2. HRMS (ESI–TOF) *m/z*: $[M+H]^+$ calculated for $C_{58}H_{99}N_4O_6S_4Si_4$: 1187.5525, found: 1187.5552.

Synthesis of BDTTh$_2$–NN.

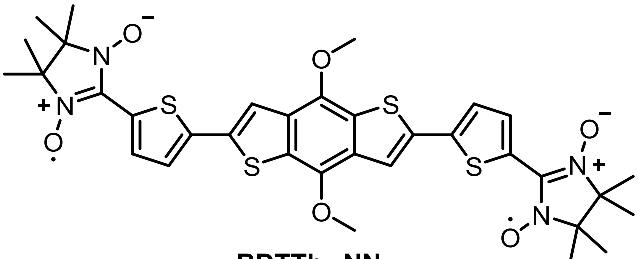

BDTTh$_2$-NN

The **BDTTh$_2$-NNSi** (0.10 mg, 0.084 mmol) was dissolved in dry THF (7 mL) and (2.4 mL) Bu$_4$NF, 1 M solution in THF was added then the mixture was stirred for 16 h at room temperature, reaction monitored by TLC. The mixture was concentrated under reduced pressure and purified column chromatography, green solid of **BDTTh$_2$-NN** (42 mg, 67%). EPR (298 K, ~10^{-4} M in toluene): nine lines, g_{iso} = 2.0065, $a_{N1/2}$ = 0.373 *mT;* HRMS (ESI-TOF) *m/z*: $[M]^+$ calculated for $C_{34}H_{36}N_4O_6S_4$: 724.1518 found: 724.1489.

Synthesis of BDTTh$_2$–IN.

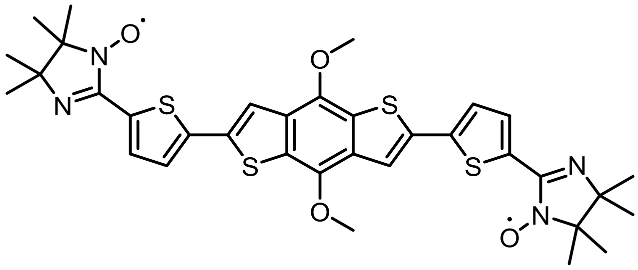

BDTTh$_2$-IN

Compound **BDTTh$_2$–NNSi** (0.10 g, 0.084 mmol) was dissolved in dry THF (10 mL) and (1 mL) Bu$_4$NF, 1 M solution in THF was added then the mixture was stirred for 1 h at room temperature. The solution was concentrated under reduced pressure. The mixture was taken in to nitromethane (5 mL) and excess MnO_2 (150 mg) was added. After ~30 minutes stirring at room temperature the solution filtered off and washed carefully with small portions of ethyl acetate on filtered. The filtrate was diluted with toluene (100 mL) and concentrated. The residue was purified by column chromatography with ethyl acetate/hexane as eluents to obtain **BDTTh$_2$–IN** as orange–red solid, (39 mg, 0.056 mmol, (67%). EPR (298 K, ~10^{-4} M in toluene): 13 lines, g_{iso} = 2.0064, $a_{N1/2}$ = 0.45, 2.3 *mT*; HRMS (ESI–TOF) *m/z*: $[M+H]^+$ calculated for $C_{34}H_{37}N_4O_4S_4$: 693.1692, found: 693.1692.

The appendix-III (**A-III**) is given for chapter–3.

Structures, refinement details of **BDT** and **BDTTh₂-NNSi**, structures of the **BDT-NN, BDT-IN**, and **BDTTh₂-NN**, NMR spectra of new compounds for **4** and **BDTTh₂-NNSi**, and DFT calculations details using Gaussian 09.

5.11 References

1. Borozdina, Y. B.; Mostovich, E.; Enkelmann, V.; Wolf, B.; Cong, P. T.; Tutsch, U.; Lang, M.; Baumgarten, M., Interacting Networks of Purely Organic Spin–1/2 Dimers. *J. Mater. Chem. C* **2014,** *2*, 6618-6629.

2. Ravat, P.; Borozdina, Y.; Ito, Y.; Enkelmann, V.; Baumgarten, M., Crystal Engineering of Tolane Bridged Nitronyl Nitroxide Biradicals: Candidates for Quantum Magnets. *Crystal Growth & Design* **2014,** *14*, 5840-5846.

3. Borozdina, Y. B.; Mostovich, E. A.; Cong, P. T.; Postulka, L.; Wolf, B.; Lang, M.; Baumgarten, M., Spin-Dimer Networks: Engineering Tools to Adjust the Magnetic Interactions in Biradicals. *J. Mater. Chem. C* **2017,** *5*, 9053-9065.

4. Barone, V.; Cacelli, I.; Ferretti, A., Magnetic Coupling in Bis-Nitronylnitroxide Radicals: The Role of Aromatic Bridges. *J. Chem. Phys.* **2009,** *130*, 094306.

5. Wautelet, P.; Le Moigne, J.; Videva, V.; Turek, P., Spin Exchange Interaction through Phenylene-Ethynylene Bridge in Diradicals Based on Iminonitroxide and Nitronylnitroxide Radical Derivatives. 1. Experimental Investigation of the Through-Bond Spin Exchange Coupling. *J. Org. Chem.* **2003,** *68*, 8025-8036.

6. Mostovich, E. A.; Borozdina, Y.; Enkelmann, V.; Remović-Langer, K.; Wolf, B.; Lang, M.; Baumgarten, M., Planar Biphenyl-Bridged Biradicals as Building Blocks for the Design of Quantum Magnets. *Crystal Growth & Design* **2012,** *12*, 54-59.

7. Ravat, P.; Ito, Y.; Gorelik, E.; Enkelmann, V.; Baumgarten, M., Tetramethoxypyrene-Based Biradical Donors with Tunable Physical and Magnetic Properties. *Org. Lett.* **2013,** *15*, 4280-4283.

8. Kolanji, K.; Ravat, P.; Bogomyakov, A. S.; Ovcharenko, V. I.; Schollmeyer, D.; Baumgarten, M., Mixed Phenyl and Thiophene Oligomers for Bridging Nitronyl Nitroxides. *J. Org. Chem* **2017,** *82*, 7764-7773.

9. Ravat, P.; Baumgarten, M., "Tschitschibabin Type Biradicals": Benzenoid or Quinoid? *Phys. Chem. Chem. Phys.* **2015,** *17*, 983-991.

10. Sarbadhikary, P.; Shil, S.; Panda, A.; Misra, A., A Perspective on Designing Chiral Organic Magnetic Molecules with Unusual Behavior in Magnetic Exchange Coupling. *J. Org. Chem.* **2016,** *81*, 5623-5630.

11. Ravat, P.; Marszalek, T.; Pisula, W.; Müllen, K.; Baumgarten, M., Positive Magneto-LC Effect in Conjugated Spin-Bearing Hexabenzocoronene. *J. Am. Chem. Soc.* **2014,** *136*, 12860-12863.

12. Yao, H.; Ye, L.; Zhang, H.; Li, S.; Zhang, S.; Hou, J., Molecular Design of Benzodithiophene-Based Organic Photovoltaic Materials. *Chem. Rev.* **2016,** *116*, 7397-7457.

13. Lu, L.; Zheng, T.; Wu, Q.; Schneider, A. M.; Zhao, D.; Yu, L., Recent Advances in Bulk Heterojunction Polymer Solar Cells. *Chem. Rev.* **2015,** *115*, 12666-12731.

14. Li, M.; Ni, W.; Wan, X.; Zhang, Q.; Kan, B.; Chen, Y., Benzo[1,2-b:4,5-b[prime or minute]]dithiophene (BDT)-Based Small Molecules for Solution Processed Organic Solar Cells. *J. Mater. Chem. A* **2015,** *3*, 4765-4776.

15. Weil, J. A. B., J. R.; Wertz, J. E., Eds., Electron Paramagnetic Resonance, Elementary Theory and Practical Applications. *VCH-Wiley Interscience: New York,* **1994**, 179.

16. Sakamoto, K. M. a. J., Spin–Spin Dipolar and Exchange Interactions in Crystalline Bisgalvinoxyl Biradical. *J. Chem. Phys.* **1978,** *68*, 1432-1438.

17. Bhattacharya, D.; Shil, S.; Misra, A.; Klein, D. J., Intramolecular Ferromagnetic Coupling in Bis-Oxoverdazyl and Bis-Thioxoverdazyl Diradicals with Polyacene Spacers. *Theor. Chem. Acc* **2010,** *127*, 57-67.

18. Shil, S.; Roy, M.; Misra, A., Role of the Coupler to Design Organic Magnetic Molecules: LUMO Plays an Important Role in Magnetic Exchange. *RSC Advances* **2015,** *5*, 105574-105582.

19. Frisch, M. J.; Trucks, G. W.; Schlegel, H. B.; Scuseria, G. E.; Robb, M. A.; Cheeseman, J. R.; Scalmani, G.; Barone, V.; Mennucci, B.; Petersson, G. A.; Nakatsuji, H.; Caricato, M.; Li, X.; Hratchian, H. P.; Izmaylov, A. F.; Bloino, J.; Zheng, G.; Sonnenberg, J. L.; Hada, M.; Ehara, M.; Toyota, K.; Fukuda, R.; Hasegawa, J.; Ishida, M.; Nakajima, T.; Honda, Y.; Kitao, O.; Nakai, H.; Vreven, T.; Montgomery, J., J. A.; Peralta, J. E.; Ogliaro, F.; Bearpark, M.; Heyd, J. J.; Brothers, E.; Kudin, K. N.; Staroverov, V. N.; Kobayashi, R.; Normand, J.; Raghavachari, K.; Rendell, A.; Burant, J. C.; Iyengar, S. S.; Tomasi, J.; Cossi, M.; Rega, N.; Millam, N. J.; Klene, M.; Knox, J. E.; Cross, J. B.; Bakken, V.; Adamo, C.; Jaramillo, J.; Gomperts, R.; Stratmann, R. E.; Yazyev, O.; Austin, A. J.; Cammi, R.; Pomelli, C.; Ochterski, J. W.; Martin, R. L.; Morokuma, K.; Zakrzewski, V. G.; Voth, G. A.; Salvador, P.; Dannenberg, J. J.; Dapprich, S.; Daniels, A. D.; Farkas, Ö.; Foresman, J. B.; Ortiz, J. V.; Cioslowski, J.; Fox, D. J., *Gaussian 09, Revision D.01*, **2009**.

20. Noodleman, L., Valence Bond Description of Antiferromagnetic Coupling in Transition Metal Dimers. *J. Chem. Phys.* **1981,** *74*, 5737-5743.

21. Noodleman, L.; Davidson, E. R., Ligand Spin Polarization and Antiferromagnetic Coupling in Transition Metal Dimers. *Chem. Phys.* **1986,** *109*, 131-143.

22. Yamaguchi, K.; Jensen, F.; Dorigo, A.; Houk, K. N., A Spin Correction Procedure for Unrestricted Hartree-Fock and Møller-Plesset Wavefunctions for Singlet Diradicals and Polyradicals. *Chem. Phys. Lett.* **1988,** *149*, 537-542.

23. Soda, T.; Kitagawa, Y.; Onishi, T.; Takano, Y.; Shigeta, Y.; Nagao, H.; Yoshioka, Y.; Yamaguchi, K., Ab Initio Computations of Effective Exchange Integrals For H–H, H–He–H And Mn_2O_2 Complex: Comparison of Broken-Symmetry Approaches. *Chem. Phys. Lett.* **2000,** *319*, 223-230.

24. Shoji, M.; Koizumi, K.; Kitagawa, Y.; Kawakami, T.; Yamanaka, S.; Okumura, M.; Yamaguchi, K., A General Algorithm For Calculation Of Heisenberg Exchange Integrals J In Multi Spin Systems. *Chem. Phys. Lett.* **2006,** *432*, 343-347.

25. Bleaney, B.; Bowers, K. D., Anomalous Paramagnetism of Copper Acetate. *Proc. R. Soc. London, Ser. A* **1952,** *214*, 451-465.

26. Johnston, D. C.; Kremer, R. K.; Troyer, M.; Wang, X.; Klümper, A.; Bud'ko, S. L.; Panchula, A. F.; Canfield, P. C., Thermodynamics of Spin S=1/2 Antiferromagnetic Uniform and Alternating-Exchange Heisenberg Chains. *Phys. Rev. B* **2000,** *61*, 9558-9606.

27. Constantinides, C. P.; Berezin, A. A.; Manoli, M.; Leitus, G. M.; Bendikov, M.; Rawson, J. M.; Koutentis, P. A., Effective Exchange Coupling in Alternating-Chains of a π-Extended 1,2,4-Benzotriazin-4-yl. *New J. Chem.* **2014,** *38*, 949-954.

28. Koßmehl, G.; Beimling, P.; Manecke, G., Über polyarylenalkenylene und polyheteroarylenalkenylene, Synthesen und charakterisierung von poly(thieno[2′,3′:1,2]benzo[4,5-b]thiophen-2,6-diylvinylenarylenvinylen)en, poly(4,8-dimethoxythieno[2′,3′:1,2]benzo[4,5-b]thiophen-2,6-diylvinylenarylenvinylen)en und einigen modellverbindungen. **1983,** *184*, 627-650.

29. Ma, L.; Yi, Z.; Wang, S.; Liu, Y.; Zhan, X., Highly Sensitive Thin Film Phototransistors Based on a Copolymer of Benzodithiophene and Diketopyrrolopyrrole. *J. Mater. Chem. C* **2015,** *3*, 1942-1948.

30. Bathula, C.; Kang, Y.; Buruga, K., Donor-acceptor polymers by solid state eutectic melt reaction for optoelectronic applications. *J. Alloys Compd.* **2017,** *720*, 473-477.

Chapter 4

Nitronyl Nitroxide Substituted 4–Phenyl–4H–dithieno[3,2–b:2',3'–d]pyrrole (DTP–Ph) Derivatives and Their Radical Cationic High Spin Molecules

Abstract: Triplet ground state high spin organic molecules are special attention due to their future application. Three nitronyl nitroxide (NN) substituted radical cationic molecules have been designed and the exchange interactions, J/k_B were calculated by DFT studies which offered triplet ground state high spin molecules with J/k_B of 5000 K, and + 965.4 K for **(Ph$_2$DTP–Ph–NN)$^{\cdot+}$** and (**Th$_2$DTP–Ph–NN)$^{\cdot+}$** while –3580 K, for (**DTP–Ph–NN)$^{\cdot+}$**, respectively. According to these molecular design, neutral NN substituted 4–phenyl–4H-dithieno[3,2–*b*:2',3'–*d*]pyrrole derivatives (**R$_2$DTP–Ph–NN, R = H, Ph** and **MeSTh)** were synthesized, and characterized by mass spectrometry, UV–Vis, EPR spectroscopy and x-ray structure study. The electrochemical properties were studied by CV. It turned out that all these compounds were exhibited two main oxidation potentials, first for radical cation and next for dication formation. Then cation and di–cation formation were also confirmed through UV–Vis absorption spectroscopy by **R$_2$DTP–Ph–NN** titrated with *tris*(4–bromophenyl)aminiumhexachloroantimonate (magic blue). During first oxidation two new peaks formed at 521 and 805 nm for **Ph$_2$DTP–Ph–NN** and 539 and 945 nm to **Th$_2$DTP–Ph–NN,** those are assigned to radical cation formation. In addition, the cation and di–cation formation were verified by EPR spectroscopy.

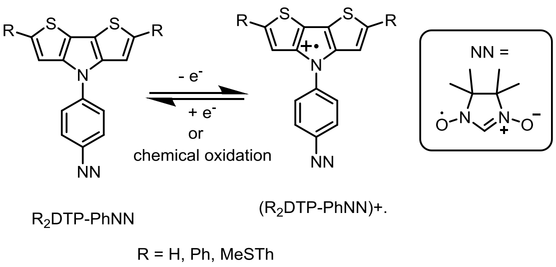

Chart 4.1: Structure of the **R$_2$DTP–Ph–NN** and **R$_2$DTP–Ph–NN$^{\cdot+}$**

4.1 Introduction

Organic high spin molecules have been attractive due to their flexible and controllable electronic properties and those were obtained by varies strategies which are summarized in the book chapters and literatures.[1-4] The high spin molecules have been used for various applications such as spintronic device, and molecular magnets.[4-6] The spin carrying units are very important in the high spin molecules, because of the kinetic stability issues of materials for the further application. To enhance kinetic stability, nitronylnitroxide (NN) iminonitroxide (IN) were the most recognized spin units for the high spin organic molecules.[7, 8] In addition, organic radical linked with conjugated triarylaminium radical cations are also of interest.[9-12] The mixed stable radical and one electron oxidized cation–radical systems are more popular, because of their fair kinetic stability and synthetic accessibility. While the parent triphenylaminium radical cation is not stable and quickly reacts via the para positions to form benzidines. The introduction of electron donating para substitutents eliminates this problem. Stable radical units linked with easily oxidizable aromatic amines are the particular interest in triplet ground state high spin molecules.[9, 10, 13] Thus, the mixed stable radical with radical cation molecules were provided for high spin triplet ground state molecules.[4, 14, 15] A series of NN substituted triarylamine (**TAA–NN**)[16, 17], fused arylamine (**FTAA–NN**), pyrazine (**PZ–NN**)[18, 19], thianthrene (**TA–NN**)[20], tetrathiafulvalene (**TTF–NN**) and pyrrole derivative (**P–NN**) molecules[6] and there radical cationic molecules were reported (figure 4.1), most of them afforded ground–state triplet diradical upon one electron oxidation. Especially 2,4–dithienylpyrrole based molecule (**N–TPN**) type molecules were highly interesting for our studies.[21]

The five–membered heteroaromatics such as thiophene and pyrrole units as the repeating π–conjugated oligomers have been more advantage than oligomers composed of six–membered aromatics. Because of the five–membered heteroaromatic oligomers exhibit better environmental stability and more effective π–conjugation due to the lower level of steric repulsion between neighboring units in planar conformations. Several examples of oligothiophenes are reported in the literature[22] but limited amount of the linear oligopyrroles are known[23-25] because of the limited synthetic access. Therefore, a pyrrole unit is frequently combined with thiophene rings in oligomer chemistry.[26-38]

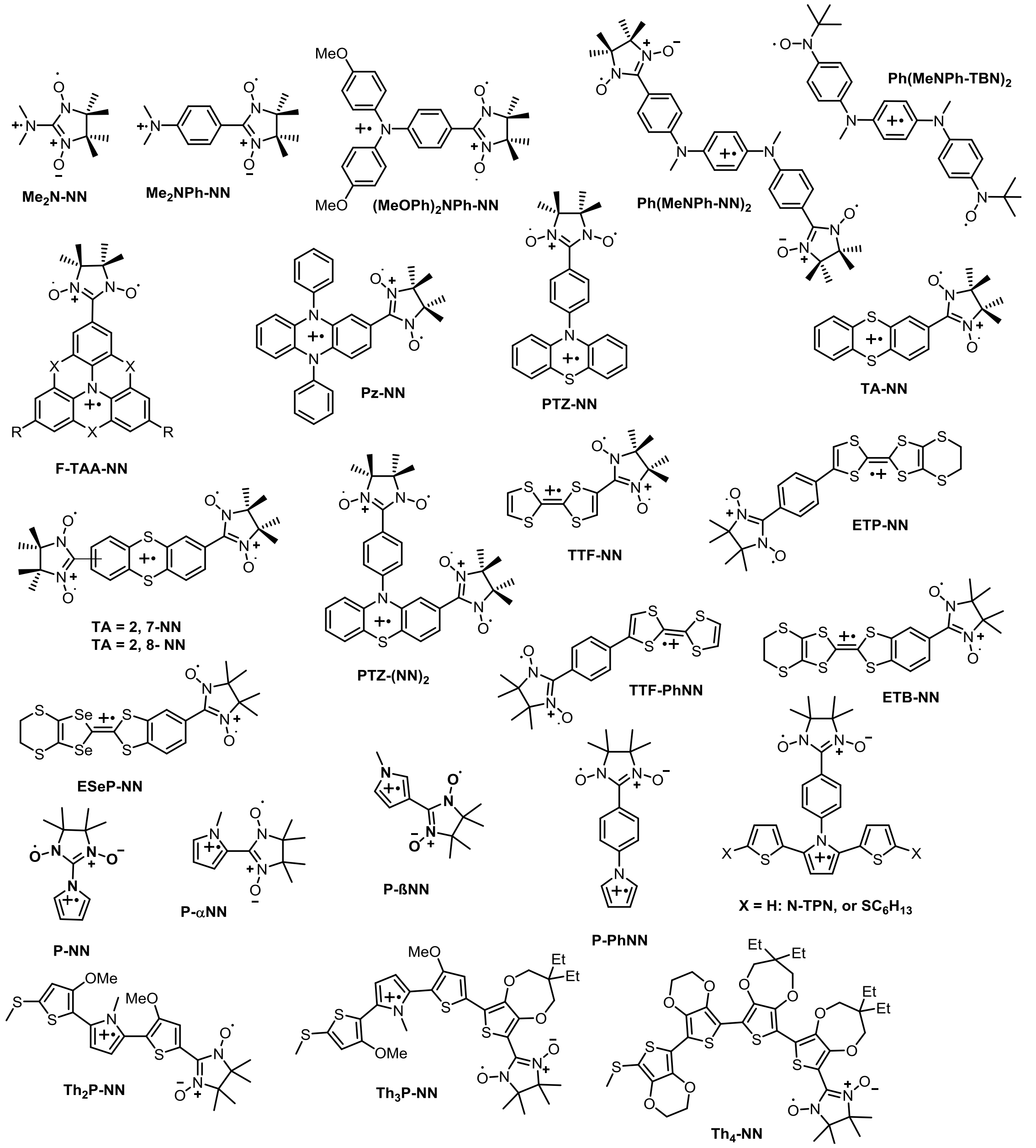

Figure 4.1: The known nitroxide radical substituted radical cationic molecules.

Fused aromatic conjugative molecules are better candidate for good electron transport properties due to their planarity than non–fused/non–planar molecules. Hence, our interest is focused on the synthesis of new stable radical species substituted with planar π–conjugated electron donor systems and their radical cations for high spin molecules. The planar molecules are more beneficial for better self–assembly[39-42], due to that enhanced *inter*– and *intra*–molecular electron transfer properties are possible than non–planar molecules.

Dithieno[3,2–*b*:2,3–*d*]–pyrrole (**DTP**) derivatives are interesting planar structure, since they possess better π–conjugation and lower ionization potential by their electron–donating nature of the molecules. They also have active two position on the thiophene, which serve to modify the energy levels to substitute different donor and or accepter units which can assistant to control the HOMO and LUMO energy level of the molecules. In our molecular design, DTP were substituted by different aryl groups for tune the electronic properties of the molecules.[43-52]

In this chapter, we report the design, synthesis, and structural, characterization of the three new NN substituted 4–Phenyl–4H-dithieno[3,2–*b*:2',3'–*d*]pyrrole (DTP–Ph) derivatives (**R_2DTP-Ph-NN**) and formation of their radical cationic (**R_2DTP-Ph-NN$^{\cdot+}$)** molecules. In addition, the exchange interactions were examined by DFT calculation.

Results and discussion

4.2 Molecular design using DFT calculations

The computations were carried out to understand the electronic structure of the molecules. All the DFT calculations were performed using the Gaussian09 package.[53] The full geometry optimizations were carried out by UB3LYP/6–31G(d) level for all the neutral radical molecules. The optimized structures and spin density distribution of the neutral radical molecules of **DTP–PhNN**, **Ph_2DTP–PhNN,** and **Th_2DTP–PhNN** are shown in figure 4.2. The bond distance between NN and Ph unit is 1.461 Å and between Ph and DTP–backbone is 1.412, these values are same for all the derivatives. The torsion between NN and its attached phenyl is slightly varies for different derivatives such as 7.2°, 1.4°, and 1.7°, similarly between phenyl and DTP–backbone also varies as 39.9, 48.9, 41.1 for **DTP–PhNN**, **Ph_2DTP–PhNN,** and **Th_2DTP–PhNN** respectively. In order to rationalize the ground state spin multiplicity of the molecules, the optimization was carried out for one electron oxidized molecular structures of **(DTP–PhNN)$^{\cdot+}$**, **(Ph_2DTP–PhNN)$^{\cdot+}$**, and (**Th_2DTP–**

PhNN)$^{\cdot+}$ and the structures are shown in figure 4.3. The cation–diradicals have two singly occupied molecular orbitals, SOMO and SOMO’, the latter resulting from the HOMO through one electron oxidation. Since the torsions are important for spin–spin interaction, thus the torsional analysis is mandatory. The torsions of the NN attached phenyl for neutral molecules are mentioned figures 4.2 for all the three derivatives.

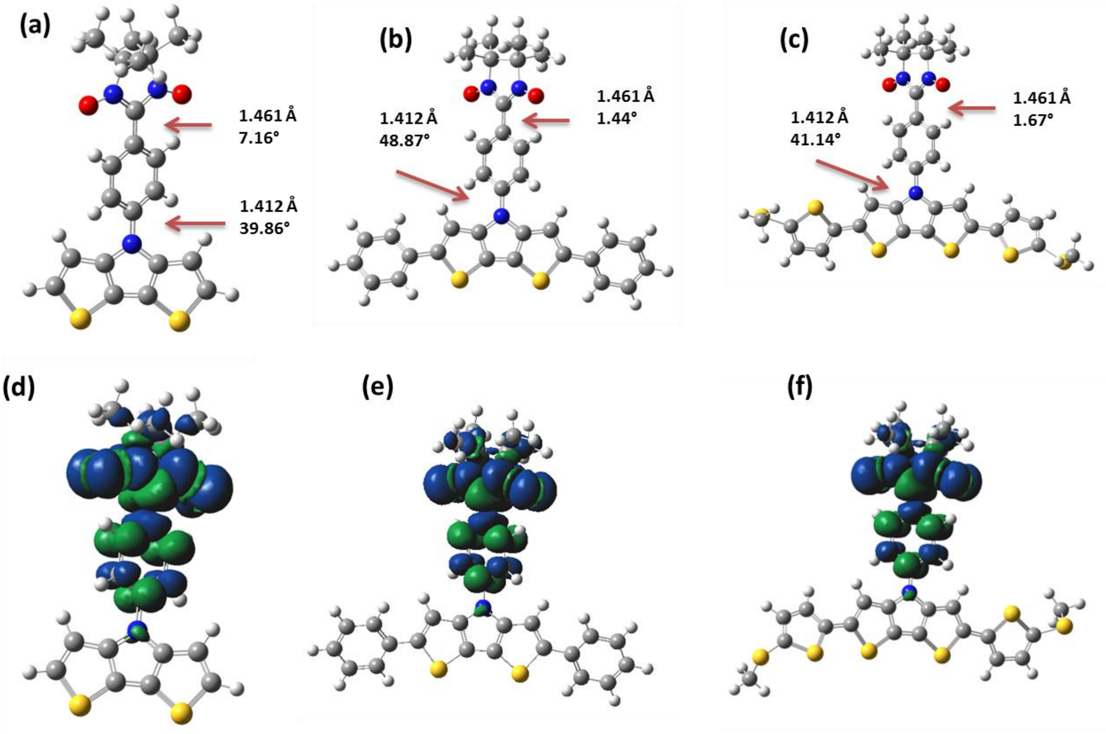

Figure 4.2: Optimized structures (a), (b), and (c), spin density distributions (d), (e) and (f) for **DTP–PhNN, Ph$_2$DTP–PhNN,** and **Th$_2$DTP–PhNN),** respectively, calculated by DFT using ublyp/6-31g(d) basis set.

From optimized structure, the spin density distribution was calculated by DFT using ublyp/6-31g(d) basis set. For neutral radical molecules of **Ph$_2$DTP–PhNN, Th$_2$DTP–PhNN** and **DTP–PhNN,** the spin densities are mostly distributed on NN unit and Ph part (figure 4.2d–2f). For the one electron oxidized molecules, the NN radical spin are more distributed on phenyl unit while extending the DTP π–bridge the spin have decreased in the Ph part. The positive charges are distributed nearly equally over the entire molecule for **Ph$_2$DTP–PhNN** and **Th$_2$DTP–PhNN** while the positive charge and the spin may be better delocalized over the extended π–unit. Less spin is on central phenyl for (figure 4.3d–f). Further, brokensymmetry (BS) approach calculations were applied to calculate exchange interaction because B3LYP hybrid function was over estimated.[54-56] The spin contaminations errors were corrected by Heisenberg–Dirac–Van Vleck (HDVV) Hamiltonian.[57-61] The J_{intra}/k_B was calculated from the optimized structure. The singlet and triplet energy were calculated by UBLYP hybrid function using 6–31G(d) basic set (to avoid Hartree-Fock contamination).

Table 4.1: Calculated triplet–, singlet–energy and exchange interactions (J_{intra}/kB) of the donor radicals cation **(R_2DTP–Ph–NN)$^{\cdot+}$**

	HF (triplet)	HF (singlet)	J_{intra}/k_B (K)
(DTP–PhNN)$^{\cdot+}$	–1922.5149694	–1922.528097	–3580
(Ph_2DTP–PhNN)$^{\cdot+}$	–2384.45220	–2384.4363728	+5000
(Th_2DTP–PhNN)$^{\cdot+}$	–3900.9501544	–3900.947097	+ 965.4

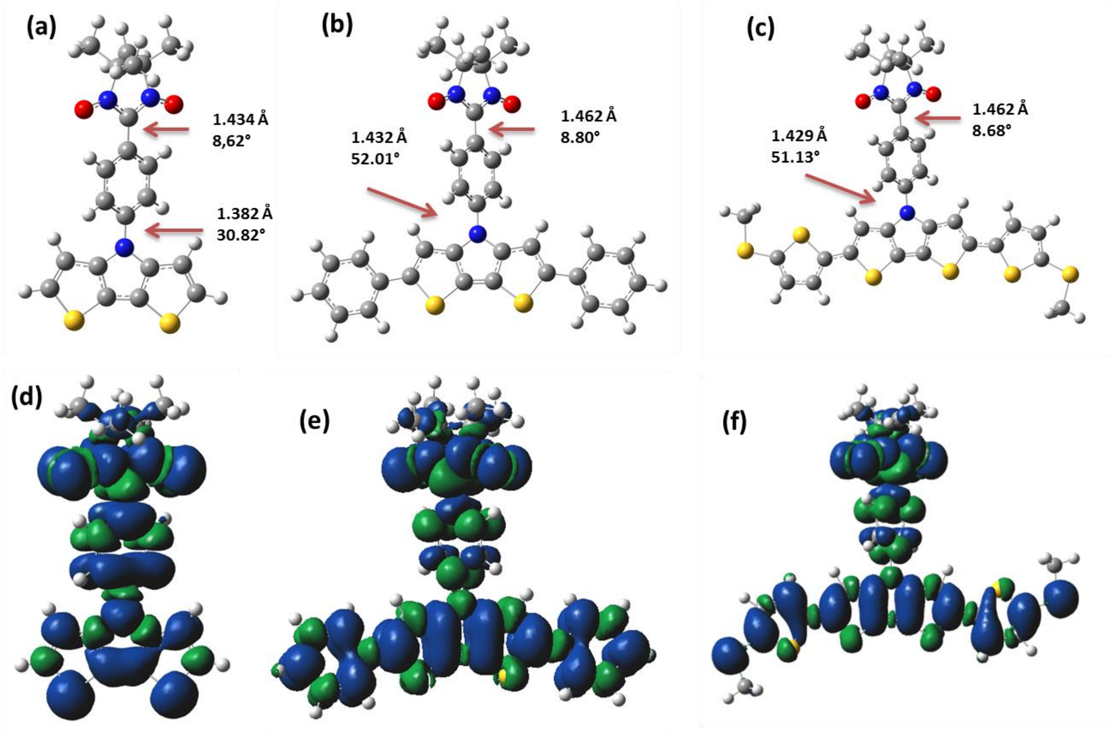

Figure 4.3: Optimized structures (a), (b), and (c) and spin density distributions (d), (e) and (f) for the **(DTP–PhNN)$^{+\cdot}$**, **(Ph_2DTP–PhNN)$^{+\cdot}$**, and **(Th_2DTP–PhNN)$^{\cdot+}$**respectively. These were calculated by DFT using broken symmetry (BS) approach calculations.

The calculated exchange interactions (J_{intra}/kB) are +5000 K, and +965.4 K for **(Ph_2DTP–PhNN)$^{\cdot+}$** and (**Th_2DTP–PhNN)$^{\cdot+}$** whereas –3580 K for (**DTP–PhNN)$^{\cdot+}$** respectively. The calculated exchange interactions (J_{intra}/kB) are also given in table 4.1. For the all the molecules, the singlet –

triplet energy gap is much higher and the energy level of the triplet is lower than the singlet state for **(Ph$_2$DTP–PhNN)**$^{\cdot+}$ and (**Th$_2$DTP–PhNN)**$^{\cdot+}$ which mean that these molecules are predicted as high spin with triplet species while singlet grout state for **(DTP–PhNN)**$^{\cdot+}$. The J_{intra}/kB values are also positive for **(Ph$_2$DTP–PhNN).+** and **(Th$_2$DTP–PhNN).+** , it means that interaction between two spins is ferromagnetic, although for **(DTP–PhNN)**$^{\cdot+}$ negative, which means that the magnetic interaction is antiferromagnetic between the NN and radical cation.

4.3 Synthesis

Scheme 4.1: Synthesis of nitronyl nitroxide substituted 4–Phenyl–4H-dithieno[3,2–*b*:2',3'–*d*]pyrrole derivatives of **R$_2$DTP–Ph–NN** (R = **R = H, Ph** and **MeSTh)**

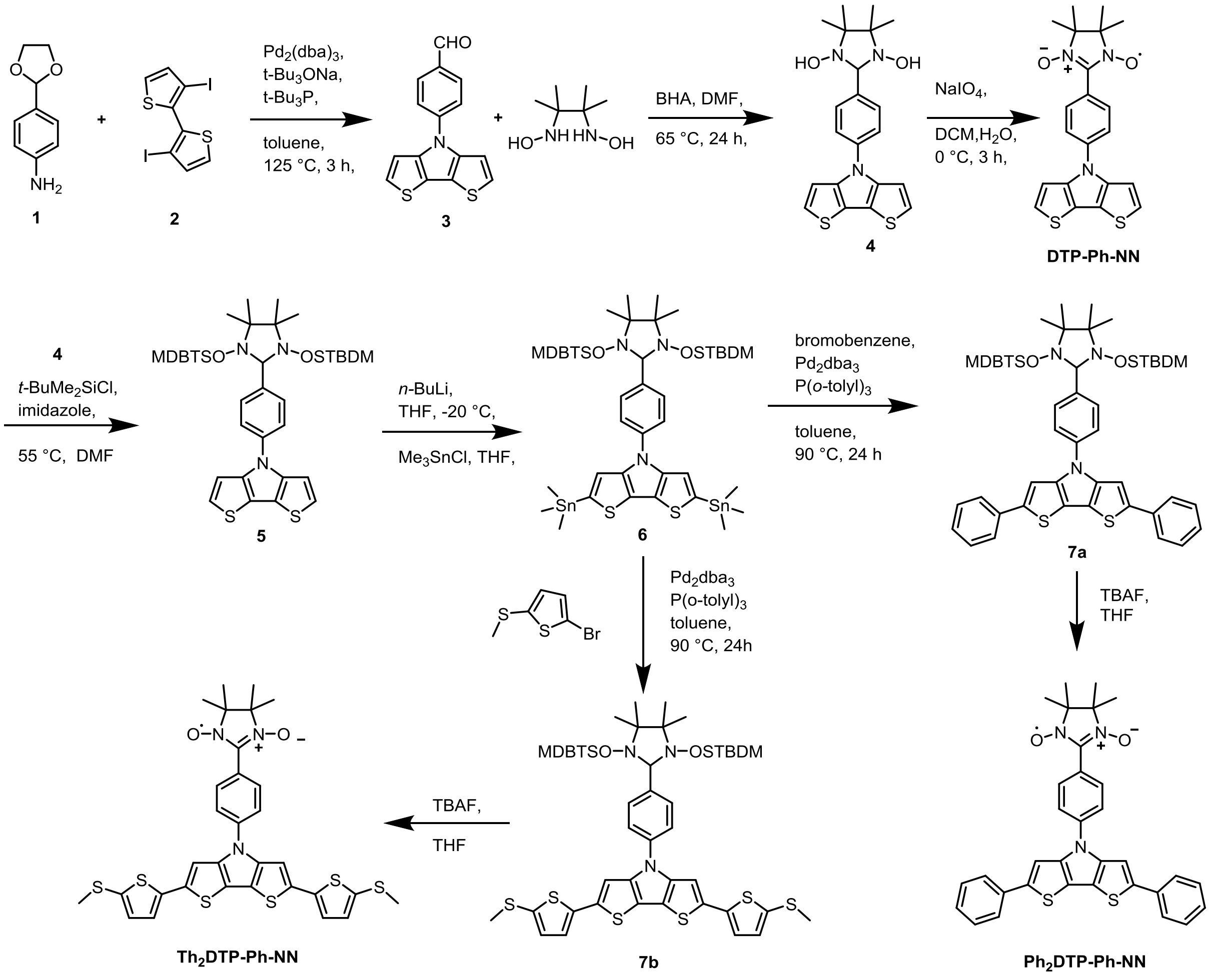

From the basic molecular design by DFT, the neutral radical molecules of **R$_2$DTP–PhNN (R = H, Ph** and **MeSTh)** were synthesized. The syntheses of **R$_2$DTP–PhNN** are demonstrated in scheme 4.1. Compound **1**[62, 63] and **2**[64] were prepared by reported procedure and **3** obtained by modified procedure with improved yield.[65] Ullman condensation for **3** with 2,3–bis(hydroxyamino)–2,3-dimethylbutane (BHA) yielded **4**.[66] Oxidation of **4** by NaIO$_4$ offered **DTP–Ph–NN**. The N–OH groups were protected with TBDMS by *tert*–butyldimethylsilyl chloride (*t*–BuMe$_2$SiCl) in the presence of imidazole in DMF as solvent to afford **5**.[54] Further, the compound **5** reacted with *n*–butyllithium solution followed by *tri*–methyltinchloride (Me$_3$SnCl) yielding **6**. Stille coupling was carried out between **6** and bromobenzene, or 2–bromo–5–(methylthio)thiophene[67] yields **7a, 7b**. Further **7a** or **7b** were reacted with tetrabutylammoniumfluoride (TBAF) to yield **Ph$_2$DTP–PhNN** and **Th$_2$DTP–PhNN**.[54] All the precursors were characterized NMR spectroscopy (appendix A-IV) and HRMS mass spectrometry.

4.4 Electrochemical studies

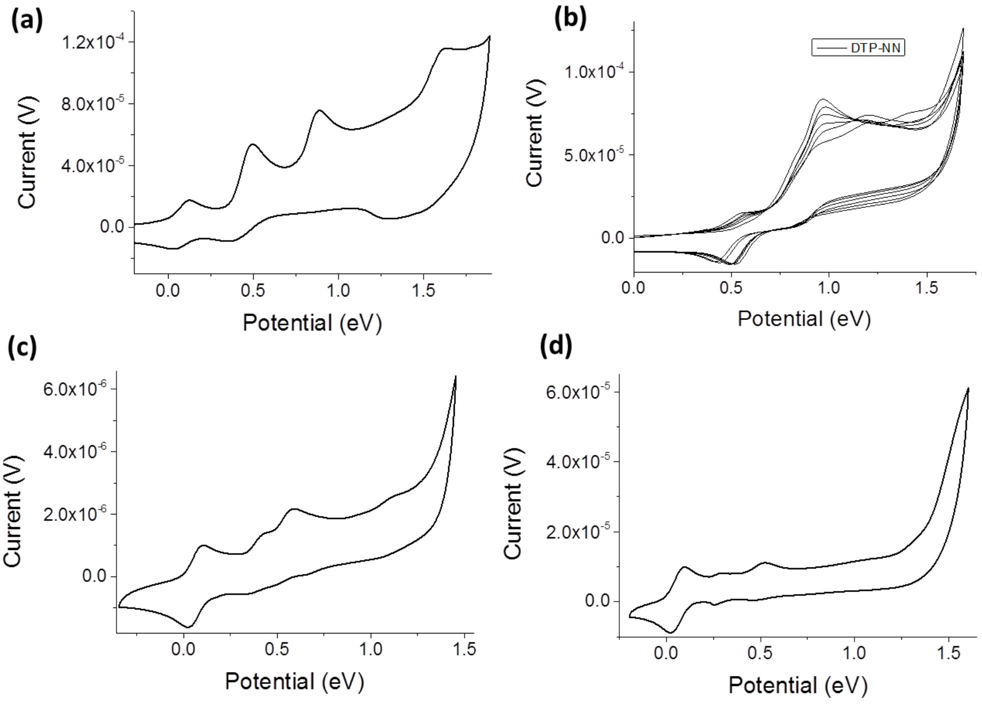

Figure 4.4: Cyclic voltammograms of (a), (b) **DTP–Ph–NN**, (c) **Ph$_2$DTP–Ph–NN** in PhCN and (d) **Th$_2$DTP–Ph–NN** in AcCN solution with 0.1M (n-C$_4$H$_9$)$_4$NBF$_4$ with scan rate = 0.1 V/s, Pt electrode.

A prerequisite for generating a radical cation molecule is that the arylamine of DPT moiety has a lower oxidation potential than those of the NN radical. Therefore, the electrochemical properties of all the molecules were investigated by the cyclic voltammetry in acetonitrile for **R_2DTP–Ph–NN, (R = H, and Th),** and benzonitrile for **Ph_2DTP–PhNN** at room temperature. The cyclic voltammograms are given in figure 4.4 for **R_2DTP–Ph–NN, (R = H, Ph and Th).** The oxidation potentials are summarized versus ferrocene/ferrocenium (Fc/Fc^+) in table 4.2. All the compounds exhibit two chemically reversible one–electron waves and another irreversible. The first oxidation occurs at +0.36, +0.34, and +0.24 (±0.02) V vs Fc/Fc+, for **DTP–Ph–NN**, **Ph_2DTP–Ph–NN** and **Th_2DTP–Ph–NN,** respectively. The first oxidation potentials were apparently lower than those of the NN unit,[6, 21] and similar compounds of **DTP**–**Ph, Ph_2DTP**–**Ph**, and **Th_2DTP**–**Ph** reported in the literature.[50-52]

Table 4.2: Oxidation potentials of donor radicals (**R_2DTP–Ph–NN)** and the g factor and $A_{N/2}$ values.

	E_1^{ox} [a]	E_2^{ox} [a]	E_3^{ox} [a]	g[b]	$^bA_{N/2}/mT$ [b]
DTP–PhNN	+0.36	+0.79	+1.14	2.006	0.37
Ph_2DTP–PhNN	+0.34	+0.49	+1.01	2.006	0.37
Th_2DTP–PhNN	+0.24	+0.42	+1.12	2.006	0.37

[a] oxidation values given in onset potential versus Fc/Fc^+ in eV with (± 0.02 eV), [b] obtained from EPR spectra with (± 0.02 *mT*).

The **DTP–Ph–NN** was polymerized at about 1.1 V (figure 4.4b) which was not our current interest. Hence, to avoid polymerization the other two molecules were protected through end–capping with phenyl and methylthio groups for **Ph_2DTP–Ph–NN** and **Th_2DTP–Ph–NN**. The extension of the π–bridge benefits better donor ability to the π–core. The first oxidation occurs by removal of one electron from the **DTP**–core, which is assigned for radical cation formation. The first oxidation potentials were lower for π–extended structures of **Th_2DTP–Ph–NN** than **Ph_2DTP–Ph–NN** and **DTP–Ph–NN.** The remaining two other oxidation peaks probably correspond to the oxidation process of the NN groups and/or the second oxidation process of the **DTP** core which allotted for the dication formation. Note that for **Ph_2DTP–Ph–NN** and **Th_2DTP–Ph–NN,** both the first and second oxidation potentials seem to be lower than those of the NN unit. It means that first and second steps were radical cation and dication formations in the oligomer moieties, respectively.

4.6 Crystal structure analysis

The structure, geometry and molecular packing of the molecules are powerful tool to analysis structure properties relationships. Therefore, crystal structure analysis is important to understand magnetic interactions in the solid state. The crystals were obtained by slow evaporation of DCM solution for **Th$_2$DTP–Ph–NN** and mixture of DCM and PhCN solution for **Ph$_2$DTP–Ph–NN** which were suitable for single crystal X–ray analysis. The blue plate **Ph$_2$DTP**–**PhNN** was crystallized with PhCN solvent molecule in orthorhombic, Pbcn space group. The structure of the molecules is given in the figure 4.5. The torsions between the radical NN and phenyl are 14.0°, which is slightly higher than for obtained from the optimized structure (1.14°) (figure 4.2.b).

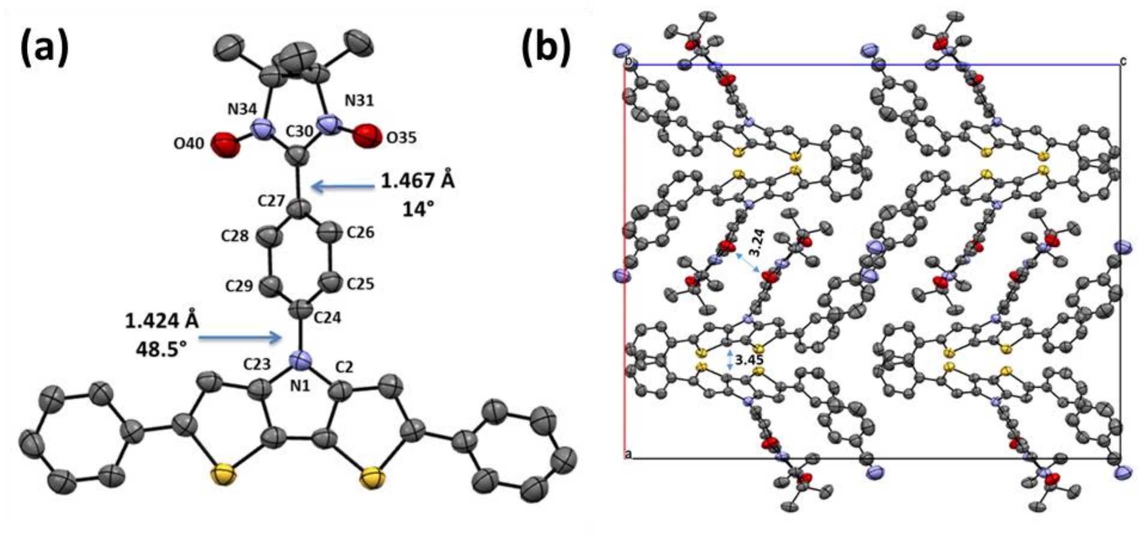

Figure 4.5: X–ray crystal structure of **Ph$_2$DTP–PhNN**, hydrogen atoms and PhCN are omitted for clarity.

The torsions between the central phenyl and π–unit is 48.5°, which is somewhat lower than 52.0° from optimized structure. Further, a molecular packing is displayed in figure 4.5.b. In the molecular packing a short intermolecular distance was found (3.24 Å) between two oxygen atoms, in addition, the other short π–π intermolecular distances are found as 3.45 Å for (S11…C5) and 3.48 for (S11…C4) between the molecules in the molecular packing.

Table 4.3: The inter–molecular interaction DFT calculation details.

	HF (triplet)	HF (singlet)	J_{inter}/k_B
(Ph_2DTP–PhNN)$_2$	– 4768.4743803	–4768.4743794	+ 0.28K
(Th_2DTP–PhNN)$_2$	–7801.4748581	–7801.474857	–0.35 K

The calculation was carried out by using UBLYP/6-31g(d) basic set in DFT

Hence, we have taken those two molecules for the inter–molecular interaction calculation as mentioned previously. The singlet and triplet energies were calculated using BLYP hybrid function and 6–31G basic set. The calculated intermolecular interaction of **Ph_2DTP-Ph-NN** is J_{inter}/k_B = + 0.281 K, which is weak ferromagnetic interaction between two molecules. The calculation details are given in table 4.3 and the inter molecular spin distribution of the molecules is shown in figure 4.6, in which the spins were shared between the molecules through space.

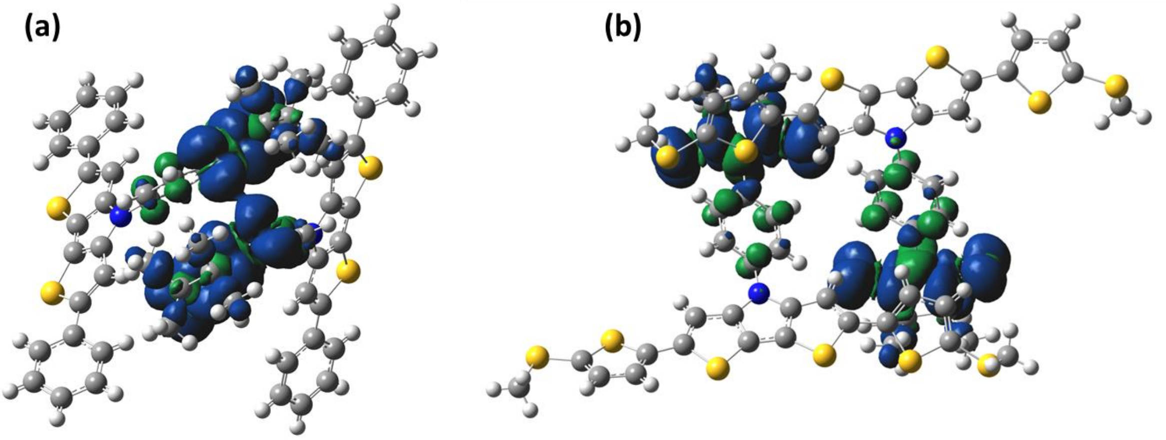

Figure 4.6: (a) dimer structure of the (**Ph_2DTP–PhNN)$_2$** and (b) **(Th_2DTP–PhNN)$_2$** for the inter molecular interaction calculation with spin distribution of the molecules.

The green block **Th_2DTP–PhNN** was crystallized in dimeric triclinic form with P–1 space group. The structure of the molecules are given in the figure 4.7. The molecular structures have two independent molecules with different orientation of the thiophene unit. In the molecule **Th_2DTP–PhNN–A**, the sulfur atoms are arranged as S5 and S13 in syn–orientations, S8 and S20 in anti–orientations while in molecule **Th_2DTP–PhNN–B,** both S5 and S13, then S8 and S20 are arranged in anti–orientations. The torsions between the radical NN and Ph are also different in both molecules 34.0° and 15.1° for **Th$_2$DTP–PhNN–A**, and **Th$_2$DTP–PhNN–B,** respectively. Similarly slightly different torsion angles were found between the center Ph and DTP core as 30.2° and 27.6° for **Th$_2$DTP–PhNN–A**, and **Th$_2$DTP–PhNN–B,** correspondingly. These variations are due to some intermolecular interaction present between the molecules and molecular arrangements in packing. In addition, we have taken dimer molecules and intermolecular interaction J_{inter}/k_B was calculated by DFT. The obtained J_{inter}/k_B *is* -0.35 K, however, which is very weak and indicates antiferromagnetic interaction.

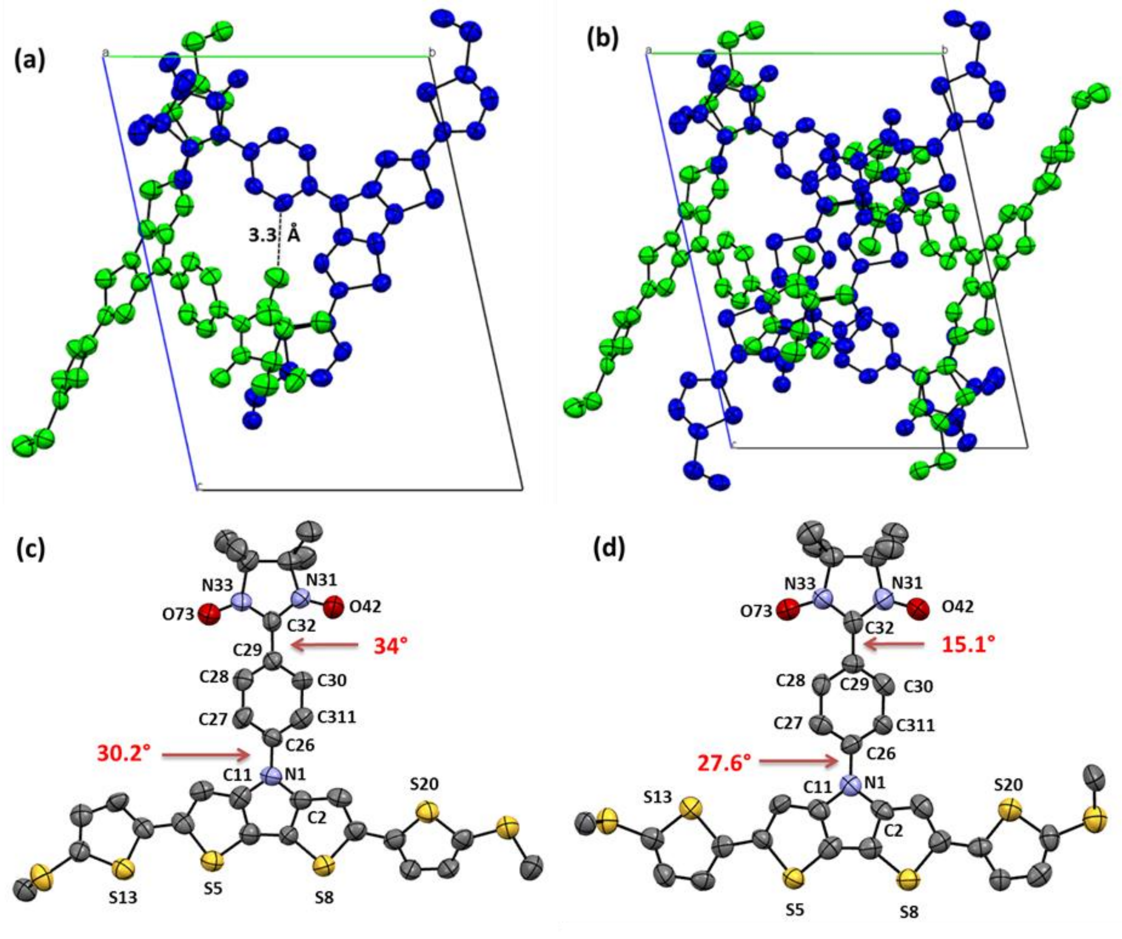

Figure 4.7: X–ray crystal structure of **Th$_2$DTP–PhNN** (a) dimeric structure, (b) crystal packing (c) molecular structure **Th$_2$DTP–PhNN –A** (d) molecular structure **Th$_2$DTP–PhNN –B**, hydrogen atoms are omitted for clarity.

4.6 Optical properties

The optical properties were studied by UV–Vis spectroscopy. The UV–Vis absorption spectra of the **R_2DTP–Ph–NN** (**R** = **Ph** and **MeSTh)** is displayed in figure 4.8. There are two main absorption bands appeared, one around 280–450 nm for π–π* transitions of the donor π–unit and another about 500-750 nm for n–π* transitions of NN radical unit which is similar to typically reported nitronylnitroxide molecules.[54]

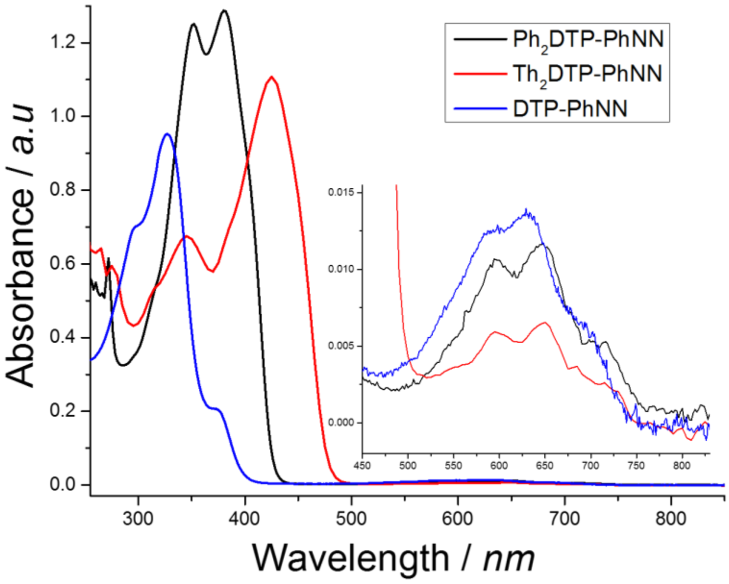

Figure 4.8: UV–Vis absorption spectra of **Ph_2DTP–PhNN** and **Th_2DTP–PhNN** in toluene (~10^{-6} M) solution. Inset zoom range (480-810 nm).

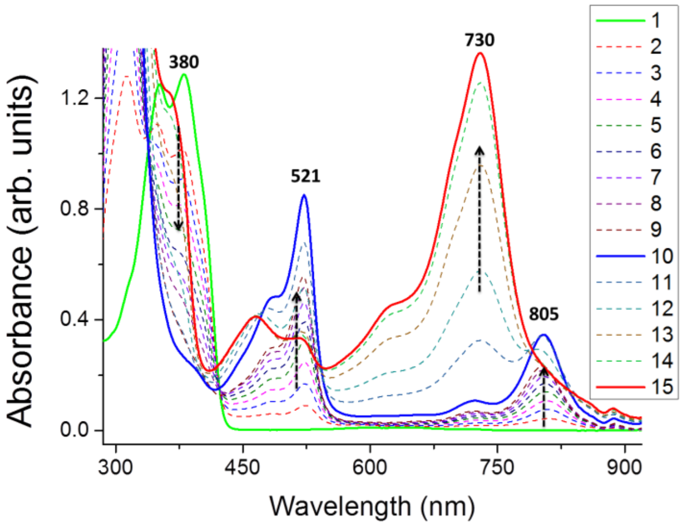

Figure 4.9. UV–Vis absorption spectra of **Ph_2DTP–PhNN** in toluene (~10^{-4} M) solution (—solid green line) and its oxidation by addition of magic blue in CH_2Cl_2 at room temperature. Note: (….broken lines) are formation of intermediates, (— solid blue line) monoradical cation, and (— solid red line) dication.

The chemical oxidation reactions were conducted by *tris*(4–bromophenyl)aminiumhexachloroantimonate (magic blue), ($(BrC_6H_4)_3N^{\bullet+}SbCl_6^-$) as the oxidant at room temperature in air, and these reactions were monitored by UV–Vis absorption spectroscopy. During first oxidation two new peaks were formed at 521 and 805 nm for **Ph₂DTP–PhNN** 539 and 945 nm for **Th₂DTP–PhNN** due to production of radical cation, at the mean time absorption band at 380 for **Ph₂DTP–PhNN** and 425 for **Th₂DTP–PhNN** were superseded. The absorption in the longer wavelength regions was assigned as the HOMO−SOMO and shorter for SOMO−LUMO transition, respectively. For second oxidation, another new peak appeared at 730 nm for **Ph₂DTP–PhNN** and 887 nm for **Th₂DTP–PhNN** and former peaks decreased (figure 4.9 and 4.10).

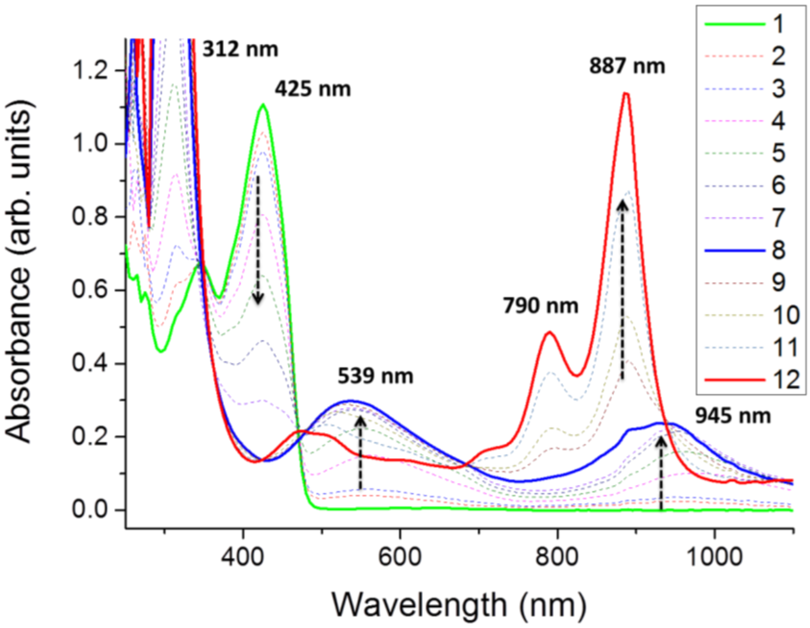

Figure 4.10. UV–Vis absorption spectra of **Th₂DTP–PhNN** in toluene (~10^{-4} M) solution (—solid green line) and its oxidation by addition of magic blue in CH_2Cl_2 at room temperature. Note: (….broken lines) are formation of intermediates, (— solid blue line) monoradical cation, and (— solid red line) dication.

4.7 EPR studies

The EPR spectra of neutral radicals of **DTP–Ph–NN, Ph₂DTP–Ph–NN** and **Th₂DTP–Ph–NN** in toluene (~10^{-4} M) in argon–saturated solution were measured at room temperature and the frozen solution at 130K. The spectra's are displayed in figure 4.11. All the molecules showed equally separated five lines at room temperature assigned to hyperfine coupling of two equivalent nitrogen nuclei of the NN unit. The isotropic hyperfine coupling constants $A_{N/2}$ = 0.37 (±0.01) *mT* and g factor g = 2.006 are nearly same for the all three radicals, this are also summarized in the table 4.2. Moreover, frozen solution spectra's are asymmetric with an anisotropic component in the spectra, which gives the different number of the shoulders in both the side of the outermost region.

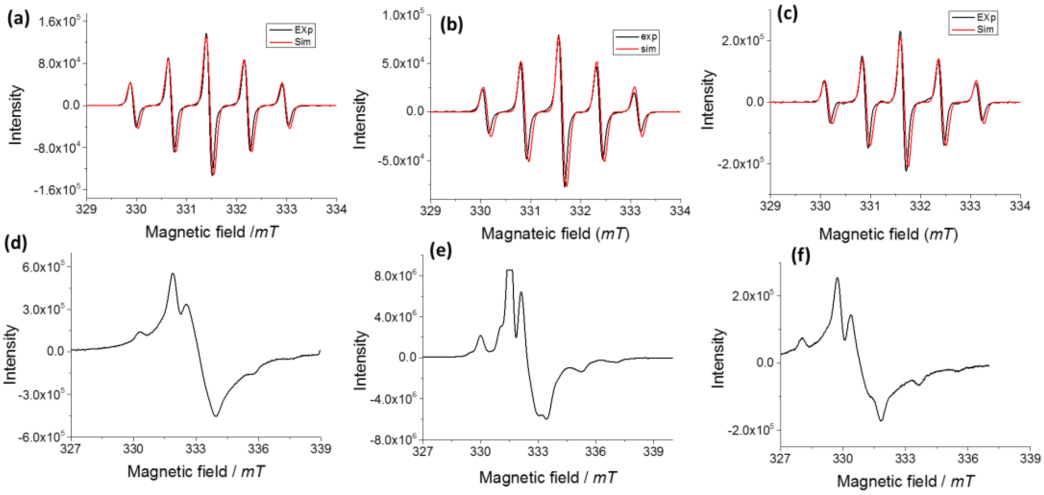

Figure 4.11: EPR spectra of the (a) **DTP-Ph–NN** at rt, (d) for at 130K, (b) **Ph$_2$DTP-Ph–NN** at rt, (e) for at 130K, (c) **Th$_2$DTP–Ph–NN** at rt, (f) for at 130K in toluene (~10^{-4} M) solution; (black) experimental, and **(**red) simulated.

Initially, we were tried to oxidize by magic blue while oxidation process, the reaction cannot monitor clearly by EPR spectroscopy. It might be the unreacted magic blue interfered resolutions of the spectra. Further, the chemical oxidation reaction was carried for all the neutral radicals by the silver hexafluoroantimonate ($AgSbF_6$) and the reaction was monitored by the EPR spectroscopy. For **DTP–Ph–NN** in DCM (blue solution) was titrated with $AgSbF_6$ as an oxidant and the spectra are given the figure 4.12.a. During addition of the oxidant to the blue solution become green and the intensity of the five line spectra is decreased, finally the all the EPR lines were diapered, this is due to decomposition of the NN, polymerisation of the molecules or some other side reaction occurred. The **Ph$_2$DTP-Ph–NN** in DCM (blue solution) become brown during addition of the $AgSbF_6$, in which the EPR spectra was recorded, there is a clear change in the spectra given in figure 4.11(b–c). After addition of one equivalent oxidant, 28 line EPR spectra were obtained and the spectrum is given in the figure 4.11(c). For **Th$_2$DTP-Ph–NN** in DCM (light blue/green solution) become dark green during addition of the $AgSbF_6$, and formed dark green precipitate. The poor soluble materials might be dimerized radical cations. The new EPR line appeared during addition of $AgSbF_6$ along with **Th_2DTP-Ph–NN** (5 line) but the spectra is not resolved as demonstrated in figure 4.11.e. The π–dimerization of dithienylpyrrole radical cation molecules is known from the literature.[68, 69] Further addition of one more equivalent of the $AgSbF_6$, kept at low temperature at –10 for 6 hours, five lines EPR spectra was retained aging for **Ph_2DTP-Ph–NN** and **Th_2DTP-Ph–NN,** the spectra are given the figure 4.11.(e and f). These results indicate the di–cation formation on the DTP core without decomposition of the NN radical.

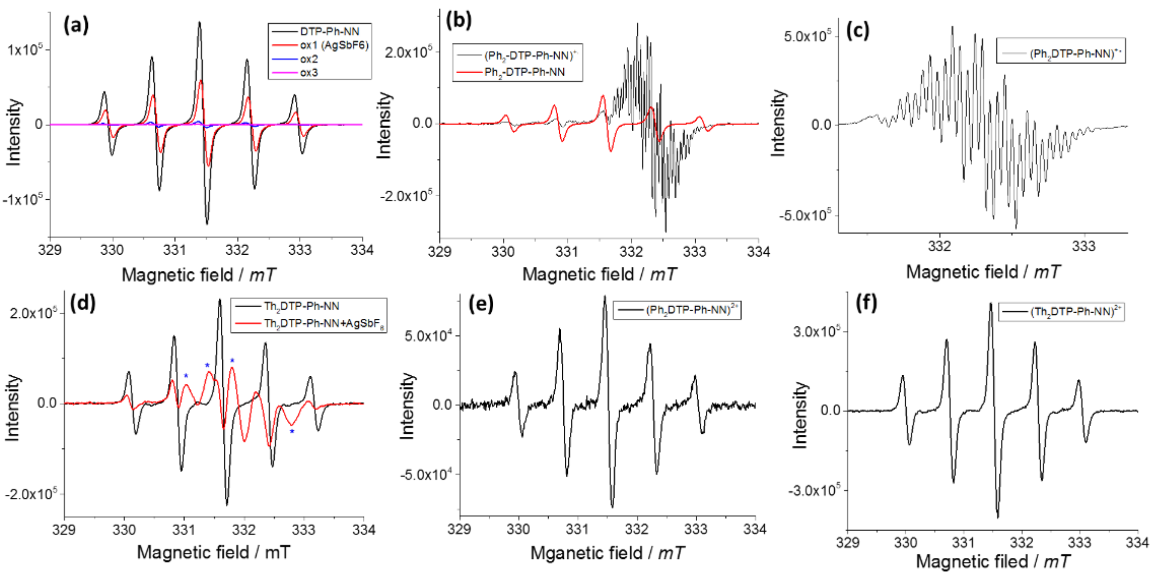

Figure 4.12: EPR spectra for during chemical oxidation reaction of (a) DTP-Ph–NN, (b), (c) Ph_2DTP-Ph–NN, (d) Th_2DTP–Ph–NN, (e) $(Ph_2DTP\text{-}Ph\text{–}NN)^{+2}$, and (f) $(Th_2DTP\text{-}Ph\text{–}NN)^{+2}$.

The proposed one electron oxidation mechanism is described in figure 4.13 for spin polarized donor radicals. A similar mechanism was also reported using molecular orbital theory to analysis one electron oxidation of the ammine–based spin-polarized donors radical and pyrrole derivatives molecules.[8] The energy level for the HOMO of the donor radical is higher than that the SOMO. Upon one electron oxidation, the one electron was removed from the HOMO of the donor radical and forms the high spin radical cationic molecule.

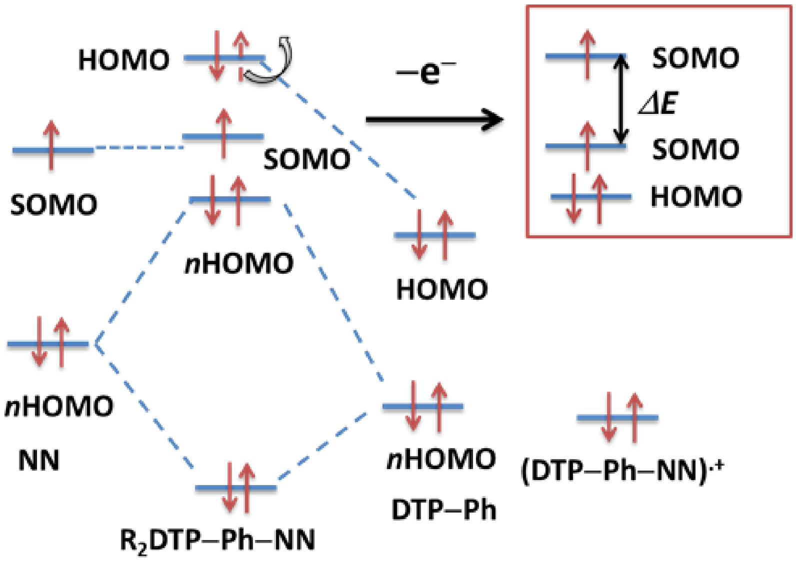

Figure 4.13: Proposed one electron oxidation mechanism for **R_2DTP–Ph–NN.**

4.8 Conclusions

Thus, three NN substituted donor π–core of (DTP–Ph) derivatives (**R_2DTP–Ph–NN)** molecules were prepared and characterized. The molecular structures and packing of **Ph_2DTP–Ph–NN** and **Th_2DTP–Ph–NN** were examined by single crystal x–ray structure analysis. The **Th_2DTP–Ph–NN** is crystalized in the dimeric form with shorter intermolecular distance of N–O…C–Ph (3.31 Å), while **Ph_2DTP–Ph–NN** crystalized in monomeric structure with smaller intermolecular distance found between two oxygen atoms for N–O…N–O (3.24 Å) in molecular packing. Upon one electron oxidation, these molecules offered triplet ground state radical cationic high spin molecules. Further charged molecules will be isolated and analyzed for magnetic properties by magnetic susceptibility. Syntheses of similar radical cationic molecules are under way. The **Ph_2DTP–Ph–NN and Th_2DTP–Ph–NN** molecules are suitable for spintronic and molecular based magnetic materials application.

4.9 Experimental section

Synthesis of 2-(4-nitrophenyl)-1,3-dioxolane.[62] The 4-nitrobenzaldehyde (3.30 g, 21.83 mmol) and p-toluenesulfonic acid monohydrate (76.5 mg, 0.402 mmol) were dissolved (75 mL) toluene in 250 mL round bottom flask. Then ethylene glycol (2.5 mL) was added, and the solution was refluxed with a Dean-Stark trap to azeotropically remove water. After 1 hour, the solution was allowed to cool to ambient temperature and 100 mL of Et_2O was added. The solution was washed twice with saturated $NaHCO_3$ solution and then with saturated NaCl solution. The solution was dried over $MgSO_4$ and evaporated to yield a pale yellow solid (4 g, 94% yield). ^1H NMR (250 MHz, CD_2Cl_2, δ, ppm): 8.20 (d, 2H), 7.65 (d, 2H), 5.87 (s, 1H), 4.07 (m, 4H).

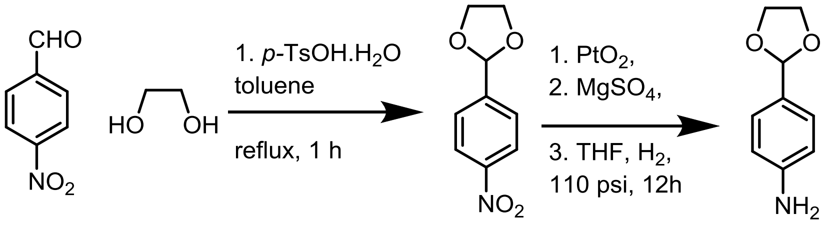

1

4-(1,3-Dioxolan-2-yl)aniline (1).[63] A pressure vessel was charged with 2-(4-nitrophenyl)-1,3-dioxolane (2.00 g, 10.25 mmol), PtO_2 (0.1 g, 0.40 mmol), $MgSO_4$ (2.5 g, 20.75 mmol), and THF (15 mL). The reaction vessel was purged with N_2 and subsequently charged with H_2 (110 psi). The reaction was stirred for 12 hr at room temperature while maintaining the H_2 pressure by periodically recharging the vessel. The reaction mixture was filtered through a fritted glass funnel, and washed with dry THF. The filtrates were combined and volatile fractions were removed to afford **1** (1.6 g, > 98%). ^1H NMR (250 MHz, CD_2Cl_2, δ, ppm): 7.22 (d, 2H), 6.64 (d, 2H), 5.63 (s, 1H), 4.03 (m, 4H).

3,3'-diiodo-2,2'-bithiophene (2).[64]

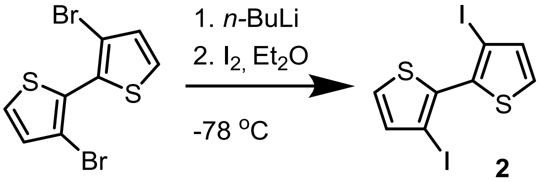

2

A 3,3’-dibromo-2,2’-bithiophene (3.01 g, 16.6 mmol) was dissolved in anhydrous Et_2O (90 mL) under a N_2-atmosphere In a flame-dried round bottom flask. Moreover, *n*-BuLi (1.6 M in hexanes, 13 mL, 18.56 mmol, 2.2 equiv.) was added dropwise at –78 °C. The reaction mixture was stirred about 1 h. A solution of I_2 (5.17 g, 18.56 mmol, 2.2 equiv.) in Et_2O (18 mL) was added dropwise, the mixture was warmed to r.t. and was stirred for another hour. The reaction was quenched by addition of saturated $Na_2S_2O_3$ (60 mL) and the layers were separated. The aqueous layer was extracted with Et_2O (2×60 mL). The combined organic layer was washed with brine, dried over $MgSO_4$ and the solvent was evaporated. The residue was recrystallized from hexanes/toluene 2:1. The **2** was isolated as an off-white crystalline solid (2.7 g, 70%).^{1}H NMR (300 MHz, CD_2Cl_2, δ, ppm): 7.46 (d, 2H), 7.18 (d, 2H).

4-(4H-dithieno[3,2-b:2',3'-d]pyrrol-4-yl)benzaldehyde, (3).[65]

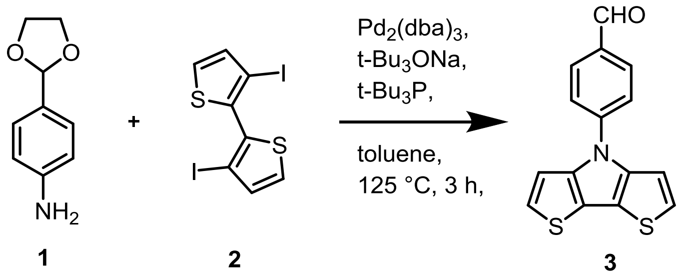

Under nitrogen atmosphere, the 500 mL round bottom flask connected with condenser and charged with 3,3'-diiodo-2,2'-bithiophene, (**2**), (8.0 g, 19.14 mmol), $Pd_2(dba)_3$ (0.887 g, 0.97 mmol) and sodium *tert*-butoxide (2.23 g, 23.20 mmol) in toluene (200 mL), and (2.9 mL) $P(^{t-}Bu)_3$ in 1 M toluene solution was added. Then, the mixture was stirred at 35 °C for 15 mints. Further, freshly prepared 4-(1,3-dioxolan-2-yl)aniline, (**1**)[63] (4.5 g, 27.24 mmol) in THF was added and the mixture was refluxed at 125 °C another 2.5 h and the reaction mixture was cooled to room temperature. The reaction mixture was filtered, extracted with diethyl ether, washed with brine solution and concentered. The residue was dissolved in THF and 1 M HCl was added and then the mixture was stirred for 2 h. Further, the reaction mixture was extracted with diethyl ether washed with brine solution. The crude mixture purified by column chromatography, yielded yellow solid (2.5 g, 46 %). ^{1}H NMR (250 MHz, CD_2Cl_2, δ, ppm): 10.03 (s, 1H), 8.06 (d, J = 7.5 Hz, 2H, Ph-H), 7.79 (d, J = 7.5 Hz, 2H, Ph-H), 7.27 (s, 4H, Th-H). ^{13}C NMR (62.90 MHz,CD_2Cl_2, δ, ppm): 191.3, 145.2, 143.9, 134.1, 132.0, 124.7, 122.5, 118.8, 113.1. HRMS m/z: calcd for $C_{15}H_9NOS_2$, 283.0126, ion formula for $[M+H]^+$, $C_{15}H_{10}NOS_2$, 284.0126; found, 284.0188.

2-(4-(4H-dithieno[3,2-b:2',3'-d]pyrrol-4-yl)phenyl)-4,4,5,5-tetramethylimidazolidine-1,3-diol (4).

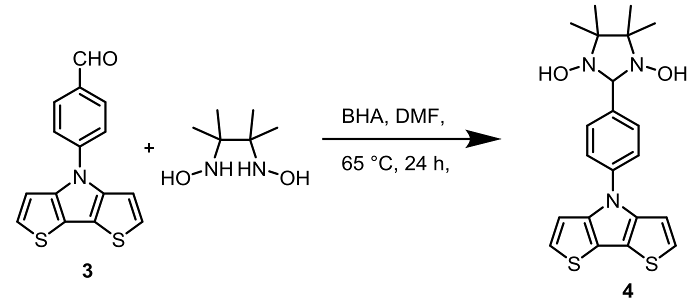

A mixture of **3** (0.290 g, 1.02 mmol) and 2,3-bis(hydroxylamino)-2,3-dimethylbutane (0.18 g, 1.22 mmol) in 15 mL of DMF was stirred at 65 C, for 24 h. The solution was concentrated and obtained residue was washed with ethyl acetate, obtained **4** as yellow solid (0.22 g, 52%). ^1H NMR (300 MHz, DMSO-d^6, δ ppm): 7.84 (s, 2 H, N-OH), 7.66 (m, 4 H), 7.47 (d, 2 H), 7.29 (d, 2 H), 4.58 (s, 1 H), 1.10 (s, 12 H. ^{13}C NMR (75 MHz, DMSO-d^6, δ ppm): 143.4, 139.9, 138.1, 130.2, 124.7, 121.4, 116.1, 112.6, 90.1, 66.2, 24.5, 17.2; ESI calculated for $C_{21}H_{23}N_3O_2S_2$, 413.12, found: 414.6, $[M+H]^+$.

Synthesis of the DTP-Ph-NN.

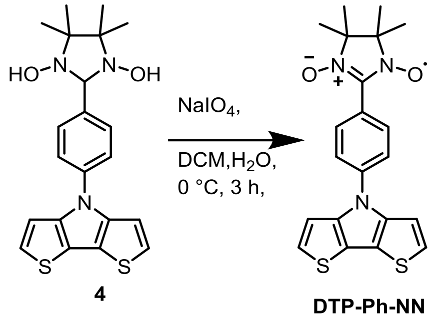

The compound **4** (0.101 g, 0.244 mmol) was dissolved in DCM and water, then $NaIO_4$ (0.057 g, 0. 267 mmol) in water was added at 0 C. The reaction mixture was stirred for 3 h at 0 C, mean time reaction was monitored by TLC. After the reaction was completed green organic phase was extracted by dichloromethane, and then washed with water and brine. The organic phase dried over $MgSO_4$ and concentrated. The residue was chromatographed over silica gel using DCM as eluent to obtain green product, 62 mg, 62 % yield; EPR (298 K, ~10^{-4} M in toluene): five lines, g_{iso}

= 2.0066, $a_{N1}/2$ = 0.37 ±0.002 *mT*. HRMS m/z: calcd for $C_{15}H_9NOS_2$, 283.0126, ion formula for $[M+H]^+$, $C_{15}H_{10}NOS_2$, 284.0126; found, 284.0188.HRMS m/z: calcd for $C_{21}H_{20}N_3O_2S_2$, 410.0997, ion formula for $[M+H]^+$, $C_{21}H_{21}N_3O_2S_2$, 411.1070; found, 411.1069.

Synthesis of 4-(4-(1,3-bis((tert-butyldimethylsilyl)oxy)-4,4,5,5-tetramethylimidazolidin-2-yl)phenyl)-4H-dithieno[3,2-b:2',3'-d]pyrrole, (5).

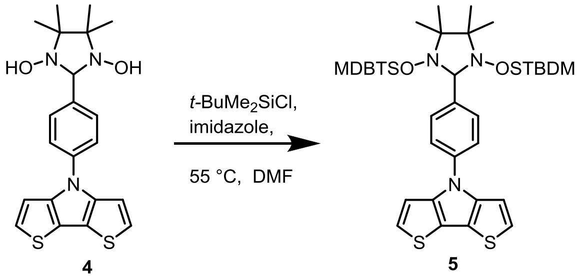

A mixture of **4,** (1.01 g, 2.44 mmol), *t*-butyldimethylsilyl chloride 1.90, 12.61 mmol), and imidazole (1.66 g, 24.42 mmol) taken in 100 mL Schlenk flask and dissolved in DMF (30 mL) and the mixture was stirred for 24 h at 55 °C under argon atmosphere. The solvent was removed under reduced pressure, and then the crude product was extracted with ether and washed with water. The ether layer was dried over magnesium sulfate and concentrated under reduced pressure. The residue was chromatographed on silica gel with hexane as the eluent to give **5,** colorless solid (1.3 g, 83%).^{1}H NMR (CD_2Cl_2, 250 MHz): δ, 7.54 (m, 4 H), 7.20 (d, 2 H), 7.12 (d, 2 H), 4.71 (s, 1 H), 1.20 (s, 12 H), 0.81 (s, 18 H), 0.01 (s, 6 H), -0.76 (s, 6 H). ^{13}C NMR (75 MHz, CD_2Cl_2,) δ, 144.8, 139.9, 132.9, 132.9, 123.9, 122.7, 116.9, 112.7, 89.9, 68.5, 27.4, 18.4, 17.5, -3.5, -4.7; HRMS m/z: calcd. for $C_{33}H_{51}N_3O_2SSi_2$, 641.2961, ion formula for $[M+H]^+$, $C_{33}H_{52}N_3O_2SSi_2$, 642.3034; found, 642.3037.

Synthesis of 2,6-distannyl DTP, 6.

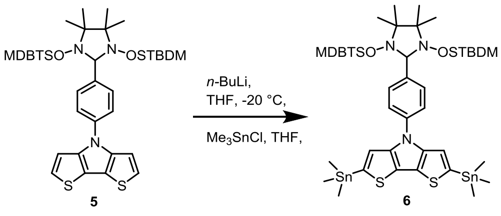

The compound **5** (1.02 g, 1.588 mmol) was dissolved in dry hexane (50 mL) and the solution was cooled to 0°C. Then tetramethylethylenediamine (**TMEDA**) (0.553 g, 0.72 mL, 4.759 mmol) was added, followed by BuLi (1.6 M in hexanes, 2.2 mL, 3.49 mmol) and the mixture stirred for 2 h at 0°C, Me_3SnCl (0.799 g, 3.97 mmol) was then added and the solution stirred overnight at rt. This mixture was poured over Et_3N-treated silica gel, filtered, and rinsed with hexane. The filtrate was concentrated via rotary evaporation and then dried overnight. The product was stored under N_2 in the freezer until further use. give **5,** colorless solid (1.4 g, 91 %).^{1}H NMR (CD_2Cl_2, 700 MHz): δ, 7.56 (d, 2 H), 7.52 (d, 2 H), 7.11 (s, 2 H), 4.72 (s, 1 H), 1.20 (s, 12 H), 0.82 (s, 18 H), 0.39 (s, 18 H), 0.02 (s, 6 H), -0.74 (s, 6 H). ^{13}C NMR (176 MHz, CD_2Cl_2,) δ, 147.7, 140.4, 140.1, 137.3, 123.6, 122.9, 122.5, 119.6, 93.02, 68.5, 26.5, 24.5, 17.4, -4.1 (Si(Me), -7.9 (Sn(Me3); HRMS m/z: calcd for $C_{39}H_{67}N_3O_2S_2Si_2Sn_2$, 969.2257, ion formula for $[M+H]^+$, $C_{39}H_{68}N_3O_2S_2Si_2Sn_2$ 970.2335; found, 970.2.

2-bromo-5-(methylthio)thiophene.[70]

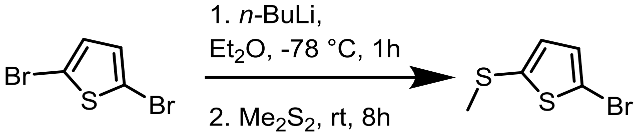

A 2,5-Dibromothiophene (4.0 g, 16.53 mmol) was dissolved in diethyl ether (30 mL) and then cooled to –78°C. A solution of *n*-butyl lithium (1.6 M in hexanes, (11.8 mL, 19.01 mmol, 1.15 eq) was slowly added while maintaining the temperature at less than –65°C. After complete mono-exchange, a solution of dimethyldisulfide (1.4 mL, 16.53, 1 eq.) in diethyl ether (2.0 mL) was added and the cooling bath was removed while stirring, allowing the mixture to warm to ambient temperature. After the addition was complete, the mixture was diluted with water (50.0 mL) and then separated. The organic layer was washed with water (2x50 mL), washed with brine (1x50 mL), dried over $MgSO_4$, and concentrated to form a black residue. The residue was passed through a silica gel plug and eluted with hexanes. Evaporation of the organics afforded the desired compound as a tan oil (3.4 g, 98 % yield). Some non-substituted thiophene was produced during the reaction and co-eluted with the product. ^{1}H NMR (CD_2Cl_2, 250 MHz): δ, 6.91 (s, 2 H), 2.472 (s, 6 H).

General procedure for Stille Coupling.

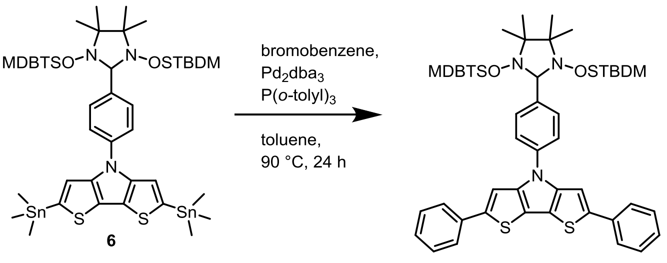

The desired intermediate **6** (0.1 mmol, 1 eq) and bromobenzene or 2–bromo–5–(methylthio)thiophene (0.25 mmol, 2.5 eq) were taken in 50 mL a Schlenk tube. The mixture was evacuated and backfilled with Ar_2 three times. And then $Pd_2(dba)_3$ (0.01 mmol, 0.1 eq), $P(o\text{-}tolyl)_3$ (0.03 mmol, 0.3 eq), and degassed toluene (20 mL) were added. The reaction was heated with stirring at 60 °C until completion (ca. 30 h).

7a, 62 %,: ^{1}H NMR (CD_2Cl_2, 700 MHz): δ, 7.65 (d, 4 H), 7.62 (d, 2 H), 7.59 (d, 2 H), 7.40 (t, 4 H), 7.37 (s, 2 H), 7.29 (t, 2 H), 4.75 (s, 1 H), 1.22 (s, 12 H), 0.84 (s, 18 H), 0.04 (s, 6 H), -0.70 (s, 6 H). ^{13}C NMR (176 MHz, CD_2Cl_2, δ, ppm): 147.8, 144.9, 143.0, 139.6, 135.8, 129.5, 137.9, 125.8, 123.1, 122.5, 116.6, 108.6, 93.6, 68.5, 26.7, 24.5, 17.1, -4.1; HRMS m/z: calcd for $C_{45}H_{59}N_3O_2S_2Si_2$, 793.3587, ion formula for [M+H]$^+$, $C_{45}H_{60}N_3O_2S_2Si_2$, 794.3665; found, 794.3.

7b, 69 %:

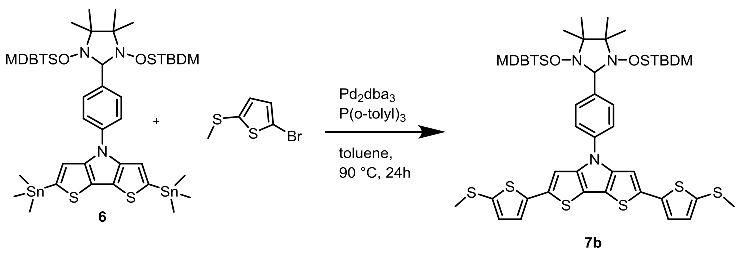

^{1}H NMR (CD_2Cl_2, 300 MHz): δ, 7.61 (d, 2 H), 7.52 (d, 2 H), 7.11 (s, 2 H), 7.06 (d, 2 H), 6.99 (d, 2 H), 4.75 (s, 1 H), 2.52 (s, 6 H), 1.21 (s, 12 H), 0.83 (s, 18 H), 0.03 (s, 6 H), -0.71 (s, 6 H). ^{13}C NMR (176 MHz, CD_2Cl_2, δ, ppm): 147.8, 144.68, 140.9, 139.3, 136.9, 135.7, 132.5, 132.2, 123.8, 123.1, 116.1, 108.9, 93.4, 68.6, 30.26, 25.5, 22.4, 18.4, -3.46; HRMS calculated for $C_{43}H_{60}N_3O_2S_6$, 898.2543, found: 898.2522, [M+H]$^+$.

General procedure for preparation for Ph_2DTP-Ph-NN and th_2DTP-Ph-NN.

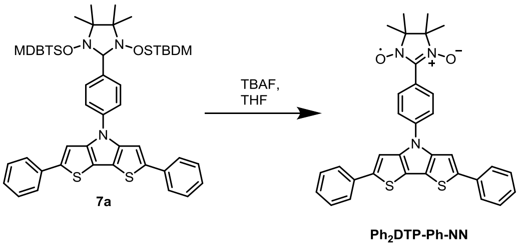

The compound **7a**, or **7b** (1 eq.) was dissolved in THF and TBAF (2 eq.) was added to the reaction mixture at room temperature. The reaction mixture was stirred for 6 h, mean time reaction was monitored by TLC. After the reaction was completed, a green solution was concentrated. The residue was chromatographed over silica gel using DCM:MeOH (99:1) as eluent.

Ph₂DTP-Ph-NN. Yield (72 %), EPR (298 K, ~10^{-4} M in toluene): five lines, g_{iso} = 2.0066, $a_{N1}/2$ = 0.37 *mT*. HRMS m/z: calcd for $C_{33}H_{28}N_3O_2S_2$, 562.1623, ion formula for $[M+H]^+$, $C_{33}H_{29}N_3O_2S_2$, 563.1696, found, 563.1692.

Synthesis of the Th₂DTP-Ph-NN.

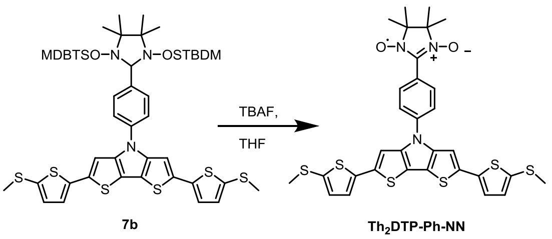

Obtain green crystalline product yield (69 %), EPR (298 K, ~10^{-4} M in toluene): five lines, g_{iso} = 2.0066, $a_{N1}/2$ = 0.37 *mT.* HRMS m/z: calcd for $C_{31}H_{28}N_3O_2S_6$, 666.9440, ion formula for $[M+H]^+$, $C_{31}H_{29}N_3O_2S_6$, 667.0584, found, 667.0.

The appendix-IV (**A-IV**) is given for chapter–3. NMR spectra of new compounds.

4.10 REFERENCES

1. Gallagher, N. M.; Olankitwanit, A.; Rajca, A., High-Spin Organic Molecules. *J. Org. Chem.* **2015,** *80*, 1291-1298.

2. Baumgarten, M., High Spin Molecules Directed Towards Molecular Magnets. In *EPR of Free Radicals in Solids II: Trends in Methods and Applications*, Lund, A.; Shiotani, M., Eds. Springer Netherlands: Dordrecht, **2012**; pp 205-244.

3. Baumgarten, M., High Spin Organic Molecules. In *World Scientific Reference on Spin in Organics*, **2017**; pp 1-93.

4. Ratera, I.; Veciana, J., Playing with Organic Radicals as Building Blocks for Functional Molecular Materials. *Chem. Soc. Rev.* **2012,** *41*, 303-349.

5. Sanvito, S., Molecular Spintronics. *Chem. Soc. Rev.* **2011,** *40*, 3336-3355.

6. Nakazaki, J.; Chung, I.; Matsushita, M. M.; Sugawara, T.; Watanabe, R.; Izuoka, A.; Kawada, Y., Design and Preparation of Pyrrole-Based Spin-Polarized Donors. *J. Mater. Chem.* **2003,** *13*, 1011-1022.

7. Sakurai, H.; Kumai, R.; Izuoka, A.; Sugawara, T., Ground State Triplet Cation Diradicals Generated from N,N-Dimethylamino Nitronyl Nitroxide and its Homologues Through One-Electron Oxidation. *Chem. Lett.* **1996,** *25*, 879-880.

8. Sakurai, H.; Izuoka, A.; Sugawara, T., Design, Preparation, and Electronic Structure of High-Spin Cation Diradicals Derived from Amine-Based Spin-Polarized Donors. *J. Am. Chem. Soc.* **2000,** *122*), 9723-9734.

9. Ito, A.; Kurata, R.; Sakamaki, D.; Yano, S.; Kono, Y.; Nakano, Y.; Furukawa, K.; Kato, T.; Tanaka, K., Redox Modulation of para-Phenylenediamine by Substituted Nitronyl Nitroxide Groups and Their Spin States. *J. Phys. Chem. A* **2013,** *117*, 12858-12867.

10. Ito, A.; Kurata, R.; Noma, Y.; Hirao, Y.; Tanaka, K., Radical Cation of an Oligoarylamine Having a Nitroxide Radical Substituent: A Coexistent Molecular System of Localized and Delocalized Spins. *J. Org. Chem.* **2016,** *81*, 11416-11420.

11. Dobrzyńska, E.; Jouni, M.; Gawryś, P.; Gambarelli, S.; Mouesca, J.-M.; Djurado, D.; Dubois, L.; Wielgus, I.; Maurel, V.; Kulszewicz-Bajer, I., Tuning of Ferromagnetic Spin Interactions in Polymeric Aromatic Amines via Modification of Their π-Conjugated System. *J. Phys. Chem. B* **2012,** *116*, 14968-14978.

12. Akihiro, I.; Daisuke, S.; Haruhiro, I.; Aya, T.; Yasukazu, H.; Kazuyoshi, T.; Katsuichi, K.; Tatsuhisa, K., Polycationic States of Oligoanilines Based on Wurster's Blue. *Eur. J. Org. Chem.* **2009,** *2009*, 4441-4450.

13. Ito, A.; Nakano, Y.; Urabe, M.; Kato, T.; Tanaka, K., Triradical Cation of p-Phenylenediamine Having Two Nitroxide Radical Groups: Spin Alignment Mediated by Delocalized Spin. *J. Am. Chem. Soc.* **2006,** *128*, 2948-2953.

14. Sugawara, T.; Komatsu, H.; Suzuki, K., Interplay Between Magnetism and Conductivity Derived from Spin-Polarized Donor Radicals. *Chem. Soc. Rev.* **2011,** *40*, 3105-3118.

15. Souto, M.; Lloveras, V.; Vela, S.; Fumanal, M.; Ratera, I.; Veciana, J., Three Redox States of a Diradical Acceptor–Donor–Acceptor Triad: Gating the Magnetic Coupling and the Electron Delocalization. *J. Phys. Chem. Lett.* **2016,** *7*, 2234-2239.

16. Kurata, T.; Koshika, K.; Kato, F.; Kido, J.; Nishide, H., An Unpaired Electron-Based Hole-Transporting Molecule: Triarylamine-Combined Nitroxide Radicals. *Chem. Commun.* **2007,** *0*, 2986-2988.

17. Kurata, T.; Koshika, K.; Kato, F.; Kido, J.; Nishide, H., Triarylamine-Combined Nitronyl Nitroxide and its Hole-Transporting Property. *Polyhedron* **2007,** *26*, 1776-1780.

18. Hiraoka, S.; Okamoto, T.; Kozaki, M.; Shiomi, D.; Sato, K.; Takui, T.; Okada, K., A Stable Radical-Substituted Radical Cation with Strongly Ferromagnetic Interaction: Nitronyl Nitroxide-Substituted 5,10-Diphenyl-5,10-dihydrophenazine Radical Cation. *J. Am. Chem. Soc.* **2004,** *126*, 58-59.

19. Masuda, Y.; Kuratsu, M.; Suzuki, S.; Kozaki, M.; Shiomi, D.; Sato, K.; Takui, T.; Hosokoshi, Y.; Lan, X.-Z.; Miyazaki, Y.; Inaba, A.; Okada, K., A New Ferrimagnet Based on a Radical-Substituted Radical Cation Salt. *J. Am. Chem. Soc.* **2009,** *131*, 4670-4673.

20. Izuoka, A.; Hiraishi, M.; Abe, T.; Sugawara, T.; Sato, K.; Takui, T., Spin Alignment in Singly Oxidized Spin-Polarized Diradical Donor: Thianthrene Bis(nitronyl nitroxide). *J. Am. Chem. Soc.* **2000,** *122*, 3234-3235.

21. Nickels, P.; Matsushita, M. M.; Minamoto, M.; Komiyama, S.; Sugawara, T., Controlling Co-tunneling Currents in Nanoparticle Networks Using Spin-Polarized Wire Molecules. *Small* **2008,** *4*, 471-475.

22. Mishra, A.; Ma, C.-Q.; Bäuerle, P., Functional Oligothiophenes: Molecular Design for Multidimensional Nanoarchitectures and Their Applications. *Chem. Rev.* **2009,** *109*, 1141-1276.

23. H., v. H. J. A. E.; L., G.; E., H. E.; J., J. R. A.; W., M. E., π-Dimers of End-Capped Oligopyrrole Cation Radicals. *Angew. Chem. Int. Ed. Engl.* **1996,** *35*, 638-640.

24. Sessler, J. L.; Aguilar, A.; Sanchez-Garcia, D.; Seidel, D.; Köhler, T.; Arp, F.; Lynch, V. M., Facile Syntheses of Quater-, Penta-, and Sexipyrroles. *Org. Lett.* **2005,** *7*, 1887-1890.

25. Ana, L.-P.; Rocío, R.-M.; Javier, A.; Carlos, C. J., Oligopyrrole Synthesis by 1,3-Dipolar Cycloaddition of Azomethine Ylides with Bissulfonyl Ethylenes. *Angew. Chem. Int. Ed.* **2007,** *46*, 9261-9264.

26. Niziurski-Mann, R. E.; Scordilis-Kelley, C.; Liu, T. L.; Cava, M. P.; Carlin, R. T., A Mechanistic Study of the Electrochemical Oxidation of 2,5-Bis(2-thienyl)pyrroles. *J. Am. Chem. Soc.* **1993,** *115*, 887-891.

27. Parakka, J. P.; Cava, M. P., Furan- and Pyrrole-Containing Analogs of α-Quinquethiophene: Spectroscopic and Electrochemical Properties. *Synth. Met.* **1995,** *68*, 275-279.

28. Kozaki, M.; Parakka, J. P.; Cava, M. P., New Thiophene−Pyrrole-Derived Annulenes Containing 6 and 10 Heterocyclic Units. *J. Org. Chem.* **1996,** *61*, 3657-3661.

29. Parakka, J. P.; Jeevarajan, J. A.; Jeevarajan, A. S.; Kispert L, D.; Cava, M. P., Heterocyclic Heptamers Containing Thiophene and Pyrrole Units: Synthesis and Properties. *Adv. Mater.* **1996,** *8*, 54-59.

30. van Haare, J. A. E. H.; Groenendaal, L.; Peerlings, H. W. I.; Havinga, E. E.; Vekemans, J. A. J. M.; Janssen, R. A. J.; Meijer, E. W., Unusual Redox Behavior of .alpha.-Oligoheteroaromatic Compounds: An Increasing First Oxidation Potential with Increasing Conjugation Length. *Chem. Mater.* **1995,** *7*, 1984-1989.

31. Alemán, C.; Domingo, V. M.; Fajarí, L.; Juliá, L.; Karpfen, A., Molecular and Electronic Structures of Heteroaromatic Oligomers: Model Compounds of Polymers with Quantum-Well Structures. *J. Org. Chem.* **1998,** *63*, 1041-1048.

32. Audebert, P.; Catel, J. M.; Le Coustumer, G.; Duchenet, V.; Hapiot, P., Electrochemistry and Polymerization Mechanisms of Thiophene−Pyrrole−Thiophene Oligomers and Terthiophenes. Experimental and Theoretical Modeling Studies. *J. Phys. Chem. B* **1998,** *102*, 8661-8669.

33. Ogura, K.; Yanai, H.; Miokawa, M.; Akazome, M., A new π-system: 1-aryl-2,5-di(2-thienyl)pyrroles. *Tetrahedron Lett.* **1999,** *40*, 8887-8891.

34. Hansford, K. A.; Perez Guarin, S. A.; Skene, W. G.; Lubell, W. D., Bis(pyrrol-2-yl)arylenes from the Tandem Bidirectional Addition of Vinyl Grignard Reagent to Aryl Diesters. *J. Org. Chem.* **2005,** *70*, 7996-8000.

35. Moreno, O. M.; M., P. T.; H., M. J.; M., S. K.; C., J. J.; A., M. K.; A., d. S. F. D.; Jean-Luc, B.; Juan, C.; T., L. N. J., Comparison of Thiophene–Pyrrole Oligomers with Oligothiophenes: A Joint Experimental and Theoretical Investigation of Their Structural and Spectroscopic Properties. *Chem. – A Europ.* **2010,** *16*, 6866-6876.

36. Fujii, M.; Nishinaga, T.; Iyoda, M., Synthesis of Thiophene–Pyrrole Mixed Oligomers End-Capped with Hexyl Group for Field-Effect Transistors. *Tetrahedron Lett.* **2009,** *50* (5), 555-558.

37. Nishinaga, T.; Tateno, M.; Fujii, M.; Fujita, W.; Takase, M.; Iyoda, M., Biradical Character of Linear π-Conjugated Oligomer Dications Composed of Thiophene, Pyrrole, and Methylthio End-Capping Units. *Org. Lett.* **2010,** *12*, 5374-5377.

38. Nishinaga, T.; Miyata, T.; Tateno, M.; Koizumi, M.; Takase, M.; Iyoda, M.; Kobayashi, N.; Kunugi, Y., Synthesis and Structural, Electronic, Optical and FET Properties of Thiophene–Pyrrole Mixed Hexamers End-Capped with Phenyl and Pentafluorophenyl Groups. *J. Mater. Chem.* **2011,** *21*, 14959-14966.

39. Zang, L.; Che, Y.; Moore, J. S., One-Dimensional Self-Assembly of Planar π-Conjugated Molecules: Adaptable Building Blocks for Organic Nanodevices. *Acc. Chem. Res.* **2008,** *41*, 1596-1608.

40. Ryan, H. M.; Tobias, S.; Wojciech, P.; Robert, G.; Klaus, M.; Wolfgang, S. H., Cooperative Molecular Motion within a Self-Assembled Liquid-Crystalline Molecular Wire: The Case of a TEG-Substituted Perylenediimide Disc. *Angew. Chem. Int. Ed.* **2009,** *48*, 4621-4624.

41. Giaimo, J. M.; Lockard, J. V.; Sinks, L. E.; Scott, A. M.; Wilson, T. M.; Wasielewski, M. R., Excited Singlet States of Covalently Bound, Cofacial Dimers and Trimers of Perylene-3,4:9,10-bis(dicarboximide)s. *J. Phys. Chem. A* **2008,** *112*, 2322-2330.

42. Abbel, R.; Grenier, C.; Pouderoijen, M. J.; Stouwdam, J. W.; Leclère, P. E. L. G.; Sijbesma, R. P.; Meijer, E. W.; Schenning, A. P. H. J., White-Light Emitting Hydrogen-Bonded Supramolecular Copolymers Based on π-Conjugated Oligomers. *J. Am. Chem. Soc.* **2009,** *131*, 833-843.

43. Ogawa, K.; Rasmussen, S. C., N-Functionalized Poly(dithieno[3,2-b:2‘,3‘-d]pyrrole)s: Highly Fluorescent Materials with Reduced Band Gaps. *Macromolecules* **2006,** *39*, 1771-1778.

44. Evenson, S. J.; Mumm, M. J.; Pokhodnya, K. I.; Rasmussen, S. C., Highly Fluorescent Dithieno[3,2-b:2′,3′-d]pyrrole-Based Materials: Synthesis, Characterization, and OLED Device Applications. *Macromolecules* **2011,** *44*, 835-841.

45. Wang, Z.; Liang, M.; Wang, L.; Hao, Y.; Wang, C.; Sun, Z.; Xue, S., New triphenylamine Organic Dyes Containing Dithieno[3,2-b:2′,3′-d]pyrrole (DTP) Units for Iodine-Free Dye-Sensitized Solar Cells. *Chem. Commun.* **2013,** *49*, 5748-5750.

46. Wang, Z.; Liang, M.; Dong, H.; Gao, P.; Su, Y.; Cai, P.; Ding, S.; Chen, J.; Xue, S., Asymmetric 8H-Thieno[2′,3′:4,5]thieno[3,2-b]thieno[2,3-d]pyrrole-Based Sensitizers: Synthesis and Application in Dye-Sensitized Solar Cells. *Org. Lett.* **2017,** *19*, 3711-3714.

47. Azmi, R.; Nam, S. Y.; Sinaga, S.; Akbar, Z. A.; Lee, C.-L.; Yoon, S. C.; Jung, I. H.; Jang, S.-Y., High-Performance Dopant-Free Conjugated Small Molecule-Based Hole-Transport Materials for Perovskite Solar Cells. *Nano Energy* **2018,** *44*, 191-198.

48. Mabrouk, S.; Zhang, M.; Wang, Z.; Liang, M.; Bahrami, B.; Wu, Y.; Wu, J.; Qiao, Q.; Yang, S., Dithieno[3,2-b:2′,3′-d]pyrrole-Based Hole Transport Materials for Perovskite Solar Cells with Efficiencies over 18%. *J. Mater. Chem. A,* **2018,** *6*, 7950-7958.

49. Barlow, S.; Odom, S. A.; Lancaster, K.; Getmanenko, Y. A.; Mason, R.; Coropceanu, V.; Brédas, J.-L.; Marder, S. R., Electronic and Optical Properties of 4H-Cyclopenta[2,1-b:3,4-b′]bithiophene Derivatives and Their 4-Heteroatom-Substituted Analogues: A Joint Theoretical and Experimental Comparison. *J. Phys. Chem. B* **2010,** *114*, 14397-14407.

50. Rasmussen, S. C.; Evenson, S. J., Dithieno[3,2-b:2′,3′-d]pyrrole-Based Materials: Synthesis and Application to Organic Electronics. *Prog. Polym. Sci.* **2013,** *38*, 1773-1804.

51. Evenson, S. J.; Pappenfus, T. M.; Delgado, M. C. R.; Radke-Wohlers, K. R.; Navarrete, J. T. L.; Rasmussen, S. C., Molecular Tuning in Highly Fluorescent Dithieno[3,2-b:2′,3′-d]pyrrole-Based Oligomers: Effects of N-functionalization and Terminal aryl Unit. *PCCP* **2012,** *14*, 6101-6111.

52. Balaji, G.; Parameswaran, M.; Jin, T. M.; Vijila, C.; Furong, Z.; Valiyaveettil, S., Synthesis and Hole-Transporting Properties of Highly Fluorescent N-Aryl Dithieno[3,2-b:2′,3′-d]pyrrole-Based Oligomers. *J. Phys. Chem. C* **2010,** *114*, 4628-4635.

53. Frisch, M. J.; Trucks, G. W.; Schlegel, H. B.; Scuseria, G. E.; Robb, M. A.; Cheeseman, J. R.; Scalmani, G.; Barone, V.; Mennucci, B.; Petersson, G. A.; Nakatsuji, H.; Caricato, M.; Li, X.; Hratchian, H. P.; Izmaylov, A. F.; Bloino, J.; Zheng, G.; Sonnenberg, J. L.; Hada, M.; Ehara, M.; Toyota, K.; Fukuda, R.; Hasegawa, J.; Ishida, M.; Nakajima, T.; Honda, Y.; Kitao, O.; Nakai, H.; Vreven, T.; Montgomery, J., J. A.; Peralta, J. E.; Ogliaro, F.; Bearpark, M.; Heyd, J. J.; Brothers, E.; Kudin, K. N.; Staroverov, V. N.; Kobayashi, R.; Normand, J.; Raghavachari, K.; Rendell, A.; Burant, J. C.; Iyengar, S. S.; Tomasi, J.; Cossi, M.; Rega, N.; Millam, N. J.; Klene, M.; Knox, J. E.; Cross, J. B.; Bakken, V.; Adamo, C.; Jaramillo, J.; Gomperts, R.; Stratmann, R. E.; Yazyev, O.; Austin, A. J.; Cammi, R.; Pomelli, C.; Ochterski, J. W.; Martin, R. L.; Morokuma, K.; Zakrzewski, V. G.; Voth, G. A.; Salvador, P.; Dannenberg, J. J.; Dapprich, S.; Daniels, A. D.; Farkas, Ö.; Foresman, J. B.; Ortiz, J. V.; Cioslowski, J.; Fox, D. J., *Gaussian 09, Revision D.01*, **2009**.

54. Kolanji, K.; Ravat, P.; Bogomyakov, A. S.; Ovcharenko, V. I.; Schollmeyer, D.; Baumgarten, M., Mixed Phenyl and Thiophene Oligomers for Bridging Nitronyl Nitroxides. *J. Org. Chem* **2017,** *82*, 7764-7773.

55. Ravat, P.; Borozdina, Y.; Ito, Y.; Enkelmann, V.; Baumgarten, M., Crystal Engineering of Tolane Bridged Nitronyl Nitroxide Biradicals: Candidates for Quantum Magnets. *Crystal Growth & Design* **2014,** *14*, 5840-5846.

56. Borozdina, Y. B.; Mostovich, E.; Enkelmann, V.; Wolf, B.; Cong, P. T.; Tutsch, U.; Lang, M.; Baumgarten, M., Interacting networks of purely organic spin-1/2 dimers. *J. Mater. Chem. C* **2014**, 6618-6629.

57. Noodleman, L., Valence Bond Description of Antiferromagnetic Coupling in Transition Metal Dimers. *J. Chem. Phys.* **1981,** *74*, 5737-5743.

58. Noodleman, L.; Davidson, E. R., Ligand Spin Polarization and Antiferromagnetic Coupling in Transition Metal Dimers. *Chem. Phys.* **1986,** *109*, 131-143.

59. Yamaguchi, K.; Jensen, F.; Dorigo, A.; Houk, K. N., A Spin Correction Procedure for Unrestricted Hartree-Fock and Møller-Plesset Wavefunctions for Singlet Diradicals and Polyradicals. *Chem. Phys. Lett.* **1988,** *149*, 537-542.

60. Soda, T.; Kitagawa, Y.; Onishi, T.; Takano, Y.; Shigeta, Y.; Nagao, H.; Yoshioka, Y.; Yamaguchi, K., Ab Initio Computations of Effective Exchange Integrals For H–H, H–He–H And Mn_2O_2 Complex: Comparison of Broken-Symmetry Approaches. *Chem. Phys. Lett.* **2000,** *319*, 223-230.

61. Shoji, M.; Koizumi, K.; Kitagawa, Y.; Kawakami, T.; Yamanaka, S.; Okumura, M.; Yamaguchi, K., A General Algorithm For Calculation Of Heisenberg Exchange Integrals J In Multi Spin Systems. *Chem. Phys. Lett.* **2006,** *432*, 343-347.

62. Briggs, J. R.; Klosin, J.; Whiteker, G. T., Synthesis of Biologically Active Amines via Rhodium−Bisphosphite-Catalyzed Hydroaminomethylation. *O. Lett.* **2005,** *7*, 4795-4798.

63. Riddle, J. A.; Jiang, X.; Huffman, J.; Lee, D., Signal-Amplifying Resonance Energy Transfer: A Dynamic Multichromophore Array for Allosteric Switching. *Angew. Chem. Int. Ed.* **2007,** *46*, 7019-7022.

64. Harschneck, T.; Zhou, N.; Manley, E. F.; Lou, S. J.; Yu, X.; Butler, M. R.; Timalsina, A.; Turrisi, R.; Ratner, M. A.; Chen, L. X.; Chang, R. P. H.; Facchetti, A.; Marks, T. J., Substantial Photovoltaic Response and Morphology Tuning in Benzo[1,2-b:6,5-b′]dithiophene (bBDT) Molecular Donors. *Chem. Commun.* **2014,** *50*, 4099-4101.

65. Vanormelingen, W.; Pandey, L.; Van der Auweraer, M.; Verbiest, T.; Koeckelberghs, G., Steering the Conformation and Chiroptical Properties of Poly(dithienopyrrole)s Substituted with Chiral OPV Side Chains. *Macromolecules* **2010,** *43*, 2157-2168.

66. Osiecki, J. H.; Ullman, E. F., Studies of Free Radicals. I. .Alpha.-Nitronyl Nitroxides, A New Class of Stable Radicals. *J. Am. Chem. Soc.* **1968,** *90*, 1078–1079.

67. Becker, D. P. C., J. N.; Fobian, Y. M.; Grapperhaus, M. L.; Hansen, D. W.; Heintz, R. M.; Kassab, D. J.; Massa, M. A.; Mcdonald, J. J.; Nagy, M. A., Heteroarylsulfonylmethyl Hydroxamic Acids and Amides and Their Use as Protease Inhibitor. *WO2004048368 A2 2004* **2004**.

68. Nishinaga, T.; Kageyama, T.; Koizumi, M.; Ando, K.; Takase, M.; Iyoda, M., Effect of Substituents on the Structure, Stability, and π-Dimerization of Dithienylpyrrole Radical Cations. *J. Org. Chem.* **2013,** *78*, 9205-9213.

69. Nishinaga, T.; Kanzaki, Y.; Shiomi, D.; Matsuda, K.; Suzuki, S.; Okada, K., Radical Cation π-Dimers of Conjugated Oligomers as Molecular Wires: An Analysis Based on Nitronyl Nitroxide Spin Labels. *Chem. – A Europ. J* **2018,** *24*, 11717-11728.

70. Szalóki, G.; Alévêque, O.; Pozzo, J.-L.; Hadji, R.; Levillain, E.; Sanguinet, L., Indolinooxazolidine: A Versatile Switchable Unit. *J. Phys. Chem. B* **2015,** *119*, 307-315.

Chapter 5

Magnetic Exchange Interaction in Nitronyl Nitroxide Radical Based Single Crystals of 3*d* Metal Complexes: A Combined Experimental and Theoretical Study

Abstract:

Four metal–organic complexes, such as Co(hfac)$_2$(NNPhOMe)$_2$; **1**, Co(hfac)$_2$(NNT)$_2$.(H$_2$O); **2**, Mn(hfac)$_2$(NNPhOMe)·x(C$_7$H$_{16}$); **3** and, Mn(hfac)$_2$(NNT)$_2$; **4** are successfully synthesized using two stable nitronyl nitroxide radicals and two metal ions in the form of M(hfac)$_2$, (where M = Co or Mn, hfac: hexafluoroacetylacetone). These complexes are investigated by single crystal x–ray diffraction, dc magnetization, infrared (IR) and electron paramagnetic resonance (EPR) spectroscopies. In addition, magnetic exchange interactions (J/K_B) are derived using isotropic spin Hamiltonian $H = -2J\Sigma(S_{metal}S_{radical})$ for the model fitting to the magnetic susceptibility data for **1**, **2, 3,** and **4**. The exchange interaction strengths found to be –328, –1.25, –248, and –256 K, for the **1, 2, 3,** and **4** metal–organic complexes, respectively. Quantum chemical density functional theory (DFT) computations carried out on several models of the metal–radical complexes in order to elucidate the magnetic interactions at molecular level. The calculations show that a small part of the inorganic spins are delocalized over the oxygen's from hfac {~0.03 for Co(II) and ~0.015 for Mn(II)}, while a more significant fraction {~0.24 for Mn(II) and ~0.13 for Co(II)} of delocalized spins from the metal ion is transferred to the coordinated oxygen atom(s) of nitronyl nitroxide.

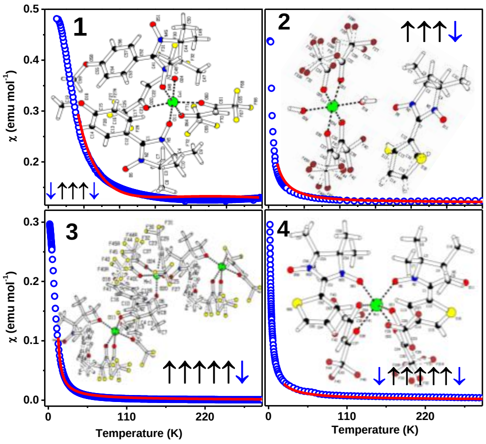

Note: Large parts of this chapter have been published in collaboration with Pramod Bhatt at *ACS Omega*, **2018**, *3*, 2918–2933.

5.1 Introduction

The synthesis of "metal–radical" coordination complexes are one of the successful methods for magnetic materials, those molecules are synthesized by organic radical reacted with spin active transition metal ions.[1] The benefit of the metal–radical" coordination complexes is that it could produce a variety of molecular structures with different magnetic dimensionalities and with unusual magnetic properties. The nitroxide radicals interact with metal ion and form metal–radical coordination complexes, the possible mode of the interactions between the magnetic orbitals of a nitroxide radical and a metal ion are given in the figure 5.1.

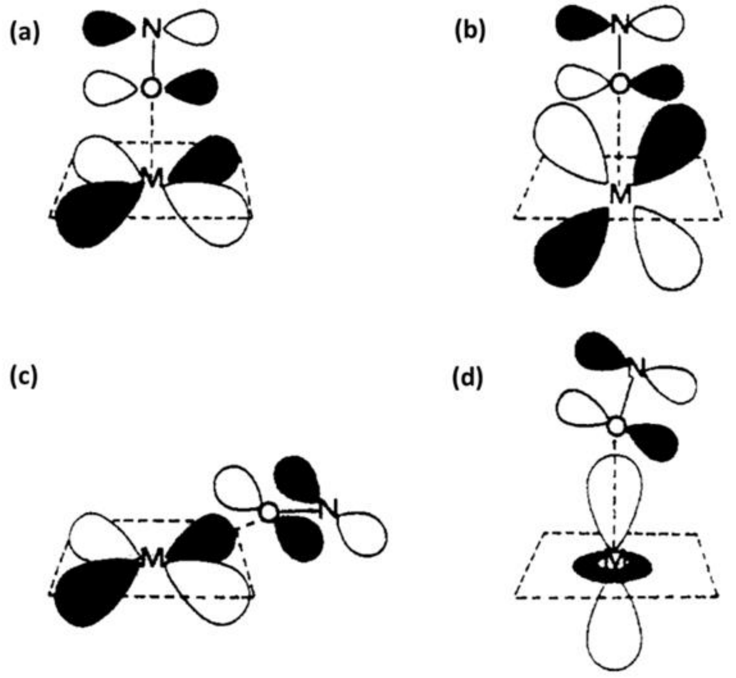

Figure 5.1: Schematic diagram of possible interactions between the magnetic orbitals of a nitroxide and a metal ion.

The magnetic interactions between metal and radical in coordination complexes are rationalized by the degree of overlap or orthogonality of the spin–active orbitals of the organic radicals with those of the metals ions. If the nitroxide radicals bind through its oxygen atom to paramagnetic metal ion two main cases can occur, in case (i), the spins orient preferentially parallel to each other resulting in ferromagnetic coupling. In case (ii) the spins orient antiparallel to each other and the results formation of a strong coordination bond, which are completely pairs the spins; otherwise, if the intensities of different total spin multiplicity are thermally populated results formation of an ferromagnetic coupled system. Moreover, most of the mono nitroxide radical only form the mononuclear complexes. The molecular chain of the metal–radical complexes are more interest than the mononuclear complexes. For example, *t–butyl* nitroxide ligands can interact with only one metal ion at a time and cannot form extended magnetic architectures. Therefore, two or more radical units are necessary in the same molecule to form chain. The nitroxide approach was numerously applied by Katsua Innoue and hiizu Iwamura for bi and triradical networks with Mn(hfac)$_2$, those are reviewed.[1,2]

The nitronyl nitroxide– and imino–nitroxide based radicals have received much attention as building block for molecular magnetic materials.[2] The nitronyl and imino–nitroxide is a stable free radical which offers many advantages.[3] These nitronyl nitroxide– and imino–nitroxide contain molecules form a molecular chain with even one radical unit in the molecules. The first chain complex of the was nitroxide–nitroxide was introduced by Gatteschi and Paul Rey in 1989.[1]

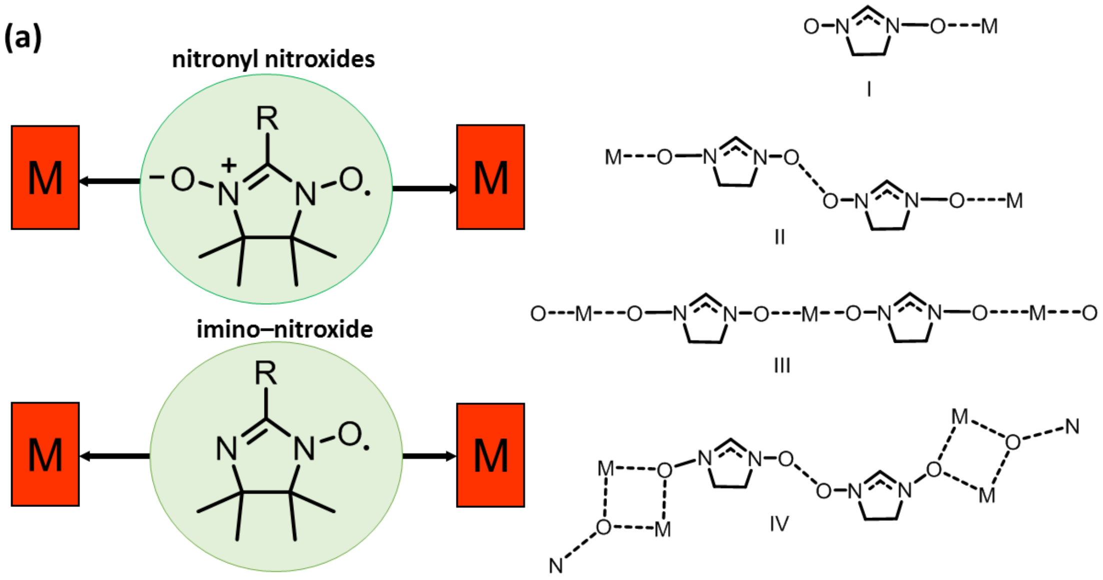

Figure 5.2: Typical coordination models of nitronyl nitroxide and metal ions.

The nitronyl–nitroxide radical can act as a bridging ligand with a spin center. It has one unpaired electron delocalized over the coordinating two oxygen atoms and antibonding π* orbitals in the plane of O–N–C–N–O while in imino–nitroxide radicals, oxygen and nitrogen atoms are coordinating (N−C−N−O) to the metal ions (figure 5.2.a). In addition, further advantages of the nitronyl–nitroxide radical can coordinate to suitable metal ions as a bis–monodentate bridging ligand or as a monodentate ligand resulting in interesting hetero–spin systems *i.e.,* hybrid complexation of different metal ions with stable free radicals (figure 5.2.b).

However, the suitable choice of transition metal ions and ligands could be another important criterion to achieve the desired magnetic dimensionality. The nitronyl nitroxides, imino nitroxides bind with metal ions {metal (II) bis–hexafluoroacetylacetonate} form a chain (1–D),[4] layers (2–D),[5] and bulk networks (3–D). Very interestingly, a nitronyl nitroxides radical with different R groups coordinates to metal ions to form variety of the structures. Some of the coordination models of the metal ions and a nitronyl nitroxides are shown the figure 5.2.b.

In model **I**, one oxygen atom binds with one metal ion to form mononuclear complexes. In model **II**, one radical oxygen bounds with one metal, while the other oxygen interacts weakly with one another radical oxygen and forms magnetic chains. In models **III**, two oxygen atoms bind to two different metal ions and the results in formation of chains, these chains either antiferromagnetic or ferromagnetic, depend on the nature of the metal ions. In model **IV**, they bind with one oxygen atom to two different metals ions, and each metal ion is bound to two radicals, with four spins arranged at vertices of diamond. The second oxygen atom then interacts with the oxygen atom of another radical, thus forming antiferromagnetic chains.

Moreover, by tailoring the intermolecular spin–spin interaction of the nitronyl nitroxide radicals (varying intermolecular arrangements), the magnetic exchange between the magnetic orbital of the transition metal and that of the coordinating nitronyl nitroxide radical can be rationalized. Such a control can be effectuated by varying the molecular fragment (*R*) to which the nitronyl nitroxide radical is attached. Moreover, the properties of the *R*–group (*R* may stand for ancillary functional group) linked to the nitronyl nitroxide ligands not only influence the intermolecular spin–spin interactions but also affect the coordination mode of the nitronyl nitroxides with metal ions, thus resulting in change of the magnetic properties of the metal–

radical complexes. In addition, a slight modification in the synthesis processes could also result in a different dimensionality of the crystal structures and, hence, of the magnetic properties.

The large amount of work on such compounds has been carried out in the past by the group of Gatteschi and his coworkers.[6-12]The various networks using 3*d* metal ions as cobalt (II), nickel (II), manganese (II), copper (II) etc. with nitronyl nitroxide radicals have been extensively studied. Apart from the 3*d* metal ions, many other rare earth/4f/5f based metal ions have also been investigated for structural and magnetic properties.[13-21] The qualitative and quantitative analysis of the magnetic properties in terms of magnetic interactions has also been investigated using inelastic neutron scattering, by EPR (Electron Paramagnetic Resonance) spectroscopy and magnetization measurements. The useful information on the nature of the exchange interaction and anisotropy, particularly, in the case of one–dimensional cobalt (II), based chain compound, had been estimated for designing new molecular magnetic materials with higher blocking temperatures. The exchange interactions between the nitronyl nitroxide radical and Cu metal ions have been extensible investigated by Fedin and coworkers using temperature dependent EPR (Electron Paramagnetic Resonance) for $Cu(hfac)_2L^R$ compound.[22-27] The results could explain the possible models for phase transitions in complexes $Cu(hfac)_2L^R$ on the molecular level. In this regard, various nitronyl nitroxide (NN) based metal complexes with different coordination species as pyridyl, bipyridyl, 2-(4-quinolyl) nitronyl nitroxide, *etc.* have been previously obtained. For example, four metal–radical complexes based on NNpPy{2-(4-pyridyl)-4,4,5,5-tetramethyl-4,5-dihydro-1H-imidazolyl-1-oxyl-3-oxide} have recently been synthesized with weak antiferromagnetic or ferromagnetic interactions and J/K_B in the range of 9.7 K to –0.32 K.[28] Similarly, metal complexation reactions of N-t-butyl-N-oxidanyl-2-amino (nitronyl nitroxide) diradical with $M(hfac)_2$ (M = Mn or Cu and hfac = hexafluoroacetylacetone) have lately been reported with a strong antiferromagnetic interaction ($J/K_B = -217$ K) between the Mn(II) spin (S = 5/2) and the diradical ($S = 1$).[29] A metal-radical complex using 2,6-NNPy {2,6-bis(3′-oxide-1′-oxyl-4′,4′,5′,5′-tetramethylimidazolin-2′-yl) pyridine} coordinated to Cu (II) has been synthesized.[30]

Ferromagnetic interaction between the axial radical and the copper center ($J_{\text{Cu-rad}}/K_B$ ~ 10 K) has been observed, whereas strong antiferromagnetic coupling ($J_{\text{Cu-rad}}$ ~ –460 K) between this metal ion and the equatorial nitroxide groups has taken place.[30] Similarly, the metal complexes made using 2-(4-quinolyl) nitronyl nitroxide (4-QNNN) and $M(\text{hfac})_2$ [M = Mn(II), Co(II), and Cu(II)] exhibit a 1-D alternating chain in which metal and radical are antiferromagnetically coupled, with magnetic exchange constant of $J/K_B = -1.2$ K.[31] Not only 3*d* metal complexes have been synthesized, a series of heterospin complexes based on lanthanides and pyridine biradicals have also been prepared. Some of them are found to show antiferromagnetic interactions between the paramagnetic ions {Ln(III) and radicals}, whereas some other compounds demonstrate ferromagnetic coupling.[32] One example of nitronyl nitroxide free radical 2-(2-pyridyl)-4,4,5,5-tetramethyl-4,5-dihydro1H-imidazolyl-1-oxy-3-oxide (NN2Py) complexed with Tb has a slow relaxation of magnetization at low temperature exhibiting a single molecule magnetic behavior.[33] However, detailed studies in terms of experimental and theoretical investigations of magnetic properties of such metal complexes are limited. Moreover, it is very interesting and desirable to understand their magnetic properties by varying their spin characteristics in such metal complexes.

In this chapter, we report synthesis of two nitronyl nitroxide radicals {**R^1** = 2-(4'-methoxyphenyl)-4,4,5,5,-tetramethylimidazoline-1-oxyl-3–oxide (NNPhOMe), and **R^2** = 2-(3-Thienyl)-4,4,5,5-tetramethylimidazoline 3-oxide 1-oxyl (NNT)} and their four metal complexes. The crystal structures and magnetic properties of the all the metal complexes were studied. The theoretical analysis of magnetic properties using DFT, quantum chemistry, thermodynamic calculations *etc.* are commonly used for calculating the exchange interactions and exchange coupling constant.[34-41] Different computational methods have been used to elucidate the mechanism of spin–spin interaction, the magnitude of effective exchange integrals, and the nature of the participating spin–active MOs.[37, 38] The influence of the used basis set was emphasized in some of the works. The model systems were excerpts from various experimentally obtained nitronyl–nitroxide based complexes with transition metal ions, which contained or did not contain unpaired electrons. In relation to the applicability of DFT to assess the magnetic interactions in the studied complexes, this is still one of the most widely applied computational techniques.[42, 43] However, it may not be the most accurate one but when it is carefully applied DFT should provide a good balance in the description of both the inorganic and the organic spin. An additional reason to use this approach is that it enables simulating larger model systems. In our case, the mechanism of spin–spin interaction depends essentially on the spin polarization along the entire organic radical and, hence, DFT is computationally more feasible than, for example, CASSCF based methods. Therefore, density functional calculations on model units of the complexes was used to supplement the experimental results with microscopic insight into the magnetic exchange interactions, namely, the relative stability of the spin states is explained with spin density distribution and delocalization over the organic radicals and with the overlap present in the singly occupied molecular orbitals (SOMOs).

Results and discussion

5.2 Synthesis of radicals and metal complexes

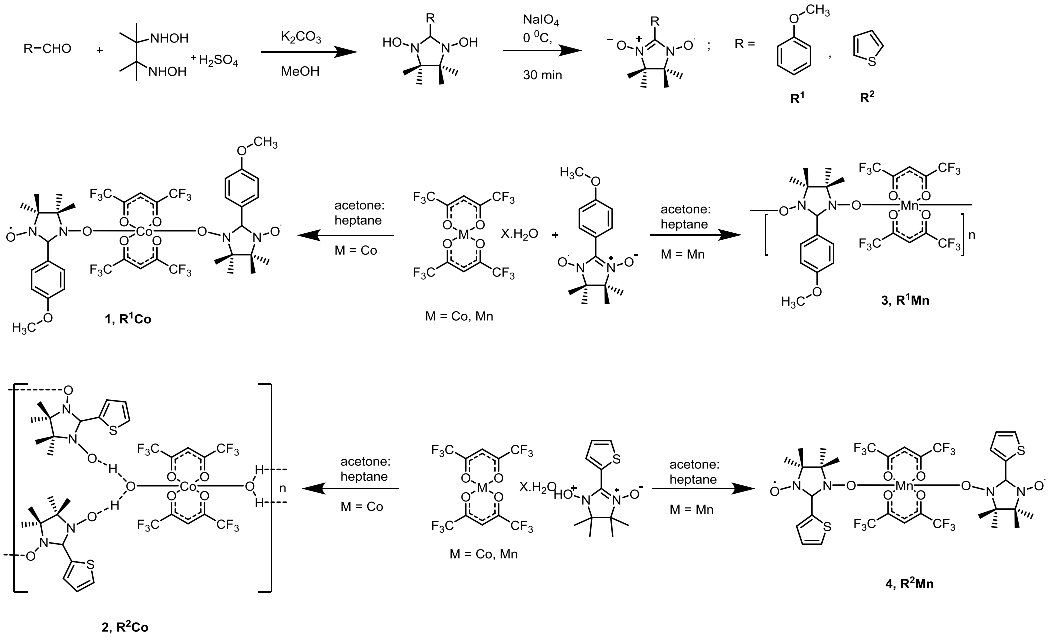

Scheme 5.1: General representations of the chemical reactions carried out for the synthesis of the organic radicals **R¹**, **R²** and their metal complexes **1, 2, 3,** and **4**.

Two nitronyl nitroxide radicals (***R***^{1} and ***R***^{2}) were synthesized by condensation of 3-bis (hydroxyamino)-2,3-dimethylbutane.H_2SO_4 (BHA.H_2SO_4) with the corresponding aldehydes and subsequent oxidation of the condensation product (N, N'-dihydroxy imidazoline) with sodium periodate in a biphasic medium, following the method described by Ullman condensation.[44] Subsequently, four metal–radical complexes were obtained using these two radicals as shown in scheme 5.I.

5.3 Crystal structure analysis

The x–ray crystallographic analysis revealed that the metal–radical complex **1** crystallizes in the triclinic crystal system with *P*–1 space group and Z = 2, as shown in figure 5.3.

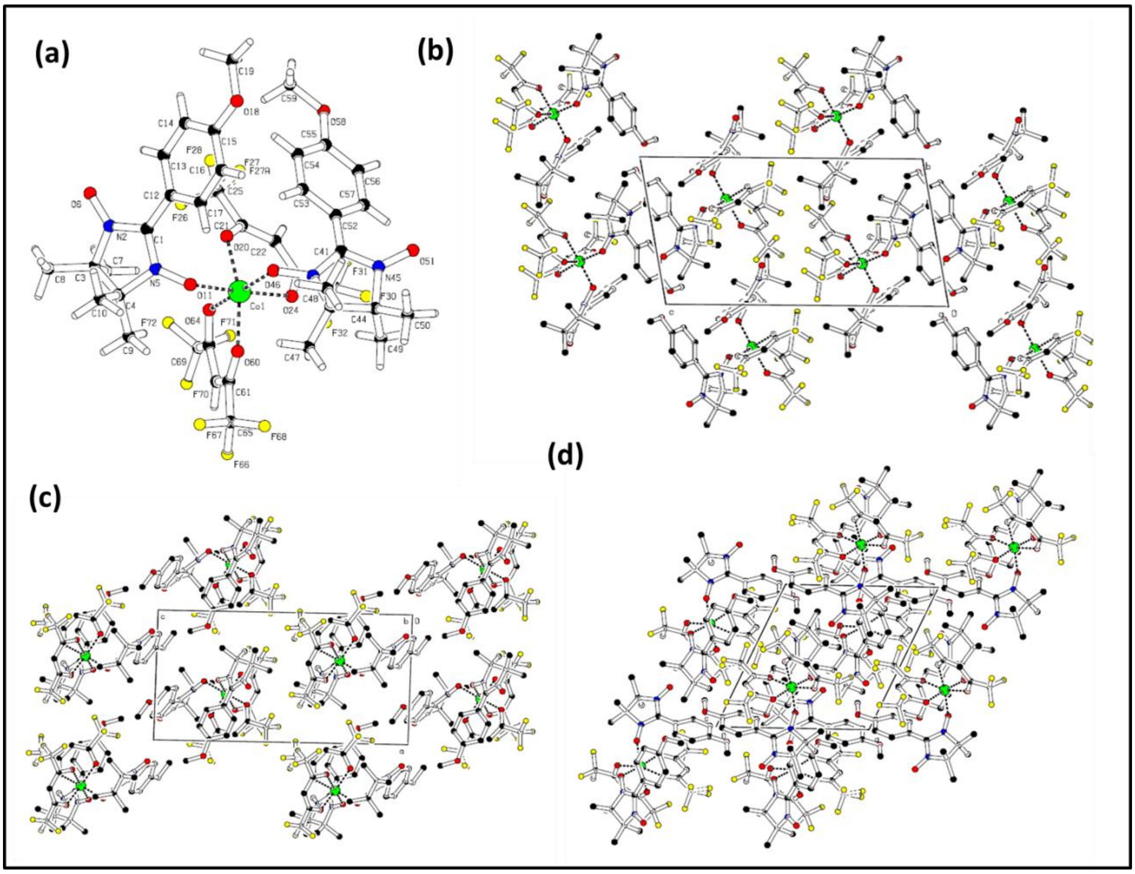

Figure 5.3: Crystal structure of the metal complex **1**. The single unit of the compound is shown in figure (a) and intermolecular arrangement for compound **1** along different viewing directions is in figures (b), (c), and (d). Hydrogen atoms are omitted for clarity of presentation.

The Co(II) is coordinated to two oxygen atoms (O11 and O46) of the two nitronyl nitroxide radicals and to four oxygen atoms (O20, O24, O60, and O64) of the auxiliary compound (hfac) molecule forming a distorted octahedral structure. The bond distances between the Co and two O atoms of the radicals are found to be different. The longer Co(1)–O(11) distance is found to be ~2.1082(15) Å whereas the shorter distance Co(1)–O(46) is found to be ~2.0527(14)Å.

Table 5.1: Crystallographic and structure refinement data for single crystals of compounds **1**, **2**, **3,** and **4**.

	1	**2**	**3**	**4**
Crystal size (mm^3)& color	0.19 × 0.22 × 0.30 Brown Block	0.03 × 0.07 × 0.42 Blue Needle	0.03 × 0.06 × 0.86 Blue Needle	0.11 × 0.18 × 0.57 Green Needle
Formula	$C_{38}H_{40}CoF_{12}N_4O_{10}$	$C_{32}H_{32}CoF_{12}O_8N_4S_2 \cdot 2H_2O$	$C_{24}H_{21}F_{12}MnN_2O_7.x(C_7H_{16})$	$C_{32}H_{32}F_{12}MnN_4O_8S_2$
Crystal system	Triclinic	Monoclinic	Monoclinic	Triclinic
Space group	P-1	P2$_1$/c	C 2/c	P-1
μ (mm^{-1})	0.51	0.791	0.481	0.54
T (̊C)	-80	-80	-80	-80
λ (Å)Mo-K$_\alpha$	0.71073	0.71073	0.71073	0.71073
Refinement Method	Full-matrix least square on F	Full-matrix least square on F	Full-matrix least square on F	Full-matrix least square on F
ρ (gcm^{-3})	1.553	1.721	1.418	1.554
a(Å)	10.8399 (5)	11.3018(4)	26.897(13)	12.2023(9)
b (Å)	11.4231 (6)	24.0068(6)	13.7633(5)	12.2478(8)
c(Å)	19.5609 (10)	11.1192(4)	23.0669(11)	15.0197(10)
α (deg.)	78.030 (4)			80.745(5)
β (deg.)	84.066 (4)	106.831(3)	125.030(3)	67.214(5)
γ (deg.)	64.434 (4)			79.499(6)
V (Å^3)	2137.21 (19)	2887.63(17)	6992.4(5)	2024.7(2)
Z	2	4	8	2
F(000)	1022	1504	3010	962
θ range (deg.)	2 to 28	2 to 28	2 to 28	2 to 28
Index ranges	-14≤h≤14 -15≤k≤15 -25≤l≤23	-15≤h≤15 -29≤k≤31 -11≤l≤14	-35≤h≤35 -17≤k≤18 -30≤l≤30	-16≤h≤16 -16≤k≤16 -19≤l≤19
Goodness of Fit on F^2	1.032	0.907	1.028	1.054
R$_{int}$	0.0291	0.0343	0.0327	0.0207
Reflections measured /unique	19665/10296	19303/7111	20051/8574	19573/9918
R^{1a}, wR^2	0.0655, 0.1208	0.0736, 0.1238	0.1193,0.2715	0.0606, 0.1524

[a] $R^1 = \sum(||F_0|-|F_C||)/\sum|F_0|$. $wR^2 = [\sum w(|F_0|^2-|F_C|^2|)^2/\sum w(F_0^2)^2]^{1/2}$

These bond lengths are comparable to the reported cobalt(II) nitronyl nitroxide complexes. The bond angles O(60)–Co(1)–O(20), O(46)–Co(1)–O(64), and O(24)–Co(1)–O(11) are found to be ~163.29(6), 173.77(6) and 173.80(6) deg., respectively. The results from the XRD measurements are given in table 5.1 and characteristic bond lengths and bond angles of the complexes are summarized in table 5.2.

Table 5.2: Bond lengths and bond angles of the metal–radical complexes obtained from the XRD study.

	Bond Length (Å)		Bond angle (deg.)	
1	Co(1)-O(60)	2.0267(15)	O(60)-Co(1)-O(20)	163.29(6)
	Co(1)-O(20)	2.0409(15)	O(60)-Co(1)-O(46)	98.48(6)
	Co(1)-O(46)	2.0527(14)	O(20)-Co(1)-O(46)	97.06(6)
	Co(1)-O(24)	2.0684(15)	O(64)-Co(1)-O(11)	101.31(6)
	Co(1)-O(64)	2.1045(15)	O(24)-Co(1)-O(11)	173.80(6)
	Co(1)-O(11)	2.1082(15)	O(46)-Co(1)-O(64)	173.77(6)
2	Co(1)-O(34)	2.0438(18)	O(34)-Co(1)-O(25)	178.30(7)
	Co(1)-O(25)	2.0448(17)	O(21)-Co(1)-O(38)	174.46(8)
	Co(1)-O(21)	2.0517(17)	O(2W)-Co(1)-O(1W)	178.15(8)
	Co(1)-O(38)	2.0577(18)	O(25)-Co(1)-O(21)	90.86(7)
	Co(1)-O(2W)	2.0954(19)	O(25)-Co(1)-O(2W)	92.37(7)
	Co(1)-O(1W)	2.096(2)	O(34)-Co(1)-O(38)	90.12(7)
3	Mn(1)-O(11)	2.106(3)	O(11)-Mn(1)-O(34)	166.02(12)
	Mn(1)-O(6)	2.126(3)	O(6)-Mn(1)-O(38)	106.78(12)
	Mn(1)-O(34)	2.148(3)	O(11)-Mn(1)-O(20)	106.48(11)
	Mn(1)-O(38)	2.151(3)	O(38)-Mn(1)-O(20)	156.29(11)
	Mn(1)-O(20)	2.158(3)	O(6)-Mn(1)-O(24)	169.54(12)
	Mn(1)-O(24)	2.165(3)	O(6)-Mn(1)-O(20)	92.32(12)
4	Mn(1)-O(6)	2.1259(16)	O(6)-Mn(1)-O(21)	101.15(7)
	Mn(1)-O(21)	2.1279(16)	O(21)-Mn(1)-O(34)	168.88(6)
	Mn(1)-O(34)	2.1293(16)	O(61)-Mn(1)-O(25)	169.48(6)
	Mn(1)-O(61)	2.1298(15)	O(6)-Mn(1)-O(38)	168.79(6)
	Mn(1)-O(25)	2.1734(17)	O(61)-Mn(1)-O(38)	96.30(7)
	Mn(1)-O(38)	2.1794(17)	O(25)-Mn(1)-O(38)	82.82(7)

The metal–radical complex **2** crystallizes in the monoclinic symmetry with space group *P*2_1/c and Z = 4 (figure 5.4). It is interesting to note that the Co metal ion is not coordinated to the nitronyl nitroxide ligand in complex **2** as metal and ligands are separated to each other as shown in figure 5.5. However, Co(II) is connected to two oxygen atoms of the two water molecules and four oxygen atoms of the auxiliary compound (hfac) molecule forming a distorted octahedral structure. The distances between Co and Doubled water O atoms of the water molecule are found to be ~2.097 and 2.094 Å, respectively. The average bond length of Co–O is ~2.0 Å, whereas the bond angles O(34)–Co(1)–O(25) and O(21)–Co(1)–O(38) are found to be ~178.29(7) and 174.48(9) deg., respectively. Since, Co(II) ion is six–coordinated by four oxygen atoms from two hfac ions and two oxygen atoms from two H_2O molecules, the Intermolecular hydrogen bonds are found in the crystal of complex **2**. The molecular arrangement of complex **2** is shown in figure. 5.4 (b, c and d). The hydrogen bonding interactions occur between two oxygen atoms from one coordinated water molecule and one uncoordinated nitronyl nitroxide. As a result, molecules are linked by weak interactions to form chain like structure as depicted in figure. 5.4.

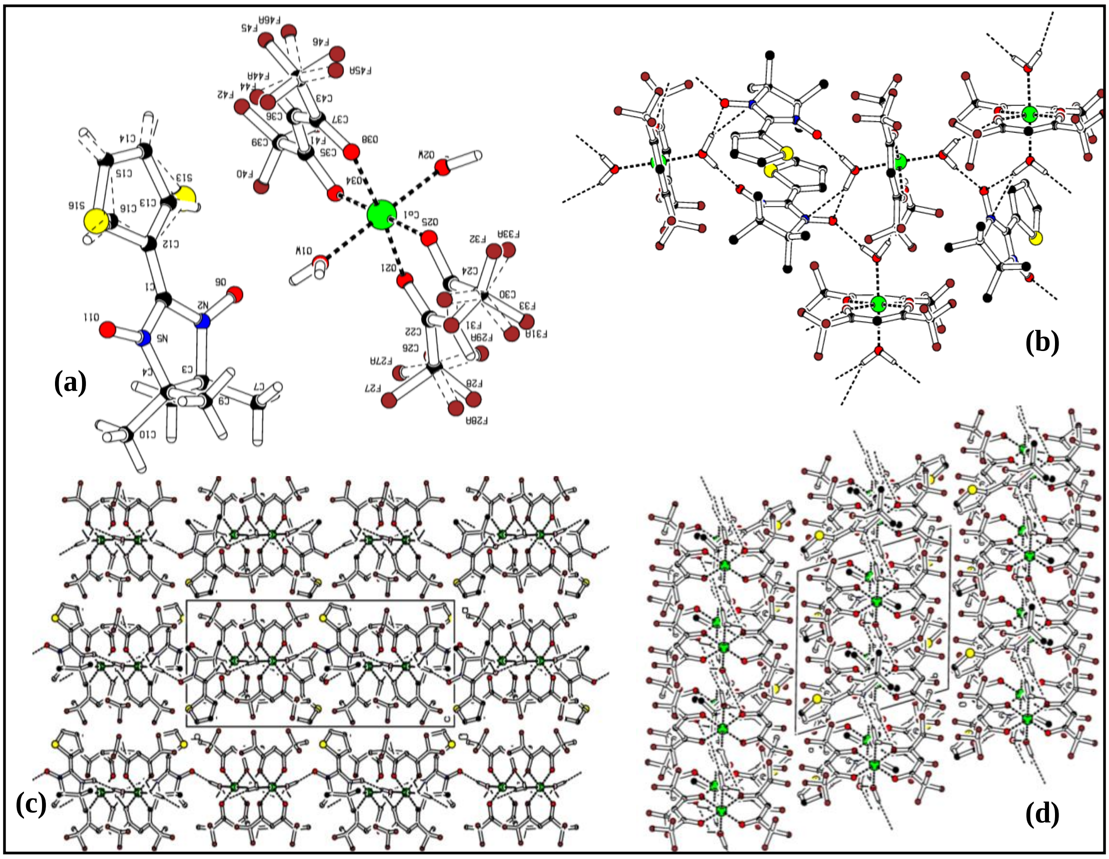

Figure 5.4: Crystal structure of single repeating unit of compound **2**. The interaction through water molecules form a chain like structure as shown along different viewing directions in figures b, c, and d. Hydrogen atoms are omitted for clarity of presenation.

The metal–radical complex **3** forms a linear chain–like structure (shown in figure 5.5), which crystallizes in the monoclinic crystal structure with space group C 2/c and Z = 8. The chain lies along the *C* axis, in which the Mn(II) metal ions are connected to two oxygen atoms of the two nitronyl nitroxide radicals and four oxygen atoms of the auxiliary compound (hfac) molecule in a distorted octahedral structure. The heptane molecule is also present in the crystal. The shortest intra– and inter–chain Mn–Mn distances are found to be ~12.05 and 26.13 Å, respectively. There are four chains per unit cell in the molecular packing. The average bond length of the Mn–O bond is ~2.1 Å. The bond angles O(11)–Mn(1)–O(34), O(38)–Mn(1)–O(20) and O(6)–Mn(1)–O(24) are found to be ~166.02(12), 156.29(11) and, 169.54(12) deg., respectively.

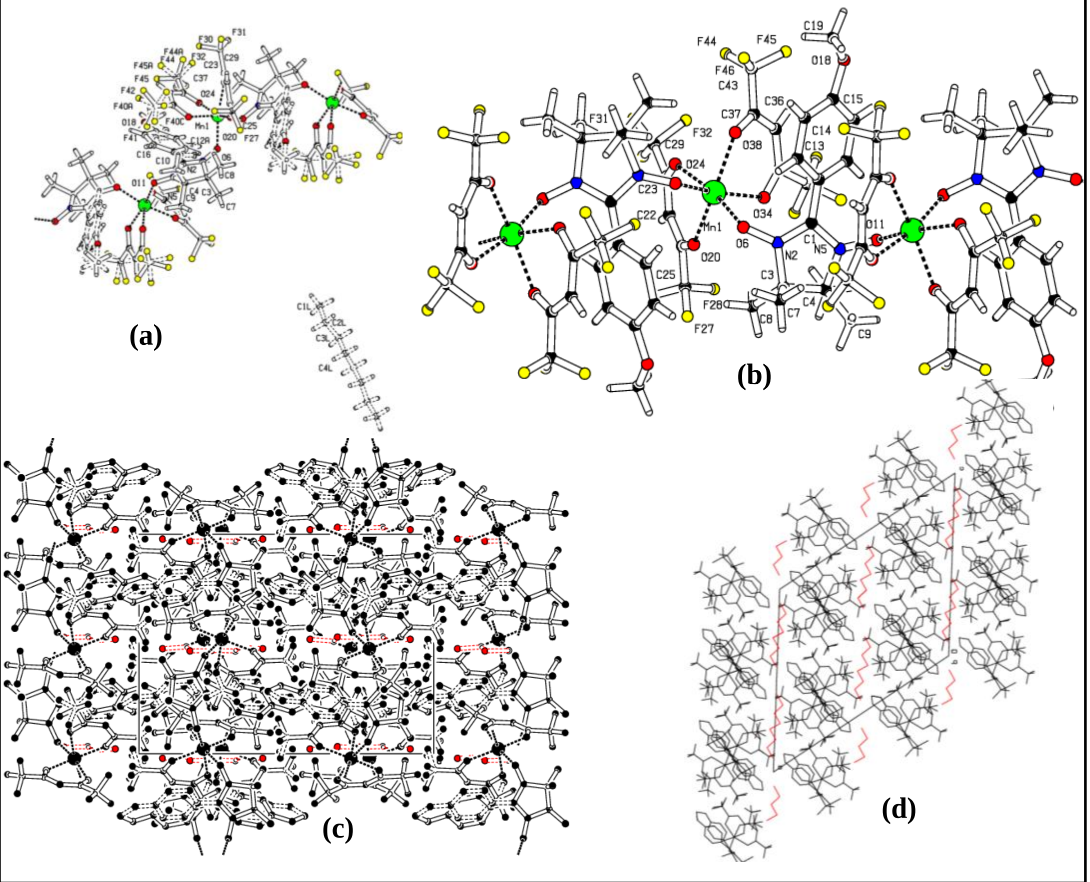

Figure 5.5: Molecular crystal structure of the metal complex **3**. The heptane molecule present in the compound is shown in (a). The formation of chain like structure using Mn atoms and radical are shown along different viewing directions in (b), (c) and (d). Hydrogen atoms are omitted for clarity of presenatation.

The metal-radical complex **4** crystallizes in the triclinic crystal structure with space group *P*-1 and Z=2 (figure 5.6). The Mn(II) metal ions are connected to two oxygen atoms of the two nitronyl nitroxide radicals and four oxygen atoms of the auxiliary compound (hfac) molecule in a distorted octahedral structure. The average bond length of the Mn-O bond is found to be ~2.100

Å. The average bond lengths of the bonds Mn(1)-O(6) and Mn(1)-O(61) are found to be ~2.125(16), and 2.129(15) Å, respectively. The bond angles O(6)-Mn(1)-O(21), O(21)-Mn(1)-O(34) and, O(61)-Mn(1)-O(25) are found to be ~101.15(7), 168.88(6), and 169.48(6) deg., respectively.

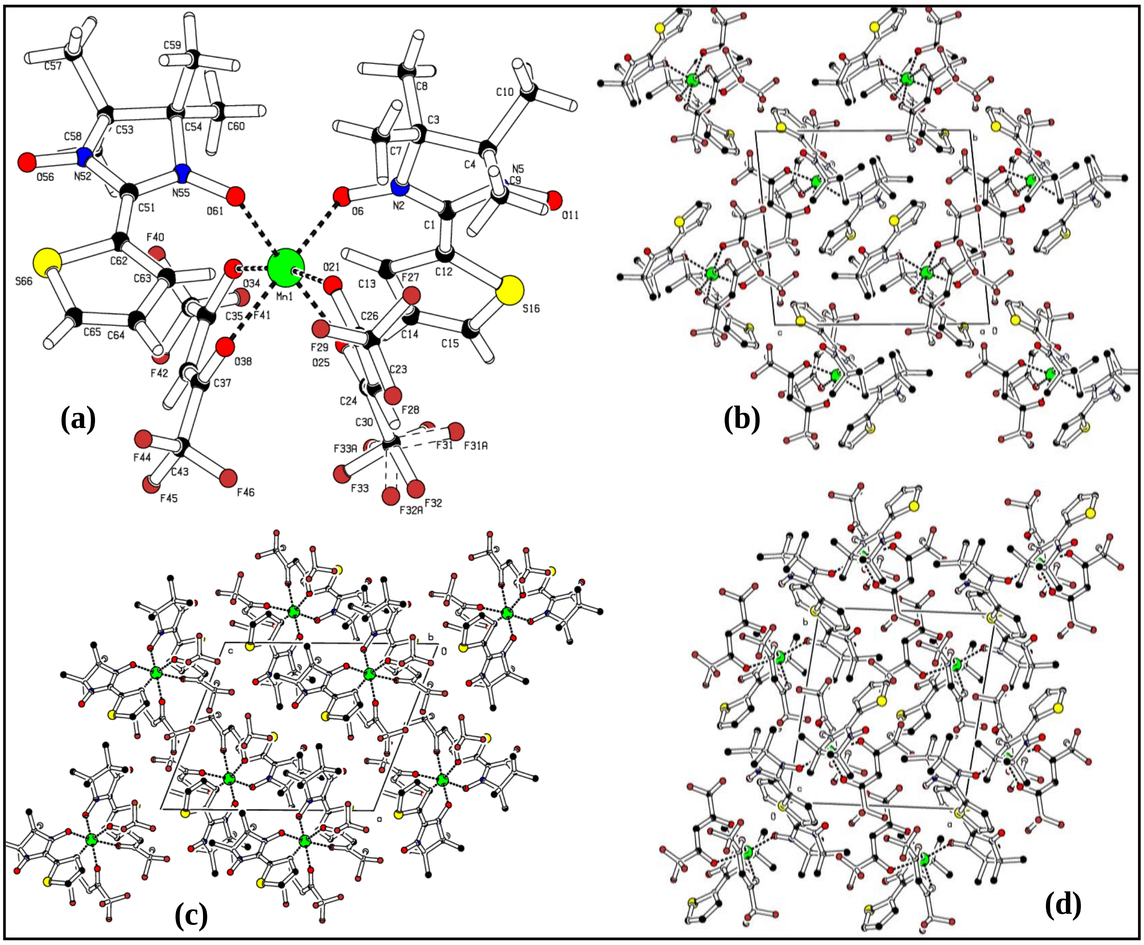

Figure 5.6: Crystal structure of the metal complex **4**. The single unit of the metal complex is shown in figure (a), whereas the formations of intermolecular structures are shown along different viewing directions in (b), (c) and (d). Hydrogen atoms are omvitted for clarity of presentation.

5.4 EPR (electron paramagnetic resonance) study

The X–band EPR spectra of the randomly oriented crystals of the metal complexes and radicals are shown in figure 5.7. The insets of figures 5.7.a. and b presented for the EPR spectra of the radicals $\boldsymbol{R}^1$ and $\boldsymbol{R}^2$, respectively. The radical $\boldsymbol{R}^1$ shows a single symmetric line at room temperature, with a peak-to-peak line width ΔBpp ~ 1.32 *mT*. The value of *g* can be calculated from ν (in GHz) and B_0 (in gauss) using the following equation:

$$g = \frac{h\vartheta}{\beta B_0} \qquad (5-1)$$

where *h* is Planck's constant, *β* is a conversion constant called the Bohr magneton, υ is frequency and B_0 is magnetic field. The measured average g-value is ~2.0065 for ***R*^{1}**. A single asymmetric line at room temperature, with a peak–to–peak line width ΔBpp ~ 1.81 mT is observed for the complex **1** at room temperature. It is therefore evident that after the synthesis of metal radical complexes, the peak–to–peak line width *ΔBpp* increases.

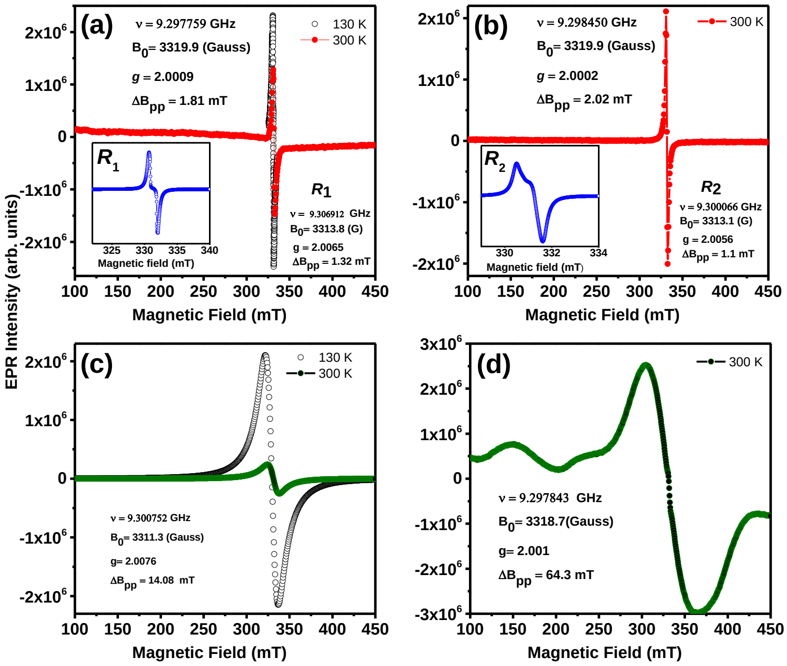

Figure 5.7: EPR spectra of randomly oriented single crystals of radicals and metal complexes **1** (a) at 300 and 130 K, **2** (b) at 300 K, **3** (c) at 300 and 130 K, and **4** (d) at 300 K. The inset of figure (a) and (b) shows the EPR spectra of the radicals **R_1** and **R_2**, respectively.

The measured average g–value is found to be ~2.0009 and ~2.0002 for **1**, and **2**, respectively. In the case of **3** metal complex, a broad and asymmetric single line is observed with a peak–to–peak line width *ΔBpp* ~14.08 mT. The *g*–value is found to be ~2.0076 for the **3** compound. However, *g*–value is found to be ~2.001 for the compound **4** along with a broad line with a peak–to–peak line width ΔB_{pp} ~64.3 mT. Since, room temperature EPR measurements sometimes not enough to fully characterize transition metal complexes, where *e.g.* for cobalt high spin d^7 (*S*=3/2), usually the relaxation times are much too fast to see the cobalt response. Even EPR data at 130 K {figures 5.7. (a) and (c)} does only show signal from the radical not metal ions.

Very low temperature (≈ 4 K) is needed to get the signals of metal (CoII) ion for high spin fast relaxation. Thus, we mainly see the free radical contribution and would need helium temperatures to find cobalt resonances. This also leads to the large difference of reported *g*–value and the one used to fit the magnetic measurements for the cobalt cases, for example, in magnetic Mn and Co complexes with a large polycyclic aromatic substituted nitronyl nitroxide [45]. Next, while discrete complexes in dilute matrix (c = $10^{-3}M$ solvent liquid or frozen) more precise characterization can sometimes be made, in concentrated solid state with neighboring spin carrying units such spectra are rarely to be analyzed, since too many effects contribute. For **3,** which gives, a broadened line can only be explained with radical Mn interaction and not only from the radical. Even more for **4**, another signal at nearly half field (160 *mT*) provides a g≈4 value.

5.5 IR (infra–red) spectra study

The IR spectra of the radicals **R^1** and **R^2** and their respective metal complexes are shown in figure 5.8. The vibrational spectra of the nitroxides are not much exploited, thus the exact group frequency of the N–O$^\bullet$ bond is not very well known.[46] Moreover, the earlier reported group frequencies of the N–O$^\bullet$ stretching vibration, ν(N–O$^\bullet$), have large variations which state that ν(N–O$^\bullet$) lies near 1350 cm^{-1} (l380 –1310 cm^{-1}),[46, 47] between 1380 –1340 cm^{-1} [48], or 1370 – 1340 cm^{-1} or 1380 –1339 cm^{-1}. In the present case, the radicals show strong signals at 1351 cm^{-1} and 1365 cm^{-1} for the **R^1** and **R^2** radicals, respectively. These are arise from the ν(N–O•) stretching of the nitronyl nitroxide moiety conforming the formation of nitronyl nitroxide radicals. Other more intense lines are observed at 1025, 1126, 1253, 1299 and 1604 cm^{-1} for the radical **R^1**. Similarly, intense lines at 1041, 1079, 1132, 1172, 1326, 1398, 1450, and 1548 cm^{-1} are observed for **R^2**. In the metal complexes, the ν(N–O•) stretching frequencies are found to shift for all compounds. This is expected since the metal ion coordinate to nitroxide group directly in the complexes except **2** where nitroxide group form H–bond with water molecules. As a result, the N–O• bond weakens and the vibrational peak appears at lower wave number. However, the frequencies ~1600 cm^{-1}

and ~1548 cm^{-1} of the radical **R^1** and **R^2** respectively shifts to higher values after formation of the metal complexes.

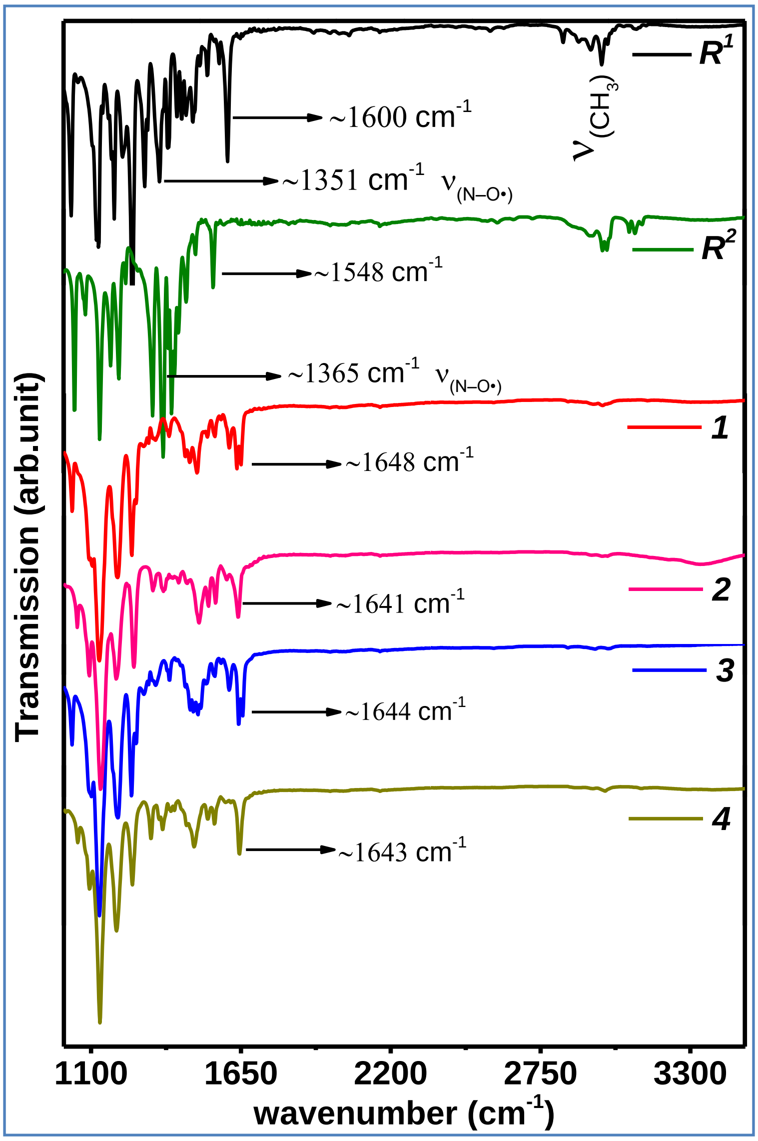

Figure 5.8: The FT–IR spectra of the radicals (**R^1** and **R^2**) and their metal complexes (**1, 2, 3**, and **4**).

5.6 Magnetic properties

Figure 5.9(a and b) shows the temperature dependence of the molar magnetic susceptibility under magnetic field of 1000 Oe for the metal complexes **1** and **2**, respectively. The temperature–dependent magnetic susceptibility was measured by Pramod Bhatt and Gerhard Jakob at the University of Mainz in the range of 5–300 K and the plot of χ versus T is provided in figure. 5.9(a) for **1**. The room temperature value of χT for complex **1** and **2** was found to be ~2.68 and ~ 2.86 emu·K·mol^{-1} respectively, which is above from the theoretically expected value (~2.625 emu·K·mol^{-1}) of χT for high spin Co(II). The higher value of χT than the expected value for a system of one cobalt (II) ion (S = 3/2) and two radicals (S = 1/2), is due to the orbital contribution of the cobalt (II) ion.

In the temperature range ~50–300 K (paramagnetic region), the susceptibility can be fitted by a straight line (shown in the inset of both figures) using the Curie–Weiss law

$$\chi = \frac{\mathrm{C}}{T-\theta_{\mathrm{p}}} \qquad (5-2)$$

where, C is the Curie constant and θ_{p} is the paramagnetic Curie temperature. The values of θ_{p} are found to be –7 and –12 K for the **1** and **2**, respectively.

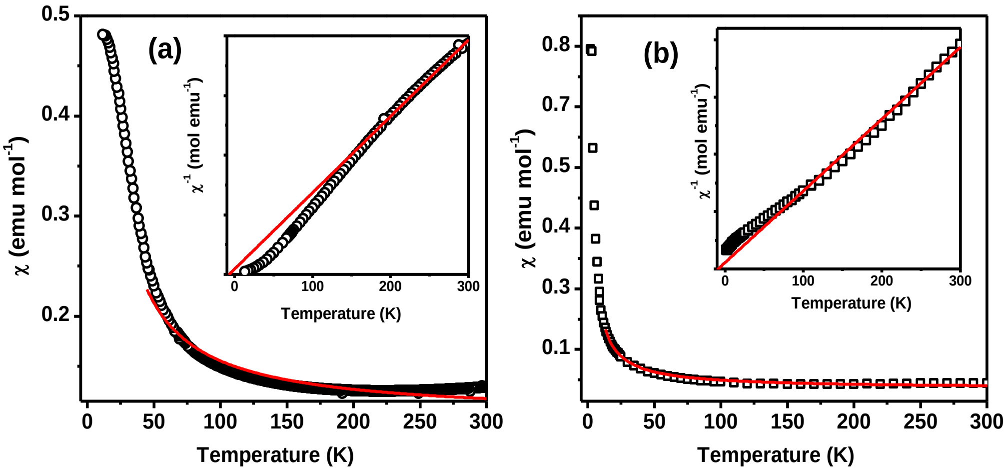

Figure 5.9: Temperature dependent molar magnetic susceptibility of randomly oriented crystals of **1** (a) and **2** (b) under magnetic field of 1000 Oe. The red lines show the fit of the magnetic data using the equation 4 given in the text for **1** and **2** metal complexes. The inset shows the Curie–Weiss law fitting of the inverse of the magnetic susceptibility data with respect to temperature using equation 5–2.

The experimentally observed effective paramagnetic moments, μ_{eff} are found to be ~ 4.41 μ_B/f.u. for **1**. These values are derived using the formula $\mu_{eff} = (3CK_B/N_A)^{1/2}\mu_B \sim (8C)^{1/2}\mu_B$, where N_A is the Avogadro's number, and K_B is the Boltzmann constant. The experimentally observed value of μ_{eff} is consistent with the theoretically calculated spin only values (4.58 μ_B/f.u.) for **1**. The Co(II) *i.e.* S = 3/2, ions are assumed to be in their high spin states, in accordance with the EPR measurements. Here, the theoretically expected (spin only) value of μ_{eff} is calculated using the formula $(\mu_{\mathrm{eff}})^2 = \Sigma[g^2\{n.S(S+1)\}]\ \mu_B^2$, where g is the gyromagnetic ratio (~2), n is the number of magnetic ions with spin S in the formula unit, and the summation Σ runs over all magnetic ions in the formula unit.

In order to understand the exchange interaction between Co(II) and nitronyl nitroxide radicals in **1**, we have used a simple isotropic Hamiltonian model to fit the temperature dependent molar magnetic susceptibility data in the paramagnetic state from 300 to 50 K . As obtained from the x–ray diffraction data, there exists a direct bonding of a spin–bearing oxygen atom of nitronyl nitroxide radicals to Co(II) which would lead to a spin–spin interaction between the metal ions and the radicals. The magnetic data also suggest that the interaction is antiferromagnetic in nature. The Hamiltonian used for the model, fitted to the magnetization data of the metal–radical interactions looks like that:

$$H = -2J\Sigma(S_{Co}S_{rad}) - DS_z^2 \qquad (5-3)$$

Where, *J* represents the magnetic coupling for the Co–radical. *S* is the average value of projection of the total spin of the cluster on the z axis; D, is the zero–field splitting parameter of the Co(II) ion. Consider the above Hamiltonian, fitting the magnetic susceptibility[49, 50] data in the paramagnetic temperature range 300–30 K has been used for compound **1**.

$$\chi = \left(\frac{2Ng^2\beta^2}{kT}\right)\frac{\exp(A_1) + 4\exp(A_3) + 4\exp(A_5)}{2\exp(A_1) + \exp(A_2) + 2\exp(A_3) + \exp(A_4) + 2\exp(A_5)} \qquad (5-4)$$

$$A_1 = [4J + \frac{5D}{4} - (4J^2 - 2DJ + D^2)^{1/2}]/kT$$

$$A_2 = (2J + \frac{D}{4})/kT$$

$$A_3 = (6J + \frac{9D}{4})/kT$$

$$A_4 = (6J + \frac{D}{4})/kT$$

$$A_5 = [4J + \frac{5D}{4} + ((4J^2 - 2DJ + D^2)^{1/2})/kT$$

Where *J* stands for the exchange interaction between Co(II) and the nitronyl nitroxide radicals, *g* is Lande's constant, K_B is the Boltzmann constant, μ_β is the Bohr magneton, and N_A is Avogadro's number. The best fit parameters J/K_B = –328 K, and *g* = 2.02, D = –2.39 K with with $R = 1.57 \times 10^{-4}$, where R is defined as $R = \Sigma[(\chi_M)^{calc} - (\chi_M)^{expt}]^2/\Sigma[(\chi_M)^{expt}]^2$. The negative value of *J* indicates an antiferromagnetic coupling between an octahedral high spin Co(II) and coordinated nitronyl nitroxide radicals. The previously reported data on the nitronyl nitroxide based metal complexes using Co(hfac)$_2$ also indicates that the oxygen atoms of the radicals are strongly antiferromagnetically coupled to Co(II) ions.[51-53] Since, the bond lengths and bond angles are comparable to those of the previously reported compounds, the antifrromagnetic interaction between metal and radicals in the **1** dimer complex is verified and quantified.

The compound **2** is not coordinated to N–O unit of the radical, however, Co ion is coordinated through the hydrogen bonding of a water molecule (model shown below). The structural analysis of the compound allows us to select exchange interaction in the following way[54].

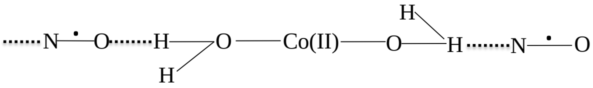

Where, each Co(II) ion interacts via OH groups of water molecules with N–O groups of two neighboring molecules. Irrespective of the method of selecting an exchange interaction, the theoretical description of its magnetic properties may be treated like a magnetic systems of Co(II) ion plus two nitroxide radicals[54] {Co(II) ion + two nitroxide radicals}. The strict analysis of the magnetic data of Co(II) complexes needs to consider the effects of spin–orbit coupling and zero–field splitting. A more elaborate model, taking into account all of these factors, may be constructed, but it will be then over parameterized. The Hamiltonian used in this case is therefore same as in the case of compound **1**. For compound **2,** the equation (5–4) has been used for fitting the magnetization data in the paramagnetic temperature range 300– 30 K. The best fit parameters J/K_B = –1.25 K, and g = 2.21, D = –0.31 K with R = 1.1× 10^{-4}, where R is defined as $R = \Sigma[(\chi_M)^{\mathrm{calc}} - (\chi_M)^{\mathrm{expt}}]^2/\Sigma[(\chi_M)^{\mathrm{expt}}]^2$.

Figure 5.10 (a and b) shows χ *vs T* curves for the metal complexes **3** and **4** respectively under the field of 1000 Oe. The compound **3** form a chain–like structure. The room temperature value of χ*T* for **3** is found to be ~4.98 emu·K·mol^{-1}, which is close to the theoretically expected value (~5.125 emu·K·mol^{-1}) of χ*T* for Mn(II). Similarly, χ*T* is found to be ~ 4.64 emu·K· mol^{-1}· Oe^{-1}

for the **4** compound, well in agreement with the theoretically expected value of χT ~ 5.125 emu·K·mol^{-1}· Oe^{-1} for the spins of Mn(II), S = 5/2, and two nitronyl nitroxide radicals of spins S = 1/2 at 300 K. The paramagnetic region is fitted by a straight line (shown in the inset of figure 5.10) using the Curie-Weiss law. The values of θ_p are found to be –16 and –9 K for the **3** and **4**, respectively.

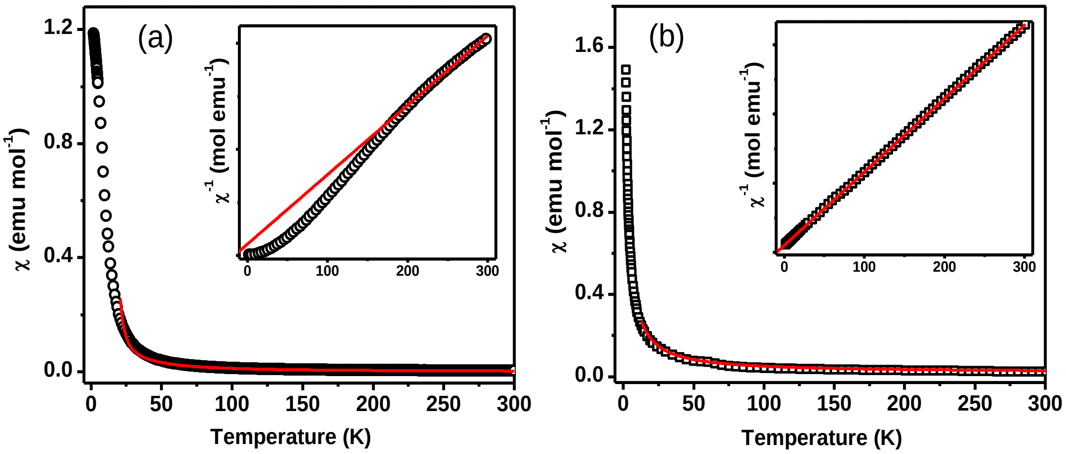

Figure 5.10: Temperature dependent magnetic susceptibility data of randomly oriented crystals of **3** (a) and **4** (b) under the magnetic field of 1000 Oe. The red line shows the fit of the magnetic susceptibility data in the temperature range of 300-20K using the equation 6 for compound **3** and equation 5–8 for compound **4** given in the text. The inset of figure shows the Curie–Weiss law fitting of the inverse of the magnetic susceptibility data with respect to temperature using equation 5–2.

The negative values of θ_p indicate that the interaction between metal ions and the organic radicals is antiferromagnetic in nature. The experimentally observed effective paramagnetic moments, μ_{eff} are found to be 6.37 μ_B/f.u. for **3**. The experimentally observed value of μ_{eff} is consistent with the theoretically calculated spin only values (6.40 μ_B/f.u.) of the compounds. The Mn(II) *i.e.* S = 5/2 ions are assumed to be in their high spin states.

For metal–complex **3**, the experimental susceptibility has been analyzed using the nearest–neighbor spin of the radical and the spin of Mn (II). The Hamiltonian is therefore defined for **3** as

$$H = -\,2J\Sigma(S_{Mn}S_{rad}) \qquad (5-5)$$

Where J is the exchange interaction between Mn(II) and the nitronyl nitroxide radicals.

Since, the x–ray diffraction provides chain–like structure for complex **3**, the exchange interaction between Mn(II) (S_{Mn} = 5/2) and the two nitronyl nitroxide radicals (S_{rad} = 1/2) in this chain–like structure has been calculated using the following susceptibility equation[55] to fit the magnetic susceptibility data.

$$\chi_{chain} = \frac{g^2}{4\,T}\left[\frac{4.75-1.62370\mathrm{X}+2.05042\mathrm{X}^2-4.52588\mathrm{X}^3-8.64256\mathrm{X}^4}{1+0.77968\mathrm{X}-1.56527\mathrm{X}^2-1.57333\mathrm{X}^3-0{:}11666\mathrm{X}^{4.5}}\right] \qquad (5-6)$$

Where x = $|J|/kT$

The best–fitted parameters are $J/\mathrm{K_B}$ = –248 K, g = 2.4, R = 1.17×10^{-4}.

Since, the compound **4** exhibit a three spin model, two nitronyl nitroxide radicals plus the Mn(II) ion, and the magnetic susceptibility data of the metal complex **4** analyzed using three spin Hamiltonian[56]

$$H = -2J\Sigma(S_{Mn}S_{rad1} + S_{Mn}S_{rad2}) \qquad (5-7)$$

The following equation derived for fitting of the magnetic susceptibility data[56, 57].

$$\chi = \left(\frac{\mathrm{N_A g^2 \mu_\beta^2}}{4\mathrm{k_B(T)}}\right)\frac{35+35\exp\left(\frac{-\mathrm{J}}{\mathrm{k_BT}}\right)+10\exp\left(\frac{-7\mathrm{J}}{\mathrm{k_BT}}\right)+84\exp\left(\frac{5\mathrm{J}}{2\mathrm{k_BT}}\right)}{3+3\exp\left(\frac{-\mathrm{J}}{\mathrm{k_BT}}\right)+2\exp\left(\frac{-7\mathrm{J}}{\mathrm{k_BT}}\right)+4\exp\left(\frac{5\mathrm{J}}{2\mathrm{k_BT}}\right)} \qquad (5-8)$$

Where J is the exchange interaction integral between Mn(II) and the nitronyl nitroxide radicals. The best-fit parameters are obtained with $2J/\mathrm{K_B}$ = –512 K ($J/\mathrm{K_B}$ = –256 K) and, g = 2.23, R = 1.08×10^{-4}.

The negative values of J indicate an antiferromagnetic coupling between an octahedral high spin of metal ions and coordinated nitronyl nitroxide radicals. The previously reported findings[31, 52, 58, 59] for similar metal–radical complexes also specify either antiferromagnetic or ferromagnetic type of interactions between the metal and nitronyl nitroxide radicals, depending on the nature of the radicals. Moreover, the reported values of magnetic exchange interactions are also in agreement with the present magnitude of J for the studied metal complexes. For example, Mn(hfac)$_2$ complexes with isoindoline nitroxide radical exhibit a ferrimagnetic nature of the compound with the value of J/K_B in the range of –162 to –214 K.[60] In another example, a ferrimagnetic chain–like structure has been observed involving Mn and nitronyl nitroxide radicals with J/K_B in the range of –329.8 to –208.2 K.[8] Similarly, Mn(hfac)$_2$ bridged [2–(3-pyridyl)(nitronyl nitoxide)–Mn(hfac)$_2$]$_2$ chain complex exhibits a large antiferromagnetic interaction of J/K_B = –185 K.[61]

In order to rationalize further the observed behavior of the four complexes, the magnetic exchange interactions for **1**, **2**, **3**, and **4** compounds are calculated theoretically and discussed.

5.7 Molecular models and computational protocol

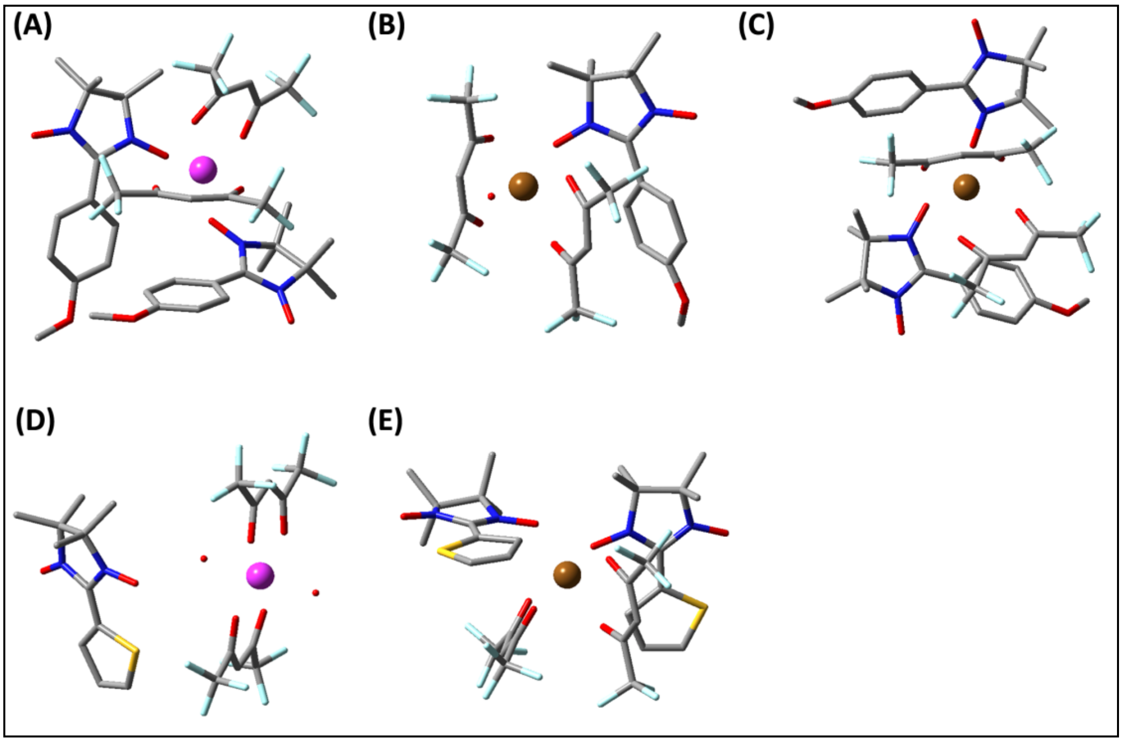

Figure 5.11: Geometry of the modelled metal–radical complexes: (A) **1**, (B) **3**, (C) **3**, (D) **2**, and (E) **4**; color code: cobalt – violet, manganese – brown, carbon – grey, nitrogen – blue, oxygen – red, fluorine – light blue, sulfur – yellow; hydrogen atoms are omitted for clarity.)

The quantum chemical calculations were carried out by Prof. Anela Ivanova from Sofia University on several models of the metal–radical complexes. The advantage of using B3LYP functional in DFT over the years that a certain amount of the exact exchange should be present in the functional if quantitative reproduction of the metal–organic spin exchange coupling is sought.

B3LYP is often employed in hybrid–spin organic–inorganic complexes[40, 41] and previous study of similar manganese(II)–nitroxide complexes[62] shown to be able to properly reproduce experimental data for the exchange coupling constant with very good accuracy and allowed clarification of the mechanism of spin–spin interaction (including reversal of the ground state multiplicity).

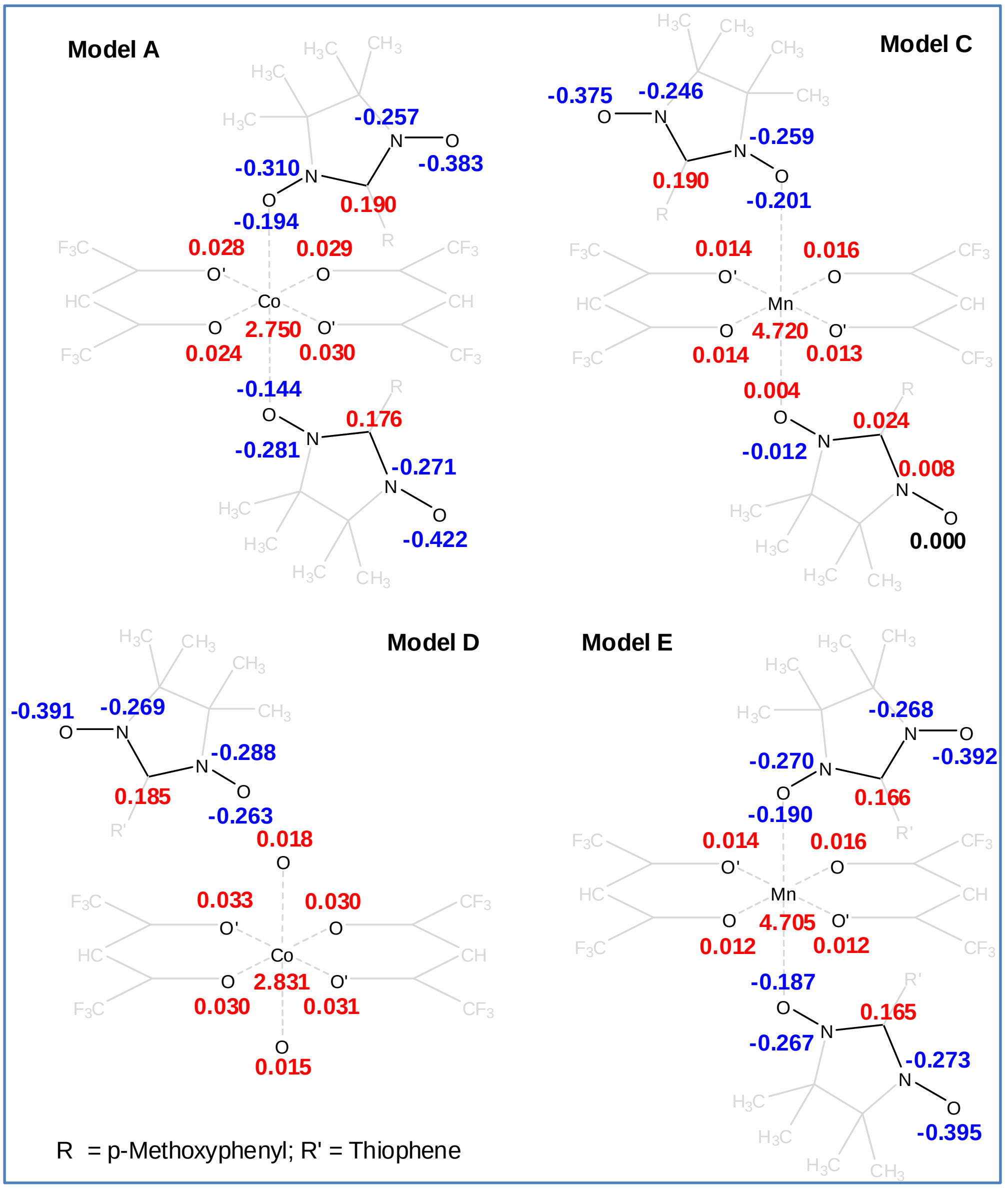

Figure 5.12: Atomic spin densities of the key atoms responsible for the spin-spin interaction in the most stable state of the modelled structures. The complete set of values of all multiplets is given in figure 5.7.2 and 5.7.3 of the supporting information.

The geometry as shown in figure 5.11 is extracted from the x–ray structures. The repeating unit of the crystals is used as a model structure in all cases. For one of the complexes (***3***), an extended geometry (figure 5.11, C) is also tested to mimic more correctly the molecular environment around the inorganic spins.

Table 5.3: Spin configurations and total energy of the spin states of the model metal–radical structures. Exchange integrals estimated from the energy difference between the most stable and the second most stable multiplet are given. Organic spins are denoted in blue in the spin configurations revealing that doublet for **1**, triplet for **2**, quintet for **3** and quartet for **4** represent the magnetic ground state.

Model	Multiplicity	Spin configuration	Energy, a.u.	J/kB, K	Model	Multiplicity	Spin configuration	Energy, a.u.	J/kB, K
A **(*1*)**	**Doublet**	↓↑↑↑↓	**-3785.40314**	**-330**	***B*** **(*3*)**	**Quintet**	↑↑↑↑↑↓	**-2940.7252**	**-244**
	Quartet	↑↑↑↑↓	-3785.39896			Septet	↑↑↑↑↑↑	-2940.7205	
	Sextet	↑↑↑↑↑	-3785.39530		***C*** **(*3*)**	Quintet	↑↑↑↑↑↓	**-3744.6488**	**-336**
						Septet	↑↑↑↑↑↑	-3744.6424	
D **(*2*)**	**Triplet**	↑↑↑↓	**-3264.58696**	**-1**	***E*** **(*4*)**	**Quartet**	↓↑↑↑↑↑↓	**-4156.7109**	**-259**
	Quintet	↑↑↑↑	-3264.58696			Sextet	↑↑↑↑↑↑↓	-4156.7060	
						Octet	↑↑↑↑↑↑↑	-4156.7003	

There, the second organic ‘radical’ bears no spin (eliminated by adding a hydrogen atom to one of the nitroxide groups) in order to have identical spin–spin coupling to model B, but at the same time it allows the same intermolecular interactions as in the x–ray structure. Even though model C is a rather artificial construct, it serves the purpose to represent properly the coordination sphere of the metal ion and allows taking into account all other interactions, e.g., electrostatic, donor–acceptor, etc., except for the spin exchange with the second radical.

It should be noted that any of the two models for complex **3** will capture only the nearest–neighbor exchange interactions and may not be quantitative for the entire spin chain. The latter would require periodic calculations, which extend beyond the scope of the study. A complete first coordination sphere of the metal ion is maintained in all models. The energy of the spin states and the exchange integrals calculated there from[62] are summarized in table 5.3. The derivation of the relationship between the energy differences and J/K_B is given in the Supporting Information. It should be noted that all the theoretical calculations are carried out at T = 0 K for all the compounds.

In all complexes, the inorganic spins are antiferromagnetically coupled to the organic ones, which coincides with the experimental measurements. The ferromagnetic states are unlikely because they lie at least 2.5 kcal/mol higher in energy than the low–spin ones (except for **2**). As could be expected, the magnitude of spin exchange depends on the local environment. In **2**, where Co(II) has no direct contact to the organic radical, the two spin states are practically degenerate because the two types of spins are isolated. In the other three systems, the exchange interaction is more appreciable, leading to J/K_B of ca. –300 K. The numerical estimates for the four complexes are very close to those obtained from the experimental data. Taking into account the proper coordination sphere of the metal, however, is more important. Inclusion of the additional organic molecule in model C, even though it has no spin itself, results in increase of the exchange by almost 100 K compared to model B. If the second radical in model C is included with its spin (the total energy values are given in the figure 5.13) then the antiferromagnetic interaction is weakened by ca. 30 K compared to the value provided by the repeating unit model. There is also some influence of the type of the organic radical on the size of spin-spin coupling: it is slightly greater in $\boldsymbol{R}^1$ based metal complexes than in $\boldsymbol{R}^2$ ones (model A vs. model E).

The atomic spin density distribution (figure 5.13 and 5.14) provides a clue towards the observed specificities. The qualitative patterns arising due to the spin–spin interaction in models A, C, and E are identical. Almost equal amount of spin (~ 0.03 for Co(II), and ~0.015 for Mn(II)) is delocalized on the coordinated oxygen atoms of hexafluoroacetylacetonate, and the remaining fraction (~0.24 for Mn(II), and ~0.13 for Co(II)) of delocalized spins from the metal ion is transferred to the coordinated oxygen atom(s) from nitronyl nitroxide. In model B, the single coordinated radical acquires less spin (0.183) from manganese and, hence, the smaller exchange integral. Another common feature of models A, C, and E is the spin redistribution that takes place upon coordination of the nitronyl nitroxide radicals. In all directly coordinated nitroxide fragments the spin from the metal ion is delocalized primarily on the oxygen atom, which possesses less spin density than its adjacent nitrogen, while the situation is reverse in the non-coordinated nitroxide group and in free nitronyl nitroxide radicals. Such an effect, but much less pronounced, is seen also in model D.

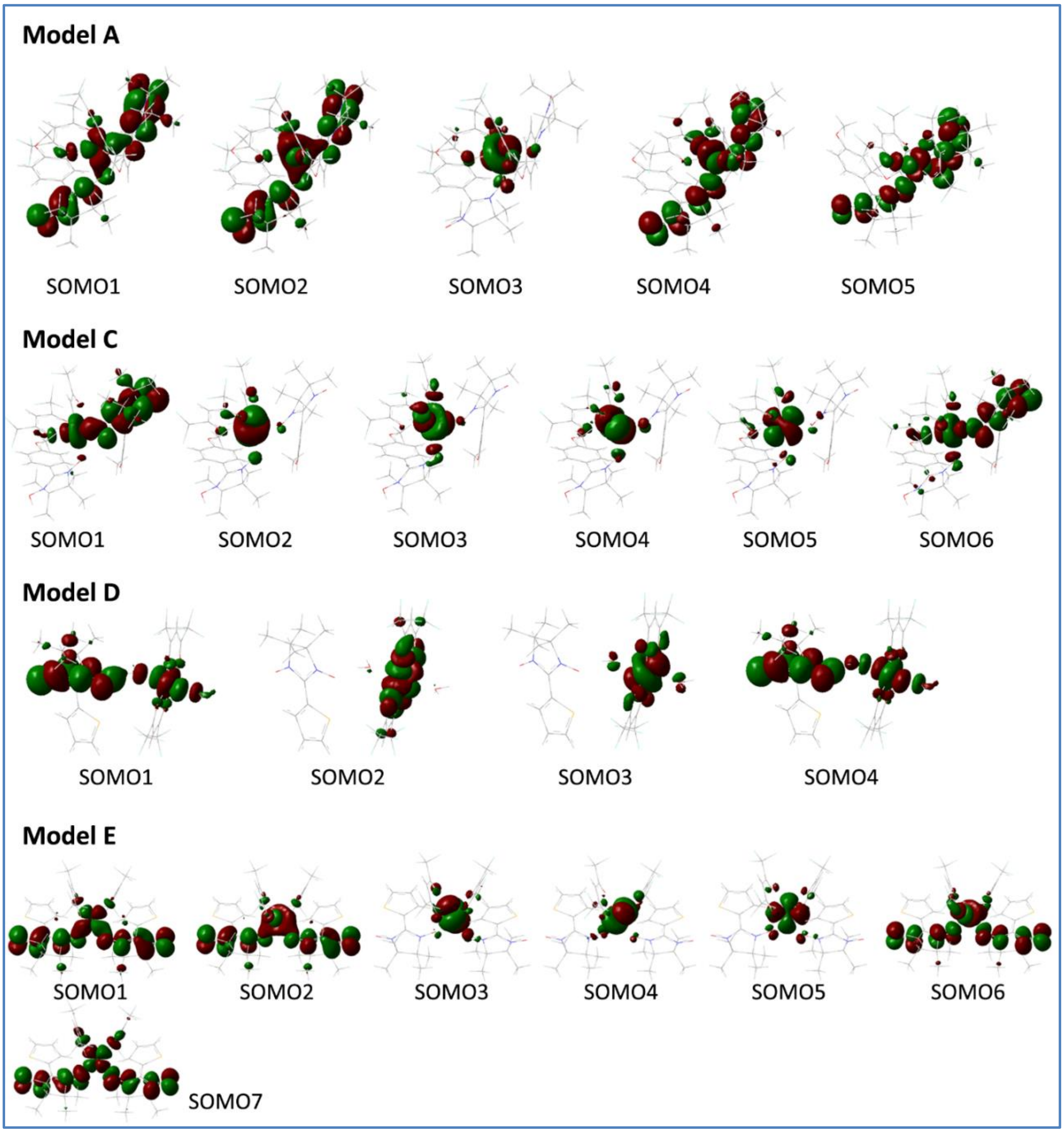

Figure 5.13: Natural singly occupied molecular orbitals (SOMOs) of the most stable spin state of the studied models.

There, the spin on the oxygen atom, which is closer to the metal ion, is reduced and that of the nitrogen is increased due to minor spin transfer along a hydrogen bond formed with the bridging water molecule. The spinless ligand in model C remains such. Only some miniscule spin delocalization/polarization is observed. The isolated nature of the organic radical in model D is confirmed by the total spin density distributed on the π-conjugated part of the nitronyl nitroxide ring. It is -0.89 to -0.95 in models A, C, and E, whereas in model D, it extends to -1.03. It should be noted that the remaining fraction of the unpaired electrons in the organic molecules is spin polarized on the phenoxy/thiophene fragment (Appendix A-V).

Although being reasonable and corresponding well to the structural characteristics of the investigated models, the sole picture of spin transfer in the hybrid systems cannot explain the specific strength of antiferromagnetic coupling in the various models. Therefore, the overlap between the inorganic ion and the organic counterpart illustrated by the natural molecular orbitals (figure 5.15) is analyzed next.

Table 5.4: Occupation numbers (N_{occ}) of the SOMOs of the modelled hybrid systems.

Model	**Orbital**	**N_{occ}**	**Model**	**Orbital**	**N_{occ}**
A	SOMO1	1.285	***C***	SOMO1	1.336
	SOMO2	1.169		SOMO2	1.000
	SOMO3	1.000		SOMO3	1.000
	SOMO4	0.831		SOMO4	1.000
	SOMO5	0.715		SOMO5	1.000
				SOMO6	0.664
D	SOMO1	1.018	***E***	SOMO1	1.337
	SOMO2	1.000		SOMO2	1.221
	SOMO3	1.000		SOMO3	1.000
	SOMO4	0.982		SOMO4	1.000
				SOMO5	1.000
				SOMO6	0.779
				SOMO7	0.663

The antiferromagnetic nature of the spin exchange becomes evident from the natural orbitals plots. In models A and E, two *d*–orbitals of the metal ions mix with the SOMOs of the organic radicals, yielding two linear combinations with bonding overlap, and two linear combinations with antibonding. Similar type of overlap takes place in model C, but only one of the *d*–orbitals of Mn(II) is involved because the model includes only one organic radical. Nevertheless, the bonding overlap seems to be the most efficient, giving rise to the strongest antiferromagnetic coupling. Model D features a different SOMO pattern. Once more, linear combinations between orbitals located on *M*(hfac)$_2$ and on the organic radical are formed. However, there is just a tiny bonding overlap between the hydrogen atom of a water molecule and one of the nitronyl nitroxide oxygen atoms in SOMO1, which gives rise to the small spin transfer discussed above. All these observations are confirmed by the occupation numbers of SOMOs summarized in table 5.4.

5.8 Conclusions

The crystal structure and magnetic properties of 4-methoxy phenyl and thiophene substituted nitronyl nitroxide based four metal complexes (**1**, **2**, **3**, and **4**) have been investigated. The magnetic measurement confirms the presence of antiferromagnetic type of interactions between the transition metal ions and the nitronyl nitroxide radicals. DFT quantum chemical calculations of the metal-radical complexes confirm antiferromagnetic spin-spin interaction, due to bonding overlap between the metal and the nitroxide contributions in the singly occupied molecular orbitals. The calculations also indicate spin delocalization from the metal ions to the organic radical in metal-radical complexes.

5.9 Synthesis, experimental and calculation details

For the synthesis of the complex **1**, Co(hfac)$_2$.2H$_2$O (96 mg, 0.18 mmol) and $\boldsymbol{R}^1$ (50 mg, 0.18 mmol) are dissolved in a mixture of acetone and heptane (10/10 mL), then the resulting solution is heated to 75°C for 1hr, and then cooled down to room temperature. Well-shaped, brown colored block-like crystals of complex **1** are obtained, which are separated out for single crystal x–ray diffraction measurements; yield, ~36 %, Anal. Calcd. for $C_{38}H_{40}CoF_{12}N_4O_{10}$: C, 45.66; H, 4.03; N, 5.60; Co, 5.90 %; Found: C, 45.79; H, 3.99; N, 5.52 %.

For the synthesis of **2**, Co(hfac)$_2$.*x*H$_2$O (105.02 mg, 0.20mmol) and $\boldsymbol{R}^2$(50 mg, 0.20 mmol) are dissolved in a mixture of acetone and heptane (10/10 mL), and then the resulting solution is stirred for 1hr. The filtrated solution is left at room temperature for crystallization. Well-shaped, blue needle–like crystals are obtained after 3 days, yield, ~29 %, Anal. Calcd. for

$C_{32}H_{32}CoF_{12}O_8N_4S_2{\cdot}2H_2O$: C, 33.70; H, 2.83; N, 3.74; S, 4.28; Co, 7.87 %: Found: C, 33.63; H, 2.92; N, 3.68; S, 5.29 %; For complex **3**, Mn(hfac)$_2$.xH$_2$O (89 mg, 0.18 mmol) and **R^1** (50 mg, 0.18 mmol) Anal. Calcd. for $C_{24}H_{21}F_{12}MnN_2O_7{\cdot}x(C_7H_{16})$: C, 39.36; H, 2.89; N, 3.82; Mn, 7.51 %; Found: C, 40.20; H, 2.48; N, 4.00 %; yield, ~40 %. For complex **4**, Mn(hfac)$_2$.xH$_2$O (96.7 mg, 0.20mmol) and ***R*^{2}** (50 mg, 0.20 mmol) are dissolved in a mixture of acetone and heptane (10/10 mL) at room temperature. After 3 days, well–shaped, blue and, green needle–like crystals of complexes **4** in millimeter of size are obtained. Anal. Calcd. for $C_{32}H_{32}F_{12}MnN_4O_8S_2$; C, 40.55; H, 3.40; N, 5.91; S, 6.77; Mn, 5.80 %; Found: C, 40.51; H, 3.20; N, 5.79; S, 6.28 %; yield, ~33 %.

The single crystal X-ray diffraction (XRD) measurements are performed on a STOE IPDS 2T diffractometer over an angular (2ϑ) range of 2°–28° using a Mo K_α radiation. A detailed structural analysis is performed on the XRD data by SHELXL-2014 (full matrix) program. The EPR measurement is carried out using a Bruker EMaxPlus A/P/W spectrometer equipped with an NMR gauss meter and a variable-temperature-control continuous-flow-N_2 cryostat (Bruker B-VT 2000). The Infrared spectra (IR) are recorded using KBr pressed pellets on a Nicolet 730 FT-IR spectrometer (Supporting information, Figure S1). The temperature dependent magnetization data are recoded using a commercial Superconducting Quantum Interference Device (SQUID, Quantum Design, USA) in the temperature range 2-300 K. Yield, ~33 %. Anal. Calcd. for $C_{32}H_{32}F_{12}MnN_4O_8S_2$; C, 40.55; H, 3.40; N, 5.91; S, 6.77; Mn, 5.80 %; Found: C, 40.51; H, 3.20; N, 5.79; S, 6.28%.

Single point computations on the X–ray geometry of each complex are performed with the DFT functional B3LYP[63-66] and basis set 6-31G*.[67] The core electrons of the metal ions are replaced by a RSC Stuttgart–Dresden ECP.[68] Unrestricted open shell wave functions are generated for all feasible spin states of the complexes (with the spins of the metal ions kept at their experimental values: $S = 3/2$ for Co(II) and $S = 5/2$ for Mn(II)). Mulliken spin densities and natural molecular orbitals are calculated to estimate the amount of spin transfer and the nature of electron exchange. All simulations are done with the program package Gaussian 09.[69]

The appendix-V **(A-V)** is given for chapter–5.

Atomic spin densities of all multiplets of models **A, B, C, D** and **E.**

5.10 References

1. Caneschi, A.; Gatteschi, D.; Sessoli, R.; Rey, P., Toward Molecular Magnets: The Metal-Radical Approach. *Ace. Chem. Res.* **1989,** *22*, 392-398.
2. Demir, S.; Jeon, I.-R.; Long, J. R.; Harris, T. D., Radical Ligand-Containing Single-Molecule Magnets. *Coord. Chem. Rev.* **2015,** *289–290*, 149-176.
3. Keana, J. F. W., Newer Aspects of the Synthesis and Chemistry of Nitroxide Spin Labels. *Chem. Rev.* **1978,** *78*, 37-64.
4. Gao, D.-Z.; Chen, J.; Wang, S.-P.; Song, Y.; Liao, D.-Z.; Jiang, Z.-H.; Yan, S.-P., Radical-Dependent Magnetic Interactions in Two 1-D Copper(II) Complexes with Nitronyl Nitroxide and Imino Nitroxide Radicals Bridged by Iminodiacetate Anion. *Inorg. Chem. Commun.* **2006,** *9*, 132-135.
5. Fegy, K.; Luneau, D.; Ohm, T.; Paulsen, C.; Rey, P., Two-Dimensional Nitroxide-Based Molecular Magnetic Materials. *Angew. Chem. Int. Ed.* **1998,** *37*, 1270-1273.
6. Caneschi, A.; Gatteschi, D.; Sessoli, R., Magnetic Properties of a Layered Molecular Material Comprising Manganese Hexafluoroacetylacetonate and Nitronyl Nitroxide Radicals. *Inorg. Chem.* **1993,** *32*, 4612-4616.
7. Caneschi, A.; Gatteschi, D.; Rey, P.; Sessoli, R., Structure and Magnetic Ordering of a Ferrimagnetic Helix Formed by Manganese(II) and a Nitronyl Nitroxide Radical *Inorg. Chem.* **1991,** *30*, 3936-3941.
8. Caneschi, A.; Gatteschi, D.; Rey, P.; Sessoli, R., Structure and Magnetic Properties of Ferrimagnetic Chains Formed by Manganese(II) and Nitronyl Nitroxides. *Inorg. Chem.* **1988,** *27*, 1756-1761.
9. Caneschi, A.; Ferraro, F.; Gatteschi, D.; Rey, P.; Sessoli, R., Structure and Magnetic Properties of a Chain Compound Formed by Copper(II) and a Tridentate nitronyl Nitroxide Radical. *Inorg. Chem.* **1991,** *30*, 3162-3166.
10. Caneschi, A.; Ferraro, F.; Gatteschi, D.; Rey, P.; Sessoli, R., Ferro- and Antiferromagnetic Coupling Between Metal Ions and Pyridine-Substituted Nitronyl Nitroxides. *Inorg. Chem.* **1990,** *29*, 4217-4223.
11. Angeloni, L.; Caneschi, A.; David, L.; Fabretti, A.; Ferraro, F.; Gatteschi, D.; Lirzin, A. l.; Sessoli, R., Crystal Structures, Magnetic and Non-Linear Optical Properties of Methoxyphenyl Nitronyl-Nitroxide Radicals. *J. Mater. Chem.* **1994,** *4*, 1047-1053.

12. Caneschi, A.; Gatteschi, D.; Lirzin, A. L., Crystal Structure and Magnetic Properties of a New Ferrimagnetic Chain Containing Manganese(II) and a Nitronyl-Nitroxide Radical. Magnetic Ordering in Mn(hfac)$_2$NITR Compounds. *J. Mater. Chem.* **1994,** *4*, 319-326.

13. Benelli, C.; Caneschi, A.; Gatteschi, D.; Pardi, L.; Rey, P., Linear-Chain Gadolinium(III) Nitronyl Nitroxide Complexes with Dominant Next-Nearest-Neighbor Magnetic Interactions. *Inorg. Chem.* **1990,** *29*, 4223-4228.

14. Benelli, C.; Caneschi, A.; Gatteschi, D.; Pardi, L., Gadolinium(III) Complexes with Pyridine-Substituted Nitronyl Nitroxide Radicals. *Inorg. Chem.* **1992,** *31*, 741-746.

15. Bernot, K.; Bogani, L.; Caneschi, A.; Gatteschi, D.; Sessoli, R., A Family of Rare-Earth-Based Single Chain Magnets: Playing with Anisotropy. *J. Am. Chem. Soc.* **2006,** *128*, 7947–7956.

16. Benelli, C.; Caneschi, A.; Gatteschi, D.; Pardi, L.; Rey, P., Structure and Magnetic Properties of Linear-Chain Complexes of Rare-Earth Ions (Gadolinium, Europium) with Nitronyl Nitroxides. *Inorg. Chem.* **1989,** *28*, 275-280.

17. Benelli, C.; Caneschi, A.; Gatteschi, D.; Pardi, L.; Rey, P., One-Dimensional Magnetism of a Linear Chain Compound Containing Yttrium(III) and a Nitronyl Nitroxide Radical. *Inorg. Chem.* **1989,** *28*, 3230-3234.

18. Benelli, C.; Caneschi, A.; Gatteschi, D.; Sessoli, R., Magnetic Interactions and Magnetic Ordering in rare Earth Metal Nitronyl Nitroxide Chains. *Inorg. Chem.* **1993,** *32*, 4797-4801.

19. Poneti, G.; Bernot, K.; Bogani, L.; Caneschi, A.; Sessoli, R.; Wernsdorfer, W.; Gatteschi, D., A Rational Approach to The Modulation of The Dynamics of The Magnetisation in a Dysprosium-Nitronyl-Nitroxide Radical Complex. *Chem. Commun.* **2007**, 1807-1809.

20. Pointillart, F.; Bernot, K.; Sorace, L.; Sessoli, R.; Gatteschi, D., Ferromagnetic Interactions in Ru(III)-Nitronyl Nitroxide Radical Complex: A Potential 2p4d Building Block for Molecular Magnets. *Dalton Trans.* **2007**, 2689-2695.

21. Bernot, K.; Pointillart, F.; Rosa, P.; Etienne, M.; Sessoli, R.; Gatteschi, D., Single Molecule Magnet Behaviour in Robust Dysprosium–Biradical Complexes. *Chem. Commun.* **2010,** *46*, 6458-6460.

22. Fedin, M.; Veber, S.; Gromov, I.; Maryunina, K.; Fokin, S.; Romanenko, G.; Sagdeev, R.; Ovcharenko, V.; Bagryanskaya, E., Thermally Induced Spin Transitions in Nitroxide Copper(II)Nitroxide Spin Triads Studied by EPR. *Inorg. Chem.* **2007,** *46*, 11405-11415.

23. Veber, S. L.; Fedin, M. V.; Potapov, A. I.; Maryunina, K. Y.; Romanenko, G. V.; Sagdeev, R. Z.; Ovcharenko, V. I.; Goldfarb, D.; Bagryanskaya, E. G., High-Field EPR Reveals the Strongly Temperature-Dependent Exchange Interaction in Breathing Crystals. *J. Am. Chem. Soc.* **2008,** *130*, 2444-2445.

24. Fedin, M. V.; Veber, S. L.; Maryunina, K. Y.; Romanenko, G. V.; Suturina, E. A.; Gritsan, N. P.; Sagdeev, R. Z.; Ovcharenko, V. I.; Bagryanskaya, E. G., Intercluster Exchange Pathways in Polymer-Chain Molecular Magnets Cu(hfac)2LR Unveiled by Electron Paramagnetic Resonance. *J. Am. Chem. Soc.* **2010,** *132*, 13886-13891.

25. Veber, S. L.; Fedin, M. V.; Maryunina, K. Y.; Potapov, A.; Goldfarb, D.; Reijerse, E.; Lubitz, W.; Sagdeev, R. Z.; Ovcharenko, V. I.; Bagryanskaya, E. G., Temperature-Dependent Exchange Interaction in Molecular Magnets Cu(hfac)$_2$LR Studied by EPR: Methodology and Interpretations. *Inorg. Chem.* **2011,** *50*, 10204-10212.

26. Fedin, M.; Ovcharenko, V.; Sagdeev, R.; Reijerse, E.; Lubitz, W.; Bagryanskaya, E., Light-Induced Excited Spin State Trapping in an Exchange-Coupled Nitroxide-Copper(II)-Nitroxide Cluster. *Angew. Chem. Int. Ed.* **2008,** *47*, 6897-6899.

27. Fedin, M. V.; Maryunina, K. Y.; Sagdeev, R. Z.; Ovcharenko, V. I.; Bagryanskaya, E. G., Self-Decelerating Relaxation of the Light-Induced Spin States in Molecular Magnets Cu(hfac)2LR Studied by Electron Paramagnetic Resonance. *Inorg. Chem.* **2012,** *51*, 709-717.

28. Jie Zhou; Lin Du; Yan Hu; Chen, P.; and, B. L.; Zhao, Q.-H., Four Discrete Transition Metal Complexes Involving Pyridyl-substituted Nitronyl Nitroxide: Syntheses, Crystal Structures, and Magnetic Properties. *Z. anorg. allg. Chem.* **2014,** *640*, 363-369.

29. Furui, T.; Suzuki, S.; Kozaki, M.; Shiomi, D.; Sato, K.; Takui, T.; Okada, K.; Tretyakov, E. V.; Tolstikov, S. E.; Romanenko, G. V.; Ovcharenko, V. I., Preparation and Magnetic Properties of Metal-Complexes from N-t-Butyl-N-oxidanyl-2-amino-(nitronyl nitroxide). *Inorg. Chem.* **2014,** *53*, 802–809.

30. Giancarlo Francese; Francisco M. Romero; Antonia Neels; Stoeckli-Evans, H.; Decurtins, S., Crystal Structures and Magnetic Properties of Metal Complexes Bearing Four Nitronyl Nitroxide Moieties in the Same Coordination Sphere. *Inorg. Chem.* **2000,** *39*, 2087-2095.

31. Wang, H.; Liu, Z.; Liu, C.; Zhang, D.; Lu, Z.; Geng, H.; Shuai, Z.; Zhu, D., Coordination Complexes of 2-(4-Quinolyl)nitronyl Nitroxide with M(hfac)2 [M) Mn(II), Co(II), and Cu(II)]: Syntheses, Crystal Structures, and Magnetic Characterization. *Inorg. Chem.* **2004,** *43*, 4091-4098.

32. Zhou, S. Y.; Li, X.; Li, T.; Tian, L.; Liu, Z. Y.; Wang, X. G., A Series of Heterospin Complexes Based on Lanthanides and Pyridine Biradicals: Synthesis, Structure and Magnetic Properties. *RSC Adv.* **2015,** *5*, 17131-17139.

33. Lannes, A.; Intissar, M.; Suffren, Y.; Reber, C.; Luneau, D., Terbium(III) and Yttrium(III) Complexes with Pyridine-Substituted Nitronyl Nitroxide Radical and Different β-Diketonate Ligands. Crystal Structures and Magnetic and Luminescence Properties. *Inorg. Chem.* **2014,** *53*, 9548-9560.

34. Souza, D. A.; Florencio, A. S.; Soriano, S.; Calvo, R.; Sartoris, R. P.; Walkimar de M. Carneiro, J.; Sangregorio, C.; Novak, M. A.; Vaz, M. G. F., New Copper(II)-Radical One Dimensional Chain: Synthesis, Crystal Structure, EPR, Magnetic Properties and DFT Calculations. *Dalton Trans.* **2009,** *0*, 6816-6824.

35. Mitsumori, T.; Inoue, K.; Koga, N.; Iwamura, H., Exchange Interactions between Two Nitronyl Nitroxide or Iminyl Nitroxide Radicals Attached to Thiophene and 2,2'-Bithienyl Rings. *J. Am. Chem. Soc.* **1995,** *117*, 2467-2478.

36. Scarrozza, M.; Vindigni, A.; Barone, P.; Sessoli, R.; Picozzi, S., Combined First-Principles and Thermodynamic Approach to M-nitronyl Nitroxide (M = Co, Mn) Spin Helices. *Phys. Rev. B* **2015,** *91*, 144422-1-144422-15.

37. Jung, J.; Puget, M.; Cador, O.; Bernot, K.; Calzado, C. J.; Le Guennic, B., Analysis of the Magnetic Exchange Interactions in Yttrium(III) Complexes Containing Nitronyl Nitroxide Radicals. *Inorganic Chemistry* **2017,** *56*, 6788-6801.

38. Jung, J.; Guennic, B. L.; Fedin, M. V.; Ovcharenko, V. I.; Calzado, C. J., Mechanism of Magnetostructural Transitions in Copper-Nitroxide-Based Switchable Molecular Magnets: Insights from ab Initio Quantum Chemistry Calculations. *Inorg. Chem.* **2015,** *54*, 6891-6899.

39. Jung, M.; Sharma, A.; Hinderberger, D.; Braun, S.; Schatzschneider, U.; Rentschler, E., Long-Distance Magnetic Interaction of Exchange-Coupled Copper Dimers with Nitronyl Nitroxide and tert-Butyl Nitroxide Radicals. *Inorg. Chem.* **2009,** *48*, 7244-7250.

40. Ovcharenko, V.; Kuznetsova, O.; Fursova, E.; Letyagin, G.; Romanenko, G.; Bogomyakov, A.; Zueva, E., Simultaneous Introduction of Two Nitroxides in the Reaction: A New Approach to the Synthesis of Heterospin Complexes. *Inorg. Chem.* **2017,** *56*, 14567-14576.

41. Jung, M.; Sharma, A.; Hinderberger, D.; Braun, S.; Schatzschneider, U.; Rentschler, E., Nitronyl Nitroxide Radicals Linked to Exchange-Coupled Metal Dimers – Studies Using X-ray Crystallography, Magnetic Susceptibility Measurements, EPR Spectroscopy, and DFT Calculations. *Eur. J. Inorg. Chem.* **2009**, 1495-1502.

42. Huang, J.; GuiqinZhang; Huang, Y.; DecaiFang; DeqingZhang, Density Functional Theory Study on Antiferromagnetic Interactions in A Silver (I) Complex Of Nitronyl Nitroxide. *J. Magn. Magn. Mater.* **2006,** *299*, 480-486.

43. Qi, S.-C.; Hayashi, J.-i.; Zhang, L., Recent Application of Calculations of Metal Complexes Based on Density Functional Theory. *RSC Adv.* **2016,** *6*, 77375-77395

44. Osiecki, J. H.; Ullman, E. F., Studies of Free Radicals. I. .Alpha.-Nitronyl Nitroxides, A New Class of Stable Radicals. *J. Am. Chem. Soc.* **1968,** *90*, 1078–1079.

45. Vaz, M. G. F.; Allão, R. A.; Akpinar, H.; Schlueter, J. A.; Sauli Santos, J.; Lahti, P. M.; Novak, M. A., Magnetic Mn and Co Complexes with a Large Polycyclic Aromatic Substituted Nitronylnitroxide. *Inorg. Chem.* **2012,** *51*, 3138–3145.

46. Rintoul, L.; Micallef, A. S.; Bottle, S. E., The Vibrational Group Frequency of the N-O• Stretching Band of Nitroxide stable Free Radicals. *Spectrochim. Acta A* **2008,** *70*, 713-717.

47. Forrester, A. R.; Hay, J. M.; Thomson, R. H., *Organic Chemistry of Stable Free Radicals*. **1968**.

48. Rozantsev, E. G.; Sholle, V. F., *Synthesis* **1970,** *190*.

49. Chen, J.; Zhang, Y.-J.; Huang, K.-T.; Huang, Q.; Wang, J.-J., Crystal Structures and Magnetic Properties of Two New Cobalt(II) Complexes with Triazole-Substituted Nitronyl and Imino Nitroxide Radicals. *Inter. J. of Inorg. Chem.* **2013,** *Article ID 272156*, 5 pages.

50. Yu, Y.-X.; Hu, H.-M.; Zhang, D.-Q.; Wang, Z.-Y.; Zhu, D.-B., Two New Nitronyl Nitroxide Radicals and Their Complexes with M(hfac)2 [M ═ Co(II), Ni(II), Mn(II)]: Syntheses, Crystal Structures,and Magnetic Characterizations. *Chin. J. Chem.* **2007,** *25*, 1259-1266.

51. Caneschi, A.; Gatteschi, D.; Laugier, J.; Rey, P., Ferromagnetic Alternating Spin Chains. *J. Am. Chem. Soc.* **1987,** *109*, 2191-2192.

52. Caneschi, A.; Gatteschi, D.; Lalioti, N.; Sangregorio, C.; Sessoli, R.; Venturi, G.; Vindigni, A.; Rettori, A.; Pini, M. G.; Novak, M. A., Cobalt(II)-Nitronyl Nitroxide Chains as Molecular Magnetic Nanowires *Angew. Chem. Int. Ed.* **2001,** *40*, 1760-1763.

53. A. Caneschi; Dante Gatteschi; N. Lalioti; R. Sessoli; L. Sorace; V. Tangoulis; Vindigni, A., Ising-Type Magnetic Anisotropy in a Cobalt(II) Nitronyl Nitroxide Compound: A Key to Understanding the Formation of Molecular Magnetic Nanowires. ***Chem. Eur. J.*** **2002,** *8*, 286-292.

54. Ikorskii, V. N.; Romanenko, G. u.; Sygurova, M. K.; V. I. Ovcharenko; Paunthou, F. L. d.; Rey, P.; Reznikov, V. A.; Podoplelov, A. V.; Sagdeev, I. Z., Magneto-Structural Correlations in Layered Polymeric Molecular Ferromagnets Based on Ni(II) and Co(II) Complexes with 3-Imidazoline Nitroxide Radicals and Methanol with Different Substituents in The Metal Cycle. *J. Struct. Chem.* **1994,** *35*, 492–504.

55. Zhang, C.-X.; Zhao, X.-Y.; Sun, N.-N.; Guo, Y.-L.; Zhang, Y., Crystal Structures and Magnetic Properties of two Complexes Synthesized from Manganese and Halogenophenyl-Substituted Nitronyl Nitroxide. *Inorg. Chim. Acta* **2011,** *367*, 135-140.

56. Kahn, O., *Molecular Magnetism*. VCH: New York, 1993.

57. Morgenstern-Badarau, I.; Laroque, D.; Bill, E.; Winkler, H.; Trautwein, A. X.; Robert, F.; Jeanninl, Y., Magnetic Susceptibility, EPR, Mossbauer, and X-ray Investigations of

Heteropolynuclear Clusters Containing Iron(III) and Copper(II) Ions: {Cu(Mesalen)}$_2$Fe(acac)(NO$_3$)$_2$ and {Cu(Mesalen)}$_3$Fe(acac)(PF$_6$)$_2$. *Inorg. Chem.* **1991,** *30*, 3180-3188.

58. Rajadurai, C.; Falk, K.; Ostrovsky, S.; Enkelmann, V.; Haase, W.; Baumgarten, M., 1-D Coordination Chains of Cu(hfac)2 and Mn(hfac)2 Bridged by Phenyl-Nitronyl Nitroxide Derivatives. *Inorg. Chim. Acta* **2005,** *358*, 3391–3397.

59. Train, C.; Norel, L.; Baumgarten, M., Organic Radicals, A Promising Route Towards Original Molecule-Based Magnetic Materials. *Coord. Chem. Rev.* **2009,** *253*, 2342–2351.

60. Smith, C. D.; Bottle, S. E.; Junk, P. C.; Inoue, K.; Markosyan, A. S., Synthesis and Properties of Mn(hfac)$_2$ Complexes of Isoindoline Nitroxide Radicals. *Synth. Met.* **2003,** *138*, 501-506.

61. Okada, K.; Beppu, S.; Tanaka, K.; Kuratsu, M.; Furuichi, K.; Kozaki, M.; Suzuki, S.; Shiomi, D.; Sato, K.; Takui, T.; Kitagawa, Y.; Yamaguchi, K., Preparation, structure, and magnetic interaction of a Mn(hfac)2-bridged [2-(3-pyridyl)(nitronyl nitroxide)–Mn(hfac)2]2 chain complex. *Chem. Commun.* **2007**, 2485-2487.

62. Ivanova, A.; Romanova, J.; Tadjer, A.; Baumgarten, M., Magnetostructural Correlation for Rational Design of Mn(II) Hybrid-Spin Complexes. *J. Phys. Chem. A* **2013,** *117*, 670-678.

63. Becke, A. D., Density-functional exchange-energy approximation with correct asymptotic behavior. *Phys. Rev. A* **1988,** *38*, 3098-3100.

64. Becke, A. D., Density-functional thermochemistry. III. The role of exact exchange. *J. Chem. Phys.* **1993,** *98*, 5648-5652.

65. Lee, C.; Yang, W.; Parr, R. G., Development of the Colle-Salvetti correlation-energy formula into a functional of the electron density. *Phys. Rev. B* **1988,** *37*, 785-789.

66. Miehlich, B.; Savin, A.; Stoll, H.; Preuss, H., Results obtained with the correlation energy density functionals of becke and Lee, Yang and Parr. *Chem. Phys. Lett.* **1989,** *157*, 200-206.

67. Ditchfield, R.; Hehre, W. J.; Pople, J. A., Self-Consistent Molecular-Orbital Methods. IX. An Extended Gaussian-Type Basis for Molecular-Orbital Studies of Organic Molecules. *J. Chem. Phys.* **1971,,** *54*, 724-728.

68. Dolg, M.; Wedig, U.; Stoll, H.; Preuss, H., Energy-adjusted ab initio pseudopotentials for the first row transition elements *J. Chem. Phys.* **1987,** *86*, 866-872.

69. Frisch, M. J.; Trucks, G. W.; Schlegel, H. B.; Scuseria, G. E.; Robb, M. A.; Cheeseman, J. R.; Scalmani, G.; Barone, V.; Mennucci, B.; Petersson, G. A.; Nakatsuji, H.; Caricato, M.; Li, X.; Hratchian, H. P.; Izmaylov, A. F.; Bloino, J.; Zheng, G.; Sonnenberg, J. L.; Hada, M.; Ehara, M.; Toyota, K.; Fukuda, R.; Hasegawa, J.; Ishida, M.; Nakajima, T.; Honda, Y.; Kitao, O.; Nakai, H.; Vreven, T.; Montgomery, J., J. A.; Peralta, J. E.; Ogliaro, F.; Bearpark, M.; Heyd, J. J.; Brothers, E.; Kudin, K. N.; Staroverov, V. N.; Kobayashi, R.; Normand, J.; Raghavachari, K.; Rendell, A.; Burant, J.

C.; Iyengar, S. S.; Tomasi, J.; Cossi, M.; Rega, N.; Millam, N. J.; Klene, M.; Knox, J. E.; Cross, J. B.; Bakken, V.; Adamo, C.; Jaramillo, J.; Gomperts, R.; Stratmann, R. E.; Yazyev, O.; Austin, A. J.; Cammi, R.; Pomelli, C.; Ochterski, J. W.; Martin, R. L.; Morokuma, K.; Zakrzewski, V. G.; Voth, G. A.; Salvador, P.; Dannenberg, J. J.; Dapprich, S.; Daniels, A. D.; Farkas, Ö.; Foresman, J. B.; Ortiz, J. V.; Cioslowski, J.; Fox, D. J., *Gaussian 09, Revision D.01*, **2009**.

Table of contents

Appendix-I

Experimental section and analytical techniques

Materials and methods

Oven-dried glassware were used for all the reactions and experiments. All manipulations were performed under a dry argon atmosphere using a standard technique. All reagents and chemicals were purchased from commercial sources and used as received, unless otherwise specified.

Column chromatography

The column chromatography was performed using by silica gel (60–120, 100–200 and 230–400 mesh). For thin layer chromatography, aluminium sheets pre-coated with silica gel (Merck, Kieselgel 60, F_{254}) were employed.

NMR spectroscopy

Proton (^{1}H NMR) and carbon (^{13}C NMR) nuclear magnetic resonance spectra were recorded using 250, 300, 500, or 700 MHz Bruker spectrometers. Chemical shifts are reported for ^{1}H NMR and ^{13}C NMR relative to residual proton or carbon resonances of the deuterated solvents.

Mass spectrometry

The high-resolution electrospray ionization mass spectrometry (HR-ESI-MS) was performed at the Institute for Organic Chemistry, Johannes-Gutenberg-University of Mainz, on an ESI-Q-TOF system (maXis, Bruker Daltonics, Germany).

EPR spectroscopy

EPR spectra were recorded in diluted and argon-purged solutions of toluene or DCM with the concentration of 10^{-4} molar unless otherwise stated by using a using a Bruker EMX-plus spectrometer equipped with the gauss meter and a variable-temperature control continuous-flow-

N2 cryostat (Bruker B-VT 2000). The g-factor corrections were obtained by using DPPH (g = 2.0037) as standard. The spectral simulation carried out using Bruker Win EPR Sim Fonia software.

Melting point

Melting points were measured on Büchi B-545 apparatus (uncorrected) by using open-ended capillaries.

UV–Vis absorption spectroscopy

UV-Vis spectra were recorded in toluene or DCM with Perkin Elmer Spectrometer (UV/Vis/NIR Lambda 900) by using 1 cm optical–path quartz cell at room temperature. The baseline was corrected by subtracting a measurement of the cuvette filled with pure solvent used for the measurement. The optical bandgap was calculated based on the onset absorption band.

Single-crystal X-ray measurements

The single crystal X-ray data were collected by Dr. Dieter Schollmeyer at Institute for Organic Chemistry, Johannes-Gutenberg-University of Mainz. The single crystal X-ray crystallographic data were collected on a Smart CCD diffractometer using a graphite monochromator Mo–Kα as a radiation source and a STOE IPDS 2T diffractometer using a graphite monochromator Mo–Kα as a radiation source and Cu–K_α IµS mirror system as a radiation source. The structures were solved by direct methods (SIR-2004) and refined by SHELXL–2014 (full matrix).

DFT Calculations

The DFT calculations were performed using either Gaussian 09. The broken-symmetry approach proposed by Noodleman*et al*.employed to elucidate the magnetic properties of the biradical species under study. The exchange coupling constant (*J*) was calculated by the generalized spin projection method suggested by Yamaguchi *et al*. For the molecule with two exchange coupled unpaired electrons, the Heisenberg-Dirac-Van Vleck (HDVV) Hamiltonian,

$$H = -2J_{12}S_1S_2,$$

S_1 and S_2 are the spin angular momentum operators.

$$\text{Exchange interaction,} \qquad J = \frac{(\mathrm{E(BS)} - \mathrm{E(T)})}{(S^2(\mathrm{T}) - S^2(\mathrm{BS}))}$$

where, E(BS) is the energy of the broken-symmetry (BS) approach, this approach uses the guess=mix keyword to build up, as initial guess, a 1:1 mixture of singlet and triplet states with $S^2 = 1$, E(T) is the energy of the triplet state with $S^2(T) = 2$, and S^2 are the eigen values of the spin operator for these states.

$$\text{Thus direct exchange yields } J = \mathrm{E(BS)} - \mathrm{E(T)}$$

Magnetic measurement

The magnetic susceptibility of the polycrystalline samples were measured by Artem S. Bogomyakov in the group of Victor I. Ovcharenko at International Tomography Center, Siberian Branch, Russian Academy of Sciences, Institutskaya Str. Novosibirsk, Russian Federation for chapter-2. Lars Postulka, Dr. Wolf Bernd in the group of Lang, Michael in Physikalisches Institut, J.W. Goethe–Universität Frankfurt, and Frankfurt, Germany for chapter-3. Dr. Gerhard Jakob, Institute of Physics, University of Mainz, Mainz, Germany for SQUID measurements for chapter-5 with a superconducting quantum interference device in the temperature range 2 to 300 K under magnetic field. Background signals of sample holder and diamagnetic correction were subtracted.

Cyclic voltammetry (CV)

CV measurements were carried out on a computer-controlled GSTAT12 in a three-electrode cell in anhydrous PhCN, acetonitrile or DCM solution of n-Bu4NPF6 (0.1 M) with a scan rate of 100 mV/s at room temperature. A Pt wire, a silver wire, and a glassy carbon electrode were used as the counter electrode, the reference electrode, and the working electrode, respectively.

Appendix-I

Chemical structure & graphics

The chemical structure and reaction scheme were drawn using ChemBioDraw Ultra 16.0. Molecular structures, crystal packing diagram, and high quality graphics were generated from Mercury 3.10.2 software using cif files.

Table A-I.1: Conversion chart for EPR units

dB	µWatt	√ µWatt	dB	µWatt	√ µWatt
40	20.1	4.4833	23	1010	**31.7805**
39	25.3	5.02991	22	1270	**35.63706**
38	31.9	5.64801	21	1600	**40**
37	40	6.32456	20	2000	**44.72136**
36	50.4	7.0993	19	2530	**50.29911**
35	63.6	7.97496	18	3180	**56.39149**
34	80	8.94427	17	4000	**63.24555**
33	101	10.04988	16	5040	**70.99296**
32	127	11.26943	15	6350	**79.68689**
31	160	12.64911	14	8010	**89.4986**
30	201	14.17745	13	10100	**100.49876**
29	250	15.81139	12	12700	**35.63706**
28	320	17.88854	11	16000	**126.49111**
27	400	20	10	20100	**141.77447**
26	510	22.58318	9	25300	**159.05974**
25	640	25.29822	8	31800	**178.32555**
24	800	28.28427	7	40100	**200.24984**
		--	6	50400	**224.49944**
dB	**µWatt**	**√ µWatt**	**dB**	**µWatt**	**√ µWatt**

1 hartree (h) = 27.2114 eV

1cm^{-1} = 1.07 x 10^{3} mT = 1.07 x 10^{4} Gauss

1 Gauss ~ 2.8 MHz = 1.39967 x g

To convert D,E from Gauss to cm^{-1} multiply by 4.6686·10^{-5}· 2.0023 cm^{-1}

1cm^{-1} = 29979.25 MHz = 10697.5 G for g=2.0023

Free electron g value: g_e = 2.0023193

Boltzmann Constant: k_B = 0.69504 cm^{-1}

Calculating the g value from the frequency and magnetic field:

g = (h/μ_B) γ / B = 714.4775 γ[GHz] / B[G]

Table A-I.2: Energy conversion chart

	hartree	eV	cm^{-1}	kcal/mol	kJ/mol	K	J	Hz
hartree	1	27.2107	219 474.63	627.503	2 625.5	315 777.	43.60 x 10^{-19}	6.57966 x 10^{+15}
eV	0.0367502	1	8 065.73	23.060 9	96.486 9	11 604.9	1.602 10 x 10^{-19}	2.418 04 x 10^{+14}
cm^{-1}	4.556 33 x 10^{-6}	1.239 81 x 10^{-4}	1	0.002 859 11	0.011 962 7	1.428 79	1.986 30 x 10^{-23}	2.997 93 x 10^{+10}
kcal/mol	0.001 593 62	0.043 363 4	349.757	1	4.18400	503.228	6.95 x 10^{-21}	1.048 54 x 10^{+13}
kJ/mol	0.000 380 88	0.010 364 10	83.593	0.239001	1	120.274	1.66 x 10^{-21}	2.506 07 x 10^{+12}
K	0.000 003 166 78	0.000 086 170 5	0.695 028	0.001 987 17	0.008 314 35	1	1.380 54 x 10^{-23}	2.083 64 x 10^{+10}
J	2.294 x 10^{+17}	6.241 81 x 10^{+18}	5.034 45 x 10^{+22}	1.44 x 10^{+20}	6.02 x 10^{+20}	7.243 54 x 10^{+22}	1	1.509 30 x 10^{+33}
Hz	1.519 83 x 10^{-16}	4.135 58 x 10^{-15}	3.335 65 x 10^{-11}	9.537 02 x 10^{-14}		4.799 30 x 10^{-11}	6.625 61 x 10^{-34}	1

Fundamental Physical Constants from NIST Most of these numbers have been taken from an old book by Karplus and Porter. [1]

[1] http://physics.nist.gov/cuu/Constants/index.html.

X–ray Crystallography

The X-ray crystallographic data were collected on a Smart CCD diffractometer using a graphite monochromator Mo-Kα as a radiation source for **3** at -100 °C for **PTP-NNSi** at -100°C and STOE IPDS 2T diffractometer using a graphite monochromator Mo-Kα as a radiation source for **5** and **PPP-NNSi** at -153 °C and for **6** at -80 °C. The structures were solved by direct methods (SIR-2004) and refined by SHELXL-2014 (full matrix).

Table A-II.1 Crystal data and structure refinement details of 3, 5, 6, PPP-NNSi and PTP-NNSi.

	3	**5**	**6**	**PPP-NNsi**	**PTP-NNSi**
Formula	$C_{23}H_{45}BrN_2O_2SSi_2$	$C_{25}H_{47}BrN_2O_2Si_2$	$C_{31}H_{59}BN_2O_4Si_2$	$C_{56}H_{98}N_4O_4Si_4$	$C_{54}H_{96}N_4O_4SSi_4$
Formula weight [g/mol]	549.76	543.73	590.79	1003.74	1009.76
Crystal system	monoclinic	triclinic	monoclinic	triclinic	triclinic
Space group	P 21/c	P -1	P 21/c	P -1	P -1
a /Å	19.907(2)	7.1928(3)	14.8434(4)	7.1802(5)	7.3684(8)
b/Å	11.6503(9)	11.2760(5)	20.1222(7)	11.4369(8)	10.9640(11)
c/Å	12.8343(12)	19.2222(9)	12.9937(4)	19.3529(16)	40.733(4)
α°	-	92.856(4)	-	98.727(6)	84.629(2)
β°	99.370(4)°	94.940(4)	111.258(2)	90.143(6)	88.353(3)
γ°	-	103.966(4)°	-	104.044(6)	73.129(3)
Z	4	2	4	1	2
wR2	0.1151	0.078	0.1143	0.1173	0.1891
R1	0.0465	0.033	0.0406	0.045	0.0753
Density gcm^{-3}	1.243	1.201	1.085	1.095	1.070
μ/mm^{-1}	1.57	1.469	0.132	0.14	0.17
no. independent reflections	7030	7340	8873	7385	14872
no. of refined parameter	249	303	418	321	632
Goodness of fit	0.943	1.039	1.034	0.922	1.043
CCDC	1501333	1501334	1501335	1507250	1507249

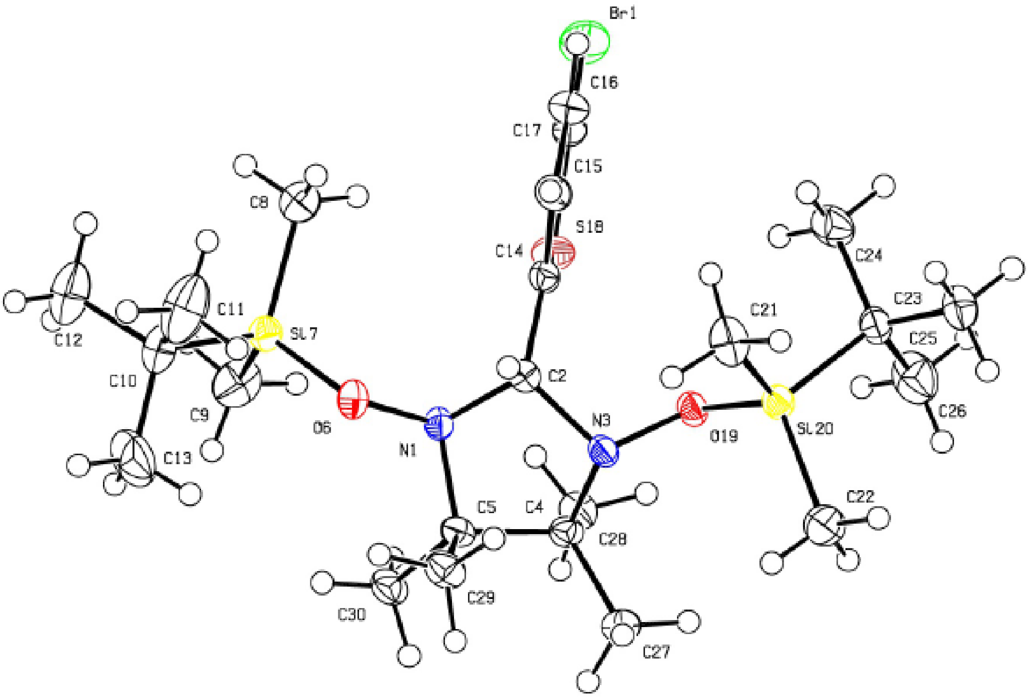

Figure A–II.1: The X-ray crystal structure of the **3** and thermal ellipsoids are drawn at 50% probability level.

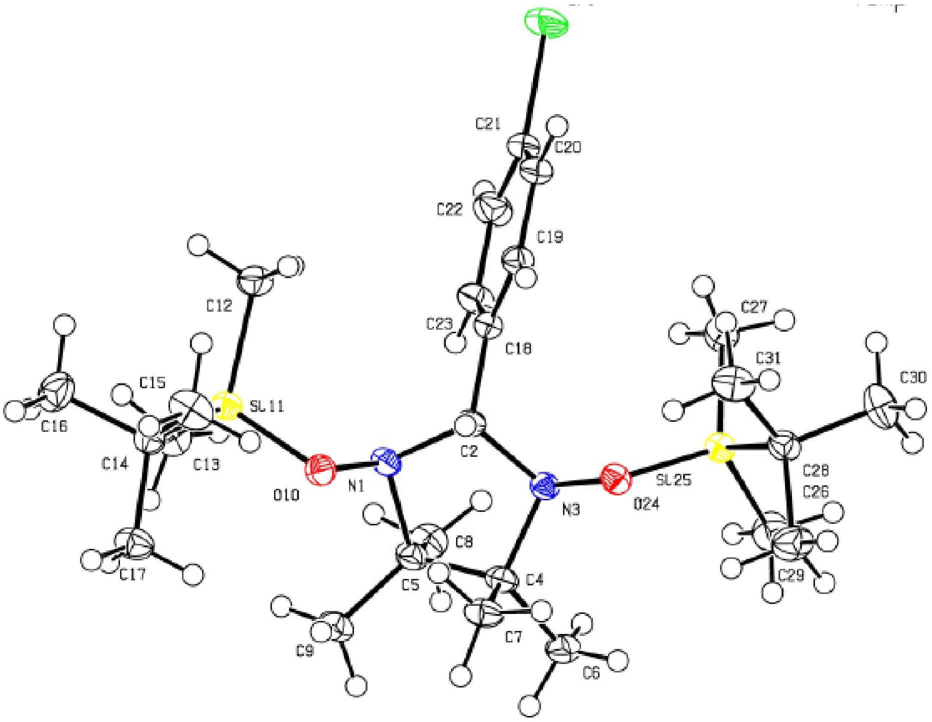

Figure A–II.2: The X-ray crystal structure of the **5** and thermal ellipsoids are drawn at 50% probability level.

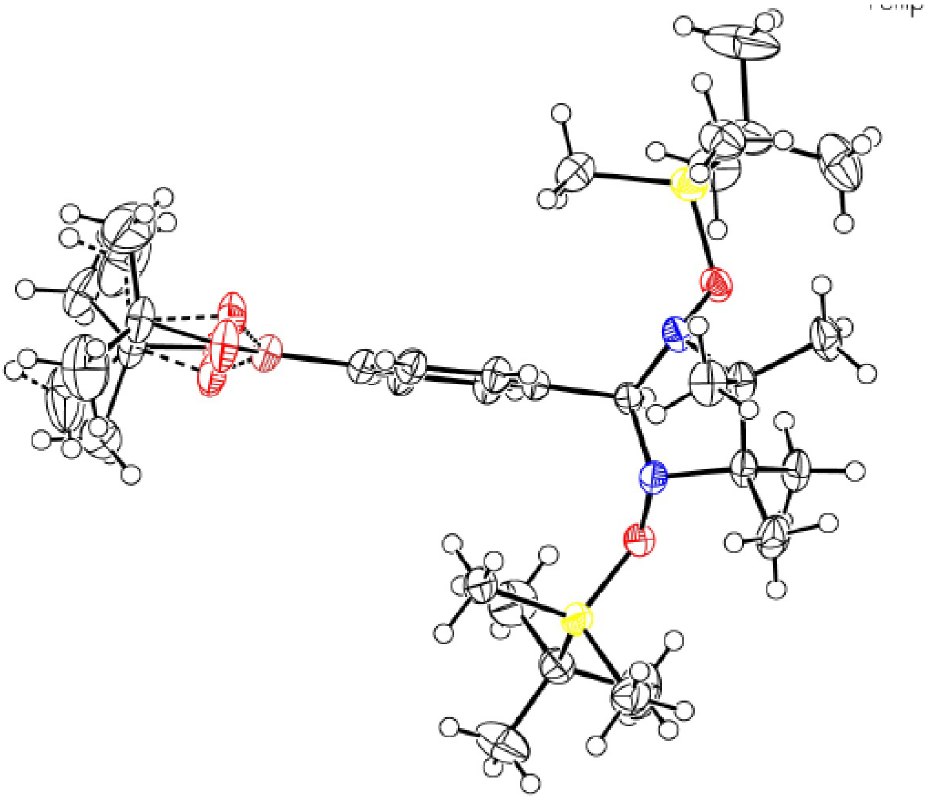

Figure A–II.3: The X-ray crystal structure of the **6** and thermal ellipsoids are drawn at 50% probability level.

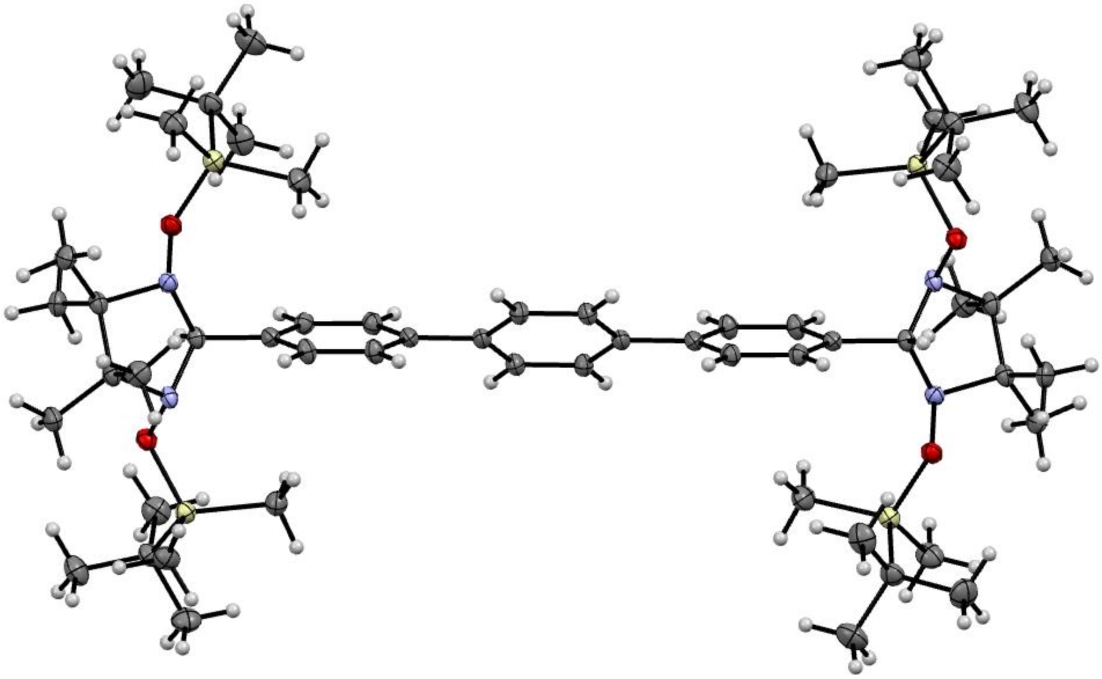

Figure A–II.4. The X-ray crystal structure of the **PPP-NNSi** and thermal ellipsoids are drawn at 50% probability level.

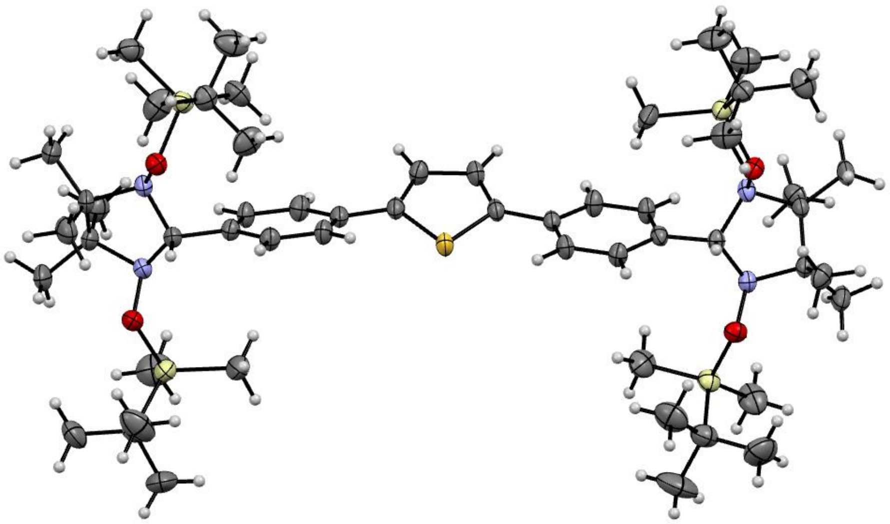

Figure A–II.5: The X-ray crystal structure of the **PTP-NNSi** and thermal ellipsoids are drawn at 50% probability level.

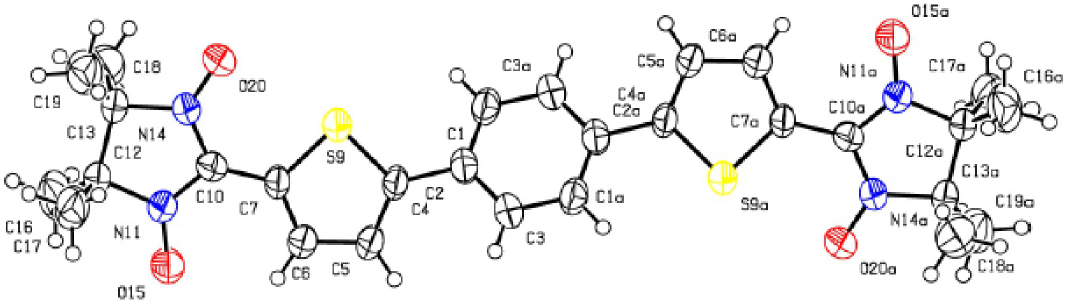

Figure A–II.6: The X-ray crystal structure of the **TPT-NN** and thermal ellipsoids are drawn at 50% probability level**.**

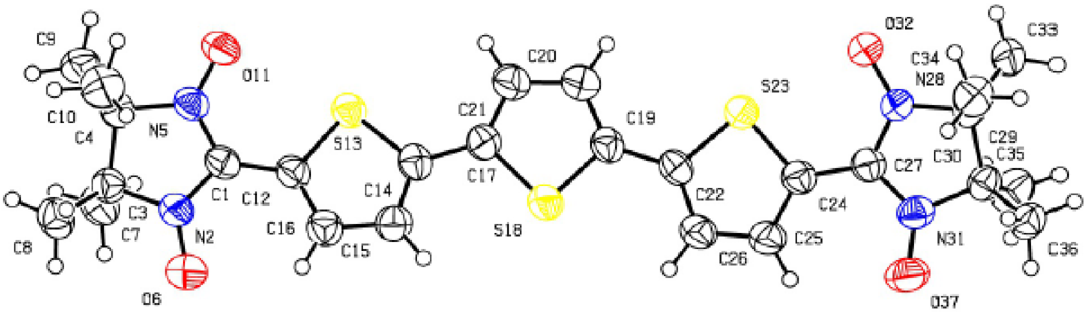

Figure A–II.7: The X-ray crystal structure of the **TTT-NN** and thermal ellipsoids are drawn at 50% probability level.

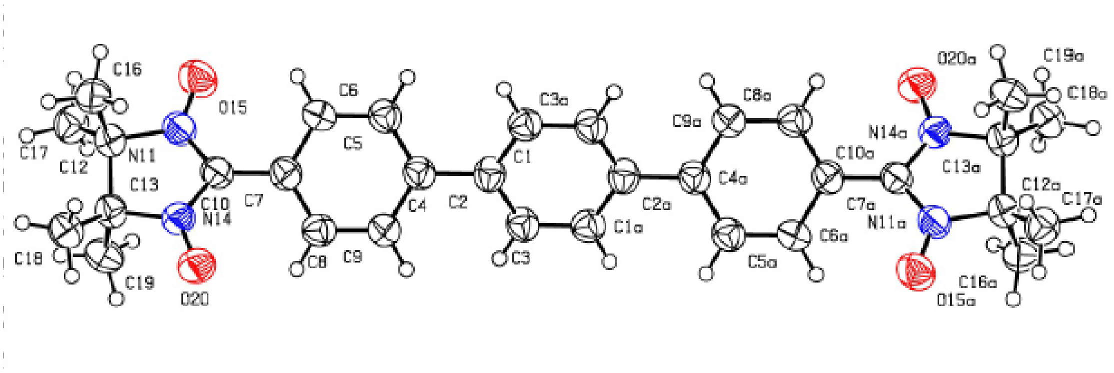

Figure A–II.8: The X-ray crystal structure of the **TPT-NN** and thermal ellipsoids are drawn at 50% probability level.

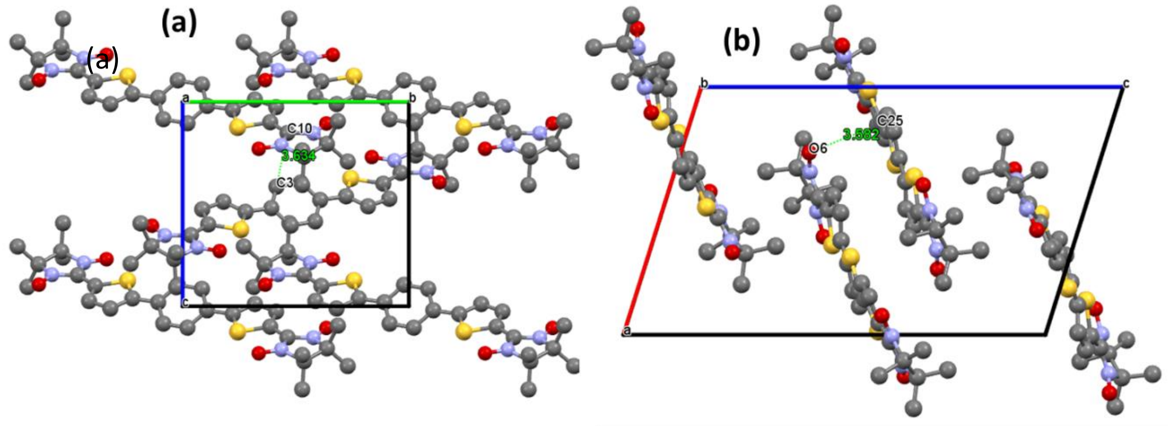

Figure A–II.9: Single crystal molecular packing of (a) **TPT–NN**, along the crystallographic a axis and (b) **TTT-NN**, along the crystallographic b axis; hydrogen atoms are omitted for clarity.

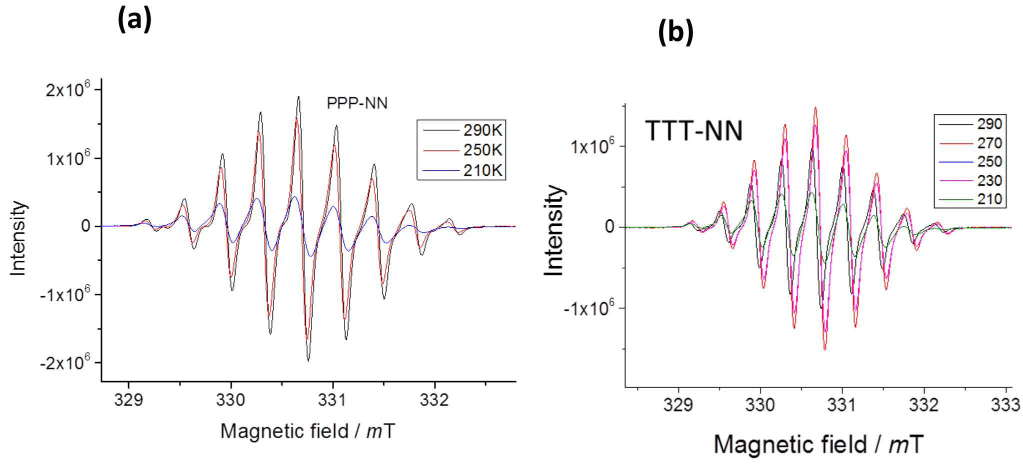

Figure A–II.10: EPR spectra of the biradicals (a) for **PPP-NN** and (b) for **TTT-NN** in toluene (≈10^{-4} M in toluene) variable temperature (290-210 K).

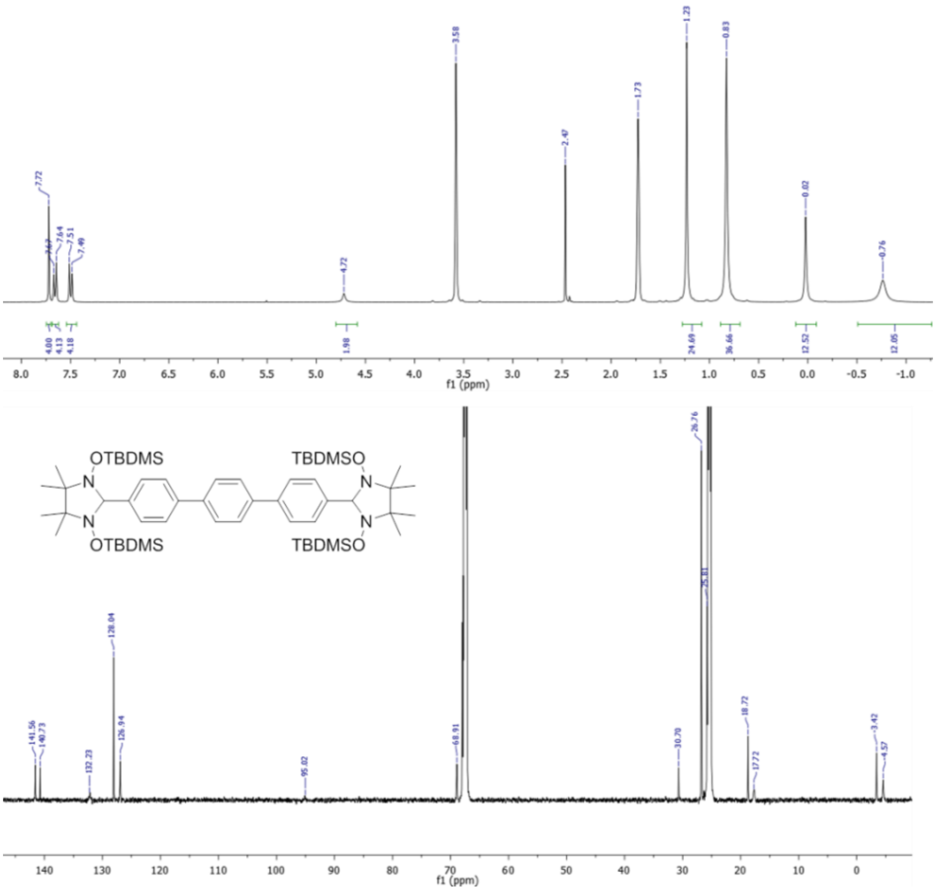

Figure A–II.11: ^{1}H NMR and ^{13}C NMR spectrum of **PPP-NNSi**

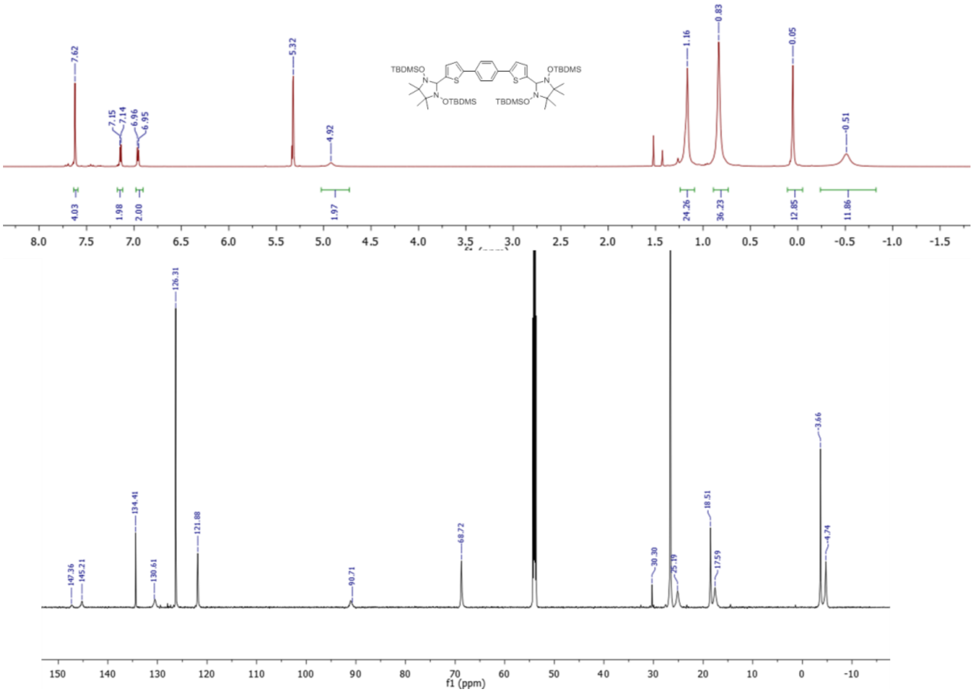

Figure A–II.12: ^{1}H NMR and ^{13}C NMR spectrum of **TPT-NNSi**

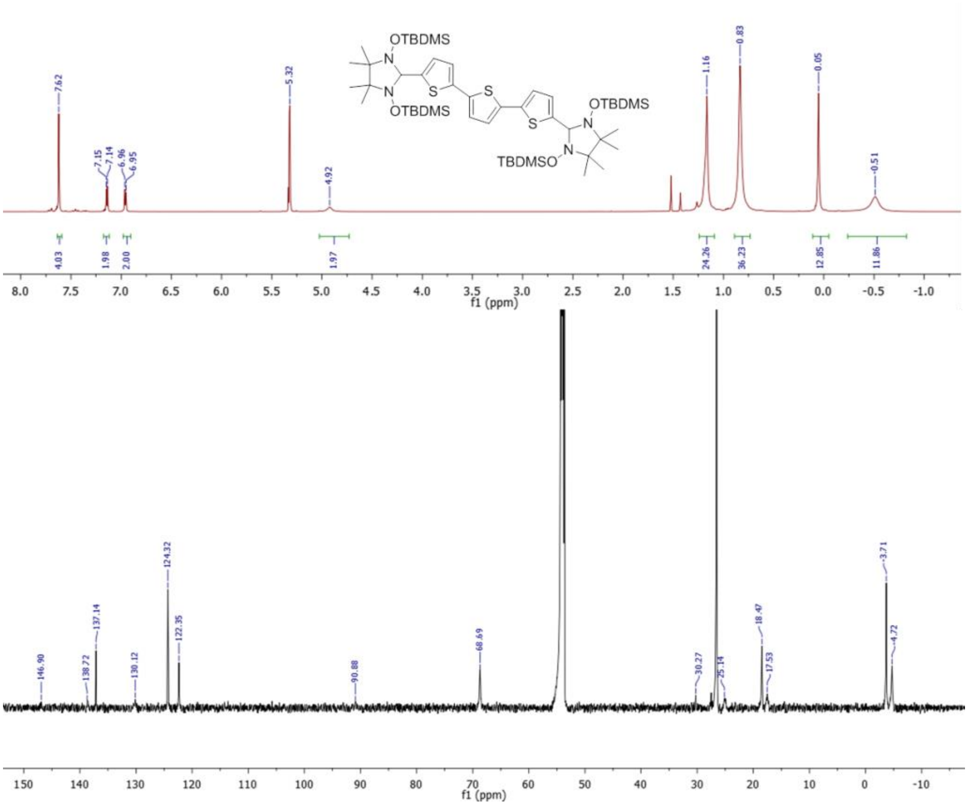

Figure A–II.3: ^{1}H NMR and ^{13}C NMR spectrum of **TTT-NNSi**

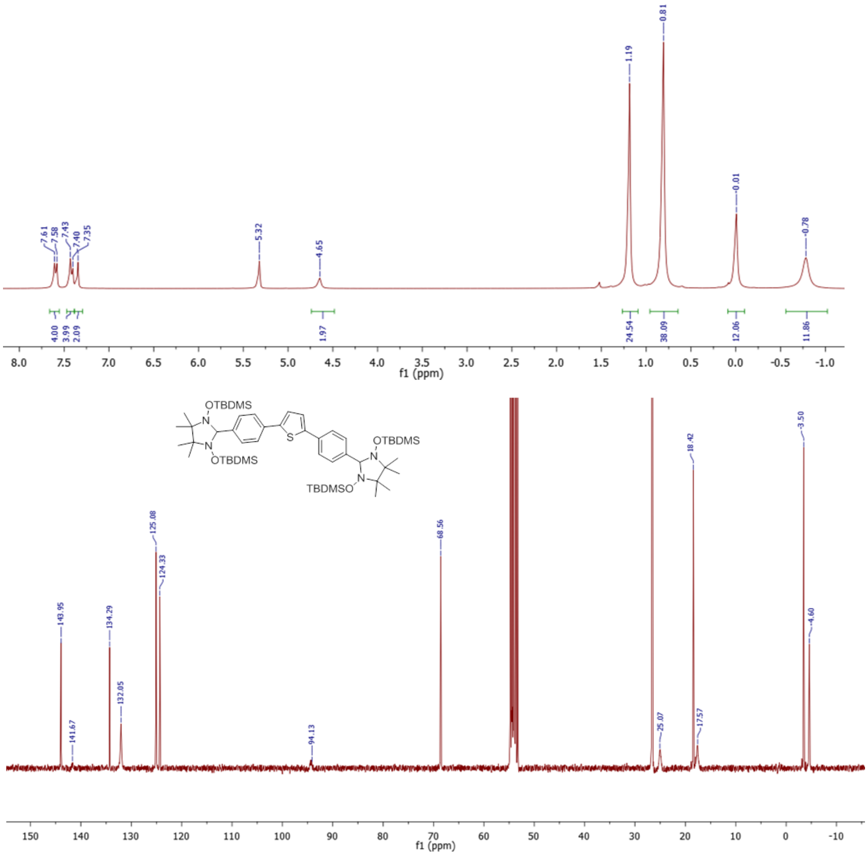

Figure A–II.14: ^{1}H NMR and ^{13}C NMR spectrum of **PTP-NNSi**

13.Calculational Details for DFT calculations using Gaussian 09 (refA-II)

1. **PPP** coordinates of optimized geometry by ub3lyp/6-31g(d)
2. **PTP** coordinates of optimized geometry by ub3lyp/6-31g(d)
3. **TPT** coordinates of optimized geometry by ub3lyp/6-31g(d)
4. **TTT** coordinates of optimized geometry by ub3lyp/6-31g(d)
5. **PPP-NN** coordinates of optimized geometry by ub3lyp/6-31g(d)
6. A triplet energy of **PPP-NN** obtained from optimized structure by using ub3lyp/6-31g(d)
7. A singlet energy of **PPP-NN** obtained from optimized structure by using ub3lyp/6-31g(d)
8. A triplet energy of **PPP-NN** obtained from optimized structure by using ublyp/6-31g(d)
9. A singlet energy of **PPP-NN** obtained from optimized structure by using ublyp/6-31g(d)
10. **PPP-NN** coordinates obtained from X-ray structure
11. A triplet energy of **PPP-NN** obtained from X-ray structure by using ub3lyp/6-31g(d)
12. A singlet energy of **PPP-NN** obtained from X-ray structure by using ub3lyp/6-31g(d)
13. A triplet energy of **PPP-NN** obtained from X-ray structure by using ublyp/6-31g(d)
14. A singlet energy of **PPP-NN** obtained from X-ray structure by using ublyp/6-31g(d)
15. **PTP-NN** coordinates of optimized geometry by ub3lyp/6-31g(d)
16. A triplet energy of **PTP-NN** obtained from optimized structure by using ub3lyp/6-31g(d)
17. A singlet energy of **PTP-NN** obtained from optimized structure by using ub3lyp/6-31g(d)
18. A triplet energy of **PTP-NN** obtained from optimized structure by using ublyp/6-31g(d)
19. A singlet energy of **PTP-NN** obtained from optimized structure by using ublyp/6-31g(d)
20. **TPT-NN** coordinates of optimized geometry by ub3lyp/6-31g(d)
21. A triplet energy of **TPT-NN** obtained from optimized structure by using ub3lyp/6-31g(d)
22. A singlet energy of **TPT-NN** obtained from optimized structure by using ub3lyp/6-31g(d)
23. A triplet energy of **TPT-NN** obtained from optimized structure by using ublyp/6-31g(d)
24. A singlet energy of **TPT-NN** obtained from optimized structure by using ublyp/6-31g(d)
25. **TPT-NN** coordinates from X-ray structure
26. A triplet energy of **TPT-NN** obtained from X-ray structure by using ub3lyp/6-31g(d)

27. A singlet energy of **TPT-NN** obtained from X-ray structure by using ub3lyp/6-31g(d)
28. A triplet energy of **TPT-NN** obtained from X-ray structure by using ublyp/6-31g(d)
29. A singlet energy of **TPT-NN** obtained from X-ray structure by using ublyp/6-31g(d)
30. **TTT-NN** coordinates of optimized geometry by ub3lyp/6-31g(d)
31. A triplet energy of **TTT-NN** obtained from optimized structure by using ub3lyp/6-31g(d)
32. A singlet energy of **TTT-NN** obtained from optimized structure by using ub3lyp/6-31g(d)
33. A triplet energy of **TTT-NN** obtained from optimized structure by using ublyp/6-31g(d)
34. A singlet energy of **TTT-NN** obtained from optimized structure by using ublyp/6-31g(d)
35. **TTT-NN** coordinates from X-ray structure
36. A triplet energy of **TTT-NN** obtained from X-ray structure by using ub3lyp/6-31g(d)
37. A singlet energy of **TTT-NN** obtained from X-ray structure by using ub3lyp/6-31g(d)
38. A triplet energy of **TTT-NN** obtained from X-ray structure by using ublyp/6-31g(d)
39. A singlet energy of **TTT-NN** obtained from X-ray structure by using ublyp/6-31g(d)

1 PPP coordinates of optimized by ub3lyp/6-31g(d)

HF = -694.363745 a.u.

Symbolic Z-matrix: Charge = 0, Multiplicity = 1

2 PTP coordinates of optimized geometry by ub3lyp/6-31g(d)

HF=-1015.121263 a.u.

Symbolic Z-matrix: Charge = 0, Multiplicity = 1

3 TPT coordinates of optimized geometry by ub3lyp/6-31g(d)

HF=-1335.8750761 a.u.

Symbolic Z-matrix: Charge = 0 Multiplicity = 1

4 TTT coordinates of optimized geometry by ub3lyp/6-31g(d)

HF=-1656.6316032 a.u.

Symbolic Z-matrix:

Charge = 0 Multiplicity = 1

5 PPP-NN coordinates of optimized geometry by ub3lyp/6-31g(d)

Charge = 0, multiplicity = 3

6 A triplet energy of **PPP-NN** obtained from optimized structure by using ub3lyp/6-31g(d)

HF=-1760.7887371 a.u.

Charge = 0 Multiplicity = 3

7. A broken symmetry energy of **PPP-NN** obtained from optimized structure by using ub3lyp/6-31g(d)/ guess=mix

HF= -1760.7887719 a.u.

Charge = 0 Multiplicity = 1

8. A triplet energy of **PPP-NN** obtained from optimized structure by using ublyp/6-31g(d)

HF =-1760.0752756 a.u.

Charge = 0 Multiplicity = 3

9. A broken symmetry energy of **PPP-NN** obtained from optimized structure by using ublyp/6-31g(d)/ guess=mix

HF=-1760.075285 a.u.

Charge = 0 Multiplicity = 1

10. **PPP-NN** coordinates obtained from X-ray structure

11. A triplet energy of **PPP-NN** obtained from X-ray structure by using ub3lyp/6-31g(d)

HF=-1760.3465866 a.u.

Charge = 0 Multiplicity = 3

12. A broken symmetry energy of **PPP-NN** obtained from X-ray structure by using ub3lyp/6-31g(d)/ guess=mix

HF=-1760.3466155 a.u.

Charge = 0 Multiplicity = 1

13. A triplet energy of **PPP-NN** obtained from X-ray structure by using ublyp/6-31g(d)

HF=-1759.5943813 a.u.

Charge = 0 Multiplicity = 3

14. A broken symmetry energy of **PPP-NN** obtained from X-ray structure by using ublyp/6-31g(d)/guess=mix

HF=-1759.5943894 a.u.

Charge = 0 Multiplicity = 1

15. **PTP-NN** optimized geometry by ub3lyp/6-31g(d)

16. A triplet energy of **PTP-NN** obtained from optimized structure by using ub3lyp/6-31g(d)

HF=-2081.5467692 a.u.

Charge = 0 Multiplicity = 3

17. A broken symmetry energy of **PTP-NN** obtained from optimized structure by using ub3lyp/6-31g(d)/ guess=mix

HF=-2081.5468615 a.u.

Charge = 0 Multiplicity = 1

18. A triplet energy of **PTP-NN** obtained from optimized structure by using ublyp/6-31g(d)

HF=-2080.8586481 a.u.

Charge = 0 Multiplicity = 3

19. A boken symmetry energy of **PTP-NN** obtained from optimized structure by using ublyp/6-31g(d)/guess=mix

HF=-2080.8586717 a.u.

Charge = 0 Multiplicity = 1

20. TPT-NN obtained from optimized structure ub3lyp/6-31g(d)

21. A triplet energy of **TPT-NN** obtained from optimized structure by using ub3lyp/6-31g(d)

HF=-2402.3108758 a.u.

Symbolic Z-matrix:

Charge = 0 Multiplicity = 3

22. A broken symmetry energy of **TPT-NN** obtained from optimized structure by using ub3lyp/6-31g(d)/guess=mix

HF=-2402.3110155 a.u.

Charge = 0 Multiplicity = 1

23. A triplet energy of **TPT-NN** obtained from optimized structure by using ublyp/6-31g(d)

HF=-2401.6482346 a.u.

Charge = 0 Multiplicity = 3

24. A broken symmetry energy of **TPT-NN** obtained from optimized structure by using ublyp/6-31g(d)/guess=mix

HF=-2401.6482693 a.u.

Charge = 0 Multiplicity = 1

25. TPT-NN coordinates obtained from X-ray structure

26. A triplet energy of **TPT-NN** obtained from X-ray structure by using ub3lyp/6-31g(d)

HF=-2401.7695769 a.u.

Charge = 0 Multiplicity = 3

27. A broken symmetry energy of **TPT-NN** obtained from X-ray structure by using ub3lyp/6-31g(d)/guess=mix

HF=-2401.7696401 a.u.

Charge = 0 Multiplicity = 1

28. A triplet energy of **TPT-NN** obtained from X-ray structure by using ublyp/6-31g(d)

HF=-2401.0605098 a.u.

29. A broken symmetry energy of **TPT-NN** obtained from X-ray structure by using ublyp/6-31g(d)/guess=mix

HF=-2401.0605266 a.u.

30. **TTT-NN** optimized geometry by using ub3lyp/6-31g(d)

31. A triplet energy of **TTT-NN** obtained from optimized structure by using ub3lyp/6-31g(d)

HF=-2723.0685795 a.u.

Charge = 0 Multiplicity = 3

32. A broken symmetry energy of **TTT-NN** obtained from optimized structure by using ub3lyp/6-31g(d)/guess=mix

HF=-2723.0688954 a.u.

Charge = 0 Multiplicity = 1

33. A triplet energy of **TTT-NN** obtained from optimized structure by using ublyp/6-31g(d)

HF=-2722.4314504 a.u.

Charge = 0 Multiplicity = 3

34. A broken symmetry energy of **TTT-NN** obtained from optimized structure by using ublyp/6-31g(d)/guess=mix

HF=-2722.4315208 a.u.

Charge = 0 Multiplicity = 1

35. **TTT-NN** coordinates obtained from X-ray structure

36. A triplet energy of **TTT-NN** obtained from X-ray structure by using ub3lyp/6-31g(d)

HF=-2722.7224882 a.u.

Charge = 0 Multiplicity = 3

37. A broken symmetry energy of **TTT-NN** obtained from X-ray structure by using ub3lyp/6-31g(d)/guess=mix

HF=-2722.7226605 a.u.

Charge = 0 Multiplicity = 1

38. A triplet energy of **TTT-NN** obtained from X-ray structure by using ublyp/6-31g(d)

HF=-2721.5401807 a.u.

39. A broken symmetry energy of **TTT-NN** obtained from X-ray structure by using ublyp/6-31g(d)/guess=mix

HF=-2721.5402271 a.u.

Reference A-II

Gaussian 09, Revision D.01: M. J. Frisch, G. W. Trucks, H. B. Schlegel, G. E. Scuseria, M. A. Robb, J. R. Cheeseman, G. Scalmani, V. Barone, B. Mennucci, G. A. Petersson, H. Nakatsuji, M. Caricato, X. Li, H. P. Hratchian, A. F. Izmaylov, J. Bloino, G. Zheng, J. L. Sonnenberg, M. Hada, M. Ehara, K. Toyota, R. Fukuda, J. Hasegawa, M. Ishida, T. Nakajima, Y. Honda, O. Kitao, H. Nakai, T. Vreven, J. A. Montgomery, Jr., J. E. Peralta, F. Ogliaro, M. Bearpark, J. J. Heyd, E. Brothers, K. N. Kudin, V. N. Staroverov, T. Keith, R. Kobayashi, J. Normand, K. Raghavachari, A. Rendell, J. C. Burant, S. S. Iyengar, J. Tomasi, M. Cossi,

N. Rega, J. M. Millam, M. Klene, J. E. Knox, J. B. Cross, V. Bakken, C. Adamo, J. Jaramillo, R. Gomperts, R. E. Stratmann, O. Yazyev, A. J. Austin, R. Cammi, C. Pomelli, J. W. Ochterski, R. L. Martin, K. Morokuma, V. G. Zakrzewski, G. A. Voth, P. Salvador, J. J. Dannenberg, S. Dapprich, A. D. Daniels, O. Farkas, J. B. Foresman, J. V. Ortiz, J. Cioslowski, and D. J. Fox, Gaussian, Inc., Wallingford CT, 2013.

Table A-III.1: Crystal data for **BDT**

formula	$C_{12}H_{10}O_2S_2$		
CCDC	1862382		
molecular weight	250.32 gmol^{-1}		
absorption	μ = 0.46 mm^{-1} corrected with 7 crystal faces		
transmission	T_{min} = 0.835, T_{max} = 0.9449		
crystal size	0.12 x 0.26 x 0.80 mm^3 colourless block		
space group	P 2_1/n (monoclinic)		
lattice parameters	a =7.9063(9)Å		
(calculate from	b =8.9584(7)Å	ß = 99.907(9)°	
5977 reflections with	c =7.9434(10)Å		
2.6° < θ < 28.1°)	V = 554.23(10)Å^3	z = 2	F(000) = 260.0
temperature	-80°C		
density	d_{xray} = 1.500 gcm^{-3}		

data collection

diffractometer	STOE IPDS 2T
radiation	Mo-K_α Graphitmonochromator
Scan – type	ω scans
Scan – width	1°
scan range	2° $\leq \theta <$ 28°
	-10 ≤ h ≤ 10 -11 ≤ k ≤ 11 -10 ≤ l ≤ 10
number of reflections:	
measured	3411
unique	1337 (R_{int} = 0.0143)
observed	1233 (|F|/σ(F) > 4.0)

data correction, structure solution and refinement

corrections	Lorentz and polarisation correction.
Structure solution	Program: SIR-2004 (Direct methods)
refinement	Program: SHELXL-2014 (full matrix). 91 refined parameters, weighting scheme: $w=1/[\sigma^2(F_o^2) + (0.0492*P)^2+0.18*P]$ with $(Max(F_o^2,0)+2*F_c^2)/3$. H-atoms refined with isotropic displacement parameters, non H- atoms refined anisotropically.
R-values	wR2 = 0.0788 (R1 = 0.0286 for observed reflections, 0.0313 for all reflections)
goodness of fit	S = 1.049
maximum deviation of parameters	0.001 * e.s.d
maximum peak height in diff. Fourier synthesis	0.42, -0.29 eÅ^{-3}
remark	molecule has C_i symmetry.

Table A-III.2: Crystal data for **BDTTh$_2$–NNSi**

formula	$C_{58}H_{98}N_4O_6S_4Si_4$		
CCDC	1862542		
molecular weight	1188.00 gmol^{-1}		
absorption	μ = 0.242 mm^{-1} corrected with 7 crystal faces		
transmission	T_{min} = 0.8354, T_{max} = 0.9739		
crystal size	0.07 x 0.16 x 0.740 mm^3 yellow needle		
space group	C 2/c (monoclinic)		
lattice parameters	a =48.0321(15)Å		
(calculate from	b =10.6191(2)Å	ß = 98.054(3)°	
17282 reflections with	c =14.3112(5)Å		
2.3° < θ < 28.5°)	V = 7227.5(4)Å^3	z = 4	F(000) = 2568
temperature	-80°C		
density	d_{xray} = 1.092 gcm^{-3}		

data collection

diffractometer	STOE IPDS 2T
radiation	Mo-K_α Graphitmonochromator
Scan – type	ω scans
Scan – width	1°
scan range	2° ≤ θ < 28° -64 ≤ h ≤ 64 -13 ≤ k ≤ 13 -19 ≤ l ≤ 15
number of reflections:	
measured	23614
unique	9067 (R_{int} = 0.0308)
observed	6185 (|F|/σ(F) > 4.0)

data correction, structure solution and refinement

corrections	Lorentz and polarisation correction.
Structure solution	Program: SIR-2004 (Direct methods)
refinement	Program: SHELXL-2014 (full matrix). 383 refined parameters, weighting scheme: $w=1/[\sigma^2(F_o^2) + (0.0614*P)^2]$ with $(Max(F_o^2,0)+2*F_c^2)/3$. H-atoms at calculated positions and refined with isotropic displacement parameters, non H-atoms refined anisotropically.
R-values	wR2 = 0.1077 (R1 = 0.0401 for observed reflections, 0.0660 for all reflections)
goodness of fit	S = 0.969
maximum deviation of parameters	0.001 * e.s.d
maximum peak height in diff. Fourier synthesis	0.29, -0.33 eÅ^{-3}
remark	molecule has C_i symmetry, crystal contains solvens (probably CH_2Cl_2) which could not be refined, SQUEEZE was used. Some CH_3 are disordered.

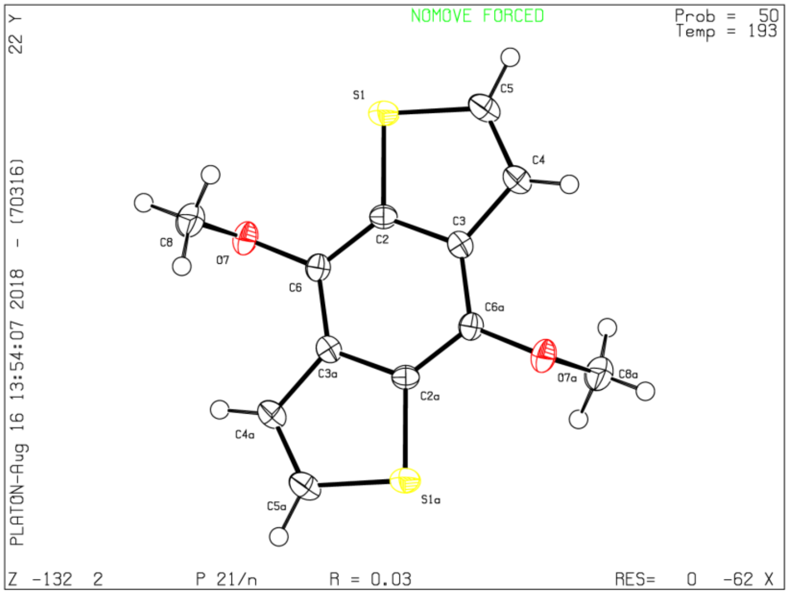

Figure A–III.1: The X-ray structure of thermal ellipsoid plot for **BDT.**

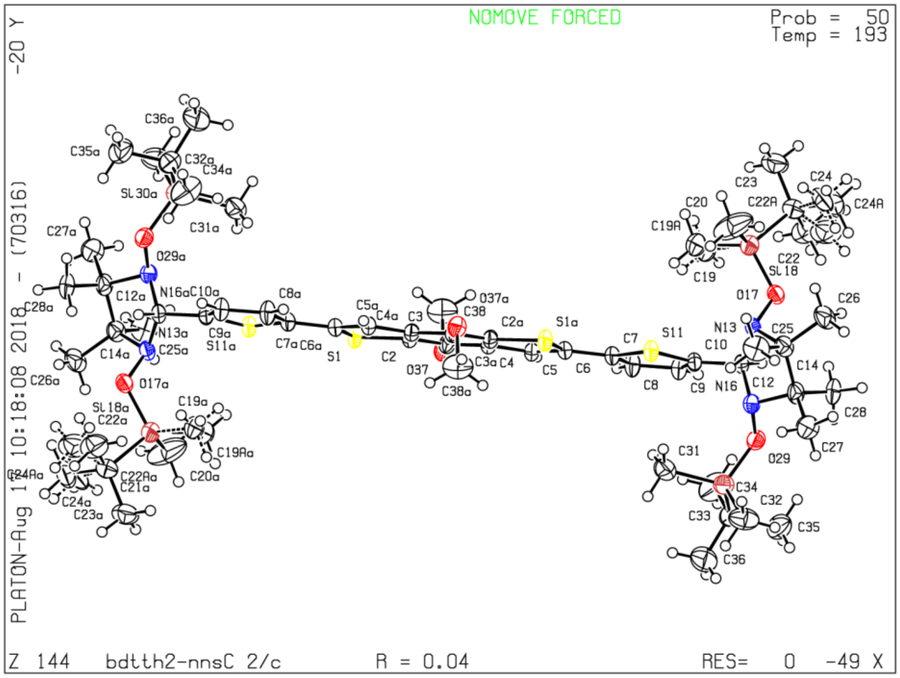

Figure A–III.2: The X-ray structure of thermal ellipsoid plot for **BDTTh2–NNSi**

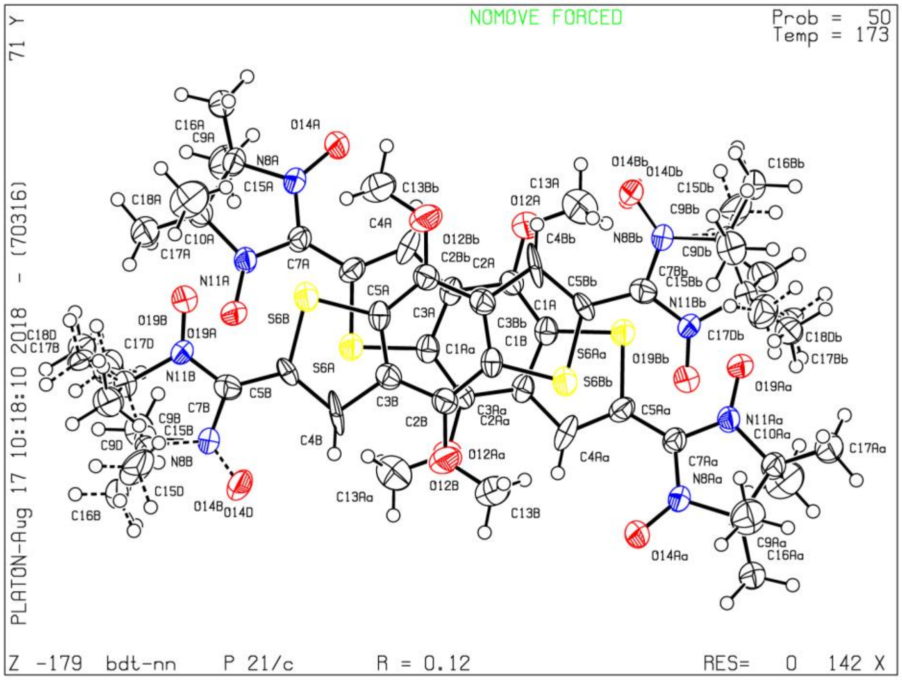

Figure A–III.3: The X-ray structure of thermal ellipsoid plot for **BDT–NN**

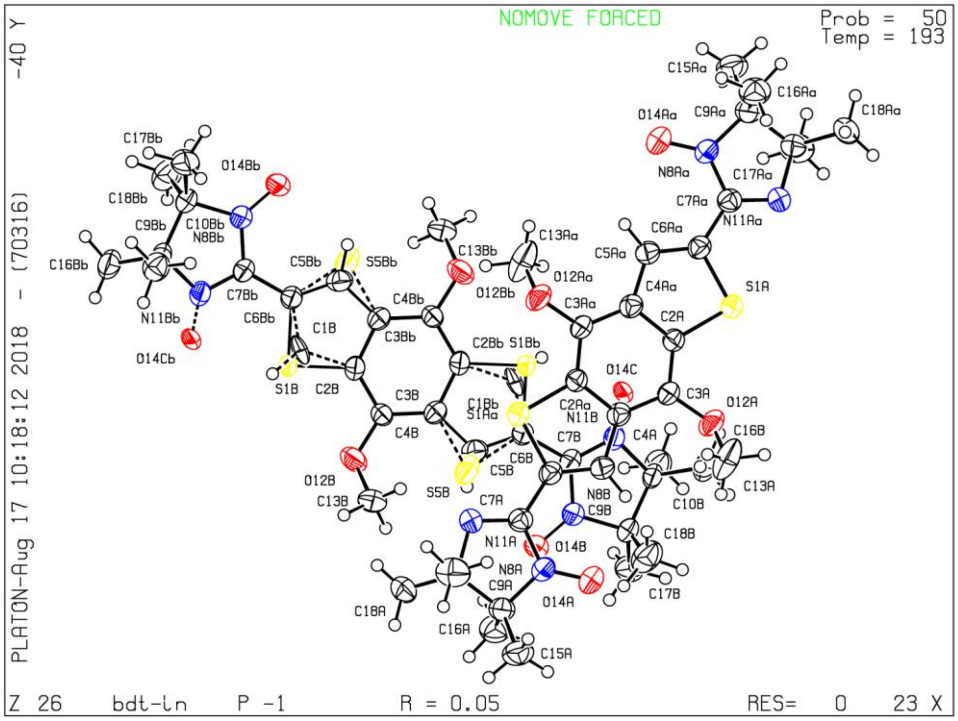

Figure A–III.4: The X-ray structure of thermal ellipsoid plot for **BDT–IN**

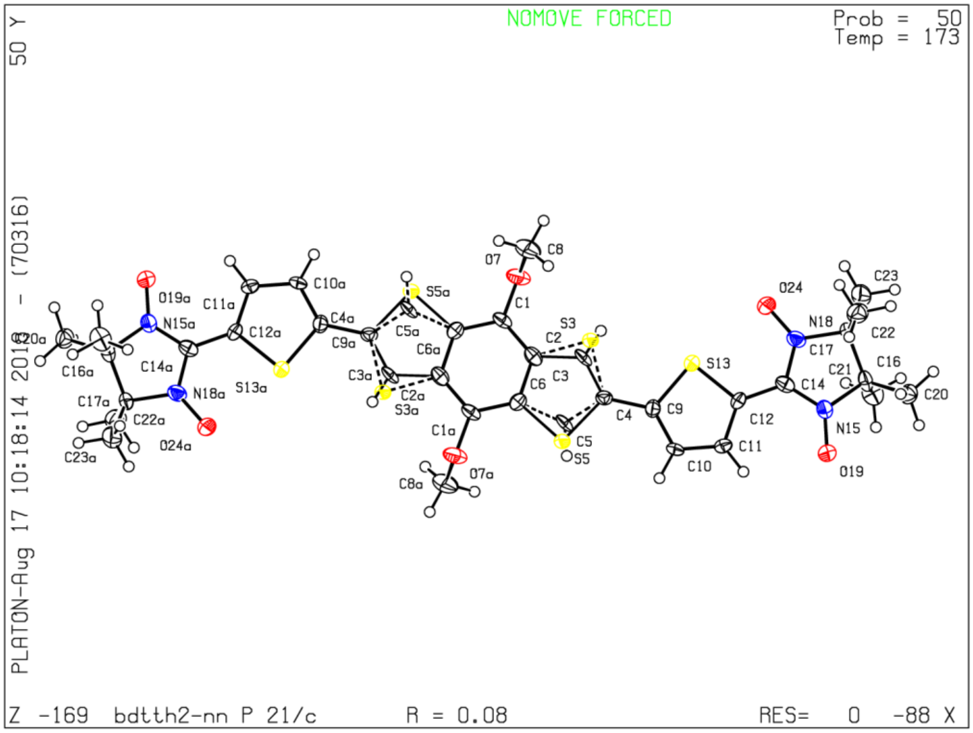

Figure A–III.5: The X-ray structure of thermal ellipsoid plot for the **BDTTh₂-NN**

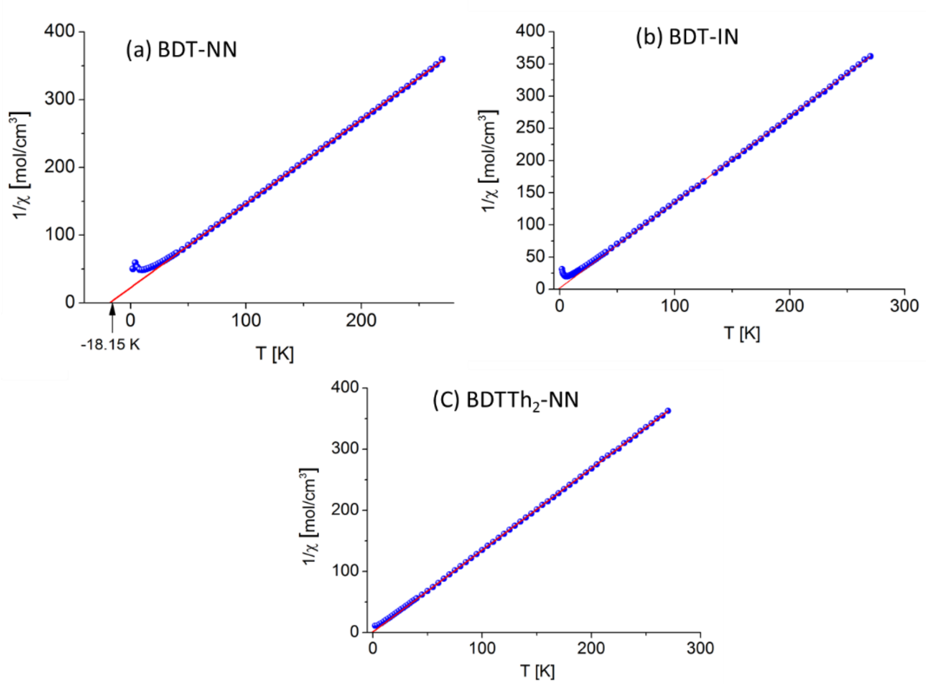

Figure A–III.6: Curie–Weiss model straight line of **BDT-NN, BDT-IN**, and **TBDTT-NN.**

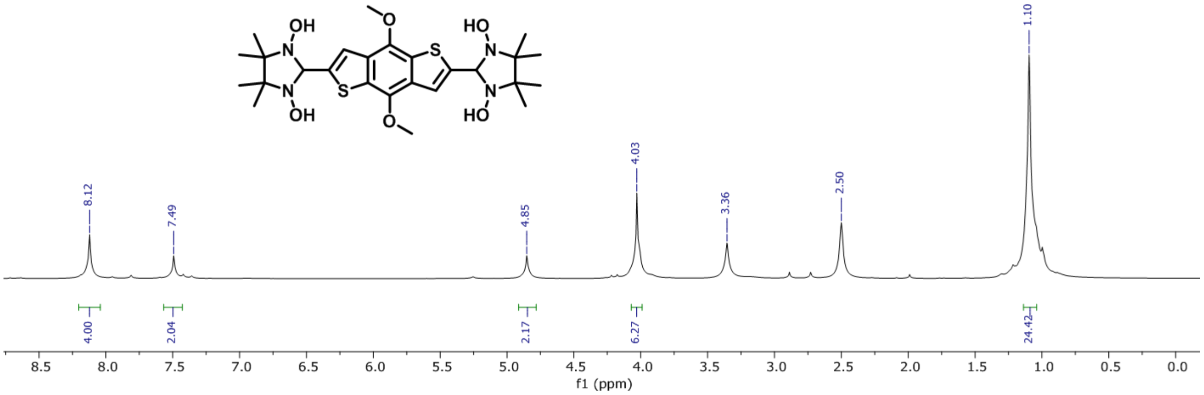

Figure A–III.7: ^{1}H NMR spectrum of **4**

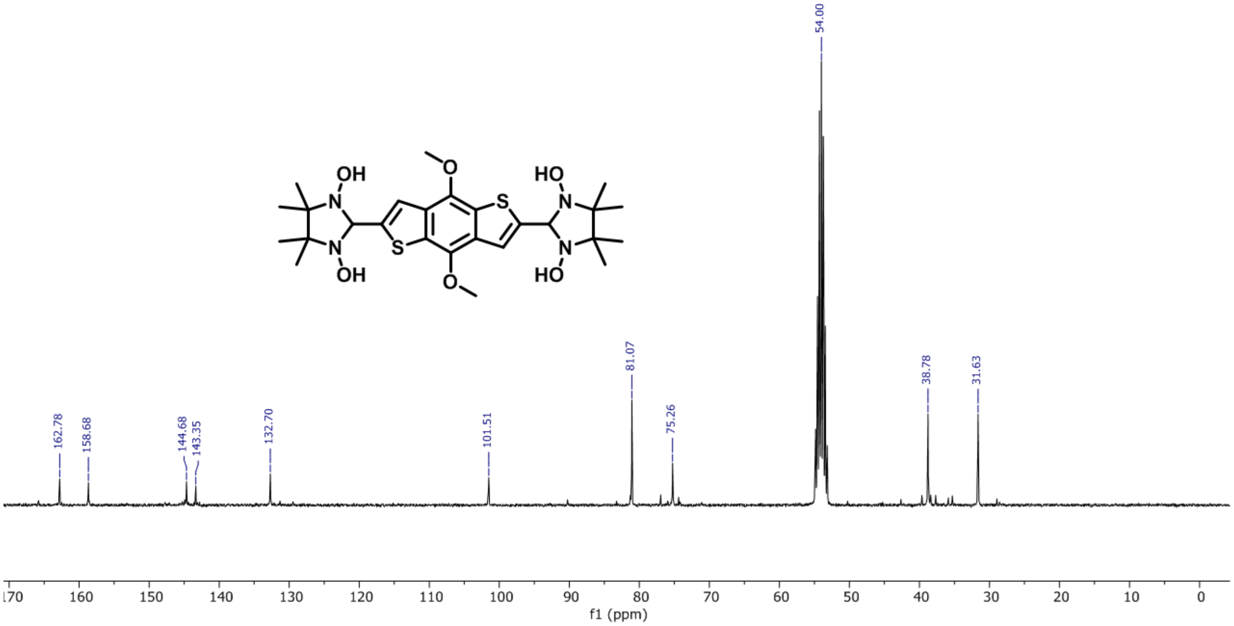

Figure A–III.8: ^{13}C NMR spectrum of **4**

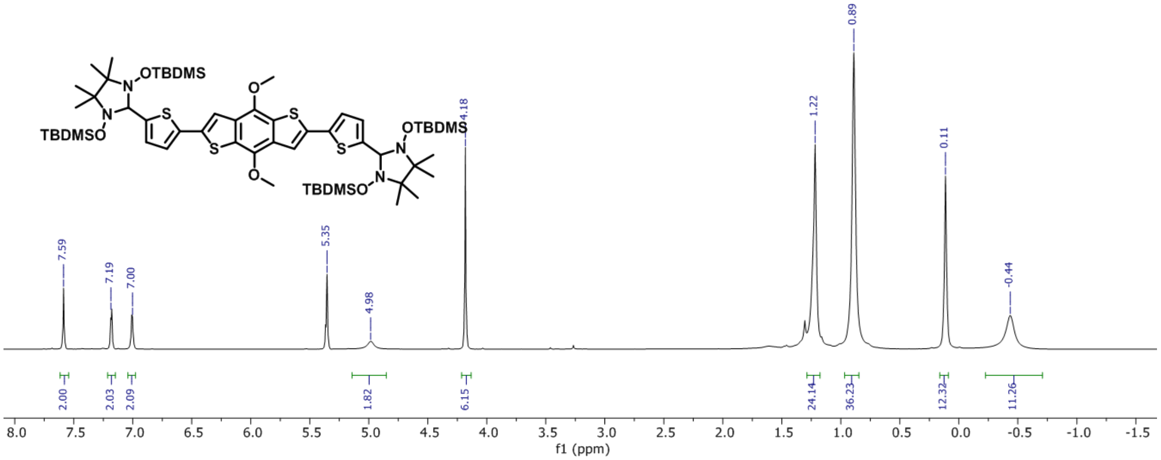

Figure A–III.9: ^{1}H NMR spectrum of **BDTTh$_2$NNSi**

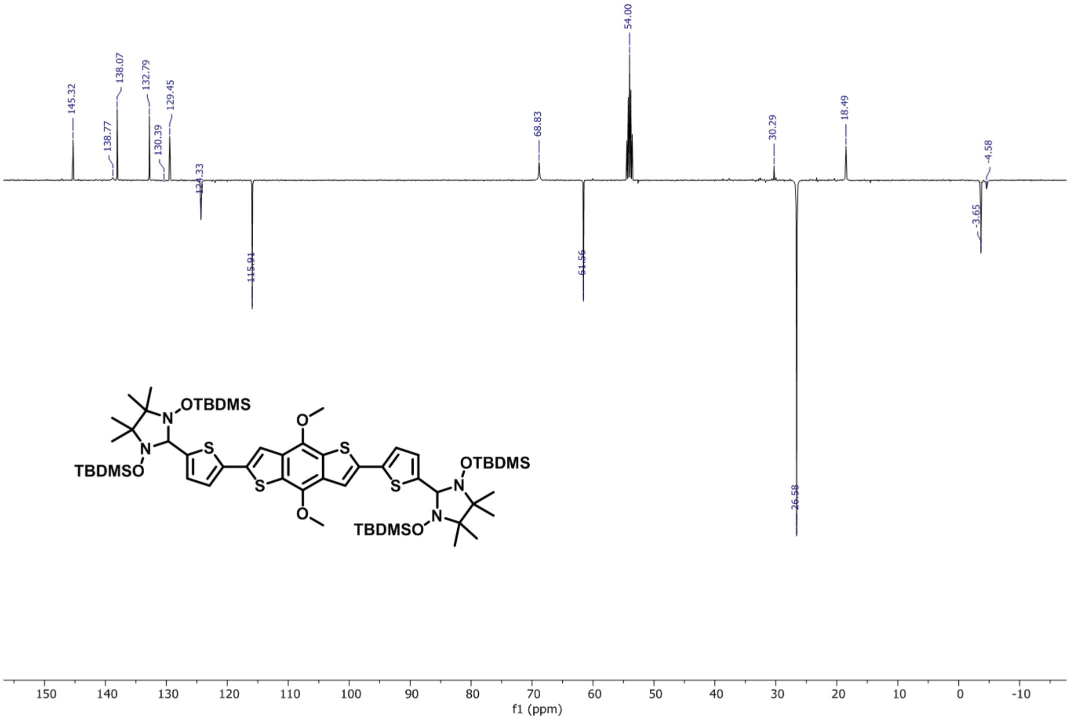

Figure A–III.10: ^{13}C NMR spectrum of **BDTTh2NNSi**

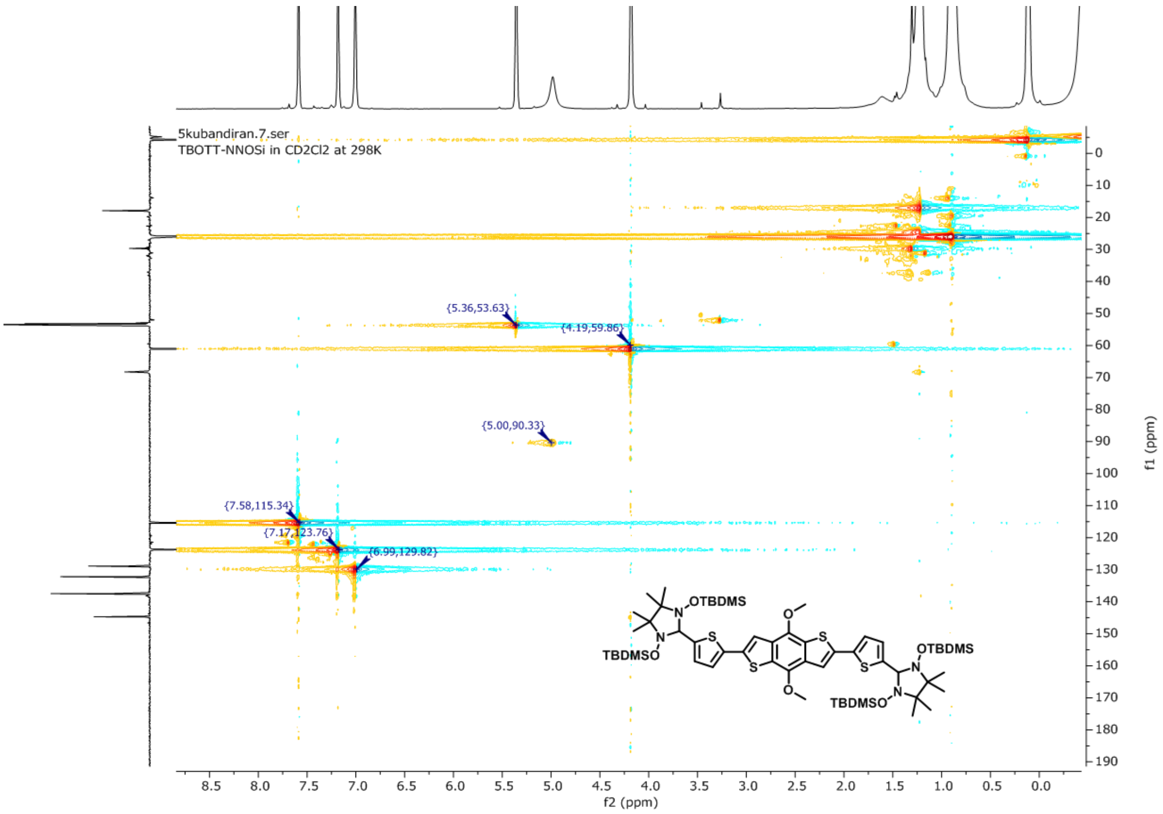

Figure A–III.11: HSQC, 2D-NMR spectrum of **BDTTh2NNSi**

10. DETAILS FOR DFT CALCULATIONS USING GAUSSIAN 09

BDT coordinates of optimized geometry by ub3lyp/6-31g(d)

HF = -1410.0847611 a.u.

Symbolic Z-matrix: Charge = 0 Multiplicity = 1

BDTTh$_2$ coordinates of optimized geometry by ub3lyp/6-31g(d)

HF = -2513.7215829 a.u.

Symbolic Z-matrix: Charge = 0 Multiplicity = 3

BDT-NN coordinates obtained from X-ray structure

A triplet energy of BDT-NN obtained from X-ray structure by using ublyp/6-31g(d) for intra molecular magnetic interaction.

HF = -2474.9270168 a.u.

Symbolic Z-matrix: Charge = 0 Multiplicity = 3

A singlet energy of BDT-NN obtained from X-ray structure by using ublyp/6-31g(d) for intra molecular magnetic interaction.

HF = -2474.9272117 a.u.

Symbolic Z-matrix: Charge = 0 Multiplicity = 1

BDT-IN coordinates obtained from X-ray structure

A triplet energy of **BDT-IN** obtained from X-ray structure by using ublyp/6-31g(d) for intra molecular magnetic interaction

HF = - 2325.134789 a.u.

Symbolic Z-matrix: Charge = 0 Multiplicity = 3

A singlet energy of **BDT-IN** obtained from X-ray structure by using ublyp/6-31g(d) for intra molecular magnetic interaction

HF = -2325.1348008 a.u.

Symbolic Z-matrix: Charge = 0 Multiplicity = 1

BDTTh$_2$-NN coordinates obtained from X-ray structure

A triplet energy of BDTTh2-NN obtained from X-ray structure by using ublyp/6-31g(d) for intra molecular magnetic interaction

HF= -3578.8089823 a.u.
Symbolic Z-matrix: Charge = 0 Multiplicity = 3

A singlet energy of BDTTh2-NN obtained from X-ray structure by using ublyp/6-31g(d) for intra molecular magnetic interaction.

HF = -3578.8089998 a.u.
Symbolic Z-matrix: Charge = 0 Multiplicity = 1

BDTTh$_2$-IN coordinates obtained from X-ray structure

A triplet energy of BDTTh2-IN obtained from X-ray structure by using ublyp/6-31g(d) for intra molecular magnetic interaction

HF = -3428.4454084 a.u.
Symbolic Z-matrix: Charge = 0 Multiplicity = 3

A singlet energy of BDTTh2-IN obtained from X-ray structure by using ublyp/6-31g(d) for intra molecular magnetic interaction.

HF = -3428.4454126 a.u.

Symbolic Z-matrix: Charge = 0 Multiplicity = 1

BDT-NN dimer structure coordinates obtained from X-ray structure

A triplet energy of **BDT-NN** of dimer structure obtained from X-ray structure by using ublyp/6-31g(d) for intermolecular magnetic interaction.

HF = -3885.1135234 a.u.
Symbolic Z-matrix: Charge = 0 Multiplicity = 3

A singlet energy of **BDT-NN** of dimer structures obtained from X-ray structure by using ublyp/6-31g(d) for intermolecular magnetic interaction.

HF = -3885.1135539 a.u.

Symbolic Z-matrix: Charge = 0 Multiplicity = 3

BDT-IN dimer structure coordinates obtained from X-ray structure

A triplet energy of **BDT-IN** of dimer structures obtained from X-ray structure by using ublyp/6-31g(d) for intermolecular magnetic interaction.

Symbolic Z-matrix: Charge = 0 Multiplicity = 3

HF = -3734.8356343 a.u.

A singlet energy of **BDT-IN** of dimer structures obtained from X-ray structure by using ublyp/6-31g(d) for intermolecular magnetic interaction.
HF = -3734.8356525 a.u.
Symbolic Z-matrix: Charge = 0 Multiplicity = 1

BDTTh$_2$-NN dimer structure coordinates obtained from X-ray structure

A triplet energy of **BDTTh$_2$-NN** obtained from X-ray structure by using ublyp/6-31g(d) for intermolecular magnetic interaction.
HF = -6091.8092971 a.u.
Symbolic Z-matrix: Charge = 0 Multiplicity = 3

A singlet energy of **BDTTh$_2$-NN** obtained from X-ray structure by using ublyp/6-31g(d) for intermolecular magnetic interaction.

HF = -6091.8093104 a.u.
Symbolic Z-matrix: Charge = 0 Multiplicity = 1

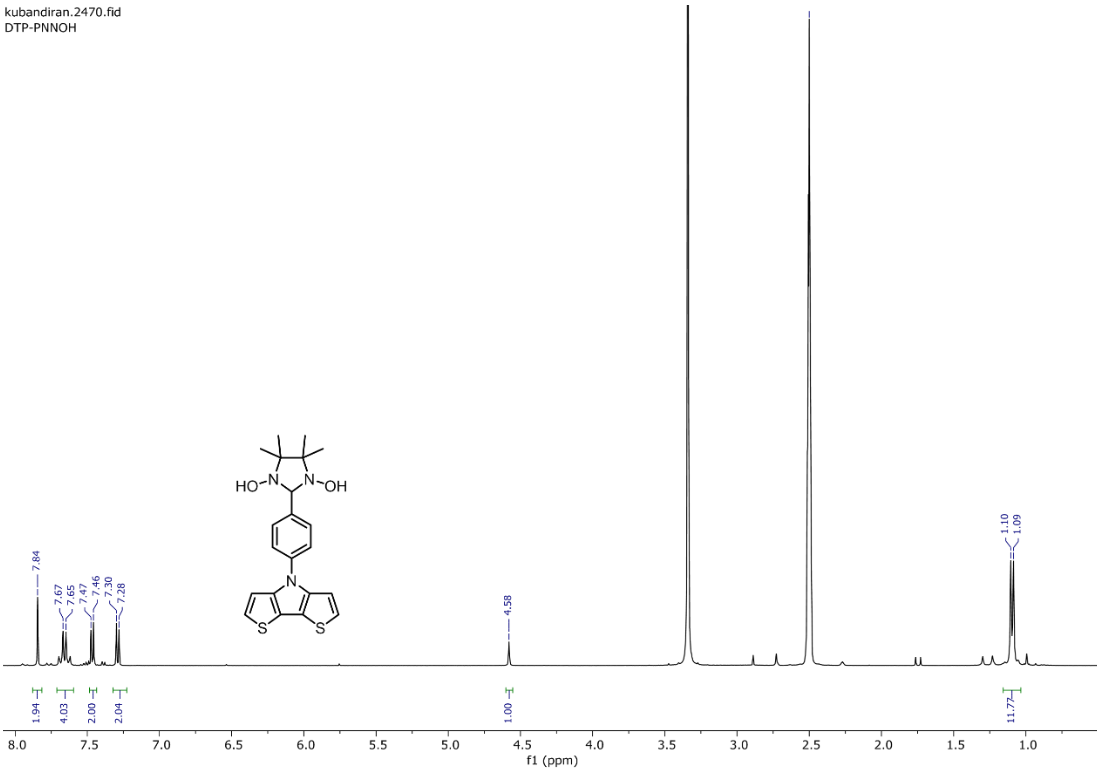

Figure A–IV.1: ^{1}H NMR spectrum of **4**

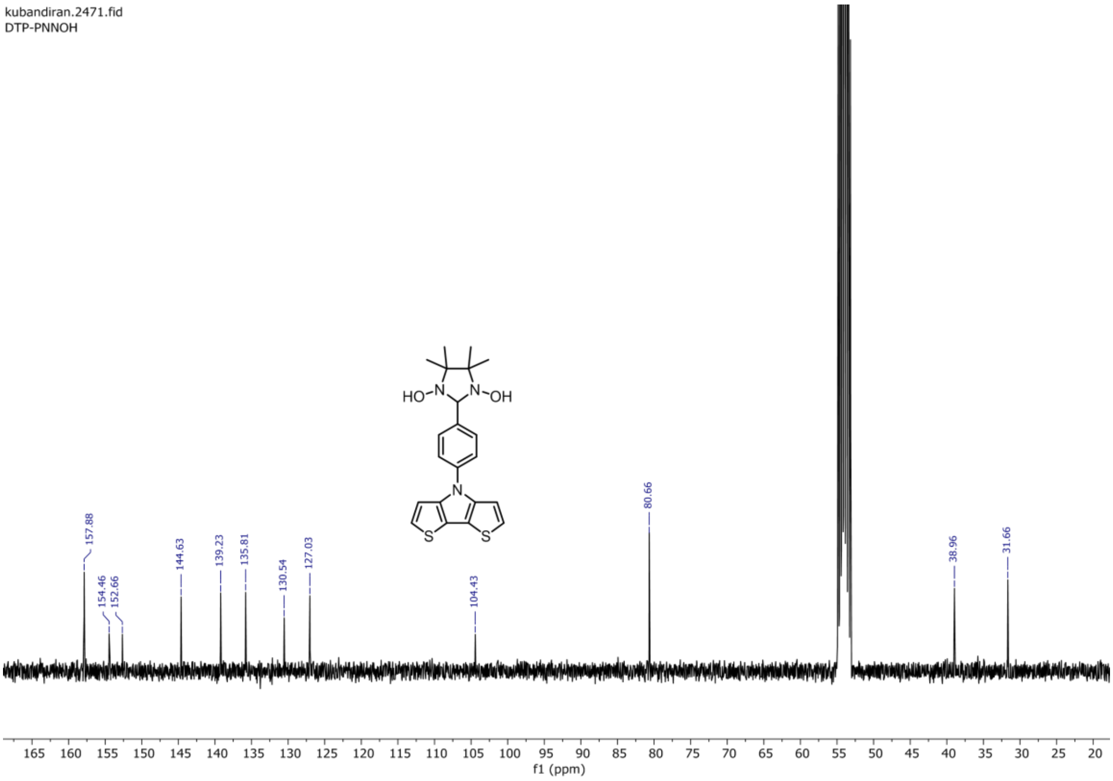

Figure A–IV.2: ^{13}C NMR spectrum of **4**

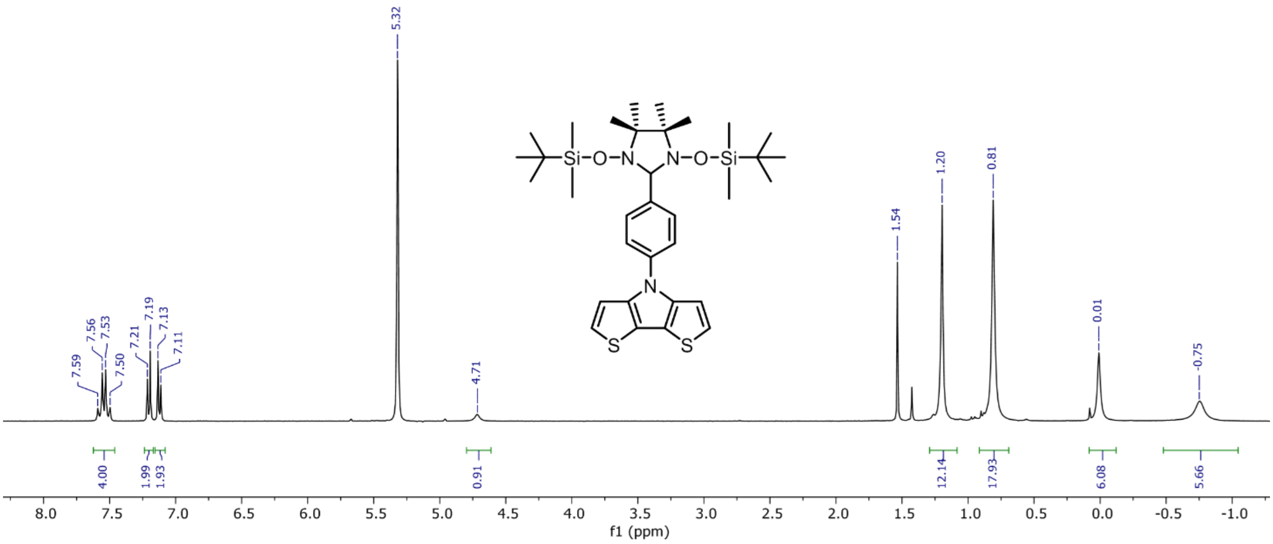

Figure A–IV.3: ^{1}H NMR spectrum of **5**

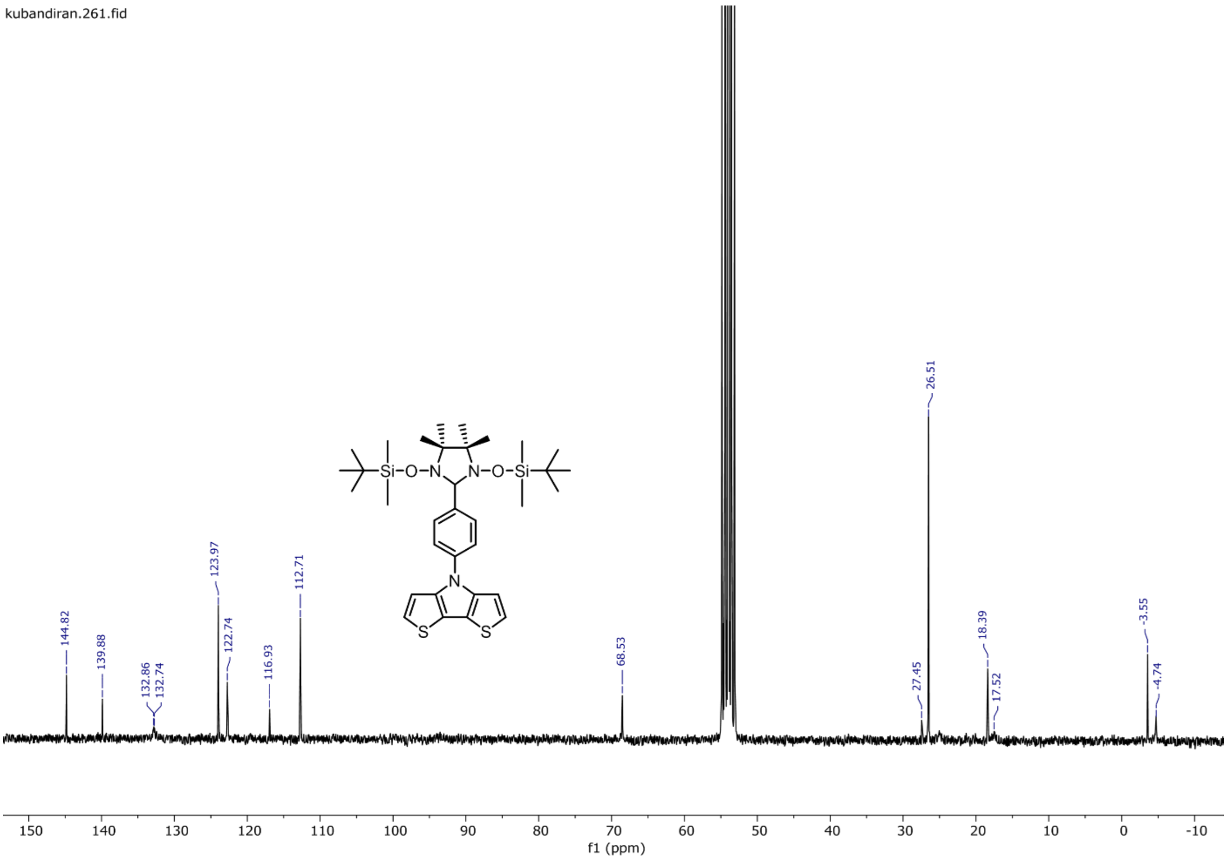

Figure A–IV.4: ^{13}C NMR spectrum of **5**

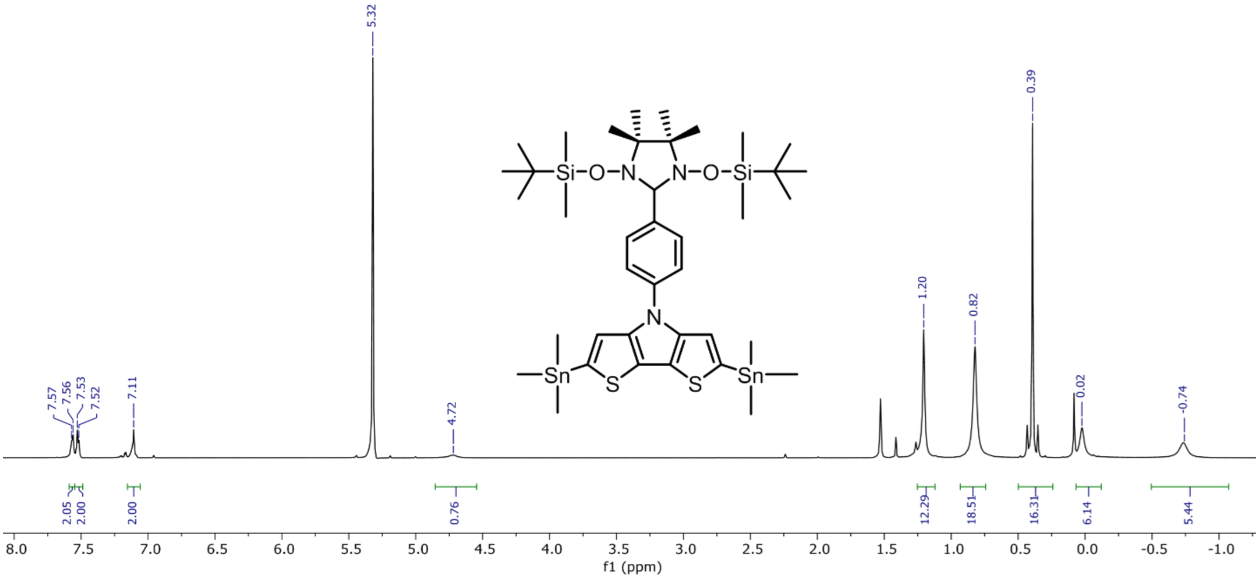

Figure A–IV.5: ^{1}H NMR spectrum of **5**

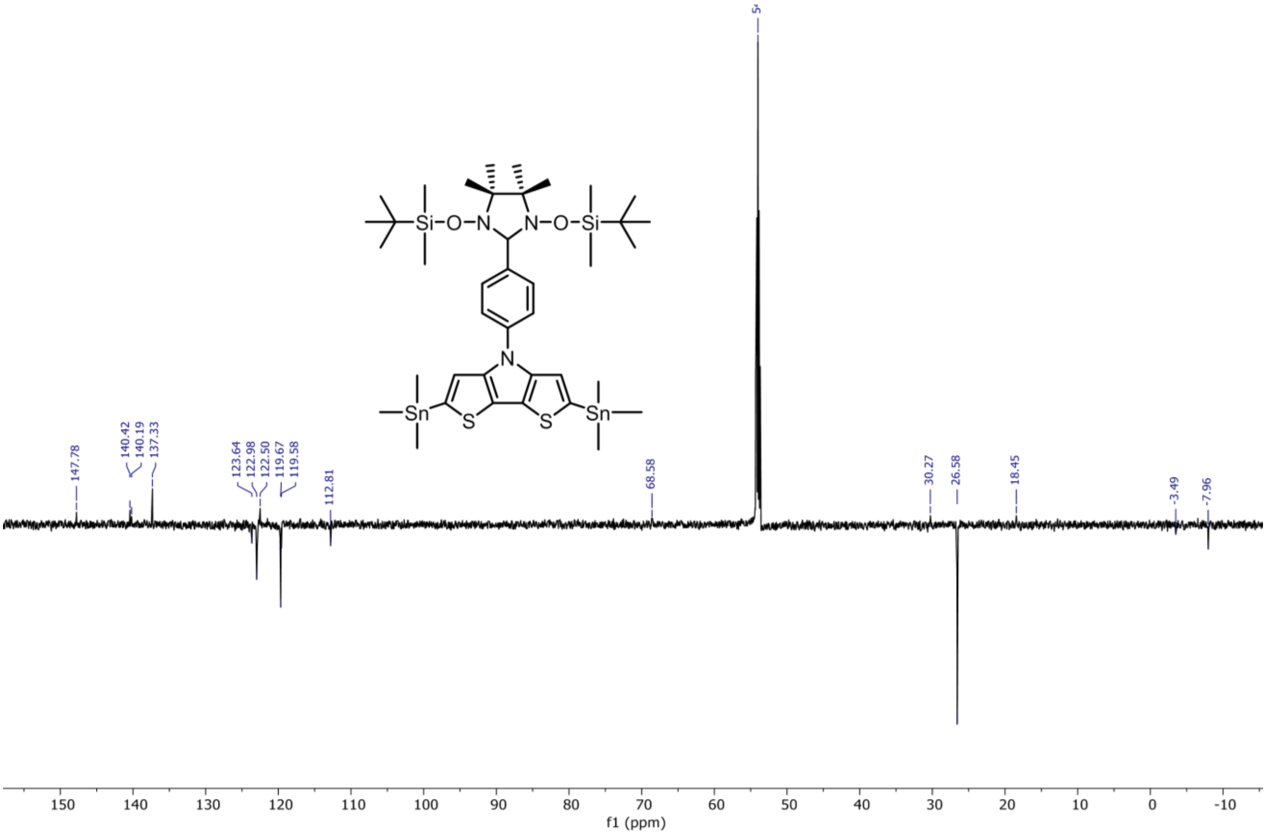

Figure A–IV.6: ^{13}C NMR spectrum of **5**

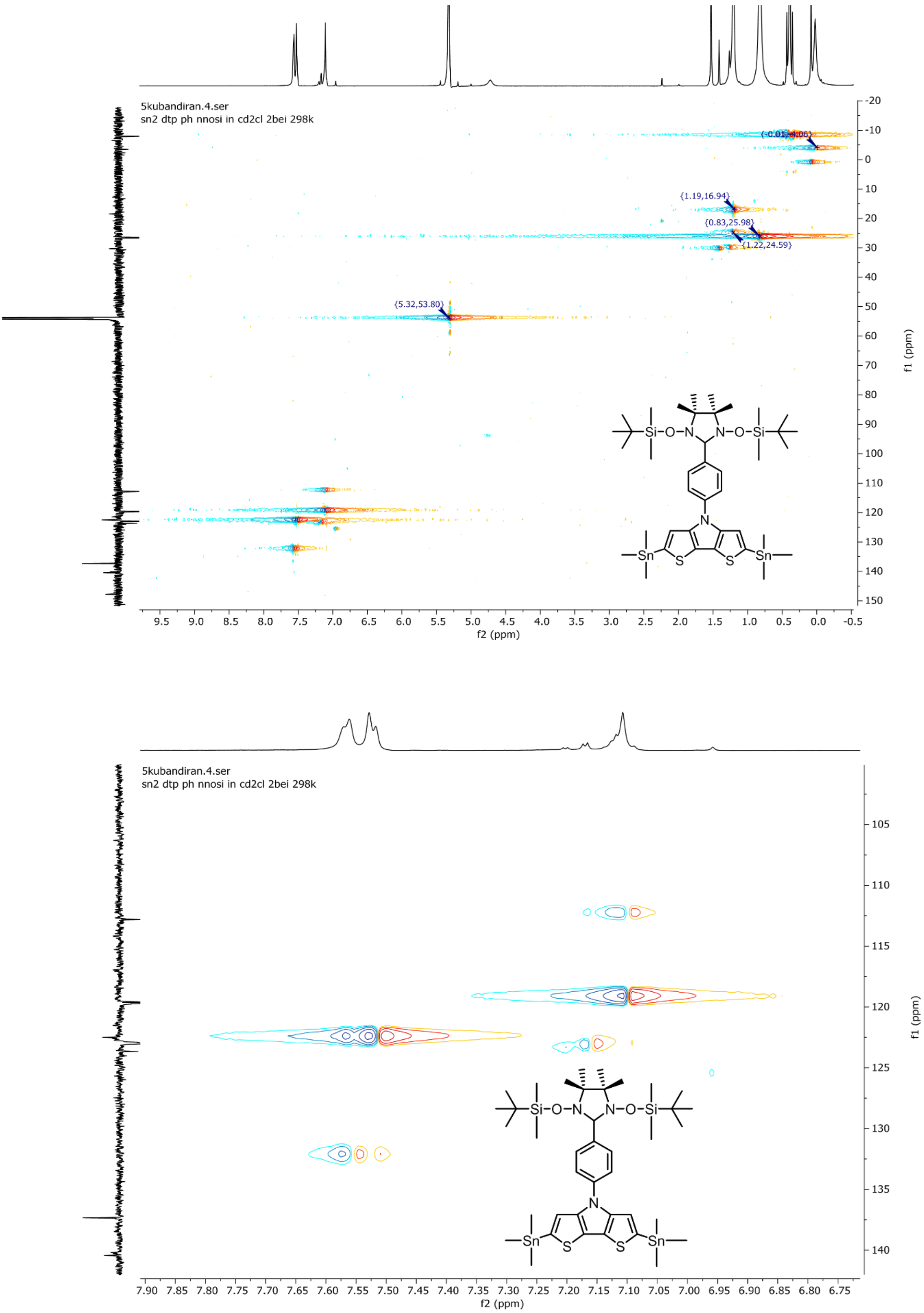

Figure A–IV.7: HSQC, 2D-NMR spectrum of **5**

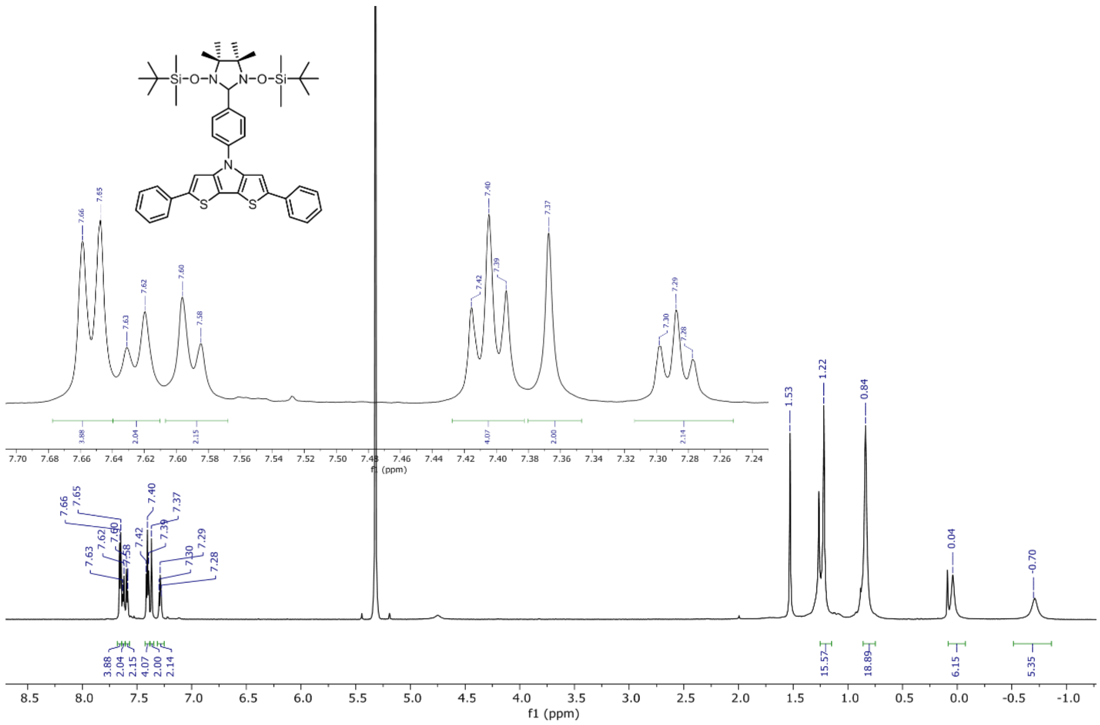

Figure A–IV.8: ^{1}H NMR spectrum of **7a**

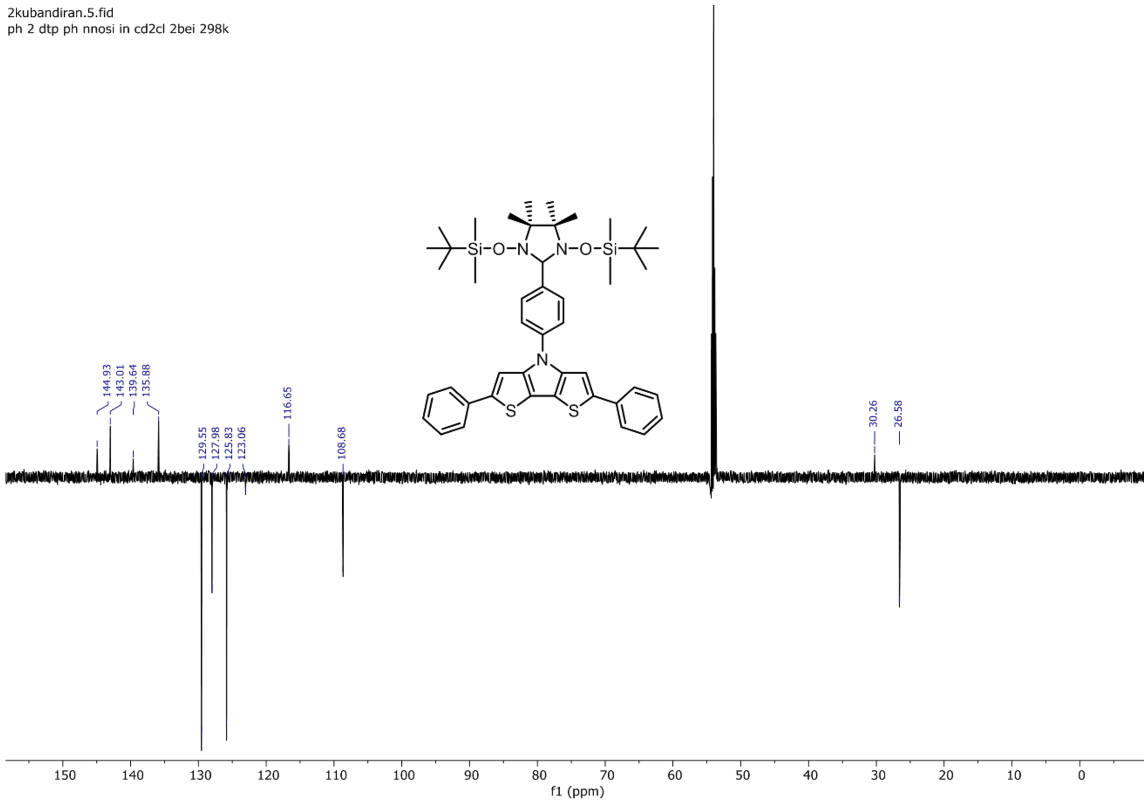

Figure A–IV.9: ^{13}C NMR spectrum of **7a**

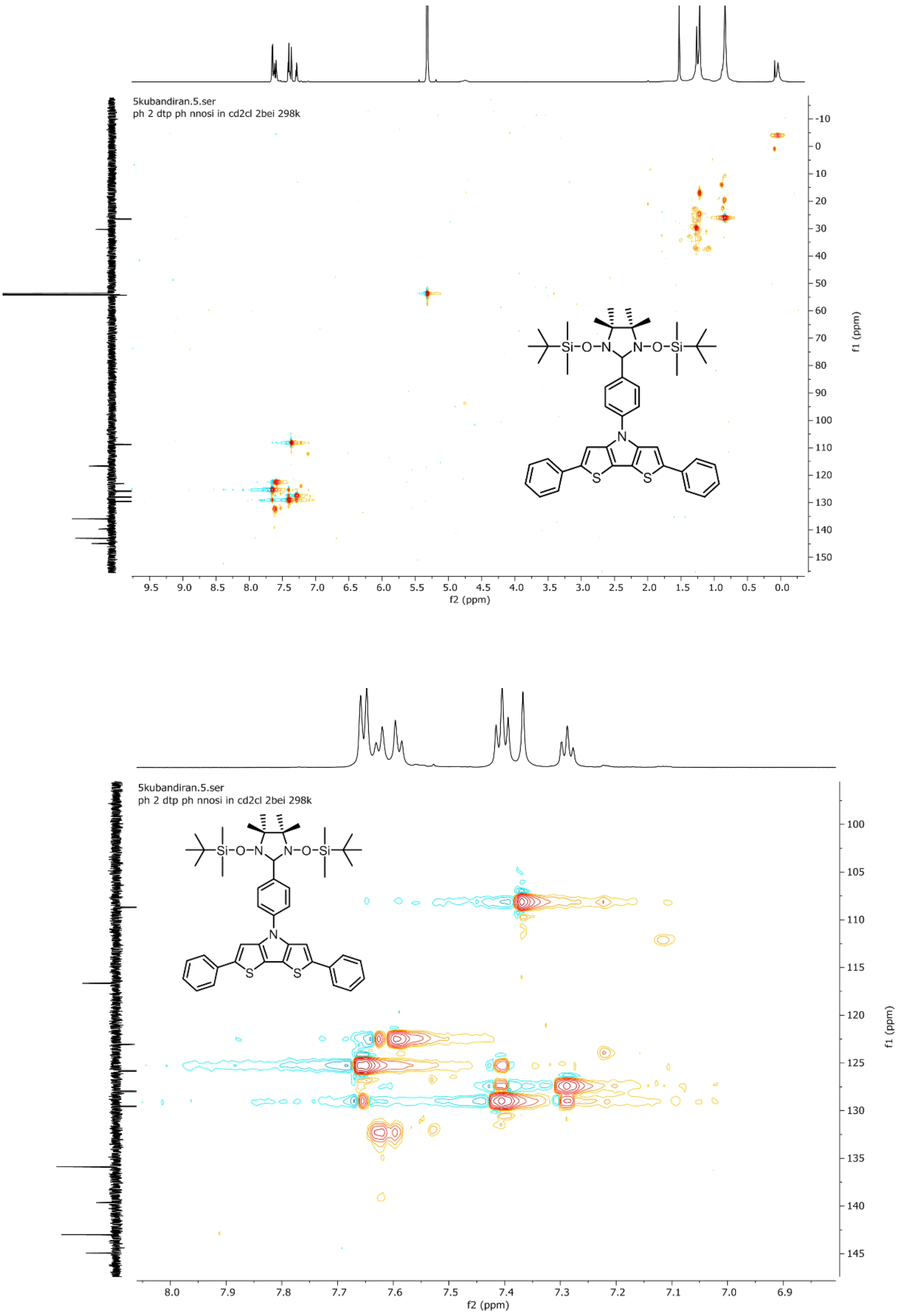

Figure A–IV.10: HSQC, 2D-NMR spectrum of **7a**

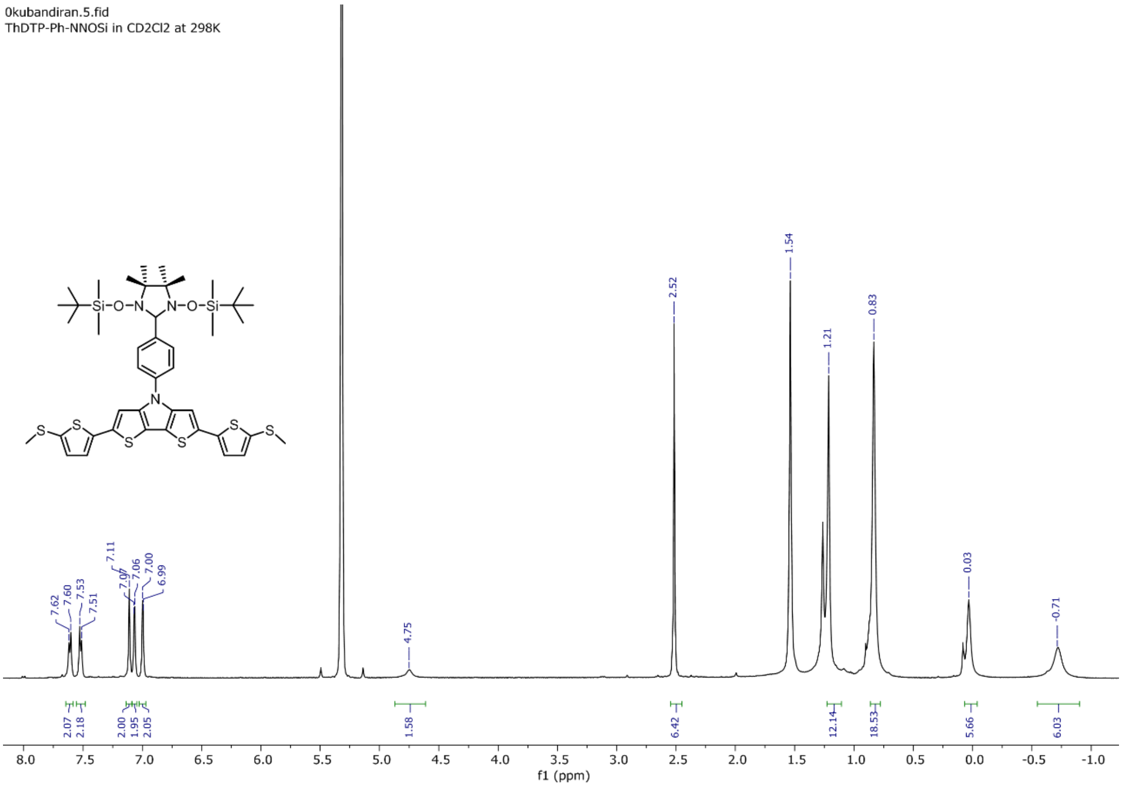

Figure A–IV.11: ^{1}H NMR spectrum of **7b**

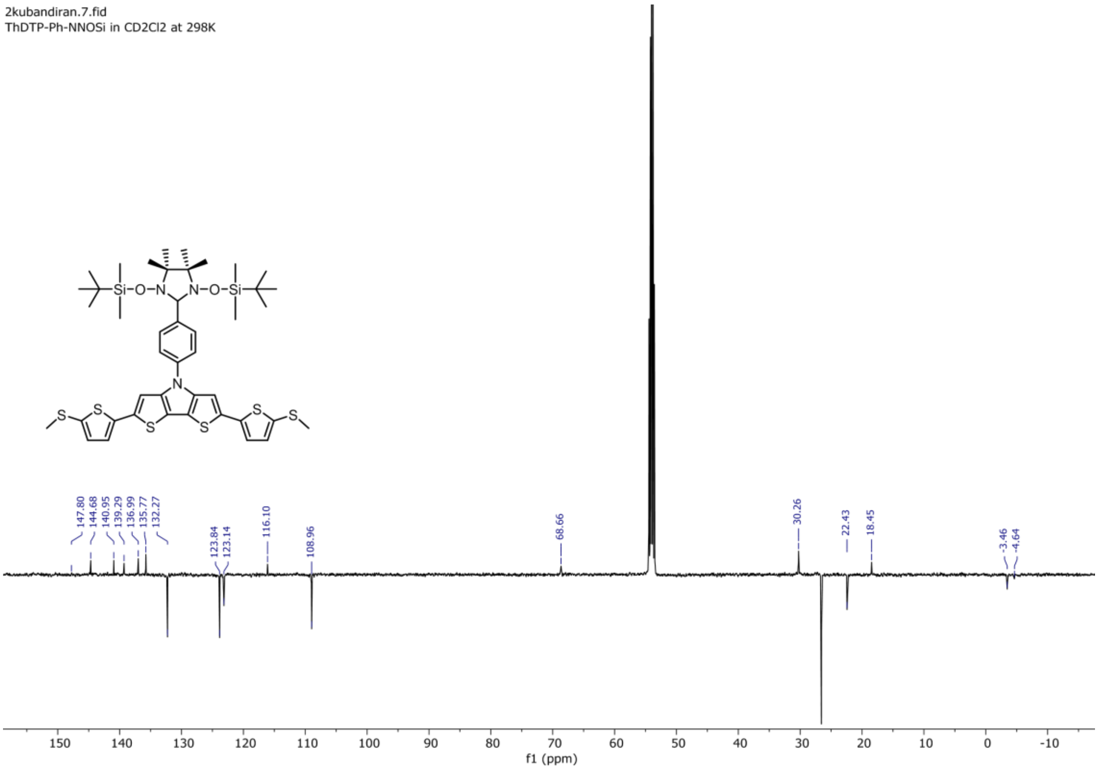

Figure A–IV.12: ^{13}C NMR spectrum of **7b**

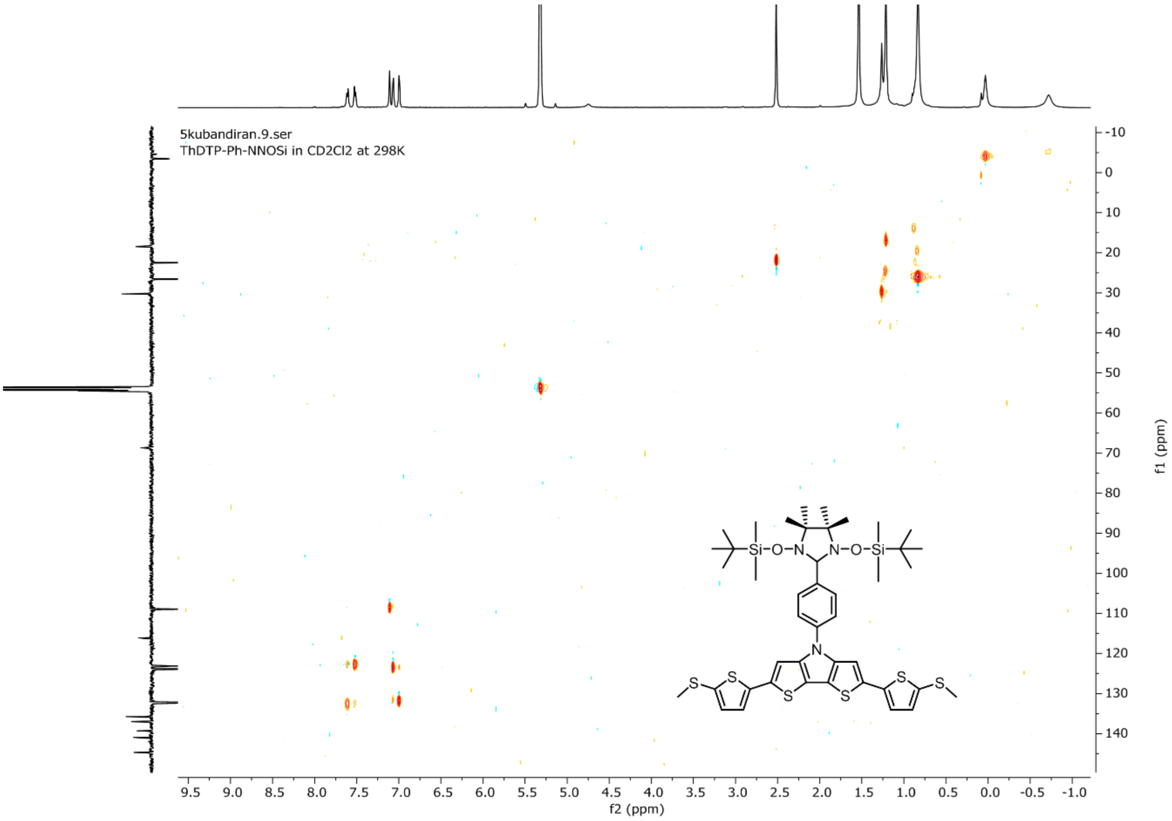

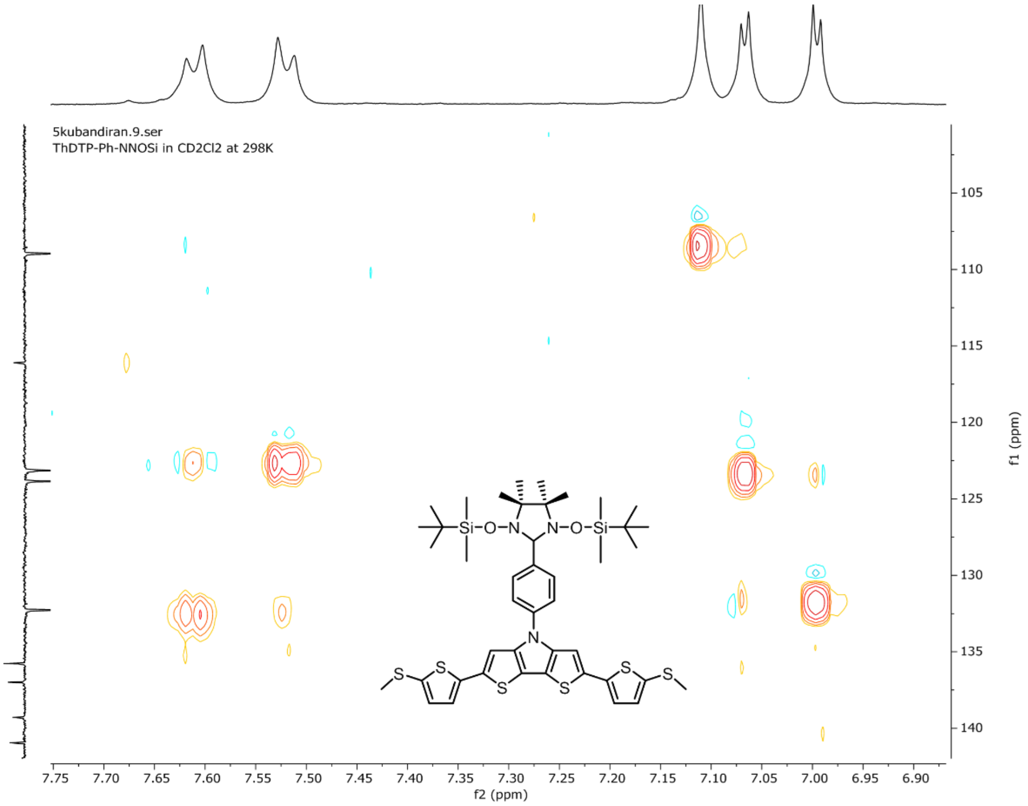

Figure A–IV.13: HSQC, 2D-NMR spectrum of **7b**

Appendix – V for chapter 5

A-V

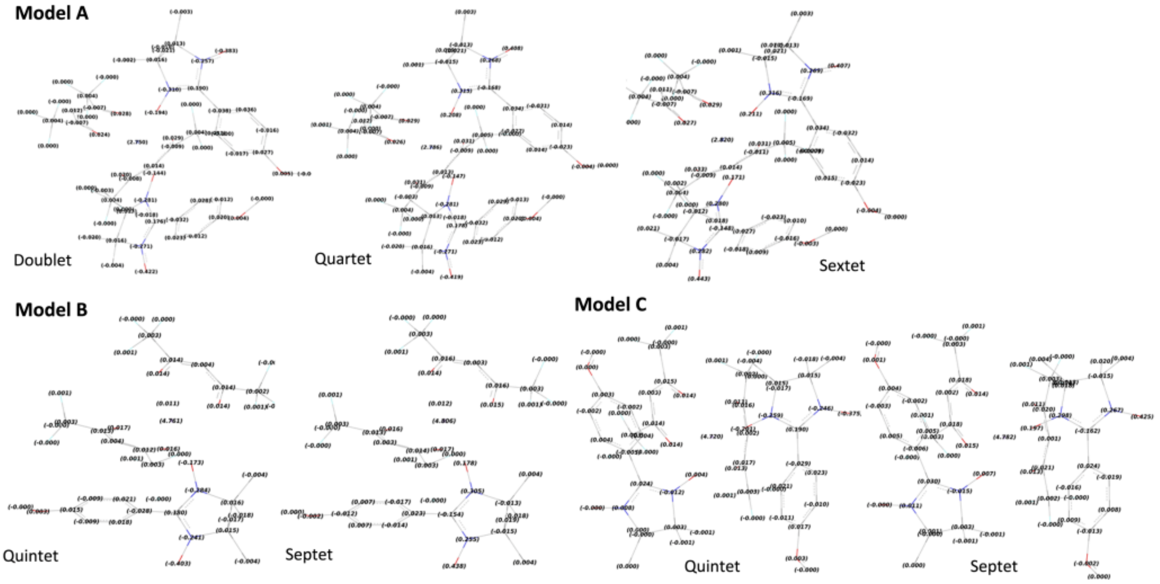

Figure A–V.1: Atomic spin densities of all multiplets of models D and Eand of the unbound radicals (with geometry taken from the X-ray structure of the complexes); hydrogen atoms are omitted because they bear negligible spin density.

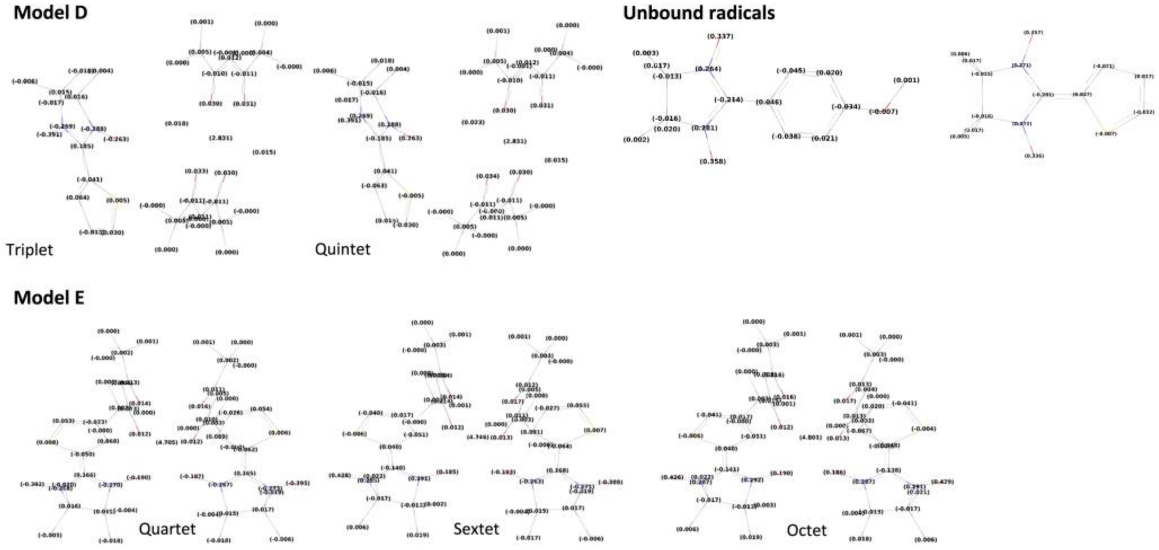

Figure A–V.2: Atomic spin densities of all multiplets of models **A**, **B**, and **C** and of the unbound radicals (with geometry taken from the X–ray structure of the complexes); hydrogen atoms are omitted because they bear negligible spin density.

Appendix – V for chapter 5

A-V